

DAL-MSS
GEOLOGICAL
R62
2009

Quaternary Landscape Evolution of the Southern Central Andes of Chile Quantified
Using Landslide Inventories, ^{10}Be and ^{36}Cl Cosmogenic Isotopes and (U-Th)/He
Thermochronology

by

José Luis Antinao Rojas

Submitted in partial fulfillment of the requirements
for the degree of Doctor of Philosophy

at

Dalhousie University
Halifax, Nova Scotia
December 2008

© Copyright by José Luis Antinao Rojas, 2008

DALHOUSIE UNIVERSITY

To comply with the Canadian Privacy Act the National Library of Canada has requested that the following pages be removed from this copy of the thesis:

Preliminary Pages

Examiners Signature Page (pii)

Dalhousie Library Copyright Agreement (piii)

Appendices

Copyright Releases (if applicable)

To my wife Elizabeth and children Newen and Sayen.

Table of Contents

LIST OF TABLES	ix
LIST OF FIGURES	x
ABSTRACT	xii
LIST OF ABBREVIATIONS USED	xiii
ACKNOWLEDGEMENTS	xiv
CHAPTER 1 Introduction.....	1
1.1. Introductory Statement.....	1
1.2. Background	4
1.2.1. Feedback between Tectonic and Surface Processes	4
1.2.2. Landscape Evolution in Convergent Margins: The Role of Landslides	5
1.2.3. The Andes: A Natural Laboratory to Analyze Landslides and Landscape Evolution.....	7
1.2.4. The Southern Central Andes of Chile.....	9
1.3. Aims and Scope for the Thesis	16
1.4. Objectives	18
1.5. A Multiple Methods Approach	19
1.5.1. Rationale for the methods used in this thesis.....	19
1.5.2. Uncertainty analysis.....	21
1.5.3. Timeframe for the present thesis	22
1.6. Structure of the Thesis	22
CHAPTER 2 Large Rockslides in the Southern Central Andes of Chile (32-34.5° S): Tectonic Control and Significance for Quaternary Landscape Evolution ..	24
2.1. Abstract.....	24
2.2. Introduction.....	24
2.3. Late Cenozoic Geologic Setting	25
2.4. Mass Wasting in the Southern Central Andes	26
2.5. Methodology	30
2.6. Results.....	33
2.6.1. Chronology and Age Distribution of Large Rockslides	39
2.6.2. Lithology.....	42
2.6.3. Geological Structures: Regional Faults	44

2.6.4. Relief.....	45
2.6.5. Slope	45
2.6.6. Precipitation and Glaciation.....	47
2.6.7. Seismicity.....	47
2.7. Discussion.....	49
2.7.1. Seismic Versus Climatic Factors as Trigger for Large Rockslides in the SCA	49
2.7.2. Controls on Distribution of Rockslide Occurrence.....	51
2.7.3. Sediment Production from Rockslides	53
2.7.4. Relevance of Rockslides for Mass Transfer in the Southern Central Andes	59
2.8. Conclusions.....	62
2.9. Appendix.....	62
2.9.1. Uncertainties in Estimated Rockslide Volumes.....	62
2.9.2. Derivation of Equations for Volume Estimation	63
2.10. Acknowledgments.....	64
2.11. References.....	65
CHAPTER 3 Quaternary Denudation Styles and Rates in the Southern Central Andes of Chile Inferred From Cosmogenic ³⁶ Cl Inventories in Stream Sediments and Modeled Fluvial Transport Rates	76
3.1. Introduction.....	76
3.2. Results.....	79
3.3. Discussion and Conclusion.....	84
3.4. References.....	87
3.5. Acknowledgments.....	91
3.6. Methods.....	91
3.6.1. Cosmogenic ³⁶ Cl in Sediments	91
3.6.2. Analysis of Fluvial Records.....	92
3.7. Supplementary Information	93
3.7.1. Supplementary Data Tables	93
3.7.2. Ackers and White (1973) bedload model description	101
CHAPTER 4 Plio-Pleistocene Exhumation and Surface Uplift of Western Cordillera Principal (33.5°S), Southern Central Andes of Chile	103
4.1. Introduction.....	103

4.2. La Gloria Pluton Area	106
4.3. Methods.....	107
4.4. Results.....	109
4.5. Discussion	112
4.5.1. Interpretation of the Age-Elevation Relationship	112
4.5.2. Thermal History Modeling	116
4.5.3. Evolution of Exhumation: Comparison with Other Thermochronometers	118
4.5.4. Overall erosional response to rapid incision and exhumation along WCP boundaries	119
4.5.5. Surface Uplift Linked to Exhumation.....	121
4.5.6. Climatic or Tectonic Trigger for Enhanced Surface Uplift and Exhumation at the End of the Pliocene.....	126
4.6. Conclusions.....	129
4.7. References.....	129
CHAPTER 5 Discussion.....	135
5.1. Introduction.....	135
5.2. Synthesis of Results	136
5.3. Pliocene to Quaternary Landscape Evolution of Cordillera Principal Between the Choapa and Cachapoal Rivers	140
5.3.1. Holocene Sediment Production by Landslides in the Maipo Catchment	141
5.3.2. Supply and Transport of Sediment at Different Time and Spatial Scales	143
5.3.3. Plio-Pleistocene Exhumation Compared to Erosion Rates	145
5.3.4. Differential Block Uplift inside WCP	148
5.3.5. Controls on Landscape Evolution.....	148
5.3.6. A General Model for Plio–Pleistocene Landscape Evolution of Cordillera Principal between 32° and 35° S	153
5.5 General Implications of the Study	157
5.5.1. Power Law Relations for Landslide Inventories.....	157
5.5.2. Landslides in Landscape Evolution	157
5.5.3. Methodological Implications for Cosmogenic Basin-Wide Erosion Rates	158
5.6. Further Questions to Be Addressed	159
5.7. Conclusions.....	160

References	161
Appendices	184
A.1. Supplementary Data File of Antinao and Gosse (2008): Large Rockslides in the Southern Central Andes of Chile (32-34.5°S): Tectonic Control and Significance for Quaternary Landscape Evolution.	184
A.1.1. Inventory Data	184
A.1.2. Detailed Examples of Rockslide-Bearing Areas in the Southern Central Andes	184
A.1.3. Cosmogenic Isotope Sample Preparation and Additional Data	195
A.1.4. References	197
A.1.5. Figure captions for the Supplementary Data File (Appendix A.1)	202
A.2. Supplementary Information for Antinao et al.: Quaternary Denudation Styles and Rates in the Southern Central Andes of Chile Inferred From Cosmogenic ³⁶ Cl Inventories in Stream Sediments and Modeled Fluvial Transport Rates	216
A.2.1. Matlab Code for Calculating ³⁶ Cl Concentration, Exposure Ages, and Erosion Rates	216
A.3. Supplementary Information for Antinao et al.: Plio-Pleistocene Exhumation and Surface Uplift of Western Cordillera Principal (33.5°S), Southern Central Andes of Chile	229
A.3.1. Analytical Results	229
A.3.2. Matlab® code used for (U-Th-Sm)/He data reduction	232
A.4. License Agreement Letter for Use of the Manuscript ‘Large rockslides in the Southern Central Andes of Chile (32-34.5°S): Tectonic Control and Significance for Quaternary Landscape Evolution’, published in Geomorphology, in the Thesis	235
A.5. Student Contribution to Manuscripts in Thesis	241

LIST OF TABLES

Table 1.1. Previous Work on Landslides and their Relevance to Landscape Evolution in Different Regions of the World	8
Table 2.1. Chronosequence Classification for the Landslide Inventory.....	32
Table 2.2. General Properties of the Rockslide Inventory.....	34
Table 2.3. Major Rockslide and Rock Avalanche Deposits in the Southern Central Andes of Chile, in Order of Decreasing Size.	36
Table 2.4. Summary of the Chronology Available for Rockslide and Rock Avalanche Deposits in the Southern Central Andes.	41
Table 2.5. Surface Exposure Ages from ¹⁰ Be and ³⁶ Cl Measurements in Boulders and Detachment Surfaces from Landslides in the Southern Central Andes of Chile.....	42
Table 2.6. Volume and Area Determination of 14 Selected Late Pleistocene-Holocene Landslides, for Estimation of a Relation Linking $V=f(A)$	54
Table 2.7. Comparison of Surface Lowering Rates (Denudation Rates) in Areas of Significant Landsliding, Rates Obtained in This Study, and Stream Incision, Sediment Transport, and Exhumation Rates from the SCA or the Vicinity.....	61
Table 3.1. Summary of Total Fluvial Transport Load, by Component, Estimated for Present Day and Last Glacial Maximum (LGM) Water Discharge Conditions in the Maipo River, San Alfonso Station.....	82
Table S1. Topography of the Catchments Selected for the ³⁶ Cl and Suspended Sediment Studies.	94
Table S2. Chemical Data for ³⁶ Cl Sediment and Rock Samples.	95
Table S3a. Summary Data for Cosmogenic ³⁶ Cl Measurements.....	99
Table S3b. Relation Between Average Upstream Slope, Average Relief and Erosion Rates Estimated From ³⁶ Cl Measurements.	99
Table S4. Summary of Suspended Sediment Data for the Three Major Rivers Draining Cordillera Principal in The Study Area, Expressed As Landscape Lowering Rates.	100
Table 4.1. Summary of aHe Ages.	112
Table 5.1. Calculation of Landscape Lowering Rates for the Maipo and Integrated Cachapoal, Aconcagua, and Choapa Catchments.....	142
Table 5.2. Comparison of Erosion and Transport Rates at Different Timescales in the Chilean Southern Central Andes.....	143
Table 5.3. Estimated Water and Sediment Discharge (from Mechanically Weathered Rock) by Major Rivers at Present Day Conditions and During LGM, Compared to Hypothetical Sediment Production by Landslides.....	144

LIST OF FIGURES

Figure 1.1. Shaded Relief DEM Showing the Main Morphostructural Units in the Southern Central Andes.	2
Figure 1.2. Schematic Depiction of the Different Surface Processes Currently Transferring Sediment from Bedrock Hillslopes to the Fluvial Network in a Setting such as the Cordillera Principal in the Southern Central Andes.....	3
Figure 1.3A. Oblique Space Shuttle Photograph of Part of the Study Area.....	12
Figure 1.3B. Representation of Characteristic Morphology for Areas inside Each Section Depicted in Fig. 1.3A.....	13
Figure 1.4. Topographic Profile at Latitude 34° S (Averaged Over a 10 km Swath, Fig. 1.5).....	14
Figure 1.5. Geological Map of the Study Area.....	15
Figure 2.1. Shaded Relief DEM (SRTM data) Showing the Main Morphostructural Units in the SCA.	27
Figure 2.2. Geological Map of the Study Area.....	28
Figure 2.3. Spatial Distribution of Rockslides inside the Study Area, Showing Relation with Morphostructural Units and Late Cenozoic Faults..	35
Figure 2.4. Rockslide Chronology.....	40
Figure 2.5. Lithological Units and Late Cenozoic Faults, and Relation to Landslides in the Study Area.	43
Figure 2.6. Distribution of Landslides Compared to Different Landscape Metrics, Present-day Precipitation, and Glacial Conditions During LGM.	46
Figure 2.7. Relation of Seismicity with the Rockslide Inventory.....	48
Figure 2.8. Estimated Location of the Detachment Point along Hillslopes for the Rockslides in the Inventory.....	50
Figure 2.9. Local Volume – Area Relationship, from Regression of Data in Table 2.6.	55
Figure 2.10. Dependence of the Landslide Frequency Density on Landslide Area for a Complete Inventory and a Historical Inventory, and the Southern Central Andes inventory.....	56
Figure 2.11. Frequency Density Functions for Different Age Classes in the SCA Inventory.	57
Figure 3.1. A. Shaded Relief Map of the Study Area and Location in Central Chile. B. Detail of the Area of WCP with Potrerillos and Macul Catchments	78
Figure 3.2. A. Detail of the Catchments with Stream Sediment samples Analyzed for ³⁶ Cl. B. Catchment-wide Average Erosion Rates Derived for Each Grain Size Fraction of Samples Analyzed in this Study.....	80

Figure 3.3. Upstream Average Slope Versus ^{36}Cl Erosion Rate for the Studied Catchments, Compared to ^{10}Be Erosion Rates Obtained for Areas with Similar Annual Precipitation.	81
Figure 3.4. A. Mean Daily Suspended Sediment Discharge and Water Discharge Data for the Maipo River at the San Alfonso Gauging Station. B. Suspended Sediment and Bedload Estimates According to the Ackers and White (1973) Model Versus Sediment Discharge Data at the San Alfonso Gauging Station.	83
Figure 3.5. Comparison of Model Total Transport of Sediment for Maipo River at San Alfonso, Suspended Sediment Transport at Aconcagua River, ^{36}Cl Catchment-Wide Average Erosion Rates for Potrerillos and Macul Catchments, and Long-Term Sediment Production by Landslides.	86
Figure 4.1. A. Shaded Relief Map of the Study area and Location in Central Chile. B. Detail of the Area of WCP Covered by the Present Study.....	105
Figure 4.2. A. Apatite (U-Th-Sm)/He (aHe) Ages for the La Gloria Pluton. B. North-South Transect (Similar to Fig. 4.1B) with the aHe Ages.....	110
Figure 4.3. Age-Elevation Relationship for the La Gloria Pluton.	111
Figure 4.4. Apatite and Zircon Fission Track Ages Obtained by Previous Studies in the Area, Shown in Relation to our Dataset (La Gloria).	114
Figure 4.5. Thermal Models from the HeFTy Code (Ketcham, 2005), for Samples TRP009 (aHe) and RCL02 (apatite fission track, Fock, 2005).....	117
Figure 4.6. Summary Interpretation of Thermochronological Data	124
Figure 4.7. Sketch of relation between hypothesized rock uplift in the WCP block at the latitude of the Colorado River valley, surface uplift, and recorded exhumation between 2-3 Ma.....	125
Figure 4.8. Sketch of the hypothesized mid-crustal block affecting tectonic evolution of the area after 2-3 Ma.	128
Figure 5.1. The Study Area, with the Distribution of the Different Studied Catchments or Component Areas of the Study.....	138
Figure 5.2. Temporal Evolution of Exhumation, Denudation and Transport Rates at Different Scales in the Southern Central Andes.	142
Figure 5.3. Distribution of Incision and Erosion Rates in and around the Study Area for a Time Window between 5 Ma and the Present.....	147
Figure 5.4. Conceptual Sketch of Landscape Evolution for the Southern Central Andes since the Miocene	154

ABSTRACT

The Andes Mountains—the largest subduction orogen in the world—are a unique natural laboratory suited to test interactions at different timescales between tectonic and surface processes. However, Andean Landscape Evolution still remains relatively understudied. This lack of knowledge will probably change during the next few years with growing understanding of Andean rates and styles of geomorphic processes.

Long term (10^6 a) landscape evolution of the high relief Cordillera Principal, in the Chilean southern Central Andes (SCA), is strongly marked by the previous tectonic history of the orogen. Exhumation rates determined from apatite (U-Th)/He low-temperature thermochronology are on the order of ~ 1 mm a⁻¹ since 2-3 Ma. The exhumation history is consistent with a segmented orogenic architecture in this region, with inherited pre-Cenozoic structures and domains that define not only the distribution of tectonic processes but also erosional styles in response to stress and deformation. Late Pliocene acceleration of exhumation from values of 0.3-0.4 mm a⁻¹ has probably occurred along with surface uplift of Cordillera Principal, creating a high elevation area still present today that displays the highest Quaternary erosion rates in the SCA. Quaternary sediment production rates from landslide inventories on a long term (10^6 a) basis (0.16 mm a⁻¹) are similar to transport rates determined at intermediate timescales (0.25-0.5 mm a⁻¹ over 10^3 - 10^4 a) with the help of terrestrial cosmogenic nuclide ³⁶Cl inventories in stream sediment. The cosmogenic nuclide study confirmed that landslides dominate denudation providing a distinctive isotopic signature to the different grain sizes of the stream sediment. At short (10 a) timescales, total fluvial transport rates, including a modeled bedload component, are similar (0.25 mm a⁻¹) to long- and intermediate-term production and transport rates. I conclude that during the Quaternary, occurrence of large landslides and increased activity of fluvial processes during glacial stages have removed efficiently mass from Cordillera Principal, in a waxing orogen. However, variability in erosion over long term timescales and the difference with inferred Quaternary exhumation indicates that a macroscale steady state has not been reached.

LIST OF ABBREVIATIONS USED

SCA	Southern Central Andes
TCN	Terrestrial Cosmogenic Nuclide
WCP	Western Cordillera Principal
CF	Cordillera Frontal
CP	Cordillera Principal
ECP	Eastern Cordillera Principal
PSRFZ	Pocuro-San Ramon Fault Zone
CC	Coastal Cordillera
CD	Central Depression
<i>fdf</i>	frequency density function
<i>pdf</i>	probability density function
Ma	Million years
ka	Thousand years
AFT	Apatite Fission Track
aHe	Apatite (U-Th)/He
PAZ	Partial Annealing Zone for fission tracks
V_L	Landslide volume
ε	factor in relation linking volume with area in a landslide (§2.7)
A_L	Landslide area
f	exponential factor in relation linking volume with area (§2.7)

ACKNOWLEDGEMENTS

I am very grateful to my advisor John for his incredible enthusiasm, support and encouragement throughout the duration of my project. His remarkable sense of humor in the field rivals with his pursue of perfection while reviewing my bad writing throughout all these years. I am also deeply indebted to Marcos Zentilli who was especially encouraging of my work during the writing stage of this thesis, and to Jose Cembrano, who back in 2002 was the first to suggest that I contacted John here at Dalhousie. I want also to express my sincere thanks to Chris Beaumont, who challenged my circular arguments and messy conjectural logic at many committee meetings.

I must acknowledge all the people in Chile and Argentina who contributed to the long field seasons between 2004 and 2007, especially my friends Rodrigo Rauld, Rita Arqueros, Magdalena Prat, Luis Lepe and Cristobal Fernández. SERNAGEOMIN in Chile provided logistic support for most of the fieldwork. Minera La Perla manager René González provided not only support for the horseback trips to the Granito and Relvo canyons, but continuous access to the Upper Colorado canyon, one of my favorite areas in the Andes of Santiago. GasAndes provided access to the Upper Maipo valley, while Aguas Andinas allowed us to sample boulders in the protected areas of the Laguna Negra-Yeso reservoirs.

Special thanks to Sophie Baker and Stella Moreiras who introduced me to the lonely landscapes of the Diamante and Mendoza rivers and who discussed with me many ideas about tectonics and surface processes in the region. I enjoyed many enlightening field discussions with Eric McDonald (DRI), Ed Evenson (Lehigh University), Rodrigo Rauld (Univ. de Chile), Danny Stockli (Kansas) and Anne Reuther. Scientific discussions with Reynaldo Charrier, Marcelo Farias, and Alejandro Fock during my frequent visits to Universidad de Chile framed much of the ideas expressed in this thesis.

Guang Yang and Anne Reuther helped me on my constant inquiries about cosmogenic isotope chemistry procedures. Debra Wheeler helped me negotiate the mineral separation process and was always a good company at long evenings of picking apatites. I am also grateful to Peter Reynolds and Keith Taylor of the Dalhousie Geochronology Centre for their support on the development of the (U-Th)/He analyses, and especially to Sandy Grist, who thought me the basics on apatite picking.

Financial contributions to this research were made through a NSERC Discovery Grant and ACOA-AIF funds to John Gosse, and a GSA Graduate Student Grant to the author. Shallow seismicity data used in Chapter 2 has been collected by Servicio Sismológico de Chile (Univ. de Chile), and R. Farías (Univ. de Chile) kindly gave access to relocated epicentral locations produced using SPHREL/SPHYFIT code (S. Roecker), in the framework of ANILLO Project ACT no. 18 (Chile). Discharge and suspended sediment records were kindly provided by J. Aguirre (Dirección General de Aguas, Chile)

I must acknowledge to all the fellow students who insisted in keeping my social calendar always busy during these years: thanks to Sofie, and especially Alan, whom was instrumental in avoiding collapse because of the 20 hours writing sessions during my last weeks at Dalhousie. We also enjoyed great arguments about cosmogenic isotopes, landscape evolution and women over long beer nights.

Finally, I must acknowledge the support of all my family and friends on this enterprise, in Halifax and Chile, especially my wife Elizabeth, son Newen, and daughter Sayen. My immense thanks to my parents Andrés and Guacolda who are a big part of my achievements and who also heroically participated in some of the fieldwork at 3400 m a.s.l. I am deeply indebted to all of you. Thanks.

CHAPTER 1 Introduction

1.1. Introductory Statement

Landslides constitute a serious natural hazard (e.g. Blodgett et al., 1998) and also play an important role in the long-term shaping of landforms (e.g. Densmore et al., 1997), and in the delivery of large volumes of sediment (up to km^3 of material in seconds, e.g. Strom and Korup, 2006) to streams in active orogens, increasing the overall efficiency of mass transfer processes between hillslopes and fluvial channels. The effect that landslides have on landscape evolution of active mountain systems has been debated (Burbank et al., 1996; Hovius et al., 1997, 2000; Korup et al., 2007), although difficulties in obtaining accurate temporal and volumetric data of stochastic events like large-scale landslides has precluded appropriate documentation of their long-term influence on landscape evolution, and current knowledge mostly has been restricted to short term (10^2 a) timescales (e.g. Hovius et al., 1997). Systematic characterization of regional scale, long-term (10^4 - 10^6 a) landslide populations and their effects on sediment production and delivery can provide the necessary data to appropriately include mass wasting processes into a more complete analysis of landscape evolution in active orogens.

This thesis aims to quantify the effect landslides have on long term landscape evolution of an active convergent margin like the southern Central Andes of Chile (Fig. 1.1) and to determine under which conditions this effect become predominant over other surface processes acting in the region (Fig. 1.2). To obtain landslide sediment production rate on a long term (10^6 a) basis, this study introduces a chronologically calibrated landslide inventory, specifically aimed for landscape evolution analysis. To compare transport rates at intermediate timescales (10^3 - 10^4 a), I introduce for the first time a method that applies cosmogenic ^{36}Cl to calculate catchment-wide average denudation rates, which is later used in the same landslide-prone area. The cosmogenic study is instrumental in solving key questions with regard to the role of mass wasting processes in landscape evolution. Finally, this thesis provides exhumation rates from a new low-temperature thermochronology study in the same area at 10^6 a timescales and compares it to the previous datasets to allow inferences about topographic and erosional steady state in the orogen. The data sets constraints and allow the development of a conceptual

landscape evolution model for the Late Pliocene and Quaternary of the southern Central Andes, which takes into account the complex tectonic and climatic factors that might have influenced this region.

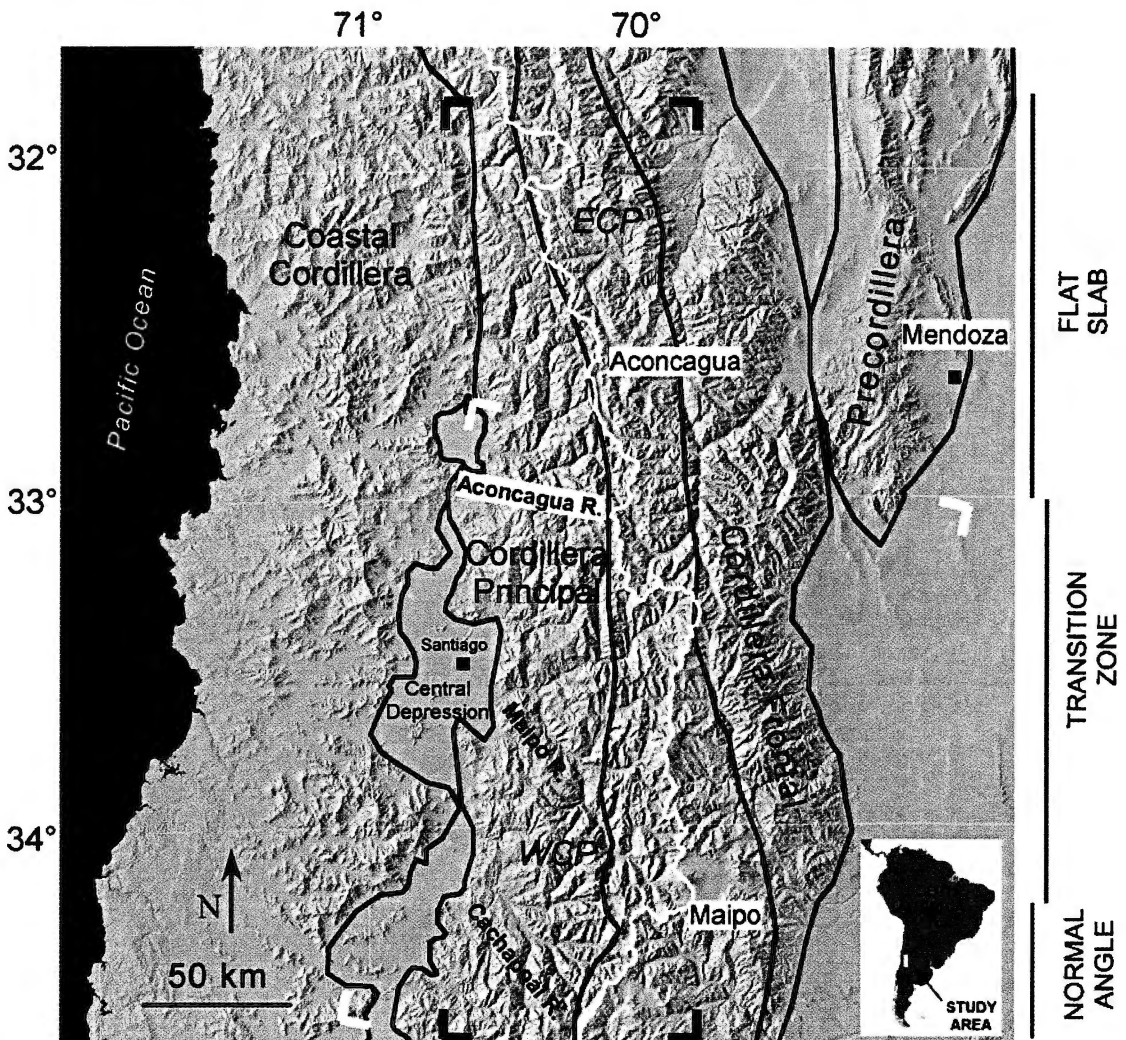


Figure 1.1. Shaded Relief DEM (SRTM data) showing the main morphostructural units in the southern Central Andes. The continental divide (white) marks the political boundary between Chile and Argentina. The study area is marked by the position of the four black line corners. The white line corners mark the area covered by the photograph shown in Fig. 1.3.

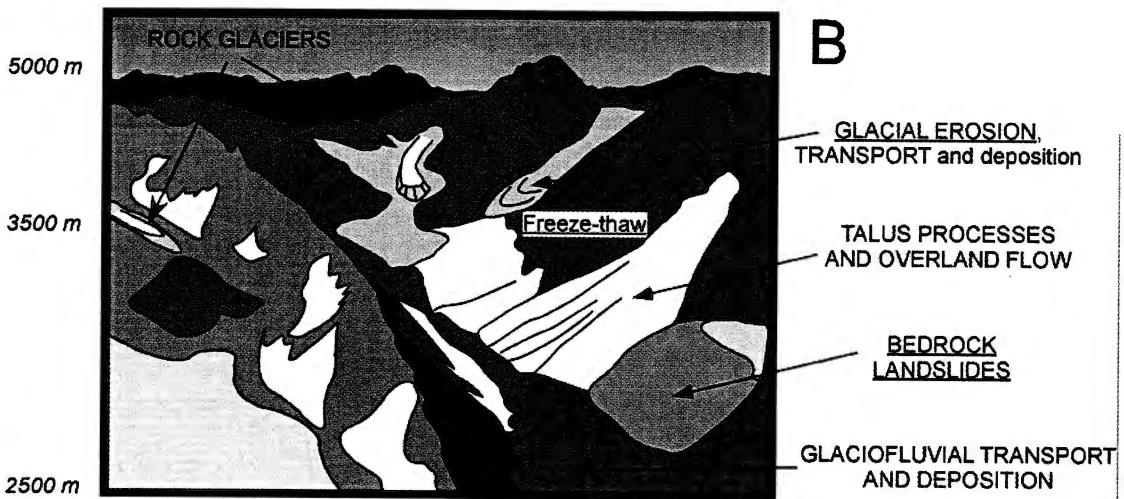
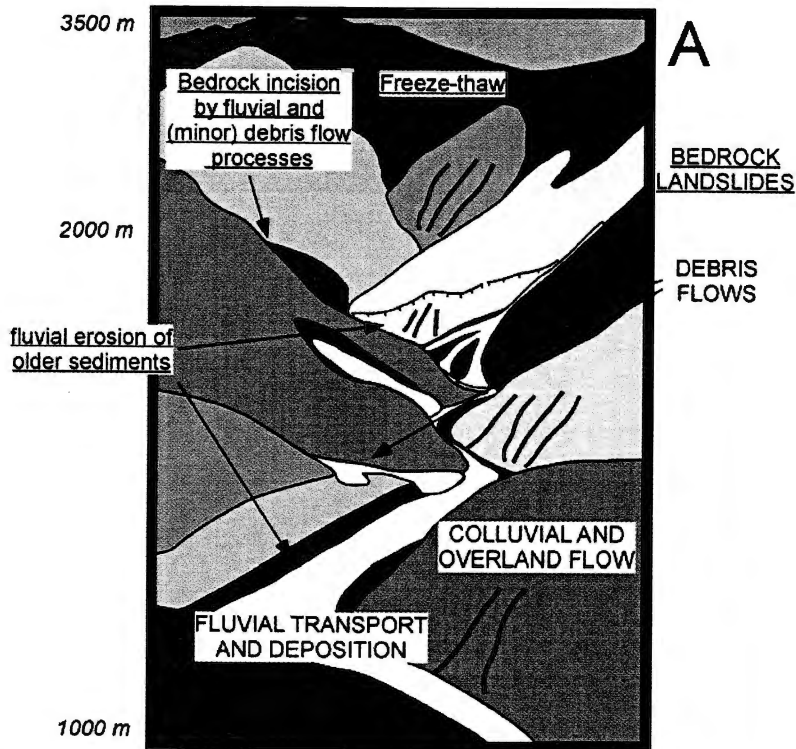


Figure 1.2. Schematic depiction of the different surface processes currently transferring sediment from bedrock hillslopes to the fluvial network in a setting such as the Cordillera Principal in the southern Central Andes (Fig. 1.1). Approximate elevations where processes operate are indicated in italics. Processes that detach bedrock are underlined; processes that can transport sediment are in uppercase. Some processes fracture bedrock and transport it at the same time, like large bedrock involved landslides. A. Main processes in the middle to low (1000-3500 m) elevation WCP (Western Cordillera Principal) B. Main processes in the middle to high (2500-5000 m) elevation Eastern Cordillera Principal (ECP).

1.2. Background

1.2.1. Feedback between Tectonic and Surface Processes

Recognition of the dynamic interaction on disparate timescales (decades to millions of years) between tectonic and surface processes appeared early in the development of geomorphological paradigms. The appreciation of this relation can be recognized for example in Hack's ideas about dynamic equilibrium in landscapes (Hack, 1960), but it can be traced back to almost a century earlier in the publications of Gilbert (1877) and Davis (1899), and it is acknowledged as a part of what is known now as Landscape Evolution Models (Pazzaglia, 2003), which are statements about the nature of the interaction between internal and external processes that change the landscape over different space and time scales. Davis (1899) described the Geographic Cycle, in which the adjustment of hillslope evolution to river incision is a dynamic feature essential in maintaining steady state topography (i.e. the elevation and shape of landforms do not change with time, despite non zero tectonic and erosional fluxes) over timescales that approach those of the lifetime of an orogen. However, Davis did not evolve an idea of how hillslopes behave over that particular time. Penck (1924) was the first to envision the response that hillslopes would show to a protracted impulse like the base level fall of an entire region —an impulse that might be triggered by tectonics. His conceptualization of hillslope evolution was driven by the idea of slope replacement (Penck, 1924); convex hillslopes were envisioned by Penck as the result of the early evolution in a waxing orogen, which still has not reached a macro-scale equilibrium between erosional and tectonic fluxes (cf. Hovius, 2000; Lavé and Burbank, 2004).

The assessment of equilibrium only can be performed under appropriate timescales. Many erosional processes are short-term (seconds to years), discrete, stochastic events, including landslides and major floods, and response times of a single hillslope in terms of sediment flux are therefore different to response times of entire continental-scale catchments, the latter corresponding to the relevant timescale to address landscape evolution of an orogen. Therefore, to address the development of either erosional or topographic steady state of any orogen (cf. Montgomery, 2001), inferences must be made on scales of thousands of km² and thousands to hundreds of thousands of years.

During most of the 20th century, analysis and incorporation of a dynamic feedback between tectonic and surface processes into landscape evolution models remained in the descriptive realm. The lack of appropriate chronological techniques hindered the complete analysis of process rates and timing of Pleistocene events, which carry with them critical information about their forcing controls. One of these controls, climate change, and specifically high variability in climate, is considered a key component thought to drive surface processes, through precipitation involvement in fluvial discharge, hillslope weathering and overall erosion (Bull, 1991; Peizhen et al., 2001). Quantification of processes acting beyond the limit of radiocarbon remained difficult until the 1980's when the advent of techniques like luminescence dating and TCN exposure dating revolutionized the way to understand quantitatively landscape evolution (e.g. Gosse and Phillips, 2001; Bierman and Nichols, 2004). At the same time, tectonic analysis approached timescales of climate change, with the help of thermochronology and neotectonic analysis, and rock deformation measured at timescales of days to millennia, enabling for the first time in the 1990s a fully coupled comparison of tectonic and surface processes to test their interplay in landscape evolution models (e.g., Wobus et al., 2005, 2006; Dadson et al., 2003; Huntington et al., 2006).

1.2.2. Landscape Evolution in Convergent Margins: The Role of Landslides

Landscape evolution in convergent margins is driven by the competition between the mainly compressional tectonic processes which accrete rock mass and produce rock uplift, and the erosional processes controlled principally by climate. Erosion styles, in turn, have been shown to depend partially on tectonically forced denudation rates (e.g., Montgomery and Brandon, 2002; Dadson et al., 2003). An end-member case is reached when a given threshold in rock uplift is passed (Burbank et al., 1996), which causes rates of erosional processes to be independent of external forcing (slope, precipitation), and only massive gravitational processes can act as a sufficiently efficient mechanism of denudation under these high rock uplift rates (e.g. Burbank et al., 1996, 2003; Lavé and Burbank, 2004; Binnie et al., 2007; Reinhardt et al., 2007).

Although it is widely recognized that landslides play a major role in the evolution of mountain regions (e.g. Burbank et al., 1996, 2003; Hovius et al., 1997, 2000; Hovius,

2000), only a few studies have determined the amount of sediment produced by mass wasting that is supplied to streams. These studies have relied mostly on historical databases and field- and remote sensing-based short-term inventories to resolve the spatial distribution of events (e.g. Adams, 1980; Keefer, 1994; Hovius et al., 1997, 2000; Barnard et al., 2001; Martin et al., 2002; Lavé and Burbank, 2004; Korup, 2005b). However, the accuracy in mapping landslide spatial and temporal distributions over short-term timescales has not been achieved over long-term timescales. Although a few studies have documented estimates for erosion rates derived from landslides for timescales on the order of millennia, these records span no more than the upper part of the Holocene (e.g. Gomez et al., 2002), usually covering only a few hundred years (e.g. Hovius et al., 1997).

The conclusion of most of these studies (Table 1.1) is that erosion rate estimates tend to be dominated by landslide-produced sediment, when compared to short term estimates by other metrics in the landscape (e.g. suspended sediment measurements). However, there is no agreement in the rates under which mass wasting becomes dominant ($0.25\text{-}1.8\text{ mm a}^{-1}$ as minimum rates for 100% dominated by landslides, with an overlap with the range $1.5\text{-}2.4\text{ mm a}^{-1}$ as maximum rates where they are not dominant). All the areas where landslides can account for up to a 100% are tectonically active and most are humid. The different properties and effects that mass wasting processes like shallow, frequent small ($10\text{-}10^5\text{ m}^3$) debris flows have compared to infrequent large catastrophic rockslides and rock avalanches ($>10^5\text{ m}^3$) also might have a bearing on the observed differences between studies.

Only a few of these studies have been accomplished in semiarid areas or in areas with a high proportion of large (areas $> 10^5\text{ m}^2$) bedrock involved landslides (rockslides and rock avalanches). It cannot be assumed that the large proportion of sediment delivered by landslides to the fluvial network in the above mentioned conditions is applicable to other climatic regimes, other landslide size-type spectra, or other timescales; therefore this effect must be investigated by extending the observational window as accurately as possible.

1.2.3. The Andes: A Natural Laboratory to Analyze Landslides and Landscape Evolution

To quantify the above mentioned threshold —over which all mass removal is performed by large scale landslides—, spatial and temporal patterns of variability in erosion and exhumation need to be analyzed. Ideally, a spectrum of conditions where to establish comparisons will be more suitable to this task, and these conditions are available for example at transitional areas where changes in climate and tectonic regimes have been recorded in time and where they also can be recognizable in space.

Even considering the advances in techniques that allow us to measure rates or timing of processes, they do not assure success in studying these phenomena and rates, as large amounts of data are still needed to assure completeness. Under this restriction, very few areas display an analysis of the whole range of interaction possibilities of tectonic and surface processes (e.g. Burbank et al., 2003; Dadson et al., 2003; Lavé and Burbank, 2004; Wobus et al., 2006, 2008). The Andes —the largest subduction orogen in the world—, still remains relatively unexplored at this respect (e.g. Schildgen et al., 2008), although this lack of knowledge will probably change during the next few years, as a growing amount of Andean data pertaining to estimates of geomorphic processes like fluvial incision, hillslope and stream sediment flux, and overall landscape erosion is being developed in different segments of the orogen (e.g., Farías et al., 2008; Hebbeln et al., 2007; Schildgen et al., 2008; Melnick, 2007, Aguilar et al., 2008, Riquelme et al., 2008), along with determination of rates and styles of tectonic processes (e.g., Farías et al., 2008; Lavenu and Cembrano, 2008). A rich and complex picture of the interactions between surface and tectonic processes is starting to appear, and future Andean analyses will provide us with a deeper understanding of these interactions.

Table 1.1. Previous work on landslides and their relevance to landscape evolution in different regions of the world.

Region (amount of annual precipitation in m)	Dominant type of landslides	Dominant volume of landslides [m ³]	Observation period for landslide occurrence [years]	Proportion of sediment flux explained by landsliding	Reference
Taiwan (1.8->7.0)	Shallow and bedrock-involved landslides	10 ² -10 ³	10-30	~100 %	Hovius et al. (2000)
Central Appalachians of Virginia (0.75-1.5)	Debris flows, shallow landslides	10 ³ -10 ⁵	50	47-63%	Eaton et al. (2003)
Southern Alps of New Zealand (1.25-15.0)	Shallow debris slides and bedrock-involved landslides	10 ² -10 ⁷	60	~100 %	Hovius et al. (1997)
Central Idaho (0.75-1.3)	Debris flows and shallow slides	Not specified	100	70-97%	Kirchner et al. (2001)
Eastern North Island, New Zealand (1.2-2.4)	Shallow landslides	10 ² -10 ³	70	15%	Reid and Page (2003)
Different regions of the planet	Shallow debris slides and bedrock-involved landslides	Not specified	Mostly 100-200, in some areas up to 1300 years	10 - >100% (means that erosion rates from landslides are larger than calculated from suspended sediment from rivers)	Keefer (1994)

One of the main features that make the Andes so interesting to study interaction between surface and tectonic processes is the presence of a large variability in climate and tectonic settings. Specifically, tectonic and climatic processes can be recognized as competing forces that shape the orogen in this orogen. Tectonic segmentation is expressed along strike (e.g. Mpodozis and Ramos, 1989) is mostly derived from and expressed in pre-Cenozoic tectonic structures that appear to control not only deformation (Giambiagi et al., 2003b) but indeed denudation styles in response to orogeny (e.g., Charrier et al., 2002, 2007; Farías et al., 2008). Differences in climate and topography along and across the Andes has caused denudation rates to vary between those similar to intracratonic areas (e.g., Dunai et al., 2005; Kober et al., 2007; Riquelme et al., 2008) to very high rates (e.g. areas inside the southern Central Andes display incision rates similar to those observed in the NW Himalaya, e.g. Farías et al., 2008; Spikings et al., 2008). These properties make the Andes a unique large-scale laboratory where relations between erosion and tectonics can be studied under a wide range of conditions.

This thesis will provide more elements to study the interaction of tectonic and surface processes in a specific area of the Andes. In this study, for example, the relation of landslide-derived sediment production and transport at different timescales will be analyzed, but by no means represents an exhaustive analysis of surface processes in the area.

1.2.4. The Southern Central Andes of Chile

The southern Central Andes of Chile (SCA) appear above a transition between flat slab and steep subduction angle of the Nazca Plate (Fig. 1.1). Between 27° and 33°S subduction is sub-horizontal and modern volcanism is absent, while between 33° and 46°S the subduction angle reaches 30° (Cahill and Isacks, 1992). Orogen-scale morphostructural units in the SCA are, west to east: Coastal Cordillera, Central Depression, and Cordillera Principal (CP, Fig. 1.3).

The Coastal Cordillera at the latitude of the study area is composed of Mesozoic intrusive and volcanoclastic rocks (Fig. 1.5), which are tilted and separated of the Cenozoic sequences by a series of reverse faults first inverted in the last compressional episode that started during the Late Miocene (Fock, 2005). The Central Depression

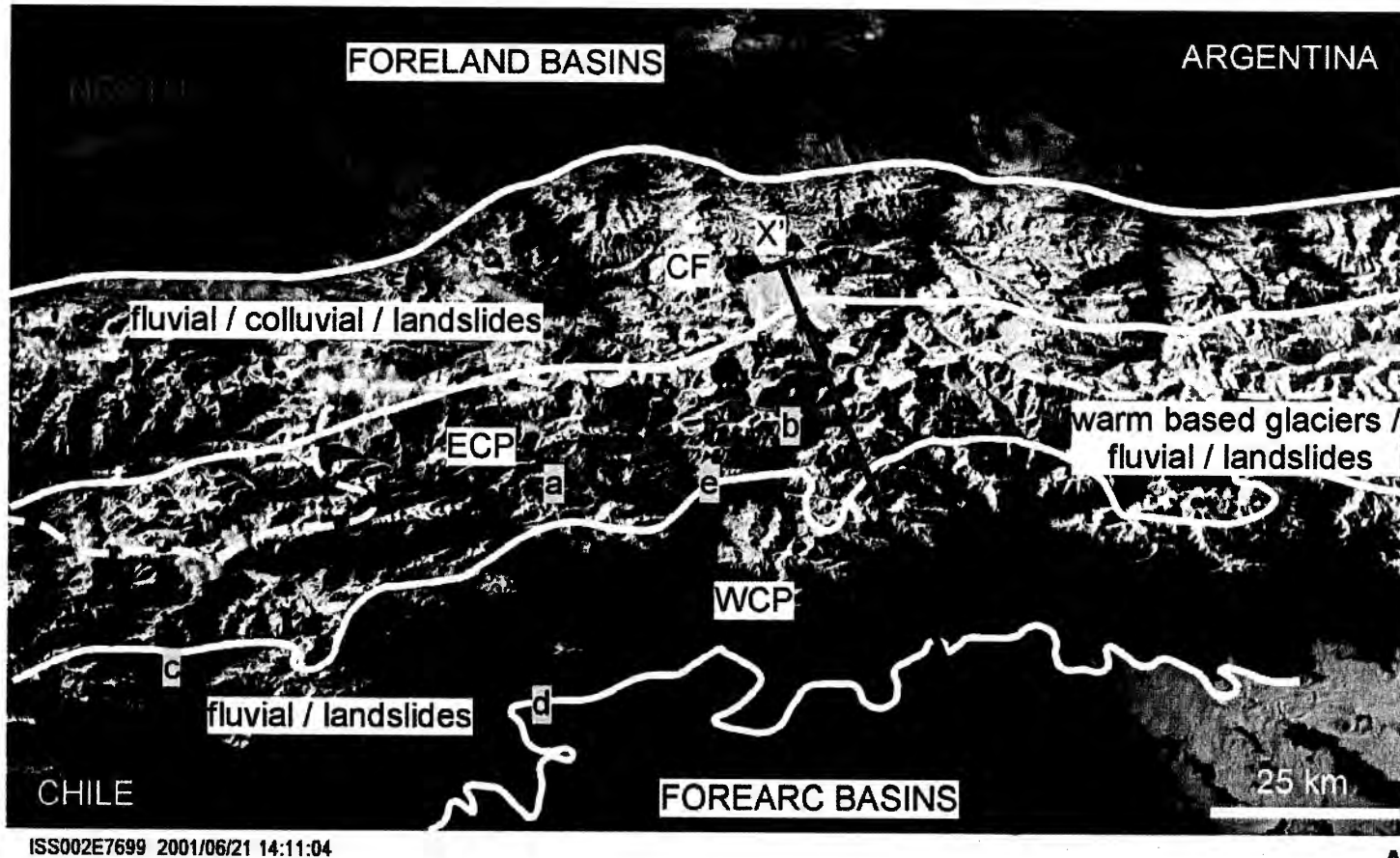
consists of a Pliocene to Quaternary sedimentary and ignimbrite fill. The sedimentary deposits have a maximum estimated thickness of 500 m beneath Santiago. The basement of the Central Depression is composed of the Mesozoic units of the eastern flanks of the Coastal Cordillera, which are in structural contact with the Cenozoic sequences of western Cordillera Principal (WCP) (Sellés, 1999; Fock, 2005). WCP (Fig. 1.4) comprises Oligocene-Miocene continental volcanoclastic rocks, intruded by Miocene-Pliocene granitoids (Fig. 1.5). The Oligocene-Miocene rocks were deposited in an extensional intra-arc basin (Abanico Basin, Charrier et al., 2007) which developed a tectonic inversion during the Late Oligocene-Early Miocene (Godoy et al., 1999; Charrier et al., 2002, 2005). This event peaked in the eastern areas during Early Pliocene times (Fock, 2005), before a well documented shift in the major axis of deformation to the foreland in Argentina (Giambiagi et al., 2003a). Near the continental divide, the eastern Cordillera Principal (ECP) comprises sedimentary and volcanic Jurassic to Cretaceous rocks organized in fold-and-thrust belts (e.g. Aconcagua Fold and Thrust Belt, AFTB) that are capped by Plio-Quaternary volcanic rocks.

In the eastern boundary of WCP, the structural history is relatively well known during the Miocene, as it is well constrained by the history of the AFTB (cf. Giambiagi et al., 2003a, Fock et al., 2006; Farías et al., 2008) although relatively few data constrains the Pliocene evolution in the area. This situation is different from the relatively well known Plio-Quaternary history of movement at the active mountain front structures in the ECP and Cordillera Frontal in Argentina (e.g., Giambiagi et al., 2003a). The structural features and timing of the tectonic events along the western boundary of the WCP (Fig. 1.3B, panel d) are not completely clear, as opposed to the ECP. Recently Rauld (2002) reported Late Pleistocene westward-verging reverse slip east of Santiago, supported later by Fock (2005) and Campbell (2005).

In Cordillera Principal, two different Late Cenozoic deformation events have been identified from microstructural analysis (e.g., Lavenu and Cembrano, 1999). One is a Pliocene E-W compression event, proposed to have happened between 4.5-2.8 Ma (Lavenu, 2006; Lavenu and Cembrano, 1999, 2008) and the last one is a proposed NS compression, Quaternary in age, deforming some of the Pleistocene fluvial terraces in the area (Lavenu and Cembrano, 1999, 2008).

Apatite fission track (AFT) and $^{40}\text{Ar}/^{39}\text{Ar}$ thermochronology indicate that the CP has been exhumed mainly during two different periods: first in the Early Miocene, and again since the Late Miocene (Kurtz et al., 1997; Maksaev et al., 2003; Fock, 2005; Farías et al., 2008). A knickpoint retreat model calibrated using local bedrock incision rates of post-Miocene sedimentary and volcanic sequences in WCP, which range between 0.02-2.4 mm a⁻¹, was used by Farías et al. (2008) to test different scenarios of surface uplift for WCP (partially concurrent with Coastal Cordillera uplift). These authors proposed a surface uplift of ~1.5-2.0 km for the Coastal Cordillera and ~2.0-2.5 km for WCP during the Late Miocene, followed by a slow erosional response inside CP. It must be noticed though that the Coastal Cordillera at these latitudes has apparently not been significantly exhumed since the Late Cretaceous-Late Eocene, as revealed by AFT data on rocks of the Coastal units in the study area (Cembrano et al., 2003; Campbell, 2005; Fock, 2005).

Morphologically, some areas of the southern Central Andes appear very similar to the NW Himalayas (e.g. Burbank et al., 1996) or the Southern Alps of New Zealand (Hovius et al., 1997; Korup, 2006a), with deeply incised bedrock valleys where relief is in excess of 3 km over a few km and slope angles commonly exceed 30°. The central part of the orogen (ECP) has wider valleys than WCP (Fig. 1.3B, panel b), with extensive alluviation and bedrock that appears only in the higher elevations ridges. Warm based glaciers appear to dominate spatially over deposits from other surface processes in this region (Fig. 1.1, Fig. 1.3B panel a), as opposed to WCP, where large landslides are prominent features in the hillslopes (Abele, 1981, 1984; Chiu, 1991; Fig. 1.4).



A

Figure 1.3. A. Oblique Space Shuttle photograph (NASA image ISS002E7699, 2001/06/21) of part of the study area (location in Fig. 1.2). The orogen is divided into regions where the indicated processes appear to dominate. Their boundaries are close to the tectonic boundaries defined for Western and Eastern Cordillera Principal (WCP and ECP) and Cordillera Frontal in Argentina. The continental divide is marked with a dashed yellow line. The approximate position of the eastern portion of the profile shown in Fig. 1.4 is marked X' and then extends towards the west.

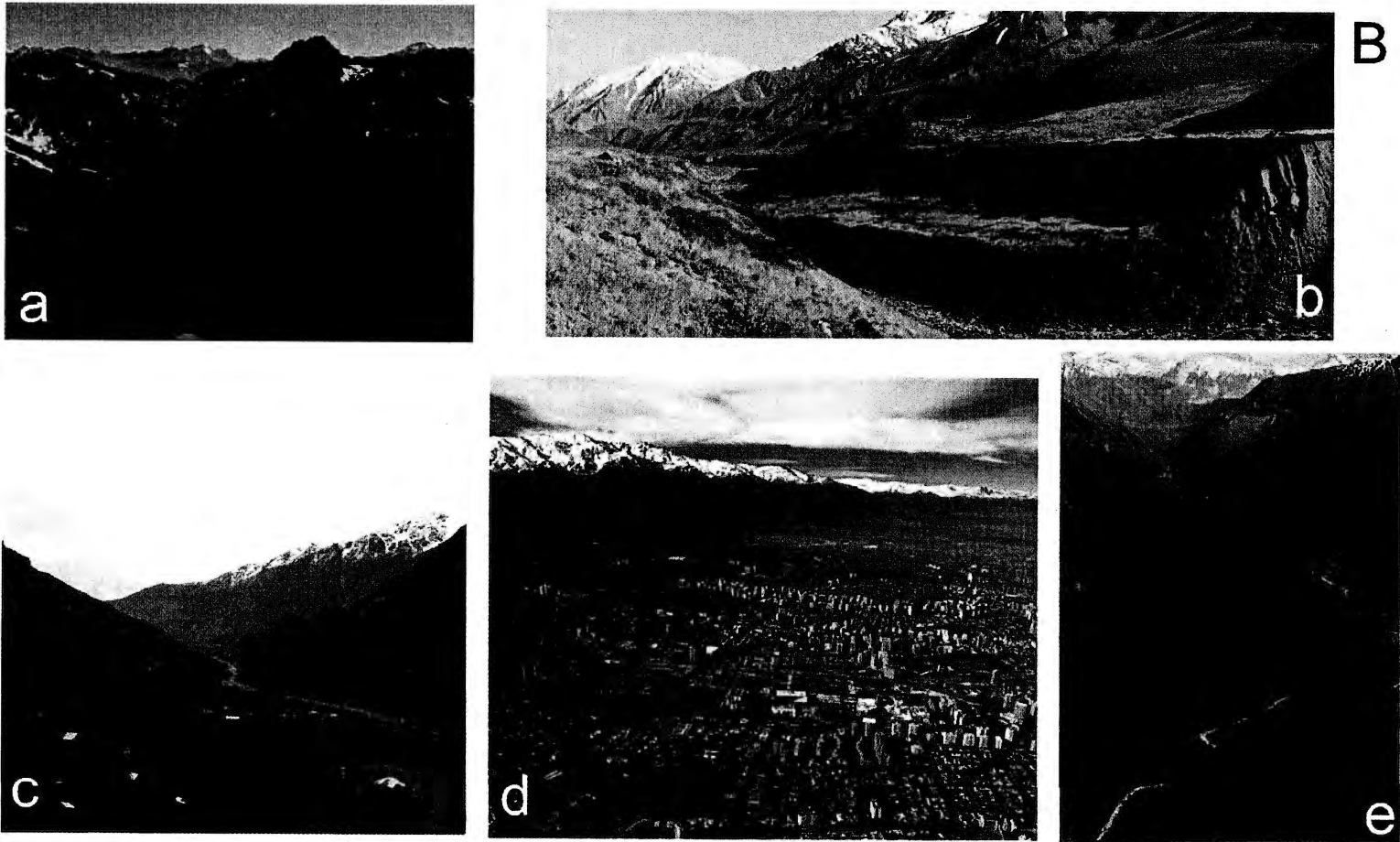


Figure 1.3B. Representation of characteristic morphology for areas inside each section: a, High altitude section of the Laguna Negra, where Pleistocene glacial deposits, rock glaciers and high elevation talus deposits coexist; b, Middle Maipo catchment, wide, alluviated reach, with cut and fill terraces, note the width of the valley; c, WCP Aconcagua valley, note canyonized lower portion; d, mountain front at the boundary between the WCP and the Central Depression showing in the foreground the city of Santiago, Chile; e, middle reach of the Maipo valley in boundary WCP-ECP, valley width decreases to the north.

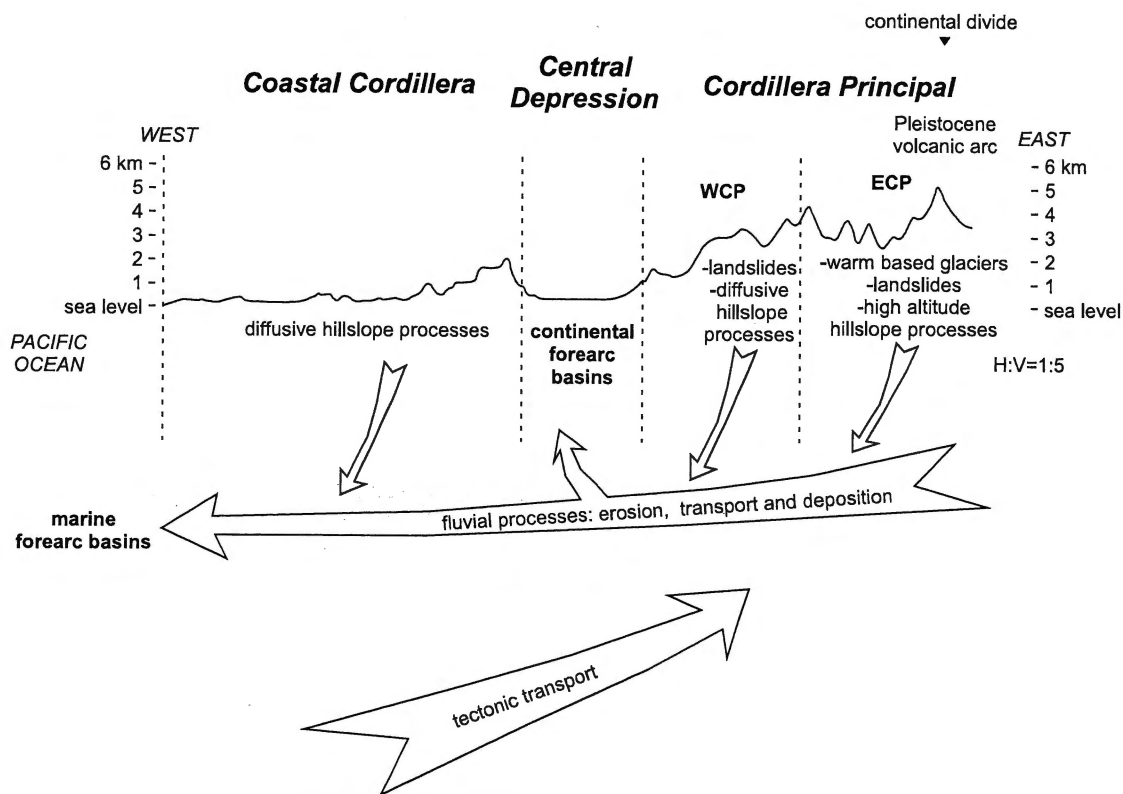


Figure 1.4. Topographic profile at latitude 34° S (averaged over a 10 km swath, Fig. 1.5). The profile shows the distinctive morphostructural units that compose the continental Andean forearc at this latitude. Arrows indicate incoming mass flux from tectonic transport which is reflected mostly in shortening or arc building in the Andes at this latitude, and sediment flux out of the orogen, generated by different processes. The sediment is routed to fluvial processes that finally transfer sediment to the continental or marine forearc basins. Surface processes that are probably most relevant to each region are indicated.

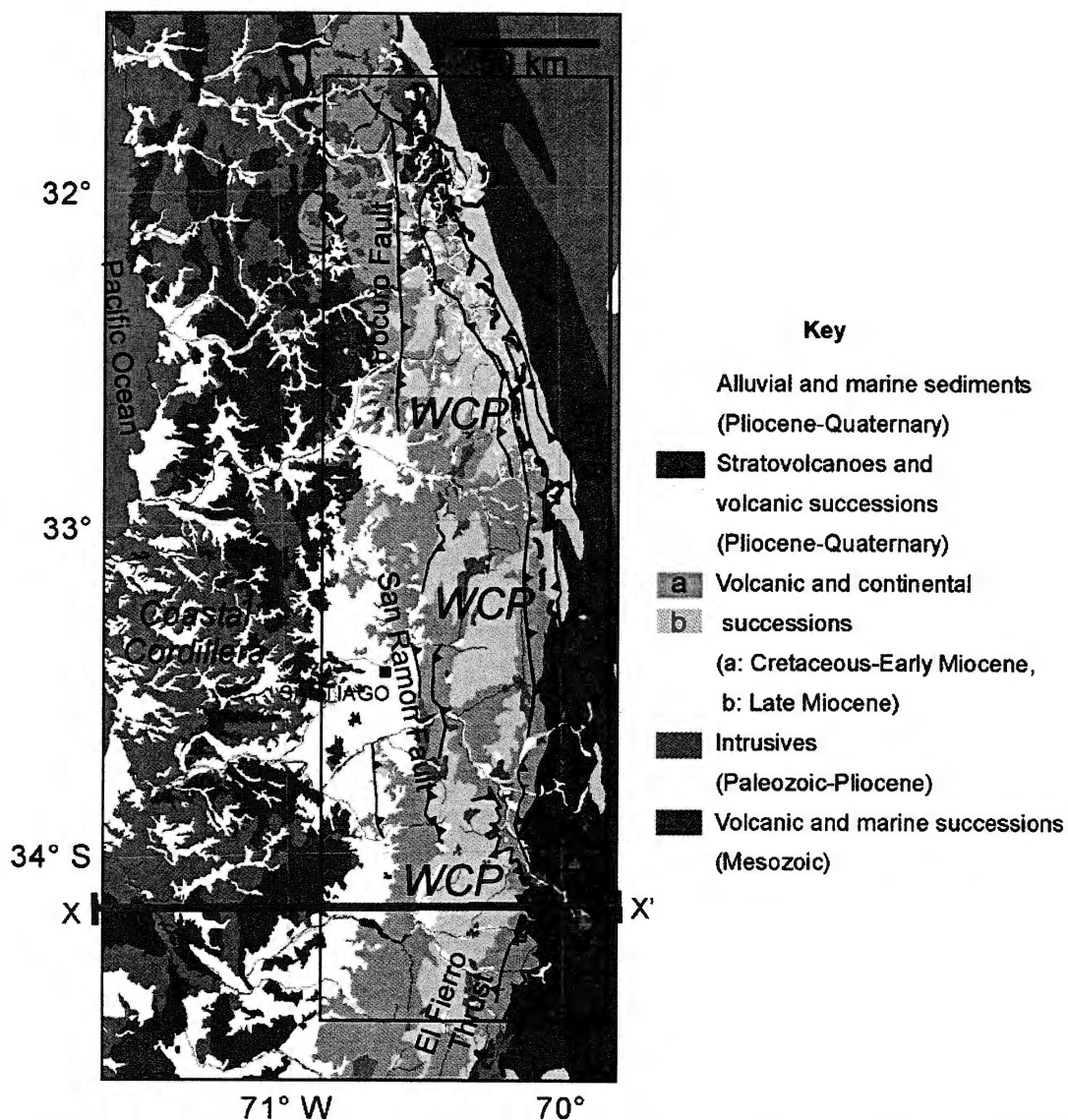


Figure 1.5. Geological map of the study area. Intrusives are mostly Palaeozoic to Cretaceous in the Coastal Cordillera (CC) and Oligocene - Pliocene in Cordillera Principal (CP); volcanic and marine sedimentary rocks are Mesozoic in CC and CP, where they are part of the Aconcagua Fold and Thrust Belt (AFTB); volcanic-continental successions are mostly Early Cretaceous in the northeastern CC and Oligo-Miocene Abanico and Farellones Formations in Western CP (WCP); Plio-Pleistocene alluvial infilling is mostly confined to present valleys and the Central Depression. Late Cenozoic faults (e.g., Thiele, 1980; Ramos et al., 1996; Rivano and Sepúlveda, 1986; Rivano et al., 1993; Godoy et al., 1999; Rauld, 2002; Giambiagi et al., 2003a; Fock, 2005) are marked with known sense of last movement. Continental divide is dashed line. Geological units in the Chilean sector modified from SERNAGEOMIN (2002); Argentinean sector modified from Ramos et al. (1996). The rectangle indicates the study area, and red line indicates the axis of the 10 km swath where mean elevation was calculated to obtain profile in Fig. 1.4.

In summary, although a well constrained history is available for certain areas of the orogen, elements of the post-Miocene tectonic and denudational evolution are still missing, like for example the timing of the last event that defined the boundary WCP-CD. The present-day landscape response, is it a continuation of the one triggered by Late Miocene uplift or there is a more recent one? What is the denudational response? Has it reached equilibrium with the tectonic rock uplift?

1.3. Aims and Scope for the Thesis

This thesis provides an analysis of denudation at different timescales for a portion of the southern Central Andes (SCA) in Central Chile (Fig. 1.2), where Miocene-recent uplift of Cordillera Principal (Farías et al., 2008) has created a spectacular combination of high relief, high altitude mountains with a large latitudinal climatic transition (e.g. Hebbeln et al., 2007). The ubiquitous landslides that appear in this region (e.g., Abele, 1981, 1984) —from frequent debris flows to infrequent large rockslides— and the apparent ease with which sediment generated from them is removed from the landscape to sedimentary basins outside the mountain belt are two field observations that immediately capture attention in this section of the orogen (Fig. 1.3).

The observations suggest that this region might be particularly fit to test the following hypotheses: a) landslides contribute a large proportion of the sediment that is being fed to the stream network in the southern Central Andes over the long term (10^6 a) (cf. Burbank et al., 1996), and b) (as a corollary) that fluvial transport outpaces sediment production on hillslopes on long term (10^6 a) timescales along Cordillera Principal, maintaining bedrock reaches and avoiding extensive alluviation inside the range —both effects are consistent with continuous landslide triggering to support the first statement.

Testing the first hypothesis is opportune because the contribution of landslides—particularly large scale mass wasting—to regional erosion rates in tectonically active mountain belts is currently being debated in other active orogens. Korup et al. (2007) found a correlation between 300 of the largest (volume $> 10^8$ m³) landslides on Earth, and regions of high long-term erosion rates (in the order of 1 mm a⁻¹ and higher). The volume estimates vary between 1-10% of the total Late Quaternary erosion in these areas.

Burbank et al. (1996, 2003), Montgomery (2001), Whipple et al. (1999) and Korup et al. (2004) have shown that regions of high erosion rates (and high fluvial bedrock incision and rock uplift) during the Quaternary correlate with large landslide occurrence, although their research did not include an estimate for the actual proportion of erosion accomplished by the slope failures. On the other hand, for areas in which there are estimates of sediment supply from landslides, the records usually span only the last few centuries due to absence of chronology on the older slides (e.g. Hovius et al., 1997, 2000; Eaton et al., 2003; Kirchner et al., 2001; Reid and Page, 2003; Keefer, 1994). These estimates (Table 1.1) indicate that in the short term most of the sediment is supplied by landslides over other surface processes, like fluvial or glacial processes (cf. Fig. 1.2).

The analysis of the second hypothesis is particularly relevant to the SCA. It has been suggested, based on models of knickpoint retreat (Farías et al., 2008), that a large surface uplift during the Late Miocene —an effect of the last E-W shortening event in this region (Lavenue and Cembrano, 1999, 2008) — has been followed by a relatively slow erosional response in the landscape (Fock, 2005; Fock et al., 2006; Farías et al., 2008). Critical assumptions for this modeling are the conditions under which fluvial incision occurs. Even quantifying long term equivalence between sediment production and transport, spatial variability might result in knickpoints not migrating at the rate they should be in ideal conditions. On the other side, if it is determined that the landscape still has not reached equilibrium between tectonic forcing and denudation after the proposed Late Miocene (~7 Ma) base level fall (Farías et al., 2008), it is possible to constrain a minimum lag time. This might be used to analyze lag time and the variables responsible for it that are involved in the development of erosional response to tectonic influx in active orogens (Hooke, 2003). The outcome is particularly valuable to constrain orogen scale evolution models.

The present work aims to test both hypotheses quantitatively, specifically trying to tackle the problem of sediment flux being brought by mass wasting over longer timescales, and finally analyzing an eventual erosional steady state condition (e.g. Montgomery, 2001) for the area using estimates of denudation along differing timescales.

1.4. Objectives

The following primary objectives are proposed:

1. To analyze and compare over different timescales (10^2 - 10^6 a) the sediment production by landslides (in this case large rockslides), with the flux from other processes (i.e. fluvial transport and glacial erosion) which act in an active convergent margin.
2. To develop a conceptual model of landscape evolution in the southern Central Andes of Chile since the Late Miocene. The conceptual landscape evolution model must be consistent with quantitative estimates derived for objective a).

The following secondary objectives must be attained to meet the two primary objectives:

- 1) to determine how much sediment is volumetrically produced by large landslides inside a particular region of the SCA.
- 2) to determine the age of landslides and therefore a sediment production rate.
- 3) to determine how much sediment has been eroded from the landslides.
- 4) to compare total sediment flux from different catchments containing landslides, at different time and size scales.
- 5) to identify specific surface processes that transport sediment from hillslopes to streams (Fig. 1.1) and determine qualitatively their relevance in the study area.
- 6) to identify changes in sediment flux downstream from large landslides.
- 7) to determine the relation between erosion rates estimated through different methods and variables such as relief, catchment size, slope, etc.
- 8) to compare estimates of erosion, incision and denudation during the Quaternary in the area using the different methods proposed in the thesis.

1.5. A Multiple Methods Approach

1.5.1. Rationale for the methods used in this thesis

To generate the different estimates of erosion and denudation that are needed for a proper comparison and testing of the stated hypotheses, the research relies on different methods spanning different timescales. For every technique used, I either developed a new methodological approach or tested the validity of the existing methodology. First, the amount of sediment fed to the stream network by landslides is quantified using the methodologies proposed by Malamud et al. (2004a,b), built upon work by Keefer (1994) and Hovius et al. (1997, 2000). Malamud et al. (2004a) stated that it might be possible to estimate denudation rates by estimating volume of historical landslide inventories in a certain region, by using their empirically fit statistical distribution of landslides area vs. frequency. However, their ideas have not been tested on a long term (10^6 a) timescale, particularly due to the difficult task of compiling an inventory of large ($> 0.1 \text{ km}^2$) landslides of known age. To perform this test, I generated a relative chronosequence of large landslides, which is calibrated against existing and new absolute geochronological data. Coupled with robust statistical models that describe landslide size populations (Malamud et al., 2004a, b; Turcotte et al., 2006), my approach allows for the first time the quantitative estimation of the long-term relevance of large landslides in landscape evolution of a specific tectonically active area.

To determine any short term (few 10^3 a) influence of landslides in the sediment flux, I introduce for the first time cosmogenic ^{36}Cl based estimates of basin wide average denudation rates through the analysis of modern stream sediment in small catchments hosting landslides. The idea of determining catchment-wide average erosion rates via terrestrial in situ cosmogenic nuclide (TCN) concentrations in fluvial sediments is a relatively new tool in geomorphology, although it has been extensively tested using cosmogenic ^{10}Be (e.g. Brown et al., 1995, 1998; Granger et al., 1996; Bierman and Steig, 1996; Matmon et al., 2003; Binnie et al., 2007; Belmont et al., 2007). TCN techniques are based on the accumulation of nuclides produced by cosmic radiation on minerals in rocks exposed near or at the surface of the Earth. The accumulation of these nuclides depends on duration of exposure and intensity of radiation but also on erosion of the

surface (e.g. Lal, 1991). Integrated sampling over the landscape —taking advantage of natural stream sediment eroded from hillslopes in whole catchments— has proven to yield reproducible estimates of erosion rates, demonstrating powerful capabilities for the understanding of areas where no other quantitative control in rates can be obtained at timescales of hundreds to tens of thousands of years (von Blanckenburg, 2005; Bierman and Nichols, 2004). The ^{36}Cl procedure that is developed and tested in this thesis represents an important contribution for the study of landscape evolution in areas lacking enough quartz for ^{10}Be analyses, or in catchments where the quartz is not homogeneously distributed. As the area is also particularly suited to study the effect of a particular process like landslides on stream sediment TCN inventories, I also aimed to test the possibility that the TCN can help evaluate the relative contributions of sediment from different processes. This possibility has been proposed in other areas (e.g. Brown et al., 1995, 1998; Reinhardt et al., 2007) although the real feasibility of differentiating the relative contributions of hillslope, landslide, and fluvial processes by TCN inventories are currently a subject of active debate (e.g., Bierman and Nichols, 2004; Bierman et al., 2007; Belmont et al., 2007).

The approach using TCN described above relates to the analysis of landscape evolution over short term ($< 10^5$ a) timescales. To obtain a long term tectonic baseline exhumation rate for the past few million years, in order to frame the denudation estimates in the area, I use apatite (U-Th-Sm)/He (aHe) thermochronology. This low temperature thermochronometer provides a means to assess the exhumation history of a ~ 10 Ma plutonic body inside the SCA study area. Apatite He thermochronology has been developed during the last 20 years (e.g., Farley, 2000; Farley et al., 2002) to measure the time since an rock ascending to the Earth's surface has cooled below a certain temperature at which point the He gas does not rapidly diffuse from the mineral (the closure temperature, T_c , of Dodson, 1973). In the case of apatite He thermochronology the T_c is $\sim 75^\circ\text{C}$, which under 'normal' geothermal gradients imply movements of rocks in the upper sections (1-4 km) of the crust, making this method very sensitive to spatial and temporal scales relevant to Late Cenozoic landscape evolution.

1.5.2. Uncertainty analysis

As it was stated before in this introductory chapter, most methodologies for analysis of Landscape Evolution have been developed during the last decades only. Some of them, like Cosmogenic Nuclide techniques (Chapters 2, 3), depend critically on the continuous improvement on analytical techniques, like mass spectrometry. The associated uncertainties for these techniques are normally in the order of 2-5% for random errors on the measurements, but it can reach 15% depending on counting statistics. For cosmogenic nuclide techniques, systematic error on the production rate estimates can reach 20% in general for any nuclide. A large final uncertainty can arise if it is considered that different authors have estimated production rates that can differ by as much as 50% on e.g. spallation ^{36}Cl production rates. In the case of He techniques (Chapter 4), critical thresholds can be used to discard data in terms of high blank He ratios, presence of undetected inclusions, etc. It is important to note that the young (up to <1 Ma) apatite He ages obtained in this study can have large errors due to the fact that the amounts measured are very close to the blank measurements. All the potential effects are considered and all the decisions made have been described in a specific section inside each chapter.

Propagation of error in the techniques that require intensive calculations has been performed either through analytical error propagation (Chapter 2, propagation in ^{36}Cl calculations, Chapter 4, (U-Th)/He age calculation) or through Montecarlo simulation (Chapter 2, volume calculations, Chapter 3, discharge evaluation). The steps used are also described in every chapter.

For comparison of measurements of a specific technique, only analytical uncertainty was considered (e.g. Chapter 3, ^{36}Cl inter-sample comparison). For inter-technique comparison, differences of up to 20-25% between estimates are considered similar if they are under 1σ uncertainty, which normally was used throughout. A 20% 1σ propagated uncertainty is not uncommon for Landscape Evolution analysis and it is only a reflection on the continuous development of the new techniques that are required to measure rates of geomorphic evolution over timescales of hundreds to hundreds of thousands of years.

1.5.3. Timeframe for the present thesis

For some of the proposed methodologies, the timeframe involved to complete the analyses was determined beforehand (i.e. in the case of ^{10}Be analyses), because there was no major technique development. However, for the ^{36}Cl and apatite (U-Th)/He methodologies, new laboratories had to be installed and operating procedures were developed or adapted, partially involving several test samples, which required between one to two years to be running at a level that was appropriate for completion of the required analyses. Most of the development was performed by the author, and it is documented in the appendices. Fieldwork was accomplished by the author during the first three years of the thesis work, in approximately six different field seasons, of about one month each, working mostly in high relief terrain.

1.6. Structure of the Thesis

In *Chapter 2*, an inventory of large landslides in the Cordillera Principal of the southern Central Andes of Chile is synthesized. Sediment production rates are estimated by applying statistical models to the observed distribution of sizes for the landslide inventory and using existing and new chronology data that provide age estimates for the events. A relation between shallow seismicity and landslide generation is hypothesized and tested using spatial statistics techniques. The overall consistency of the tectonic features in the area with the occurrence of landslides is also discussed in this chapter.

In *Chapter 3*, the ^{36}Cl basin-wide average erosion rate estimation technique is used to analyze sediment flux from small catchments over millennial timescales. Results are compared with the data presented in Chapter 2, and with the analysis of 10-20 years of suspended sediment data for three major rivers in the area, a dataset which also served as basis for the study of bedload contribution and its relation to suspended and dissolved load in the Maipo river, in the central part of the study area. This is the first time the ^{36}Cl erosion rate estimation technique is developed and used successfully.

In *Chapter 4*, an Apatite (U-Th-Sm)/He thermochronological study is used to constrain Plio-Pleistocene exhumation of a sector of WCP in the SCA, comparing it to other author's low temperature thermochronology data for the area and to the above

mentioned estimates of sediment production and transport, for the SCA. Implications for tectonic and landscape evolution of the area are discussed.

In *Chapter 5*, the geological, tectonic and landscape evolution implications of the data collected are discussed, and a conceptual landscape evolution model for the Quaternary of the southern Central Andes of Chile is proposed.

Chapter 6 displays all references and *Chapter 7* presents appendices for all chapters, including all landslide inventory, TCN, and aHe data tables. Matlab® in-house codes that were used to perform data reduction and modeling for the different techniques used in this study are also displayed in this last chapter.

CHAPTER 2 Large Rockslides in the Southern Central Andes of Chile (32-34.5° S): Tectonic Control and Significance for Quaternary Landscape Evolution

Paper published in *Geomorphology*, doi:10.1016/j.geomorph.200.08.008

Jose Luis Antinao¹, John Gosse

Earth Sciences Department, Dalhousie University, Halifax B3H 4J1 Canada

2.1. Abstract

The distribution and age of large (>0.1 km²) Pliocene to recent rockslides in the Chilean Cordillera Principal (32-34.5°S), Southern Central Andes has been analyzed to determine the rockslide triggering mechanisms and impact on regional landscape evolution. Most of the rockslides appear in western Cordillera Principal and cluster along major geological structures. Variographic analyses show spatial correlation between rockslides, geological structures and shallow seismicity. A relative chronosequence was calibrated with existing ¹⁴C and ⁴⁰Ar/³⁹Ar dates and new cosmogenic nuclide exposure ages for selected rockslides. Estimates of rockslide induced sediment yield were calculated with empirical relations for rockslide area distributions. Throughout the Quaternary, rockslides have delivered sediment to streams at rates equivalent to denudation rates of $0.10 \pm 0.06 \text{ mm a}^{-1}$, while estimates using short term (20 a) seismicity records are $0.3_{-0.2}^{+0.6} \text{ mm a}^{-1}$. The estimates of sediment transfer and the spatial distribution of rockslides reflect a landscape in which tectonic and geological controls on denudation are more significant than climate.

2.2. Introduction

The Southern Central Andes (SCA) of Chile host some of the highest peaks (>6000 m) and largest relief (>2000 m) of the Andes, and have experienced combinations of compressional, extensional, and strike slip tectonics throughout the Late Cenozoic (Giambiagi et al., 2003; Charrier et al., 2007). Large rockslides (catastrophic bedrock

¹ Corresponding author.

E-mail addresses: jantinao@dal.ca (J.L. Antinao), john.gosse@dal.ca (J. Gosse).

involved landslides $> 0.1 \text{ km}^2$ in area) appear as prominent morphological features in the region (e.g. Abele, 1984), and exceed 1 km^3 of mobilized rock. They influence catchment hydrology and in part control the genesis, transport and delivery of sediment to the lowlands. A thorough analysis of Andean rockslide distribution and triggers has not been conducted despite the prominent role they may play in landscape evolution, sediment transfer, and hazards in the area.

We hypothesize that Quaternary rockslides in the SCA have been triggered by shallow seismicity. To test the hypothesis, we produced a new, field-based inventory of large rockslides for the Chilean SCA high relief zone between latitudes $32\text{-}34.5^\circ\text{S}$, and compared rockslide occurrence patterns to lithology, geological structures, and seismicity records. If the link between rockslide distribution and shallow seismicity can be demonstrated, it will be possible to use patterns of recent rockslides to predict the location of unrecognized (blind or unmapped) active faults. In addition, an inventory of large rockslides compiled over a broad area and long time can provide estimates of sediment generation at geodynamical space and time scales (Malamud et al., 2004a), overcoming the short-term bias present in most landslide inventories used in landscape evolution analyses (e.g. Hovius et al., 1997; Lavé and Burbank, 2004).

A multi-criteria relative chronosequence is developed for the rockslides and calibrated with previous and new geochronological data. This temporal framework, coupled with statistical analysis of rockslide areas and volumes, permits the estimation of long- ($10^5\text{-}10^6\text{a}$) and short- (decadal) term rockslide derived sediment fluxes. The estimated sediment yields help to quantify the role of rockslides in this region relative to other active orogens (e.g., Burbank et al., 1996, 2003).

2.3. Late Cenozoic Geologic Setting

The SCA have formed above a transition between flat slab and steep subduction angle of the Nazca Plate (Fig. 2.1). Between 27° and 33° S subduction is sub-horizontal and modern volcanism is absent, while between 33° and 46° S the subduction angle reaches 30° (Cahill and Isacks, 1992). Orogen-scale morphostructural units in the Chilean SCA are, west to east: Coastal Cordillera, Central Depression, and Cordillera Principal (CP, Fig. 2.1). The Western CP (WCP, Fig. 2.2) comprises Oligocene-Miocene

continental volcanoclastic rocks, intruded by Miocene-Pliocene granitoids. The Oligocene-Miocene rocks were deposited in an extensional intra-arc basin (Abanico Basin, Charrier et al., 2007) which developed a tectonic inversion during the Late Oligocene-Early Miocene (Godoy et al., 1999, Charrier et al., 2002, 2005), peaking in the eastern areas during Early Pliocene times (Fock, 2005). Near the continental divide, the eastern CP (ECP) comprises sedimentary and volcanic Jurassic to Cretaceous rocks organized in fold-and-thrust belts (e.g. Aconcagua Fold and Thrust Belt, AFTB) that are capped by Plio-Quaternary volcanic rocks. In the western boundary of the WCP, the structural features and timing of the tectonic events are not clear. Lavenu and Cembrano (1999) referred to this boundary as an inactive fault of unspecified sense, while Rauld (2002) reported Late Pleistocene westward-verging reverse slip east of Santiago, supported later by Fock (2005) and Campbell (2005).

Apatite fission track and $^{40}\text{Ar}/^{39}\text{Ar}$ thermochronology indicate that the CP has been exhumed mainly during two events: first in the Early Miocene, and again since the Late Miocene (Kurtz et al., 1997; Maksaev et al., 2003; Fock, 2005). The Coastal Cordillera at these latitudes has apparently not been significantly exhumed since the Late Cretaceous-Late Eocene (Cembrano et al., 2003; Campbell, 2005; Fock, 2005). Fariás et al. (2008) compiled local incision rates of post-Miocene sedimentary and volcanic sequences, which range from 0.02 to 2.4 mm a⁻¹, and proposed a higher surface uplift in the centre of the orogen.

2.4. Mass Wasting in the Southern Central Andes

Mass wasting is ubiquitous throughout the Andes (Blodgett et al., 1998; Schuster et al., 2002) but only a few areas have been studied systematically in terms of slide age, triggering mechanism, and link to tectonics or climate (e.g. Puna, NW Argentina, Hermanns et al., 2000, 2001, 2006). In Chile, attention has focused on high frequency small-volume historical landsliding close to transportation and energy corridors and urban areas (Hauser, 2000; Naranjo and Varela, 1996; Sepúlveda et al., 2006).

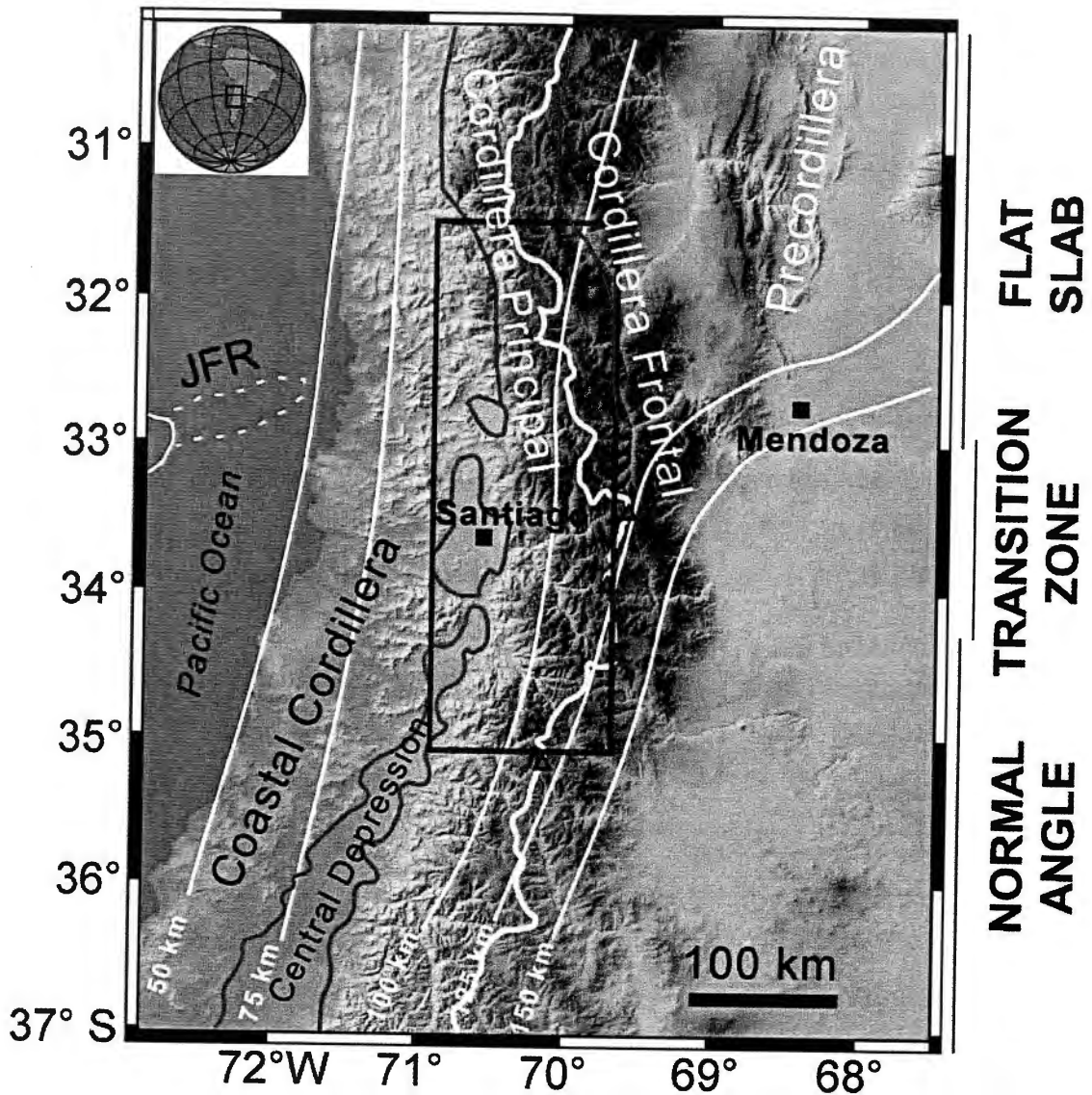


Figure 2.1. Shaded Relief DEM (SRTM data) showing the main morphostructural units in the SCA. In white, depth contours of the Benioff plane marking the interplate seismicity between the subducted slab and the upper plate (e.g., Cahill and Isacks, 1992). The continental divide is shown, marking also the political boundary between Chile and Argentina. Pleistocene volcanoes are marked by triangles. Inset: study area (Fig. 2.3). JFR: Juan Fernandez Ridge; where dashed, already subducted.

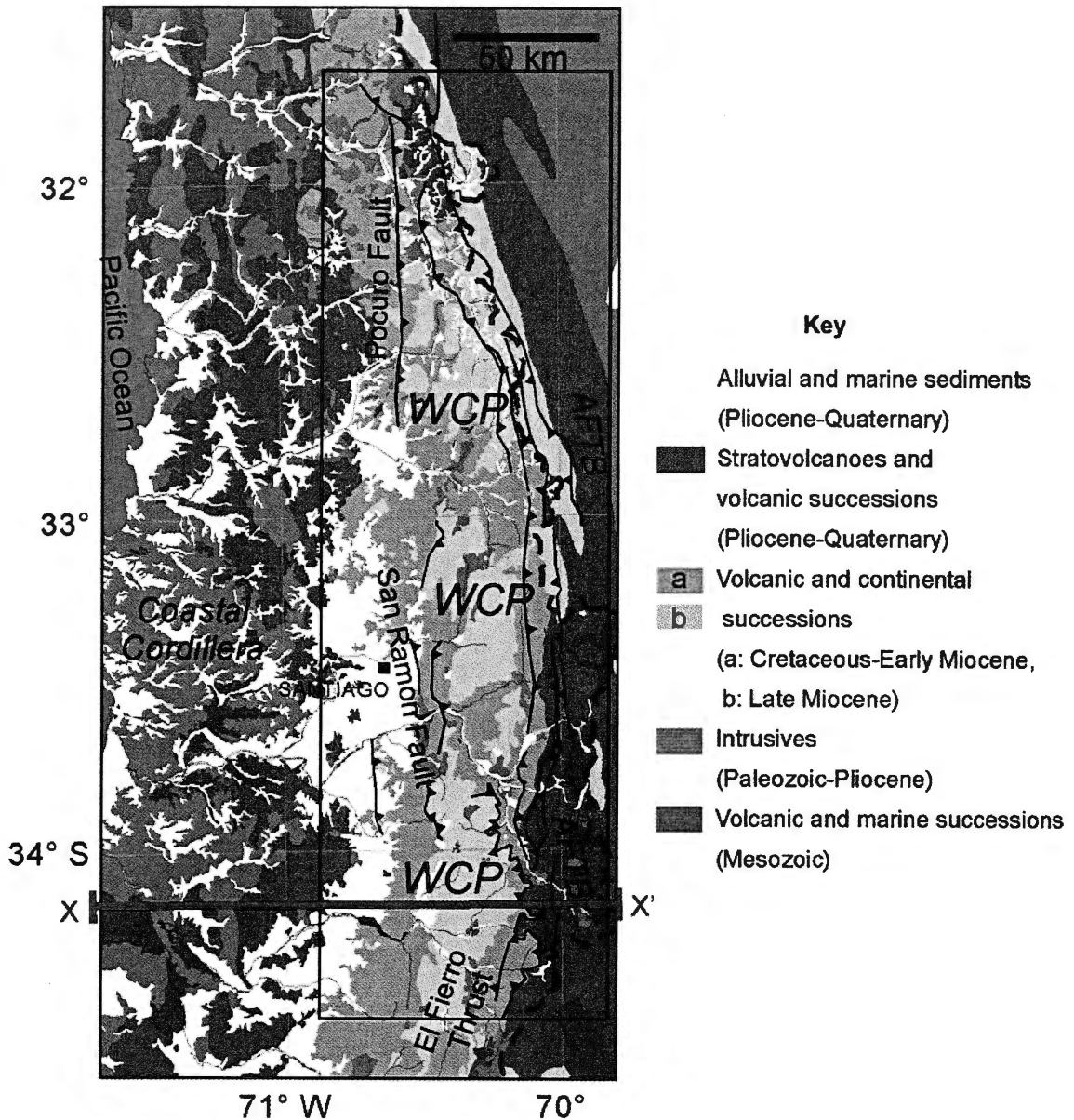


Figure 2.2. Geological map. Intrusives are mostly Palaeozoic to Cretaceous in the Coastal Cordillera (CC) and Oligocene - Pliocene in Cordillera Principal (CP); volcanic and marine sedimentary rocks are Mesozoic in CC and CP, where they are part of the Aconcagua Fold and Thrust Belt (AFTB); volcanic-continental successions are mostly Early Cretaceous in the northeastern CC and Oligo-Miocene Abanico and Farellones Formations in Western CP (WCP); Plio-Pleistocene alluvial infilling is mostly confined to present valleys and the Central Depression. Late Cenozoic faults (e.g., Thiele, 1980; Ramos et al., 1996; Rivano and Sepúlveda, 1986; Rivano et al., 1993; Godoy et al., 1999; Rauld, 2002; Giambiagi et al., 2003; Fock, 2005) are marked with known sense of last movement. Continental divide is dashed line. Geological units in the Chilean sector modified from SERNAGEOMIN (2002); Argentinean sector modified from Ramos et al. (1996). The rectangle indicates the study area.

Large rockslides—cohesive body landslides normally exceeding 10^6 m^3 (Abele, 1974) including debris slides and rock slides of Cruden and Varnes (1996), and rock avalanches (Scheidegger, 1973; Hewitt, 2006)—are pervasive in CP between 32° and 34.5° S. Abele (1984) was the first to differentiate the deposits from glacial sediment on a combined textural-morphological basis and although some slides have been mapped (e.g. Charrier; 1983; Moreno et al.; 1991; Rivano and Sepúlveda, 1986; Rivano et al., 1993; Sellés and Gana, 2001; SERNAGEOMIN, 2002) rockslide age or trigger has not been established. Absolute geochronology of the landslides indicates that the record spans the last 5 Ma (Godoy et al., 1994a, b; Encinas et al., 2006; Moreno et al., 1991).

Triggering mechanisms for the large rockslides have not been resolved. Some authors (e.g. Abele, 1984; Godoy et al., 1994b) have suggested that seismic shaking is the main trigger in the AFTB, while others (e.g. Godoy et al., 1994a) have proposed that intense rainfall has triggered some of the Late Pliocene to Early Pleistocene rockslides along the western boundary of Cordillera Principal (Pocuro and San Ramón faults, Fig. 2.2). None of the proposed mechanisms has been verified for pre-historical slides and little is documented about landsliding rates and their temporal variation and relation with Late Cenozoic tectonic activity.

We recognize that small (10^5 - 10^6 m^3 of sediment) debris flows are generally storm-triggered with recurrences of years to decades (Naranjo and Varela, 1996; Sepúlveda et al., 2006) and they transfer sediment between the hillslopes and streams within the WCP. In many locations the flows remobilize material from large rockslides which become saturated or oversteepened following incision (Hauser, 1985, 2000). However, the preservation of debris flows is poor, even for large events (e.g. 1987 Parraguire flow; 10^7 m^3 ; Hauser, 2000, 2002; Fig. 2.3) because they leave thin sediment sheets that are rapidly buried or eroded by glacial or fluvial processes along major valleys in the SCA (Moreno et al., 1991; Chiu, 1991). The short-term climate control on debris flow events, their poor preservation, and the observation that without large rockslides many debris flows would not exist, made us to focus our analysis only on the large rockslides.

2.5. Methodology

Topographic maps at scales of 1:25.000 and 1:50.000 and DEMs at 30 and 90 m resolution provided the base for the inventory. Remote mapping following methodologies of Hovius et al. (1997), Korup et al. (2004) and Korup (2005, 2006) was performed using aerial photographs at scales 1:30 000, 1:60 000, and 1:70 000, and ASTER and Landsat images. For inventory purposes, a 0.1 km² area covered by the rockslide deposits was our minimum cut-off (Abele, 1974), which approximately corresponds to the minimum volume cutoff of $0.5 \times 10^6 \text{ m}^3$ for rock avalanches proposed by Scheidegger (1973) and Keefer (1984).

Rockslides were mapped using criteria of Abele (1974), Erismann and Abele (2001), Hewitt (1999, 2002), and Crozier (1986) to distinguish them from colluvial, glacial, or paraglacial deposits. We carefully considered previous interpretations of rockslide and glacial deposits in the area (e.g., Brügggen, 1950; Marangunic and Thiele, 1971; Caviedes, 1972; Thiele, 1980). In the field, the toe and lateral sections of the deposit were verified, and the crown was examined for cracks, slickensides, clayey surfaces, or lithological contacts which could provide evidence for triggering mechanisms. Hand-held GPS-altimeter measurements were used to delineate boundaries and estimate present and eroded rockslide volumes on selected rockslides (§2.7.3.1) using algorithms implemented either on GIS or mathematical software (see Appendix, §2.9.1, for uncertainty analysis). For all rockslides, deposit planforms were digitized as polygons using orthorectified photographs and digital topography with a mapping resolution of 100 m (minimum pixel size). Morphometric (including total area and estimated volume) and relational rockslide variables (comparisons with slope, relief, and other variables from DEMs) were extracted by standard GIS queries.

A relative chronosequence for all slides was developed, and it was based mainly on morphology (topographic roughness contrast between the rockslide and surrounding areas, degree of preservation of surface features like ridges and reverse slopes, extent of dissection of the slide and alteration of the original drainage network), relative weathering of exposed rock boulders and surfaces, relative soil development on stable slide surfaces, and differences in scarp and deposit albedo in aerial photographs. Field

estimates of soils chronosequence parameters (McDonald et al., 2003) aided in the relative chronology. Homogeneity of the volcanic and volcanoclastic lithologies enhanced the reliability of these criteria (Table 2.1).

We linked landslide chronosequences in neighbouring catchments where elevation-precipitation gradients were predictable, tuning them according to this variability. Fourteen new terrestrial cosmogenic nuclide (TCN) exposure ages, along with available dates and stratigraphic relations were used to calibrate the chronosequence. The lack of detail in the assigned chronology compared for example to the one developed by Mather et al. (2003) arises from the larger study area and the limited ability to account for morphology and weathering differences associated with latitudinal precipitation gradients (annual precipitation increases southwards along the WCP from 200 mm a⁻¹ at 32°S to 600 mm a⁻¹ at 34.5°S). The precision is sufficient to establish general trends and allow inferences of sediment flux rates over long timescales but is too imprecise to resolve synchronicity associated with single paleoseismic or paleoclimate events.

To analyze potential relationships between rockslide occurrence and lithology, structures, precipitation, local relief, slope, and seismicity, the data were digitized, converted to continuous numerical fields and resampled on 1 km grids. A structure density grid for the variographic analysis was calculated over windows with 5 km radius for the entire study area, to reflect the number of 1 km squares containing a fragment of a prominent fault. The rockslide and seismicity density grids were computed similarly. Monte Carlo simulation, randomly varying the position for resampling, showed that the outcome of the analysis is independent of the nature of the sampling inside the 1 km cells, given the resolution of the different datasets. The rockslide distribution was compared to the variables stated above using standard GIS histograms or variographic techniques (Matheron, 1962; Isaaks and Srivistava, 1989). Variographic analysis was performed to investigate the degree of spatial correlation of rockslides with the variables. Standardized variograms (Pannatier, 1996) for different directions test similarities in the spatial structure of the data. The variogram surface and derived zonal anisotropy (Pannatier, 1996) obtained for non-standard variograms were used as indicators of spatial correlation. Ellipses were fitted to the variographic surfaces to describe modelled exponential ranges in all directions.

Table 2.1. Chronosequence classification for the inventory (after Keaton and Rinne, 2002; Mather et al., 2003). The relevance of the factors for placement of a deposit in the chronosequence is higher in the left side and lower in the right.

Activity state		Condition of main scarp and lateral margins	Slide surface morphology	Drainage disruption (used in larger events)	Inventory class age (estimated age)
Active	Moved within the last 500 years	Sharp; fresh rock faces; streams pushed to the edge of deposit; high albedo in surface, toe and scarp as seen in aerial photographs	Hummocky; ridges and fresh scarps on the deposit; reverse slopes; higher topographic roughness compared to surrounding areas	High degree of disruption of local drainage; lake formed on main stem or clear evidence of disruption, with active erosion on the toe if reaching main stem.	Holocene (Historic)
Inactive	Young	Relatively sharp; lateral streams fed by small tributaries draining the landslide body, talus slopes developed on scarp, high albedo in scarp and toe	Hummocky; relatively sharp and fresh scarps; reverse slopes; undrained depressions	Landslide-dammed lake present or evident and possibly an overflow event has occurred	(Late) Holocene
	Mature	Smoothed; lateral streams fed by tributaries flowing off the main body of the slide	Smooth, rolling topography, filled depressions (normally site of thicker soils)	Disrupted and disjointed internal drainage network; landslide-dammed lake present but one or several overflow events have occurred	(Early) Holocene
	Old or relict	Dissected, vague lateral margins; no lateral drainage, high albedo in talus slopes only, low albedo on body and scarp.	Smooth; undulating topography; normal stream pattern, roughness similar to surrounding hillslopes	Landslide dammed lake absent; lacustrine deposits, dam morphologies and deposits of catastrophic outburst may be found	Late Pleistocene
	Fossil or ancient	Rounded lateral margins; sections may not be identifiable; generally low albedo throughout.	Fragments integrated into the landscape with very little indication of the original slide features	Lack of evidence of lacustrine deposits or outburst deposits downstream	Early-Middle Pleistocene

Cumulative inventory volumes over long-term timescales were estimated using methods proposed by Malamud et al. (2004a,b), and then used to estimate sediment flux from large rockslides employing the time interval given by the landslide chronosequence. Rockslide volumes were estimated from the corresponding areas, using a relation derived from our data, but that has also been empirically observed in rockslide inventories at different size scales (Abele, 1974; Hovius et al., 1997; Hungr, 2006).

2.6. Results

Summarized and complete versions of the rockslide inventory are provided in Table 2.2 and the Supplementary Data File (SDF, Appendix A.1), respectively. Within the ~15,000 km² area studied, 378 rockslides were identified (Fig. 2.3). Rockslides that are relevant in terms of size, age or other features are presented in Table 2.3. The SDF contains detailed descriptions of areas where specific spatial relationships between rockslide location and local geological and topographical features are present.

Most rockslides are located in CP with a clustered distribution (Fig. 2.3) along linear patterns, for example along major river valleys and fault zones. In the WCP, the majority of the rockslide deposits obstruct drainages instead of flowing downstream (e.g. Yeso-Mesón Alto, Salto del Soldado, Maitenes del Colorado, Ingenio, Codegua, and Pangal rockslides; see Table 2.3). To the east in the AFTB, large rockslides are not pervasive, although this effect might be caused by higher mobility and hence a lower relative preservation in this area (Hauser, 2002; Sepúlveda et al., 2006). Large rockslides are rare to the west of the CP in the Coastal Cordillera.

Table 2.2. General properties of the rockslide inventory. Landslide names refer to those reported in the Supplementary Data File (SDF).

Number of rockslides	378
Total area mapped (km ²)	14 980
Average landslide size (area in km ²)	2
Proportion of total area in the inventory (% of total) contributed by landslides:	
larger than 1 km ²	90
larger than 10 km ²	31
Largest area (km ²) rockslides	
Colon-Coya composite rockslide/rock avalanche	140
Agua Amarga – Las Arpas rockslide	31
Las Hualtatas rockslide/rock avalanche	19
Total volume (km ³) present as rockslide deposits (estimated from area distribution, using scaling relations in section 2.7.3.1, and not considering individually measured landslides)	100
Largest run-out (km) rockslides	
Colon-Coya composite rockslide/rock avalanche	21
Las Hualtatas rockslide/rock avalanche	12
Maximum run-up (m)	1250
Olivares rockslide	

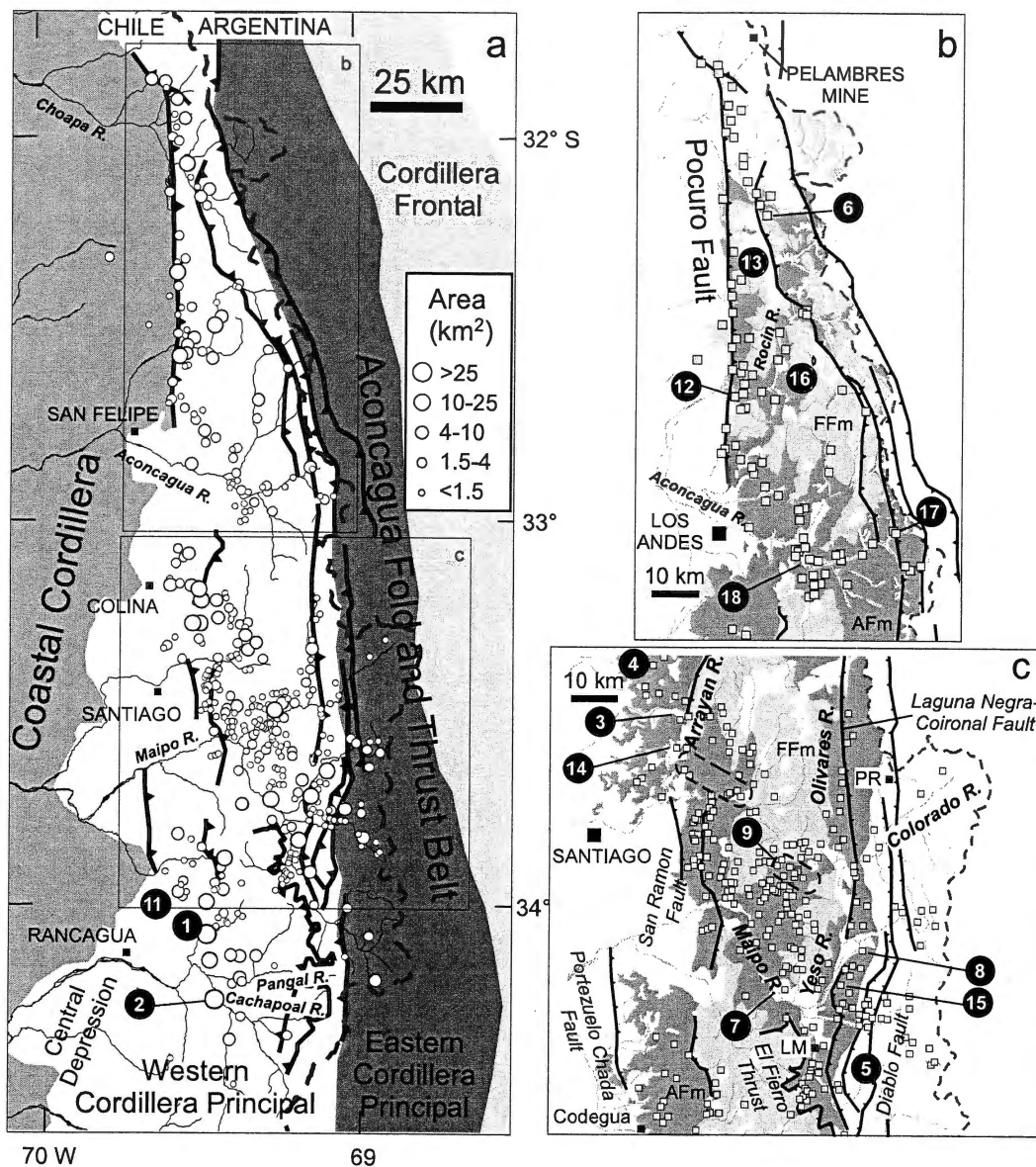


Figure 2.3. **a.** Spatial distribution of rockslides inside the study area, showing relation with morphostructural units and Late Cenozoic faults (compiled from the same sources as Fig. 2.2). Numbers inside fill circles indicate selected rockslides and rock avalanches listed in Table 2.3. Landslide planform area was used to scale symbols. **b.** Detail of the north-western area, the gray shading indicates the Oligocene-Miocene units in Western Cordillera Principal: AFm, Abanico Formation (stippled ellipses indicate areas of lacustrine continental facies), FFm, Farellones Formation; **c.** Detail of the south-eastern area. LM: Las Melosas, site of 1958 M 6.9 shallow earthquake (e.g., Sepúlveda et al., 2008), PR: Parraguirre River headwaters, site of the 1987 rockfall and subsequent debris flow through Colorado and Maipo River valleys (e.g., Hauser, 2002).

Table 2.3. Major (mostly $>2 \text{ km}^3$ in volume) rockslide and rock avalanche deposits in the Southern Central Andes of Chile, in order of decreasing size. Numbers in parentheses refer to Figure 2.3. Italics indicate calculated parameters using scaling relationship described in §2.7.3.1. n.e.: not estimated, mainly due to poor constraining on deposit extent.

Name	Area of deposit (km^2)		Volume (km^3)		Runout of debris				Controlling factors	Lithologies affected	Estimated Age (Ref.)
	Exposed now	Original (estimate)	Estimated now	Original (estimate)	Source height (m a.s.l.)	Lowest altitude reached [§] (m a.s.l.)	Maximum travel (km)	H/L [†]			
Colón – Coya rock avalanche or volcanic debris avalanche (1)	140.8	>190	7.3	26	2550	1000	21	0.07	Instability of volcanic edifice: lahar or debris avalanche? Hot, wet in sectors, more a dry, cold, rock avalanche in others. Considered a composite deposit.	Farellones Fm. Miocene volcanic rocks, the deposit has pockets of Pliocene ash	Late Pliocene (Godoy et al., 1994a, Encinas et al., 2006)
Las Arpas (2)	31.26	39.5	12.5	n.e.	2200	950	9.25	0.13	More competent rocks over folded and altered rocks	Farellones Fm. tuffs over Abanico Fm. lavas and breccias	Late Pleistocene (Charrier, 1983)
Las Hualtatas (3)	19.27	29.1	5.9	n.e.	2500	1000	12	0.12	More competent rocks over highly fractured altered rocks in the Pocuro – San Ramón Fault zone	Abanico Fm?, tuffs/lavas over sandstones, epiclastic rocks	Early – Middle Pleistocene (Wall et al., 1999)
Cerro Vizcachas N (4)	16.97	21.1	4.8	n.e.	2800	1150	7.8	0.21	More competent rocks over highly fractured altered rocks, nearby Pocuro Fault zone, incision by (paleo) Colina River.	Farellones Fm. tuffs/dacitic domes over Abanico Fm. lavas and breccias	Late Pleistocene (Wall et al., 1999)
Cerro El Salto (5)	16.89	21.5	1.34	n.e.	3000	1600	4.5	0.3	Partial contact between volcanoclastic rocks and San Gabriel intrusive, alteration zone running from Quelltehue towards the south; unfavorable slope/bedding.	Abanico Fm., highly altered andesitic lavas	Early – Middle Pleistocene (this study)

§Measured today. It could be lower, specifically in older rockslides and rock avalanches.

†From: maximum drop / maximum travel. Equivalent to $\tan f$, being f the fahrböschung angle (e.g., Erismann and Abele, 2001)

	<i>Area of deposit(km²)</i>		<i>Volume (km³)</i>		<i>Runout of debris</i>						
Batuco – Tranquilla S (6)	16.77	24	2.5	3.8	3200	1234	10.25	0.19	Unfavorable slope/bedding, Pocuro Fault zone and related west-vergent reverse structures in the proximity, contact intrusive-volcanic rocks.	Abanico Fm. lavas, tuffs, breccias, intruded by Miocene monzodiorites	Late Pleistocene (this study)
El Ingenio (7)	16.11	21	4.4	n.e.	2350	1050	6.5	0.2	More competent rocks over folded and altered rocks.	Distal tuffs, breccias, lavas, Abanico Fm?	Late Pleistocene (Godoy et al., 1994b)
Yeso – Meson Alto (8)	15.78	22.7	4.3	4.5	3800	2250	7.6	0.2	Overtuned tight fold, Laguna Negra fault?	Andesitic lavas, breccias, granodiorite	Holocene (this study; Abele, 1984)
El Laurel (9)	13.99	23.6	3.6	n.e.	2250	1250	5	0.2	More competent rocks over highly fractured altered rocks, fluvial incision by (paleo) Colorado River	Farellones Fm. tuffs over Abanico Fm. lavas, breccias and sandstones	Late Pleistocene (Moreno et al., 1991)
Peuco (10)	12.97	n.e.	3.2	n.e.	3100	2200	8	0.11	More competent rocks over highly fractured altered rocks, fluvial incision	Farellones Fm. tuffs over Abanico Fm. lavas, breccias and sandstones	Late Pleistocene (this study)
Cerro Guanaco (11)	12.43	n.e.	3	n.e.	2250	1100	5.6	0.2	More competent rocks over folded and altered rocks, fluvial incision by (paleo) Codegua river	Miocene tuffs over Oligocene lavas and breccias	Late Pleistocene (this study)
Estero Maquis (12)	12.23	n.e.	2.9	n.e.	2700	1275	9.6	0.15	More competent rocks over highly fractured altered rocks, Pocuro Fault	Miocene rhyolitic tuffs over Oligocene lavas and breccias	Late Pleistocene (This study and Rivano et al., 1993)
Cabeza de Toro (13)	11.58	n.e.	2.7	n.e.	2700	1700	4.7	0.21	More competent rocks over highly fractured altered rocks, Pocuro Fault, unfavourable slope/bedding relation	Miocene rhyolitic tuffs over Oligocene lavas and breccias	Early to Middle Pleistocene (this study)
Loma Huinganal (14)	11.26	n.e.	2.6	n.e.	2850	1500	6.5	0.2	More competent rocks over highly fractured altered rocks, Pocuro Fault	Farellones Fm. andesites over Abanico Fm. tuff breccias.	Early to Middle Pleistocene (Wall et al., 1999)
San Nicolás - Las Cortaderas (15)	10.9	13.65	2.4	n.e.	3500	1850	5.1	0.31	Overtuned tight fold, unfavorable slope/bedding relation.	Abanico Fm. lavas, tuffs, breccias, highly fractured	Holocene (Abele, 1984)

	<i>Area of deposit(km²)</i>		<i>Volume (km³)</i>		<i>Runout of debris</i>						
Llaretas del Rocín (16)	10.33	n.e.	0.5	2.5	3250	2150	5	0.22	Unfavorable slope-bedding relation, fold, incision by Rocin River.	Farellones Fm. lavas and breccias over Abanico Fm. andesitic lavas.	Late Pleistocene (This study)
Portillo – Laguna del Inca (17)	4.82	5.5	1.1	1.2	3900	2050	7.8	0.23	Overtuned tight fold, backthrust unfavorable to high slope in a glaciated catchment	Highly fractured and altered Abanico Fm. andesitic lavas.	Late Pleistocene-Holocene (Rivano et al., 1993)
Salto del Soldado (18)	2.17	2.2	0.2	0.2	2250	1550	3	0.23	Altered contact between volcaniclastic rocks and intrusive, unfavorable slope/bedding relation.	Abanico Fm. lavas, tuffs, breccias, intruded by Miocene monzodiorites	Late Pleistocene (this study and Rivano et al., 1993)

2.6.1. Chronology and Age Distribution of Large Rockslides

Ages range from Late Pliocene (Colón-Coya rockslide, ca. 5 Ma, Table 2.3) to Historic (Cortaderas and Manzanito debris slides during 1958 Las Melosas earthquake, Fig. 2.3c). Besides direct chronologic constraints available for large pre-historic rockslides in the area (Table 2.4; Fig. 2.4), relative chronostratigraphical markers were used (fluvial terraces, moraines, ash fall levels).

Fourteen new TCN ages (Table 2.5) were used to further constrain the chronology. Fourteen of the samples dated boulders on rockslide surfaces and one sample dated a slickensided bedrock surface at the base of a slide scarp. The replicate ages fall within the previously established chronosequence interval, except for sample MAC002 which we interpret as a result of a younger exposure by boulder toppling or washing of finer material covering the deposit (Fig. 2.4). Only a few of the boulder TCN ages are within their 2σ analytical precisions, impeding precise determination of the age of most events, and confirming that even in large landslides a large number ($n>6$) of samples is needed to constrain accurately the events involved (e.g., Ivy-Ochs et al., 2008). In samples MAC001 and POT008 (both ~80 ka), and PAN003 (~24 ka), we interpret them as representing inheritance, a feature that is far more common in landslide boulders (e.g., Ivy-Ochs et al., 2008; Nichols et al., 2006) than in moraine boulders.

A large number of Holocene rockslides appear concentrated along the eastern boundary of the Abanico Formation outcrops east of Santiago (Fig. 2.4), and in the lower reach of the Colorado (Maipo) river valley. On the western side of WCP, rockslides with mostly Holocene ages appear in the northern and southern tips of the Pocuro - San Ramón fault zone (PSRFZ, Rivano and Sepúlveda, 1986; Rauld, 2002). There is also a relative abundance of old (Middle Pleistocene or older) rockslides in the central - western areas, around Colina and north of Santiago and on the higher altitude block (eroded surface starting at 2200 m on the west with eastern peaks up to 4000 m) between Maipo, Colorado and Yeso rivers (Fig. 2.3).

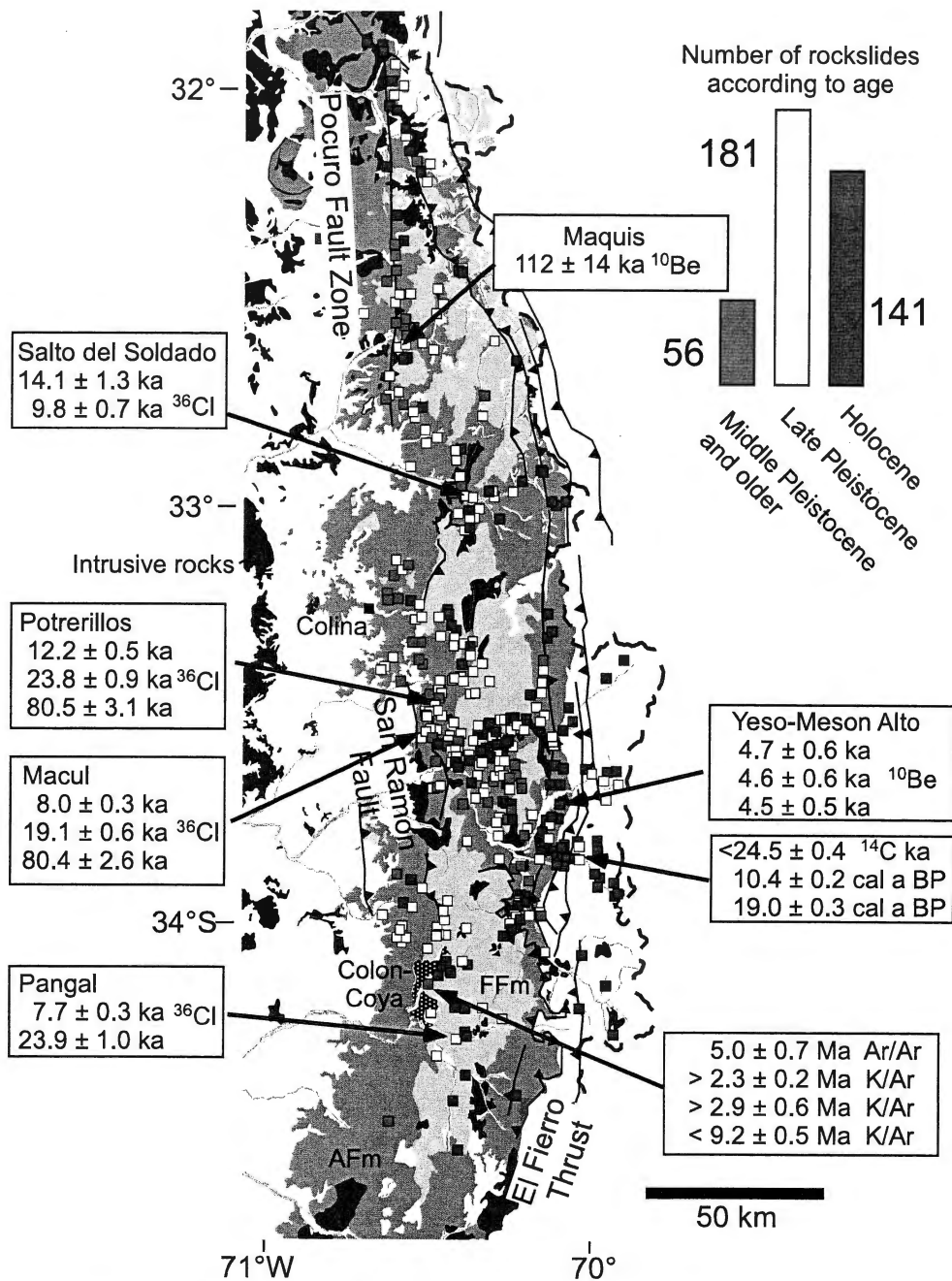


Figure 2.4. Rockslide chronology. Symbol colors correspond to relative chronosequence. The Pliocene Colón – Coya composite deposit (Coya) appears stippled, with ages marked. Ages for rockslides based on published data and new TCN data (this study) are indicated in ka with 1σ uncertainty (Tables 2.4 and 2.5). The proportion of landslides in each age group is shown in the upper right corner. Major faults and fault systems are marked. Lithological units are shown in gray shadings: AFm = Oligocene-Miocene Abanico Formation, FFm = Miocene Farellones Formation.

Table 2.4. Summary of the chronology available for rockslide and rock avalanche deposits in the Southern Central Andes. Detailed description of these sites can be found in the Supplementary Data File.

Landslide	Age	Reference
<i>Holocene-Upper Pleistocene</i>		
-La Engorda composite deposit	<24.5±0.4 ¹⁴ C ka	Moreno et al. (1991) calibrated (when possible) according to Stuiver et al. (2005).
-Quebrada Morales rockslide	10.4 ± 0.2 cal ka 19.0 ±0.3 cal ka	
<i>Middle Pleistocene</i>		
-Coyanco, Cerro San Simón, El Ingenio rockslides	<0.45±0.07 Ma	Stern et al. (1984) fission track age on zircon in ash layer overlying the deposits.
<i>Pliocene – Lower Pleistocene</i>		
-Colon-Coya composite deposit	>2.3±0.2 Ma (a) (>2.9±0.6 Ma) (a) 5.0±0.7 Ma (b) <9.2±0.5 Ma (c)	(a) Charrier and Munizaga (1979) K-Ar age on lava flows overlying the deposits. (b) Encinas et al. (2006) fission track age on zircon in ash layer interbedded with the deposit. (c) Cuadra (1986) K-Ar age on Farellones Formation volcanic rocks that failed.

Table 2.5. Surface exposure ages from (a) ^{10}Be and (b) ^{36}Cl measurements in boulders and detachment surfaces from landslides in the Southern Central Andes of Chile. Unit refers to classification in the relative chronosequence (H: Holocene, LP: Late Pleistocene). ^{10}Be production rates were calculated using four different time-dependent scaling schemes described in Balco et al. (2008), summarized in (c). Chemistry data for calculation of ^{36}Cl production rates and methodological summary in SDF.

(a) Beryllium- 10 ages

Sample ID	Unit	Lat. [°S]	Long. [°W]	Elev. [m a.s.l.]	Boulder Height [m]	Prod. Rate [atom g ⁻¹ (*)	$^{10}\text{Be}/^{9}\text{Be}$ [10^{-13} atom atom ⁻¹]	Conc. [10^5 atom g ⁻¹]	Age [ka] and uncert., average of columns A-C in Table 3c	
MES001	H	33.66	70.12	2722	3.0	29.30	2.883	1.205	4.7	0.6
MES002	H	33.66	70.12	2725	2.0	28.92	3.546	1.142	4.6	0.6
MES003	H	33.66	70.12	2755	4.0	29.71	3.358	1.118	4.5	0.5
MAQ002	LP	32.51	70.57	1427	4.0	12.40	20.69	15.26	112	14

Note: Standard used in AMS measurements: 07KNSTD3110, $^{10}\text{Be}/^{9}\text{Be}=2.85\text{E}-12$. The ^{10}Be half life assumed for these 2007 analyses was 1.36 Ma.

(*) Calculated with a time-constant production rate model.

(b) Chlorine – 36 ages

Sample ID	Unit	Lat. [°S]	Long. [°W]	Elev. [m a.s.l.]	Boulder Height [m]	Local prod. rate [atom g ⁻¹]	$^{36}\text{Cl}/\text{Cl}$ [10^{-15} atom atom ⁻¹]	Cosmogenic ^{36}Cl in rock [10^5 atom g ⁻¹]	Age (*) [ka]	Uncert. 1σ [ka]
SOLD004	LP	32.90	70.35	1731	Sliding surface	30.35	172.9	4.221	14.1	1.3
SOLD006	LP	32.90	70.35	1575	1.0	28.54	106.31	2.759	9.8	0.7
PAN001	H	34.24	70.38	1488	4.0	11.77	62.08	0.898	7.7	0.3
PAN003	H	34.24	70.38	1413	3.0	11.58	158.7	2.687	23.9	1.0
MAC001	LP	33.5	70.49	1562	7.0	5.13	519.5	3.769	80.4	2.6
MAC002	LP	33.5	70.49	1737	2.0	14.17	180.8	1.124	8.0	0.3
MAC003	LP	33.5	70.49	1631	1.5	12.85	333.9	2.400	19.1	0.6
POT008	LP	33.4	70.45	1467	0.7	9.97	1056	7.322	80.5	3.1
POT009	LP	33.4	70.45	1496	1.5	9.90	170.5	1.189	12.2	0.5
POT010	LP	33.4	70.45	1455	1.5	9.80	369.7	2.271	23.8	0.9

(*) Calculated assuming no erosion, minimum age of the surface. The ^{36}Cl half life is 301 ka.

Note: Standard used in AMS measurements: NIST SRM 4943

(c) Summarized Be-10 ages [ka] and uncertainty [ka] for different scaling schemes, calculated using the online code by Balco et al. (2008)

Sample	A. Desilets et al. (2006)		B. Dunai (2006)		C. Lifton et al. (2005)		D. Time-dependant Lal(1991)/Stone(2000)		Average of columns A-C and uncertainty	
MES001	4.7	0.6	4.9	0.6	4.6	0.5	4.2	0.4	4.7	0.6
MES002	4.5	0.5	4.7	0.6	4.5	0.5	4.0	0.4	4.6	0.6
MES003	4.3	0.5	4.6	0.5	4.3	0.4	3.9	0.4	4.5	0.5
MAQ002	116	14	113	14	112	11	109	10	112	14

2.6.2. Lithology

At least 85% of the rockslides in the Chilean side of the SCA have developed in or along the boundary of the Oligo-Miocene Abanico Fm. (Fig. 2.5a,b) even though it represents less than one third of the total bedrock surface area in the continental forearc (Fig. 2.2). Most rockslides have resulted from failure of competent rocks (Farellones Fm. or volcanic Abanico Fm.) interbedded with or overlying highly fractured units (fine

sedimentary and volcanoclastic Abanico Fm.). In places, distal volcanoclastic (ignimbrite) and sedimentary units (lacustrine facies) (Thiele, 1980; Sellés, 1999) may have contributed to the failure along WNW trending zones in the Abanico basin (Rivera and Cembrano, 2000; e.g. rockslides at El Laurel, Colorado River, Cuesta Maitenes, and lower Arrayán River, Table 2.3, Fig. 2.3c).

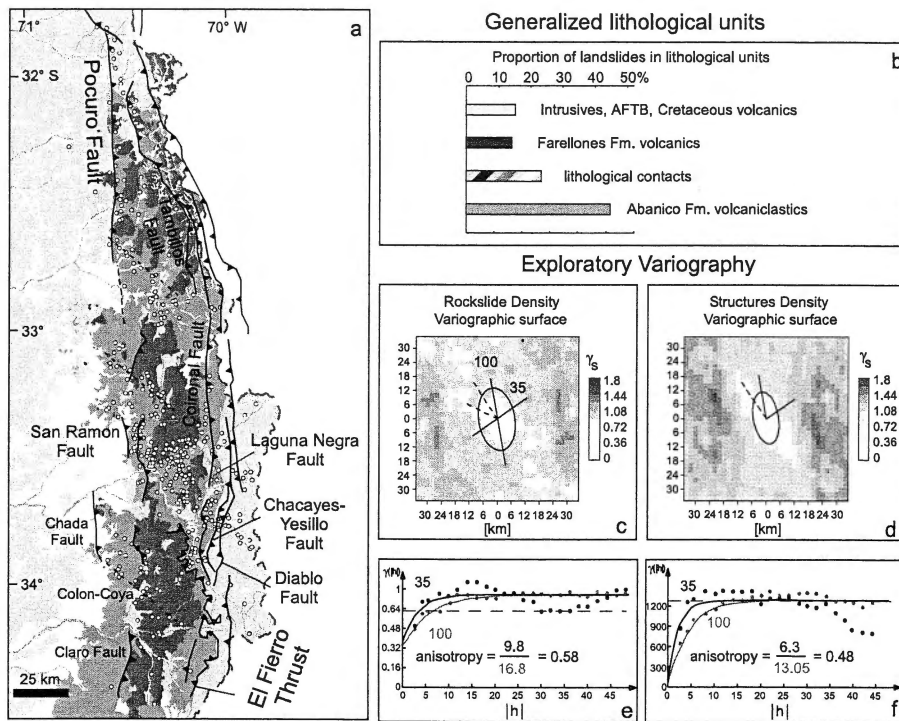


Figure 2.5. *a.* Lithological units and Late Cenozoic faults, and relation to landslides (circles) in the study area. Dashed lines show location of NW-WNW trends that appear unrelated to observed faults or structures. *b.* Proportion of landslides that were generated in a particular lithological unit; *c, d.* Variographic (standardized) surfaces for rockslide and structures density, calculated using Variowin® by Pannatier (1996). They show how the variability on the analyzed parameters depends on a particular direction, which is shown here starting as 0 towards east direction, and then increasing anticlockwise. Following a particular direction from the center of the diagram towards the edge indicates how far sampling points must be for their variability γ to reach the variance of the entire population (the distance at which they are equal is called the range). An ellipse has been fit with its major and minor axes being the directions of largest and smallest ranges modelled considering an exponential variation in directions N55°E and N10°W. *e.* Rockslide density variogram data and best-fit exponential model for the two directions portrayed above, showing the population variance as a dashed line, and the calculated anisotropy from the estimated ranges, *f.* Structures density variogram data and best-fit exponential model.

2.6.3. Geological Structures: Regional Faults

Rockslides within the CP are preferentially distributed along straight segments of faults (e.g. the PSRFZ, Fig. 2.3a) and structural discontinuities except where abutted by intrusive bodies (e.g. along the Olivares, Yeso, and Maipo River valleys; Fig. 2.3b). These structures are Late Cenozoic fault systems developed through Oligo-Miocene volcanic sequences in WCP and Late Miocene-Quaternary thrusts in the AFTB (Charrier et al., 2005; Rauld, 2002). Rockslides appear highly correlated with thrusts and backthrusts especially near the boundary between WCP and the AFTB (e.g. Maipo River valley at Los Queltehues; the Upper Aconcagua valley). This trend is also observed in Argentina along thrusts in the AFTB and Cordillera Frontal (Espizúa et al., 1993; Fauqué et al., 2000; Moreiras, 2006). WNW rockslide distribution patterns in the WCP that end either at the PSRFZ on the west or the Diablo-El Fierro-Yesillo system on the east, appear unrelated to the above mentioned structures (Fig. 2.5a, §2.6.2).

The relation between structures and rockslides marks important differences among WCP, ECP, and the Coastal Cordillera. The ECP does not hold a larger proportion of rockslides than the WCP, despite the fact that the AFTB displays high angle thrusts and backthrusts, and more fractured rocks that include fissile shales and gypsum diapirs with highly irregular tectonic contacts. In the Coastal Cordillera study area, geologic structures do not show an association with rockslides and the high steep slopes west of Santiago, Rancagua and San Felipe (Fig. 2.3a) appear devoid of large rockslides. The variograms reveal a similar spatial trend in the rockslide density and structure density grids (Fig. 5c, d). The higher and lower modelled range directions, indicated by the ellipses, match in both variables. The major axis orientation of the ellipse indicates the trend that the rockslide clusters follow, mimicking the N-S structural grain of the orogen. Zonal anisotropy was estimated to be 0.48 ± 0.16 and 0.58 ± 0.20 for rockslide and structure density respectively (Fig. 2.5 e,f), being indiscernible at 95% confidence interval, considering the uncertainty in the fit of the exponential model in each case. The N20-30W ellipse (only major axis marked) reflects the structures north of Aconcagua River. The two above mentioned ellipses also appear in the rockslide density variographic surface model (Fig. 2.5c), showing that rockslides follow structures that generated failure-prone zones, like major tectonic boundaries and river valleys. A third, WNW

pattern in the rockslide diagram (Fig. 2.5c) has no equivalent structural pattern but is equivalent to the orientation of fine sedimentary units described above (§2.6.2).

2.6.4. Relief

Local relief was calculated from 90 m SRTM data (corrected using digitized 1:50,000 scale topographical maps in areas of low coverage), using a circular moving window of 5 km radius, averaged over 1 km and grouped in 500 m bins (Fig. 2.6a). One of the highest relief regions in the western side of the Andes occurs between 33° and 34° S and large rockslides are more common there than immediately north and south within the study area. However, most areas with relief > 1500 m share the same proportion of rockslides when this proportion is normalized by the area covered by that relief range inside the study region. Almost all rockslides occur where relief >1500 m but there are some large areas with this relief but lacking rockslides (e.g. Coastal Cordillera west of San Felipe and Santiago basins, and regions of relief >2500 m, inside CP; Fig. 2.6a).

2.6.5. Slope

The overall correlation of slope (SRTM data averaged over 1 km) and occurrence of rockslides appears to be low, and on slopes with inclinations above 0.27 (~15°) the same proportion of rockslides (Fig. 2.6b) is held in different slope bins, suggesting decoupling of these two variables. We realize that large rockslides modify the original morphology surrounding the deposit and that therefore regional slope angles are not reliable indicators for causes and triggering of large rockslides (Korup, 2006). More relevant though, is the lack of events in areas of high slopes of the AFTB and Coastal Cordillera.

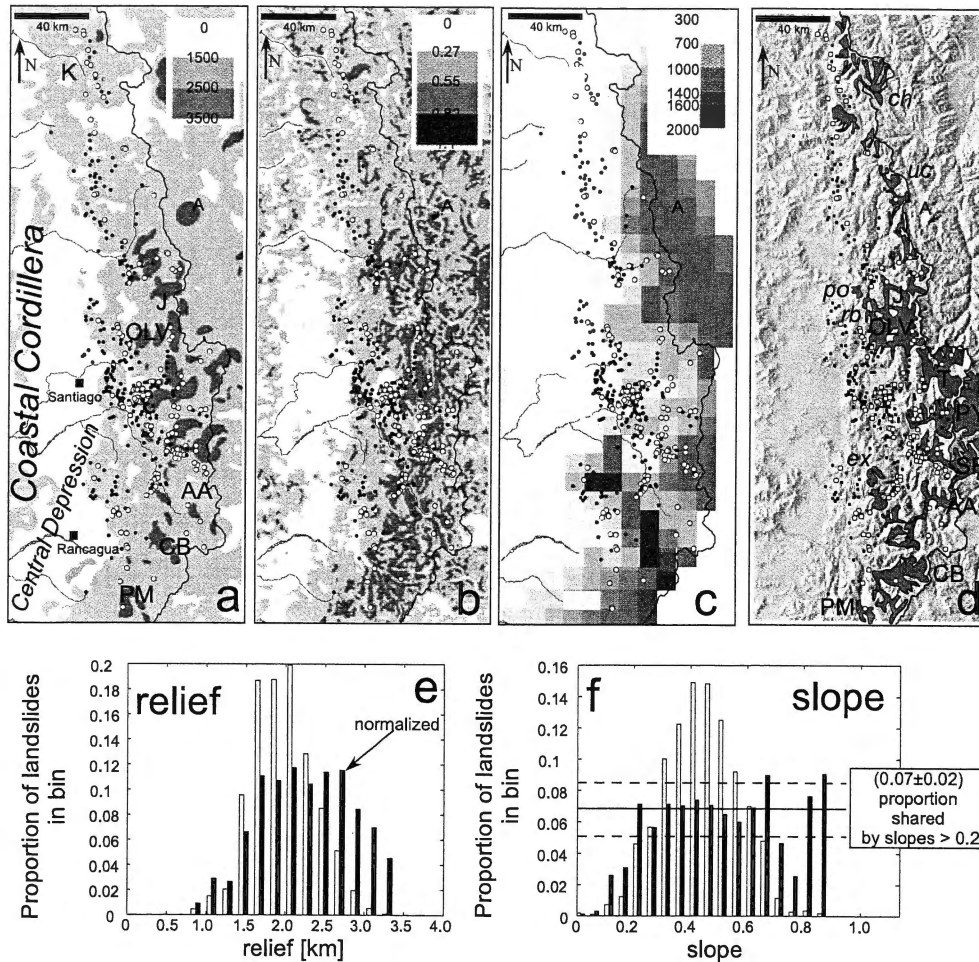


Figure 2.6. Distribution of landslides compared to different landscape metrics, present-day precipitation, and glacial conditions during LGM. In panels a-d, Holocene rockslides are marked with white circles, Late Pleistocene and older rockslides appear as black circles. a. Local relief (over a 5 km moving window, from corrected SRTM data). Other features shown are: volcanoclastic Cretaceous rocks (K), and the Aconcagua Massif (A) in Argentina. Glacier systems and ice fields are named after present-day remnants: Juncal (J), Olivares (OLV), Argüelles-Alvarado (AA), Catedral-Barroso (CB), Palomo (PM). b. Mean slope (over a 1 km moving window, from corrected SRTM data), c. Mean total annual precipitation [mm a^{-1}] from records of last 60 a (Dirección General de Aguas, Chile), d. Estimated Last Glacial Maximum ice extent (see text for references). Major glacier systems are named like in panel a., but adding Tupungato-Piuquenes (T), and San Francisco-Plomo-Yeso (PY-SF). LGM glacier systems only displaying glacial sediments and landforms today but no ice remnants except for rock glaciers: Extravío (ex), Rio Blanco-Riecillos-Arrayan (rb), Pocuro-Las Ollas (po), Upper Colorado (Aconcagua catchment, uc), Upper Choapa and Sobrante catchments indistinct (ch). e, f. histograms depict proportion of rockslides in a determined relief or slope bin. Darker bars indicate normalized proportions relative to the complete surface area encompassed by the relief or slope bin in the study region.

2.6.6. Precipitation and Glaciation

No correlation between rockslide occurrence and present-day total precipitation is observed (annual totals, averaged for the last 30 a, Fig. 2.6c). Precipitation type, and distribution throughout the year, also investigated, showed no incidence on rockslide occurrence. Most of the present-day precipitation along the western mountain front of CP is rain during winter frontal storms, with minor observed effects on stability of slopes, except for the frequent occurrence of relatively small ($\sim 10^6$ m³) debris flows with recurrence intervals of years to decades (Sepúlveda et al., 2006). Although the present-day pattern of precipitation does not necessarily reflect Quaternary conditions, the latitudinal influence of the westerlies must have been similar. Precipitation increases southward in the field area, with an enhancement in the overall amount during the LGM (e.g. Heusser, 1989, 1990; Zech et al., 2006; Lamy et al., 1999). With similar lithologies and relief, a hypothetical southward increase in rockslide density is not recorded in our inventory.

Glaciation limits proposed by previous authors (e.g., Caviedes, 1972; Thiele, 1980, Chiu, 1991) were verified and redrawn when field observations indicated so (Fig. 2.6d). Rockslides occur predominantly in regions outside LGM ice limits. Most of the evidence for Pleistocene rockslides in the glaciated areas of the southern WCP may have been completely erased by LGM glacial activity (e.g, areas CB and PM, Fig. 2.6d). However, despite the high relief in these glaciated areas, Holocene rockslides are not prevalent, with most of the high angle slopes being covered by talus.

2.6.7. Seismicity

2.6.7.1. Subduction (Interplate) Seismicity

Large subduction earthquakes in the area (e.g. Beck et al., 1998; Pardo et al., 2002) may play a role in triggering large rockslides ($> 10^8$ m³, e.g., Keefer, 1994, 2002; Rodríguez et al., 1999). However, recent large earthquakes, like the 1906 Valparaiso (Ms 8.4), 1943 Illapel (Ms 7.9), and 1985 San Antonio - Valparaiso (Ms 7.8) events, have not generated large rockslides and only small rock falls and debris slides have been reported (Erikson and Högstedt, 2004). In addition, rockslides are more pervasive inside the CP above the deeper Benioff Zone (Fig. 2.7) where earthquake energy at the surface is

weaker relative to areas above shallower Benioff Zones, a pattern that is opposite to the one expected if subduction seismicity were the main trigger.

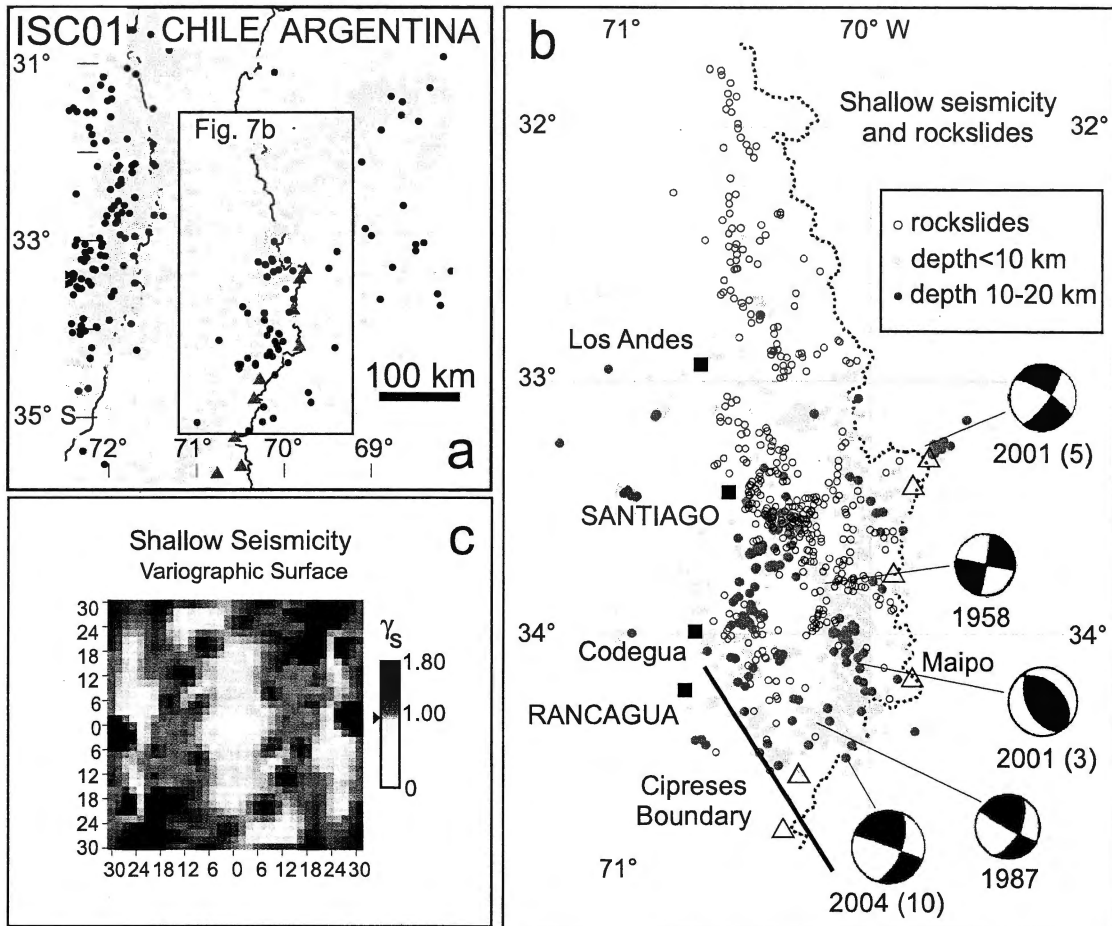


Figure 2.7. Relation of seismicity with the rockslide inventory. **a.** Seismicity according to the International Seismicity Catalog, up to 2001 (ISC01, gray dots: all events; black dots: shallow seismicity, <20 km deep). Note the concentration of shallow seismicity in the study area. **b.** Shallow seismicity according to unpublished data (R. Farías, Univ. de Chile) including original data published in Barrientos et al. (2004) with published fault plane solutions for the area, year of the event, and depth (in parenthesis, data from Alvarado et al., 2005). Rockslide inventory is shown in open circles. The Cipreses Boundary delimitates an area of increased seismicity and mass wasting to the northeast. Pleistocene-Holocene volcanic centers are marked by open triangles. **c.** Variographic surface for shallow seismicity density (gridded to 1 km), covering the whole study area.

2.6.7.2. Shallow (Intraplate) Seismicity

A zone of high density shallow (<20 km depth) seismicity (Barrientos et al., 2004; Alvarado et al., 2005) corresponds with the area where rockslides concentrate in the SCA (Fig. 2.7). In the southwestern region, where the Abanico Fm develops a tightly folded

pattern (Charrier, 1983) there is a clear delimitation of an area with low rockslide density and low shallow seismicity from an area with higher spatial densities of both variables to the northeast (Fig. 2.7b), following approximately the direction of Cipreses River (cf. Brüggén, 1950 and Fig. 1 in Godoy et al., 1999). In WCP, a correspondence between shallow seismicity and the PSRFZ is clearly evident (Fig. 2.7b). Concentration of shallow seismicity in the upper Cachapoal and middle-upper Maipo valleys (Barrientos et al., 2004) and along the faults defining the Olivares River valley also coincides with rockslide clusters. A diffuse clustered pattern is shown by rockslides at Codegua, and the eastern Colón-Coya area, in an area of high seismicity (Fig. 2.5, 2.7) that can be followed in depths of 10-20 km following a NNE trend that ends in an area of increased rockslide occurrence trending WNW just east of Santiago. East and southeast of this area where a recent concentration of seismic activity has been detected in the headwaters of the Cachapoal River (Charrier et al., 2005), rockslide occurrence is scarce (Fig. 2.3).

We tested the relation between shallow seismicity and rockslide occurrence using variographic analysis of different seismicity datasets (Fig. 2.7c), which were compared to structure and rockslide patterns. A clear correlation appears between rockslide density and shallow seismicity density measured during the last 20 years, with a regional pattern similar to the one defined by structure density, i.e. a clear NS trend and NNW and WNW patterns that are obscured but still noticeable in the variographic surface (Figs. 2.5c,d, 2.7c).

2.7. Discussion

2.7.1. Seismic Versus Climatic Factors as Trigger for Large Rockslides in the SCA

While it is likely that some large rockslides and the majority of debris flows correspond to weather-induced failures, the distribution of the majority of rockslides do not follow any known climate patterns, past or present. The lack of an increasing north-south trend in rockslide density does not support a link with the strong southward increase in precipitation in the WCP throughout the late Cenozoic (Lamy et al., 1999; Zech et al., 2006; Fig. 2.6c). Nor is any west-east trend evident in the rockslide inventory, which is contrary to the rainshadow effect.

On the other hand, the clustering of rockslides and shallow seismicity (Fig. 2.7) indicates a causal relation. Shallow seismicity is consistent with ongoing tectonic activity in WCP, (Fariás et al., 2006), and occurrence of rockslides close to Late Cenozoic faults (Fig. 2.5) suggests direct triggering of rockslides through strong ground acceleration, possibly enhanced by topographic amplification. This relationship is supported by the observation that for more than 80% of the rockslides, the rockslide detachment surface is in the upper third of the hillslope (Fig. 2.8). This observation indicates a strong topographic amplification signal, in contrast with pore pressure induced failures which tend to exhibit lower detachments. The absence of large-scale paleoseismic features outside CP, closer to the interplate seismogenic zone, and specifically of large rockslides, is consistent with the corollary that subduction earthquakes do not generate the majority of large rockslides in the study region. We propose that medium to large magnitude ($M= 5-7$) shallow earthquakes spatially related to NS and oblique-to-the-orogen structures inside the CP have caused the majority of large rockslides throughout the Quaternary.

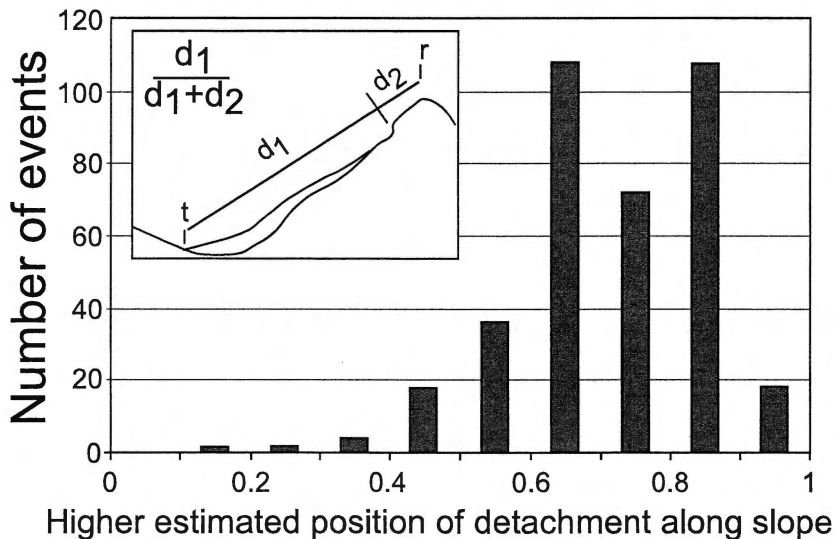


Figure 2.8. Estimated location of the detachment point along hillslopes for the rockslides in the inventory. The total number of landslides corresponds to those with appropriate constraints, and it might not be representative of shallow failures in the AFTB which may have been erased from the record.

We recognize two caveats in our interpretation. 1. The present-day distribution of seismicity is taken as a proxy for Quaternary seismicity because paleoseismic analyses are not available. 2. The paucity of rockslides during historical strong shallow

earthquakes in the area (e.g. 1958 M 6.9 Las Melosas event, Sepúlveda et al., 2008) is contrary to empirical model predictions of landslides (e.g. Keefer, 1994) for the same earthquakes. However, these models have been derived mostly from inventories of shallow landslides not occurring in areas of high relief and on bedrock slopes (cf. Keefer, 1994; Rodríguez et al., 1999). The extrapolation of these calibrated models to different geological environments and the larger magnitude rockslides in our study is non-trivial. The paucity of inventories recorded after large magnitude-low frequency events in high relief regions preclude further generalisation.

2.7.2. Controls on Distribution of Rockslide Occurrence

2.7.2.1 Non-Uniform Rockslide Occurrence in the ECP and WCP

The glaciated areas of the AFTB in the ECP display fewer rockslides than the rest of the area, except in specific regions (PY-SF in Fig. 2.6d), where we hypothesize that shallow seismicity has triggered large rockslides during post-glacial times. This hypothesis is consistent with the observation that areas of present-day low seismicity appear to correlate with lower density of rockslides. Low post-LGM rockslide density in areas inside the AFTB with high present-day shallow seismicity (Fig. 2.7b) might be explained by a different mechanism for landsliding. One possibility is that seismically induced rock strength reduction (Dramis and Blumetti, 2005; Molnar et al., 2007) is pervasive in the AFTB rocks. These rocks will be prone to fail as small, composite rockfalls which when mixed with ice and water (Hauser, 2002; Sepúlveda et al., 2006) evolve into debris flows and sheets that have poor preservation. This pattern is observed in the Mendoza River (Espizúa et al., 1993), immediately to the east of our study area, where flows are the predominant present-day failure mode in the highly fractured Mesozoic rocks of the AFTB. Rockslides in the relatively less fractured Cenozoic volcanic rocks occur mostly as relatively large coherent deposits, similar to what we observe in WCP.

To further explain the lower frequency of large rockslides in the more heavily glaciated ECP, it is possible that the paraglacial stress release (Cruden and Hu, 1993; Ballantyne and Stone, 2004) after the last deglaciation has not yet reached its maximum and that there is high potential for some of these areas to develop rockslides in the near future. This seems at odds with data from most deglaciated areas of the world and with

the greater relative abundance of Holocene rockslide ages. Alternatively, most of these glaciated areas in the ECP might have not developed postglacial failures because they are 'stress-hardened' as suggested by Jarman (2006) to explain the absence of large rock-slope failures in regions that experienced recurrent glaciations during the Pleistocene. This seems unlikely given the amount of highly fractured volcanic and sedimentary rocks present in the area (cf. Molnar et al., 2007), as opposed to the crystalline rocks studied by Jarman (2006).

2.7.2.2 Tectonic Control of Large Rockslides

The uniform distribution of rockslides over wide ranges of relief and slope (Fig. 2.6) and the lower density of rockslides in glaciated areas suggest that stream incision and glaciation are not the primary controls on rockslide occurrence. The distribution of Quaternary rockslides around NS structures like the PSRFZ, Laguna Negra-Coironal Faults, and the northern El Fierro Thrust, suggests Quaternary activity along these fault zones, as it has been shown elsewhere for compressive or transpressional fault systems in high-relief areas where present-day shallow seismicity is prevalent (Philip and Ritz, 1999; Sato et al., 2006; Jibson et al., 2006). Late Pleistocene activity along the PSRFZ system has recently been documented (Rauld, 2002). If taken at face value, our hypothesis implies that the main fault systems bounding WCP on the west, and the Laguna Negra-Coironal and Chacayes-Yesillo faults in the east (Fig. 2.5a), have been active during the whole Quaternary, holding shallow seismicity that in turn triggers large rockslides. At the boundary between WCP and the AFTB, movements along these faults started in the Late Miocene and continued at some point during the Pleistocene (Fock, 2005). Therefore, it is not surprising that rockslide distributions support the notion that the entire WCP block in the study area has experienced surface uplift during the Pleistocene, extending the surface uplift proposed by previous authors for the Late Miocene (Fock et al., 2006; Farías et al., 2008).

Not only NS systems appear to concentrate rockslides, WNW rockslide trends are scattered across the area, but they match mapped lithological properties only in one area (east of Santiago, Fig. 2.3). In most other regions (Fig. 2.5) the WNW trends occur in the same lithological unit. We therefore propose that these rockslides are related to large

scale WNW structural and tectonic patterns already hypothesized (e.g. Rivera and Cembrano, 2000) but scarcely described.

2.7.3. Sediment Production from Rockslides

2.7.3.1. Volumetric Analysis of Selected Rockslides and a Local Volume-Area Relationship

To facilitate an areal proxy for rockslide volume, an assessment of volume (V) versus area (A) was completed following Hovius et al. (1997) and Malamud et al. (2004a, b), using deposit dimensions to fit a relation of the form $V = \varepsilon A^f$ on a representative number of well preserved Late Pleistocene and Holocene rockslides (Table 2.6). This relationship should be valid for our older rockslides as long as most of the failures are coherent and partially retain the original geometry. There is a remarkable similarity in the values for f (1.56 ± 0.17) and ε ($\log \varepsilon = -1.68 \pm 1.21$) shown by SCA rockslides (Fig. 2.9) with those derived elsewhere, under differing distributions of slide sizes, and tectonic and climatic regimes (Abele, 1974; Hungr, 2006; Korup, 2006). Apparently lower f (~ 1) exponents (Simonett, 1967; Guthrie and Evans, 2004) are valid for smaller (10^3 - 10^5 m²) landslides, increasing up to 1.6-1.7 for larger ones (Korup, 2006; this study), implying a large difference when incorporating these relations into total inventory volume estimations (§2.7.3.2).

Table 2.6. Volume and area determination of 14 selected Late Pleistocene-Holocene landslides, for estimation of a relation linking $V=f(A)$.

Rockslide	Inventory No.	Volume (m ³)	Estimated uncertainty in volume (%) ²	Method(s) ³	Area (m ²)
Mesón Alto – Yeso (8) ⁴	67	4.50E+09	10	b-c	1.57E+07
Llaretas del Rocín (16)	330	4.58E+08	(20)	b	1.03E+07
Estero Potrillos Olivares	294	3.20E+09	(20)	b	8.70E+06
Teniente	375	2.33E+08	(20)	b	7.53E+06
Portillo (17)	211	1.15E+09	60	b-d	4.80E+06
Río Argüelles	328	4.02E+08	(20)	b	3.66E+06
Río Negro del Maipo	327	1.05E+09	(20)	b	3.27E+06
Pochoco	278	1.94E+08	25	a-b	2.85E+06
Tornamesa	346	4.12E+07	50	a-b	2.52E+06
Salto del Soldado (18)	222	1.65E+08	20	a-b	2.18E+06
Maitenes	27	1.98E+08	10	a-b	2.10E+06
San Simón	107	1.34E+08	10	a-b	1.65E+06
Potrerillos S	126	1.25E+07	20	a-b	4.36E+05
Potrerillos N	125	2.32E+06	20	a-b	1.25E+05

² Estimate based on propagated uncertainties for calculations based on different methods. Parentheses indicate assumed uncertainty for the method in a particular rockslide.

³ Methods: a, GPS-altimeter measurements; b, estimated from crown and escarpment measurements on DEM using methods by Cruden and Varnes (1996); c, geophysical (gravity) profiling on the deposit (Marangunic and Thiele, 1971); d, field measurements from Godoy et al. (1994b).

⁴ Numbers in parenthesis refer to identification of rockslide in Table 2.3. All other rockslides can be found on the Supplementary Data File included in the appendices (§7.1) under their inventory number.

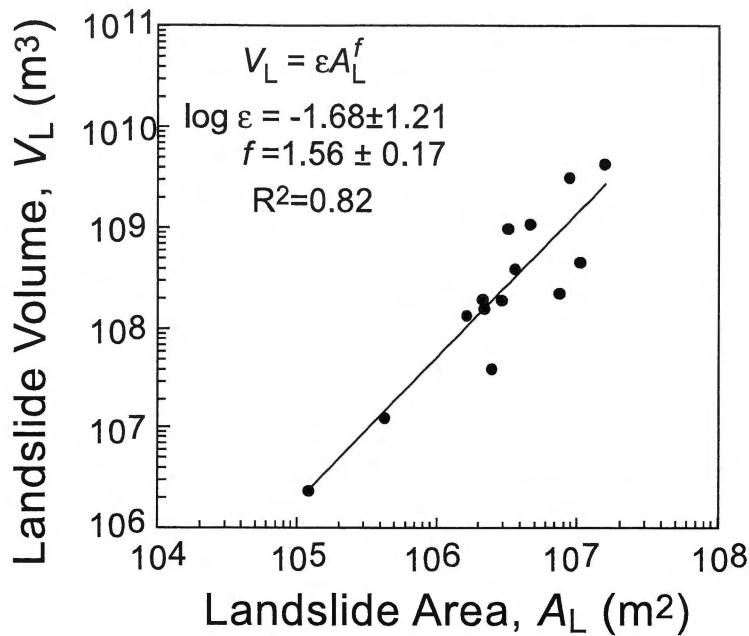


Figure 2.9. Local volume – area relationship, from regression of data in Table 2.6. Generalized regression was used to fit the parameters, as both variables show large uncertainties.

2.7.3.2. Cumulative Inventory Volumes and Rockslide Derived Denudation Rates

To estimate a cumulative rockslide volume over the entire Quaternary, the size distribution of rockslides must be considered to account for rockslide erosion and burial. Rockslide area follows an inverse power-law distribution, like other landslide inventories (e.g., Hovius et al., 1997), with a rollover of the frequency density function (fdf) for small ($<2 \text{ km}^2$) sizes (Fig. 2.10). Assuming that the dataset is complete for the large rockslides, the slope of the fdf over a range of rockslide areas can be estimated and this will allow estimating total inventory volumes, compensating for the missing (buried or eroded) rockslides (Hovius et al., 1997, Malamud et al., 2004b) that might be reflected in the rollover of the fdf .

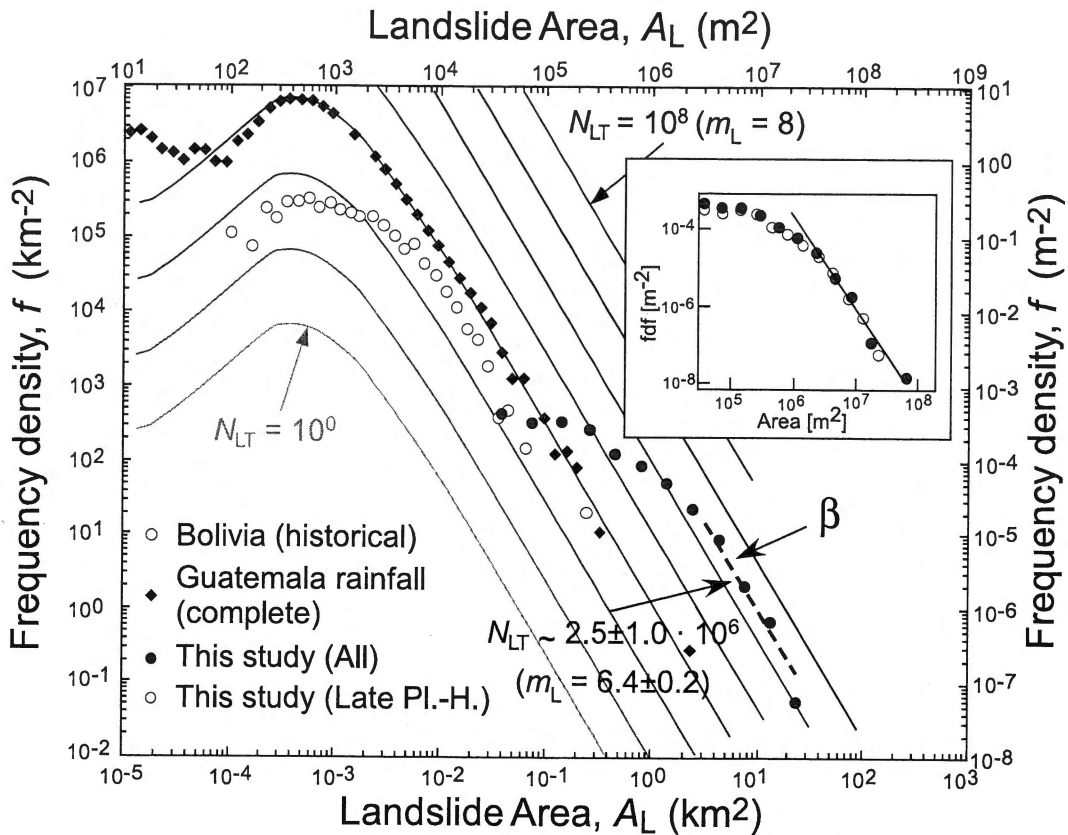


Figure 2.10. Dependence of the landslide frequency density (fdf , number of landslides in a particular area bin, normalized per bin area, for a detailed explanation, the reader is referred to Malamud et al., 2004a) on landslide area for a complete inventory (Guatemala) and a historical inventory (Bolivia), both after Malamud et al. (2004a), and the Southern Central Andes inventory ($n=378$, 13 bins). N_{LT} = Total number of landslides. Note the match of both historical inventories with the tail slope (β) of the distribution predicted by Malamud et al. (2004a), which is shown as curves modelled from $m_L=1$ to 8 (see text for explanation). The $m_L=6.4$ curve is shown. The inset shows the fdf for the complete SCA inventory compared to the one presented by Late Pleistocene-Holocene slides. The two smaller size bins in the SCA inventory correspond to counts possibly affected by undersampling, as these landslides ($<0.1 \text{ km}^2$ area) were considered only in connection to larger deposits, and were not mapped systematically.

We investigated how the fdf changes with different age classes (Fig. 2.11). Even for the Holocene dataset, erosion and burial distort the slope of the distribution at small sizes, with a knee at about 2 km^2 . The knee displaces to larger sizes as datasets get older, implying that erosion and burial eventually affects larger rockslides when they are left to erosion for longer periods (10^5 a).

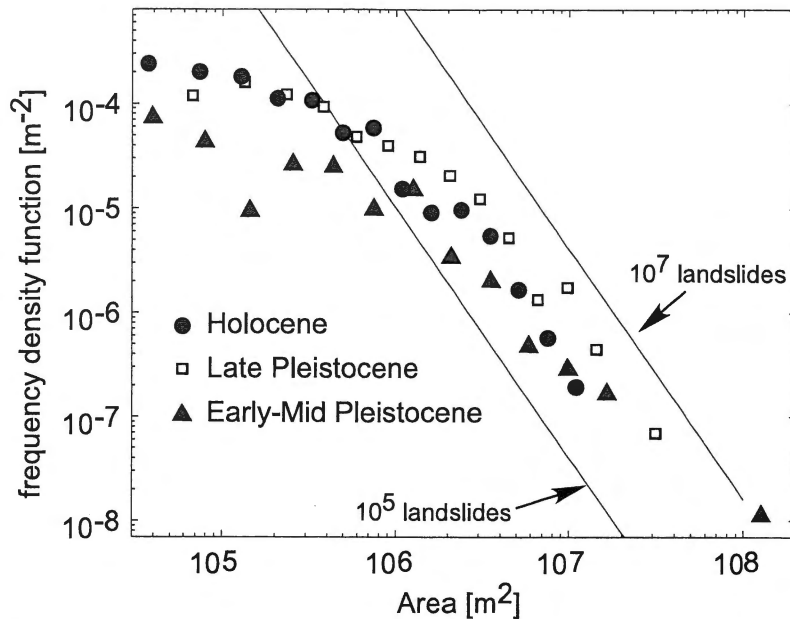


Figure 2.11. Frequency density functions for different age classes in the SCA inventory. The two lines depict model fits of the gamma distribution of Malamud et al. (2004a) in the size range of interest, for two modelled total number of landslides. Note that in all cases, the distributions have the same slope (β) in the larger landslides. Erosion and burial tend to shallow the slope of the distribution as they get older, affecting increasingly larger sizes.

The β slope derived for our larger rockslides (Fig. 2.10) is similar to that derived empirically by Malamud et al. (2004a, Appendix, §2.9.2) for well mapped historical rockslide events. This suggests that the *fdf* of Malamud et al. (2004a) is valid over areas of 1-100 km², and although their distribution was used to reconstruct our inventory for rockslide areas between 10⁻¹ and 10² km², a simple power law also could be used with the same results. The use of large rockslides provides insights into longer-term landscape evolution, while allowing for a better control on volume, sediment dilatancy and post-depositional compaction. Its use implicitly assumes that smaller soil and debris slides are derived from the large events, which is observed to be common in our study area.

As apparently neither full glacial nor Holocene (interglacial) climatic conditions have a distinct effect on rockslide triggering, we assumed independency of climatic conditions during the whole Quaternary, and we based our reconstruction on the relatively well preserved Holocene rockslide inventory. If glacial conditions do increase the frequency of landsliding, the sediment production estimate must therefore be regarded

as a minimum. The cumulative magnitude of the Holocene inventory, m_L (logarithm of the total number of rockslides in the distribution, N_{LT}), was obtained from the best-fit for the power-law tail of the distribution (Fig. 2.11). $m_L = 5.8 \pm 0.2$, hence $N_{LT} = 6.5 \pm 2.5 \times 10^5$ rockslides, and integrating the distribution over areas 10^{-1} to 10^2 km², $V_{LT,Holocene} = 16 \pm 11$ km³ (Appendix, §2.9.2). The total volume produced over the entire Quaternary (1.8 Ma) is $V_{TotalQ} = 2880 \pm 2340$ km³, and a mean landscape denudation rate equivalent to 0.10 ± 0.06 mm/a can be estimated over 14,000 km². This calculation considers 20% of volume expansion for rockslide deposits compared to original bedrock material (Chen et al., 2006), and 1% compaction after a few years of rockslide deposition (Chang et al., 2006). The uncertainty is based on propagation of error in the variables used in equation A2-4 (Appendix, §2.9.2).

The Late Pleistocene inventory has been significantly eroded in both volume and number of rockslides if compared to an extrapolation of the Holocene record back to 125 ka. The observed distribution of Late Pleistocene-Holocene rockslides (Fig. 2.10) is not different from the distribution of all rockslides >2 km². After ~ 100 ka an erosional equilibrium develops such that the volume of rockslides generated is equivalent to the rockslide volume removed from the record by erosional or burial processes. This conclusion is supported by the observation that 85% of the rockslides in the inventory are Late Pleistocene-Holocene (Fig. 2.4). The remaining fraction comprises rockslides with volumes mostly larger than the median volume of the population, and its size distribution is not useful to quantify sediment production rates.

2.7.3.3. Sediment Volume Estimation Assuming Shallow Seismicity as Main Rockslide Trigger

To complete our analysis, we linked the triggering mechanism with sediment flux to provide a predictive model of landscape evolution in the SCA. If we assume that rockslides are seismically triggered, the Gutenberg-Richter relation can be combined with our denudation observations to estimate rockslide volumes for given earthquake magnitudes (e.g. Keefer, 1994; Malamud et al., 2004b, Appendix, §2.9.2). The results must be used with caution because there is no independent relationship between earthquake magnitude and rockslide event magnitude developed for our region, so it is necessary to use data compiled from historical accounts of earthquakes triggering

landslides elsewhere (Keefer, 1984). As Malamud et al. (2004b) pointed out, the total number of landslides, and hence V_{LT} , not only depend on earthquake magnitude, but also on parameters like focal depth and topographic amplification, which in our area apparently play major roles. Still no analytical relationship has been derived to account for these factors, therefore casting a large uncertainty in the subsequent analysis.

Local seismicity parameters were defined by Barrientos et al. (2004) for shallow events, and their validity is restricted to magnitudes between 3.5 and 5.5. Following Malamud et al. (2004b), a volumetric rate \dot{V}_L at which landslide material is generated by earthquakes is (Appendix, §2.9.2):

$$\dot{V}_L = 10^{-11.26 \pm 0.52} (\ln 10) b \dot{a} \int_{M_{\min}}^{M_{\max}} 10^{(1.42-b)M} dM \quad [\text{km}^3 \text{ a}^{-1}] \quad (1),$$

which leads to a total maximum available flux of $2.7^{+6.7}_{-1.9} 10^{-3} \text{ km}^3 \text{ a}^{-1}$ if $\log \dot{a} = 7.8 \pm 0.1 \text{ a}^{-1}$ and $b = 1.40 \pm 0.02$. Averaged over the area where seismicity parameters were derived (10,000 km^2 , Barrientos et al., 2004), the equivalent contribution of rockslides to denudation (i.e. sediment production rates) approaches $0.3^{+0.6}_{-0.2} \text{ mm a}^{-1}$. Barrientos et al. (2004) noticed that their parameter b is excessively high and, if lowered, may shift the estimation up by an order of magnitude. The large uncertainty in this figure and the 3-fold discrepancy between these rates and those derived from empirical area rockslide distributions (§2.7.3.2) highlights the need for a quantitative, physical approach to the problem, or at least empirical derivations that include focal depth and topographic amplification as critical factors.

2.7.4. Relevance of Rockslides for Mass Transfer in the Southern Central Andes

The calculated sediment production rates by rockslides fall within the range of rates reported for similar landslide-prone areas (Table 2.7). At these rates, it has been proposed that a combination of rockslides and other surface processes like shallow landslides and diffusive colluvial processes is responsible for mass transfer out of an active orogen (e.g., Lavé and Burbank, 2004). However, when compared to local incision rates in WCP and to existent information on stream sediment transport on major rivers draining the study area (Ayala et al., 1984), sediment production by large rockslides

appear to be of the same order of magnitude as stream sediment discharge. The only other process that could bring as much sediment as rockslides could be glaciers. We obtained data for glacial erosion (Table 2.7, data from Singer et al., 1997), but it must be noted erosion rates quoted are derived from estimates of denudation of a volcanic edifice at 36° S, where the glaciers should have been more important as denudational agents than in our study area (of which less than 20% was glaciated, Fig. 2.6d). The relevance of rockslides as sediment feeders to the fluvial network might diminish north of 32° and south of 35° S, as seismicity decreases (Fariás et al., 2006). More data on sediment transfer by processes like glaciers, hillslope diffusion (creep) and small scale high-frequency debris flows, in addition to accurate relations between paleoseismicity and rockslide occurrence are required to test these ideas.

Table 2.7. Comparison of surface lowering rates (denudation rates) in areas of significant landsliding (a), the sediment production rates obtained in this study (note that the seismicity-derived rate is valid for as long as seismicity has been present in the area, which we estimate as the same as the time for large rockslide occurrence) (b), and stream incision, sediment transport, and exhumation rates from areas in the SCA or the vicinity (c). Note different timescales involved.

	Rate [mm a ⁻¹]	Period [a]	Reference
a) Site (indicating type of mass wasting)			
Vancouver Island (<i>spt</i> ⁵)	0.06	50	Guthrie and Evans (2004)
San Gabriel Mountains (<i>skpt</i>)	0.08-0.28	15-100	Lavé and Burbank (2004)
Southern Alps, New Zealand (<i>psk</i>)	4-9	40-60	Hovius et al. (1997)
SE Eastern Cordillera, Bolivian Andes (<i>p</i>)	4-14	35	Blodgett (1998)
b) Lowering rate from mass wasting (this study)			
Southern Central Andes of Chile (<i>kt</i>)	0.1±0.06	1.8·10 ⁶	This study
Southern Central Andes of Chile (<i>kt</i>)	0.3 ^{+0.6} _{-0.2}	1.8·10 ⁶⁶	This study
c) Exhumation, local incision rates, and sediment transport for the SCA			
Stream incision rates (34-35°S, western boundary of WCP)	0.06-0.08	(0.9-2.3)·10 ⁶	Different sources compiled by Farías et al. (2008)
Stream incision rates (33-35°S, boundary WCP-AFTB)	0.3-2.4	(0.45-1.1)·10 ⁶	
Stream incision rates (35°S, western CF, Argentina)	0.1-0.5	0.65·10 ⁶	Baker et al. (submitted)
Suspended sediment transport (Maipo River)	0.1	30	Ayala et al. (1984)
Glacial erosion(36°S)	0.3-0.6	0.95·10 ⁶	Singer et al. (1997)

⁵ Note: *s* debris slides on soil, *k* rockslides, *p* rainfall triggered, *t* seismically induced.

⁶ Assuming that triggering by shallow seismicity has persisted over the entire Quaternary

2.8. Conclusions

We propose and provide the first test of a hypothesis that links rockslides with Late Cenozoic structures and present-day shallow seismicity (<20 km deep), suggesting a causative relationship between active tectonics in the western Cordillera Principal and large rockslides. Based on an inventory of large Late-Pliocene to Holocene rockslides, we propose that shallow seismicity is the primary trigger for large rockslides in the southern Central Andes of Chile. Using two methods to estimate sediment yield by rockslides, we show that rockslides account for net denudation rates of $0.10 \pm 0.06 \text{ mm a}^{-1}$ over the entire Quaternary and $0.3_{-0.2}^{+0.6} \text{ mm a}^{-1}$ over a period where shallow seismicity has predominated (based on 20 year seismicity records). The difference between these estimates reflects the empirical nature of the relations used, specifically the weak relation between magnitude of earthquakes and rockslide volumes.

The inferred seismic control of rockslide occurrence and the relevance of rockslides in sediment generation in the western SCA when compared against fluvial and glacial processes suggest that Quaternary landscape evolution has been strongly influenced by tectonics. The role of climate could be more relevant in the AFTB where Pleistocene glaciations might have dominated sediment production and transfer.

2.9. Appendix

2.9.1. Uncertainties in Estimated Rockslide Volumes

Uncertainty in estimates of rockslide volume was analyzed by comparing our estimates with independent volume determinations (mainly using geophysical methods, e.g. the Mesón Alto-Yeso rockslide; Marangunic and Thiele, 1971, described in the SDF). The difference between our and the geophysical estimates of the original and present-day volume approaches 5% and partly reflects the uncertainty of our method. Deposit thickness measured under different conditions (slope, lithology, relative age) may vary individually around 5-10%, less than quoted by Hovius et al. (1997) for their area-volume relationships. Estimated uncertainties using Monte Carlo simulation for volume reconstruction of smaller rockslides, however, show up to 20% of difference, depending on how rockslides fill the valleys. This uncertainty is similar to the one

estimated for reconstructed volumes in the Karakoram region (Hewitt, 2002, 2006) and in NW Argentina (e.g. Hermanns et al., 2006). This amount is considered to be the upper boundary of uncertainty, and was used in the area-volume relationship analysis (§2.7.3.1).

2.9.2. Derivation of Equations for Volume Estimation

a) Obtaining a total volume from the rockslide inventory reconstructed using an empirical frequency density function (*fdf*).

A volume distribution must be integrated over a range of sizes of interest:

$$V_{LT} = \int V_L dN_L \quad (\text{A2-1}).$$

For any inventory, $dN_L = p(A_L)N_{LT}dA_L$, then

$$V_{LT} = \int_A \varepsilon A_L^f p(A_L) N_{LT} dA_L \quad (\text{A2-2}).$$

Assuming that $p(A_L)$ follows a gamma distribution (Malamud et al., 2004a), with $a=1.28 \cdot 10^{-3} \text{ km}^2$, $s=1.32 \cdot 10^{-4} \text{ km}^2$, $\rho=1.4$,

$$p(A_L; \rho, a, s) = \frac{1}{a\Gamma(\rho)} \left[\frac{a}{A_L - s} \right]^{\rho+1} \exp\left[-\frac{a}{A_L - s} \right] \quad (\text{A2-3})$$

Integrating over A_{\min} , A_{\max} , when $A_L \gg s$,

$$V_L = \frac{N_{LT} \varepsilon a^\rho}{\Gamma(\rho)} \int_{A_{\min}}^{A_{\max}} A_L^{f-\rho-1} \exp(-a/A_L) dA_L \quad (\text{A2-4})$$

b) Obtaining a total volume from earthquake-triggered rockslides.

Following Malamud et al. (2004b), if \dot{N}_{CE} is the cumulative number of earthquakes with a moment magnitude greater than or equal to M in a specified region and time, the Gutenberg-Richter relation:

$$\log \dot{N}_{CE} = -bM + \log \dot{a} \quad (\text{A2-5}),$$

can be combined with an estimation of rockslide volumes due to seismically triggered mass-wasting (e.g., Keefer, 1984):

$$\log V_{LT} = 1.42M - 11.26(\pm 0.52) \quad (\text{A2-6}),$$

where M is earthquake magnitude, to derive a volumetric rate \dot{V}_L at which rockslide material is generated by earthquakes, by integrating the total volume V_{LT} of rockslide

material generated by each individual earthquake of magnitude M over $M_{\min} \leq M \leq M_{\max}$:

$$\dot{V}_L = - \int_{M_{\min}}^{M_{\max}} V_{LT}[M] \cdot d\dot{N}_{CE}[M] \quad (\text{A2-7}).$$

From A2-5, $d\dot{N}_{CE} = -b a (\ln 10) 10^{-bM} dM$, and replacing $V_{LT}[M]$ from A2-6,

$$\dot{V}_L = 10^{-11.26 \pm 0.52} (\ln 10) b a \int_{M_{\min}}^{M_{\max}} 10^{(1.42-b)M} dM \quad (\text{A2-8}).$$

2.10. Acknowledgments

Thanks to C. Beaumont, R. Charrier, A. Fock, E. McDonald, R. Rauld, R. Farías, and M. Zentilli, for stimulating discussions. JLA was funded by a Dalhousie Graduate Scholarship and a Geological Society of America Student Grant (#7864-05). ACOA-AIF Award 1005052 and NSERC-Discovery Grant awarded to JCG supported cosmogenic measurements, computational analysis and fieldwork. Guang Yang and Anne Reuther assisted in ^{10}Be and ^{36}Cl sample processing at Dalhousie University. Dr. Robert Finkel supervised ^{10}Be AMS measurements at LLNL CAMS facility. Dr. Marc Caffee supervised ^{36}Cl measurements at PRIME Lab, Purdue University. John Stone (Univ. of Washington) kindly granted access to his Mathematica code for calculating ^{36}Cl production rates and ages. SERNAGEOMIN provided logistical support for most of the fieldwork. Shallow seismicity data has been collected by Servicio Sismológico de Chile (Univ. de Chile); epicentral locations have been relocated by R. Farías (Univ. de Chile) using SPHREL/SPHYFIT code (S. Roecker), in the framework of ANILLO Project ACT no. 18 (Chile). We thank O. Korup and Stella M. Moreiras for their constructive reviews.

2.11. References

- Abele, G., 1974. Bergsturze in den Alpen, ihre Verbreitung, Morphologie und Folgeerscheinungen. *Wissenschaftliche Alpeinvereinshefte* 25, 230 pp.
- Abele, G., 1984. Derrumbes de montaña y morrenas en los Andes chilenos. *Revista de Geografía Norte Grande* 11, 17-30.
- Alvarado, P., Beck, S., Zandt, G., Araujo, M., Triep, E., 2005. Crustal deformation in the south-central Andes backarc terranes as viewed from regional broad-band seismic waveform modelling. *Geophysical Journal International* 163, 580-598.
- Ayala, L., Lopez, A., Bzdigian, A., 1984. Producción de sedimento en cuencas andinas de Chile. In: *Proceedings, Programa Hidrológico Internacional (IHP), Jornadas de Hidrología de Nieves y Hielos en América del Sur*. 22 p.
- Balco, G., Stone, J. O., Lifton, N. A., Dunai, T. J., 2008. A complete and easily accessible means of calculating surface exposure ages or erosion rates from ^{10}Be and ^{26}Al measurements. *Quaternary Geochronology* 3, 174-195.
- Ballantyne, C.K., Stone, J.O., 2004. The Beinn Alligin rock avalanche, NW Scotland: cosmogenic ^{10}Be dating, interpretation and significance. *The Holocene* 14, 448-453.
- Barrientos, S., Vera, E., Alvarado, P., Monfret, T., 2004. Crustal seismicity in central Chile. *Journal of South American Earth Sciences* 16, 759-768.
- Beck, S., Barrientos, S., Kausel, E., Reyes, M., 1998. Source characteristics of historic earthquakes along the central Chile subduction zone. *Journal of South American Earth Sciences* 11, 115-129.
- Blodgett, T.A., 1998. Erosion rates on the NS Escarpment of the Eastern Cordillera, Bolivia, derived from aerial photographs and Thematic Mapper Images. Ph. D. Thesis, Cornell University, Ithaca, New York.
- Blodgett, T.A., Blizard, C., Isacks, B.L., 1998. Andean Landslide Hazards. In: Kalvoda, J., Rosenfeld, C. L. (Eds.), *Geomorphological Hazards in High Mountain Areas*, Kluwer Academic Publishers, Amsterdam, pp. 211-227.
- Brüggen, J., 1950. *Fundamentos de la Geología de Chile*. Editorial Nascimento, Santiago, 378 pp.

- Burbank, D. W., Blythe, A. E., Putkonen, J., Pratt-Sitaula, B., Gabet, E., Oskin, M., Barros, A., Ojha, T. P., 2003. Decoupling of erosion and precipitation in the Himalayas. *Nature* 426, 652-655.
- Burbank, D. W., Leland, J., Fielding, E., Anderson, R. S., Brozovic, N., Reid, M. R., Duncan, C., 1996. Bedrock incision, rock uplift and threshold hillslopes in the northwestern Himalayas. *Nature* 379, 505-510.
- Cahill, T.A., Isacks, B.L., 1992. Seismicity and shape of the subducted Nazca Plate. *Journal of Geophysical Research* 97, 503-517.
- Campbell, D., 2005. Termocronología del sector comprendido entre los ríos Rocín y Aconcagua: Implicancias en la evolución Meso-Cenozoica de la zona. M. Sc. Thesis, Departamento de Geología, Universidad de Chile, Santiago.
- Caviedes, C., 1972. Geomorfología del Cuaternario del valle de Aconcagua, Chile Central. *Freiburger Geographische Hefte* 11, 153 pp.
- Cembrano, J., Zentilli, M., Grist, A., Yáñez, G., 2003. Nuevas edades de trazas de fisión para Chile Central (30-34°S): Implicancias en la exhumación y alzamiento de los Andes desde el Cretácico. Proc. 10th Congreso Geológico Chileno, Concepción, Chile.
- Chang, K., Taboada, A., Chan, Y., Dominguez, S., 2006. Post-seismic surface processes in the Jiufengershan landslide area, 1999 Chi-Chi earthquake epicentral zone, Taiwan. *Engineering Geology* 86, 102-117.
- Charrier, R., 1983. Hoja El Teniente. Carta geológica de Chile, Instituto de Investigaciones Geológicas, Santiago 155 pp.
- Charrier, R., Baeza, O., Elgueta, S., Flynn, J.J., Gans, P., Kay, S. M., Muñoz, N., Wyss, A. R., Zurita, E., 2002. Evidence for Cenozoic extensional basin development and tectonic inversion south of the flat-slab segment, southern Central Andes, Chile (33°-36° S.L.). *Journal of South American Earth Sciences* 15, 117-139.
- Charrier, R., Bustamante, M., Comte, D., Elgueta, S., Flynn, J.J., Iturra, N., Muñoz, N., Pardo, M., Thiele, R., Wyss, A. R., 2005. The Abanico extensional basin: Regional extension, chronology of tectonic inversion and relation to shallow seismic activity and Andean uplift. *N. Jb. Geol. Palaont. Abh.* 236, 43-77.

- Charrier, R., Munizaga, F., 1979. Edades K-Ar de volcánitas Cenozoicas del sector cordillerano del río Cachapoal, Chile (34° 15' de Latitud Sur). *Revista Geológica de Chile* 7, 41-51.
- Charrier, R., Pinto, L., Rodríguez, M.P., 2007. Tectonostratigraphic evolution of the Andean orogen in Chile. In: Moreno, T., Gibbons, W. (eds). *The Geology of Chile*. Geological Society, London, pp. 21-114.
- Chen, R., Chang, K., Angelier, J., Chan, Y., Deffontaines, B., Lee, C., Lin, M., 2006. Topographical changes revealed by high-resolution airborne LiDAR data: The 1999 Tsaoling landslide induced by the Chi-Chi earthquake. *Engineering Geology* 88, 160-172.
- Chiu, D., 1991. Geología del relleno Cuaternario de las hoyas de los ríos Yeso, Volcán y Maipo, este último entre las localidades de Guayacán y los Queltehues, Región Metropolitana, Chile. B. Sc. Thesis, Departamento de Geología, Universidad de Chile, Santiago.
- Crozier, M.J., 1986. *Landslides: causes, consequences & environment*. Croom Helm, Dover.
- Cruden, D.M., Hu, X. Q., 1993. Exhaustion and steady state models for predicting landslide hazards in the Canadian Rocky Mountains. *Geomorphology* 8, 279-285.
- Cruden, D.M., Varnes, D.J., 1996. Landslide types and processes. In: Turner, A. K., Schuster, R. L. (Eds.), *Landslides: Investigation and Mitigation*. Transportation and Road Research Board, National Academy of Science, Washington, D.C., Special Report 247, pp. 36-75.
- Cuadra, P., 1986. Geocronología K-Ar del yacimiento El Teniente y áreas adyacentes. *Revista Geológica de Chile* 27, 3-26.
- Desilets, D., Zreda, M., Prabu, T., 2006. Extended scaling factors for in situ cosmogenic nuclides: New measurements at low latitude. *Earth and Planetary Science Letters* 246, 265-276.
- Dramis, F., Blumetti, A.M., 2005. Some considerations concerning seismic geomorphology and paleoseismology. *Tectonophysics* 408, 177-191.

- Dunai, T., 2001. Influence of secular variation of the magnetic field on production rates of in situ produced cosmogenic nuclides. *Earth and Planetary Science Letters* 193, 197–212.
- Encinas, A., Maksaev, V., Pinto, L., Le Roux, J.P., Munizaga, F., Zentilli, M., 2006. Pliocene lahar deposits in the Coastal Cordillera of central Chile: Implications for uplift, avalanche deposits, and porphyry copper systems in the Main Andean Cordillera. *Journal of South American Earth Sciences* 20, 369-381.
- Erikson, I., Högstedt, J., 2004. Landslide hazard assessment and landslide precipitation relationship in Valparaíso, central Chile. M. Sc. Thesis, Geography Department, Göteborg University, Göteborg.
- Erismann, T.H., Abele, G., 2001. Dynamics of rockslides and rockfalls. Springer, Berlin, 316 pp.
- Espizua, L.E., Bengochea, J.D., Aguado, C.J., 1993. Mapa de riesgo de remoción en masa en el valle del Río Mendoza. In: XII Congreso Geológico Argentino y II Congreso de Exploración de Hidrocarburos, Actas, VI, pp. 323-332.
- Farías, M., Charrier, R., Carretier, S., Martinod, J., Fock, A., Campbell, M., Cáceres, L., Comte, D., 2006. Late Miocene regional surface uplift and slow response of erosion in the Andes of central Chile: Implications for the geodynamics in subduction zones. *Eos Trans. AGU, Fall Meeting Suppl.* 87, paper T11A-0411.
- Farías, M., Charrier, R., Carretier, S., Martinod, J., Fock, A., Campbell, D., Cáceres, J., Comte, D., 2008. Late Miocene high and rapid surface uplift and its erosional response in the Andes of central Chile (33°–35°S). *Tectonics*. 27, TC1005, doi: 10.1029/2006TC002046.
- Fauqué, L.E., Cortes, J.M., Folguera, A., Etcheverría, M., 2000. Avalanchas de roca asociadas a neotectónica en el valle del río Mendoza, al sur de Uspallata. *Revista de la Asociación Geológica Argentina* 55, 419-423.
- Fock, A., 2005. Cronología y tectónica de exhumación en el Neógeno de los Andes de Chile Central entre los 33° y los 34° S. M. Sc. Thesis, Departamento de Geología, Universidad de Chile, Santiago.

- Fock, A., Charrier, R., Farías, M., Muñoz, M., 2006. Fallas de vergencia Oeste en la Cordillera Principal de Chile Central: Inversión de la cuenca de Abanico (33°-34°S). *Revista de la Asociación Geológica Argentina, Serie D, Publicación Especial No. 10*, pp. 48-55.
- Giambiagi, L.B., Ramos, V., Godoy, E., Álvarez, P., Orts, S., 2003. Cenozoic deformation and tectonic style of the Andes between 33° and 34° south latitude. *Tectonics* 22, 1041.
- Godoy, E., Lara, L., Burmester, R., 1994a. El 'lahar' cuaternario de Colon-Coya: Una avalancha de detritos pliocena. *Proc. 7th Congreso Geológico Chileno, Concepción, Chile, Vol. 1*, pp. 305-309.
- Godoy, E., Lara, L., Ugalde, I., 1994b. Derrumbes de cerro holocenos en los Andes Centrales de Chile. *Proc. 7th Congreso Geológico Chileno, Concepción, Chile, Vol. 1*, pp. 310-314.
- Godoy, E., Yáñez, G., Vera, E., 1999. Inversion of an Oligocene volcano-tectonic basin and uplifting of its superimposed Miocene magmatic arc in the Chilean Central Andes: first seismic and gravity evidences. *Tectonophysics* 306, 217-236.
- Guthrie, R.H., Evans, S.G., 2004. Analysis of landslide frequencies and characteristics in a natural system, coastal British Columbia. *Earth Surface Processes and Landforms* 29, 1321-1339.
- Hauser, A., 1985. Flujos de barro en la zona preandina de la Región Metropolitana: características, causas, efectos, riesgos y medidas preventivas. *Revista Geológica de Chile* 24, 75-92.
- Hauser, A., 2000. Remociones en masa en Chile, Servicio Nacional de Geología y Minería, Santiago, Boletín 59.
- Hauser, A., 2002. Rock avalanche and resulting debris flow in Estero Parraguirre and Río Colorado, Región Metropolitana, Chile. In: Evans, S. G., DeGraff, J. V. (Eds.), *Catastrophic landslides; effects, occurrence, and mechanisms*. Geological Society of America, *Reviews in Engineering Geology*, Vol. 15, pp. 135-148.

- Hermanns, R.L., Niedermann, S., Villanueva Garcia, A., Schellenberger, A., 2006. Rock avalanching in the NW Argentine Andes as a result of complex interactions of lithologic, structural and topographic boundary conditions, climate change and active tectonics. In: Evans, S. G., Scarascia-Mugnozza, G., Strom, A., Hermanns, R. L. (Eds.), *Landslides from Massive Slope Failures*. Kluwer, Dordrecht, pp. 497-520.
- Hermanns, R.L., Niedermann, S., Villanueva Garcia, A., Sosa Gomez, J., Strecker, M.R., 2001. Neotectonics and catastrophic failure of mountain fronts in the southern intra-Andean Puna Plateau, Argentina. *Geology* 29, 619-623.
- Hermanns, R.L., Trauth, M. H., Niedermann, S., McWilliams, M., Strecker, M. R., 2000. Tephrochronologic constraints on temporal distribution of large landslides in northwest Argentina. *Journal of Geology* 108, 35-52.
- Heusser, C. J., 1990. Ice age vegetation and climate of subtropical Chile. *Palaeogeography, Palaeoclimatology, Palaeoecology*. 80, 107-127.
- Heusser, C.J., 1989. Southern Westerlies during the Last Glacial Maximum. *Quaternary Research* 31, 423–425.
- Hewitt, K., 1999. Quaternary moraines vs. catastrophic rock avalanches in the Karakoram Himalaya, Northern Pakistan. *Quaternary Research* 51, 220-237.
- Hewitt, K., 2002. Styles of rock avalanche depositional complexes conditioned by very rugged terrain, Karakoram Himalaya, Pakistan. In: Evans, S., DeGraff, J. V. (Eds.), *Catastrophic landslides: effects, occurrence, and mechanisms*. Geological Society of America, *Reviews in Engineering Geology*, Vol. 15, pp. 345-377.
- Hewitt, K., 2006. Disturbance regime landscapes: mountain drainage systems interrupted by large rockslides. *Progress in Physical Geography* 30, 365-393.
- Hovius, N., Stark, C.P., Allen, P.A., 1997. Sediment flux from a mountain belt derived by landslide mapping. *Geology* 25, 231-234.
- Hungr, O., 2006. Rock avalanche occurrence, process and modeling. In: Evans, S. G., Scarascia-Mugnozza, G., Strom, A., Hermanns, R. L. (Eds.), *Landslides from Massive Slope Failures*. Kluwer, Dordrecht, pp. 243-266.
- Isaaks, E.H., Srivastava, R.M., 1989. *An introduction to applied geostatistics*. Oxford University Press, Oxford, 561 pp.

- Ivy-Ochs, S., Poschinger, A.V., Synal, H.-A., Maisch, M., 2008. Surface exposure dating of the Flims landslide, Graubunden, Switzerland. *Geomorphology*, doi:10.1016/j.geomorph.2007.10.024
- Jarman, D., 2006. Large rock slope failures in the Highlands of Scotland: Characterization, causes and spatial distribution. *Engineering Geology* 83, 161-182.
- Jibson, R. W., Harp, E. L., Schulz, W., Keefer, D. K., 2006. Large rock avalanches triggered by the M 7.9 Denali Fault, Alaska, earthquake of 3 November 2002. *Engineering Geology* 83, 144-160.
- Keaton, J.R., Rinne, R., 2002. Engineering-geology mapping of slopes and landslides. In: Bobrowsky, P. T. (Ed.), *Geoenvironmental mapping: methods, theory and practice*. Balkema, Rotterdam, pp. 9-28.
- Keefer, D. K., 1984. Landslides caused by earthquakes. *Geological Society of America Bulletin* 95, 406-421.
- Keefer, D. K., 1994. The importance of earthquake-induced landslides to long-term slope erosion and slope-failure hazards in seismically active regions. *Geomorphology* 10, 265-284.
- Keefer, D. K., 2002. Investigating landslides caused by earthquakes - a historical review. *Surveys in Geophysics* 23, 473-510.
- Korup, O., 2005. Large landslides and their effect on sediment flux in South Westland, New Zealand. *Earth Surface Processes and Landforms* 30, 305-323.
- Korup, O., 2006. Effects of large deep-seated landslides on hillslope morphology, western Southern Alps, New Zealand. *Journal of Geophysical Research* 111, F01018.
- Korup, O., McSaveney, M. J., Davies, T. R. H., 2004. Sediment generation and delivery from large historic landslides in the Southern Alps, New Zealand. *Geomorphology* 61, 189-207.
- Kurtz, A., Kay, S. M., Charrier, R., Farrar, E., 1997. Geochronology of Miocene plutons and Andean uplift history in the El Teniente region, central Chile (34° - 35° S). *Revista Geológica de Chile* 24, 75-90.
- Lal, D., 1991. Cosmic ray labeling of erosion surfaces: in situ nuclide production rates and erosion models. *Earth and Planetary Science Letters* 104, 424-439.

- Lamy, F., Hebbeln, D., Wefer, G., 1999. High-resolution marine record of climatic change in mid-latitude Chile during the last 28,000 years based on terrigenous sediment parameters. *Quaternary Research* 51, 83–93.
- Lavé, J., Burbank, D., 2004. Denudation processes and rates in the Transverse Ranges, Southern California; erosional response of a transitional landscape to external and anthropogenic forcing. *Journal of Geophysical Research* 109, F01006, doi: 10.1029/2003JF000023.
- Lavenu, A., Cembrano, J., 1999. Compressional and transpressional stress pattern for Pliocene and Quaternary brittle deformation in fore-arc and intra-arc zones (Andes of Central and Southern Chile). *Journal of Structural Geology* 21, 1669-1691.
- Lifton, N., Bieber, J., Clem, J., Duldig, M., Evenson, P., Humble, J., Pyle, R., 2005. Addressing solar modulation and long-term uncertainties in scaling secondary cosmic rays for in situ cosmogenic nuclide applications. *Earth and Planetary Science Letters* 239 140-161.
- Maksaev, V., Zentilli, M., Munizaga, F., Charrier, R., 2003. Denudación/alzamiento del Mioceno Superior-Plioceno Inferior en la Cordillera de Chile Central (33-35° S) inferida por dataciones por trazas de fisión en apatito de plutones miocenos. Proc. 10th Congreso Geológico Chileno, Concepción, Chile.
- Malamud, B., Turcotte, D., Guzzetti, F., Reichenbach, P., 2004a. Landslide inventories and their statistical properties. *Earth Surface Processes and Landforms* 29, 687-711.
- Malamud, B., Turcotte, D., Guzzetti, F., Reichenbach, P., 2004b. Landslides, earthquakes, and erosion. *Earth and Planetary Science Letters* 229, 45-59.
- Marangunic, C., Thiele, R., 1971. Procedencia y determinaciones gravimétricas de espesor de la morena de la Laguna Negra, Provincia de Santiago, Comunicaciones 38, 25 pp.
- Mather, A.E., Griffiths, J.S., Stokes, M., 2003. Anatomy of a 'fossil' landslide from the Pleistocene of SE Spain. *Geomorphology* 50, 135-149.
- Matheron, G., 1962. *Traité de Géostatistique appliquée*, Tome I., Editions Technip, Paris, 333 pp.

- McDonald, E.V., McFadden, L.D., Wells, S.G., 2003, Regional response of alluvial fans to the Pleistocene-Holocene climatic transition, Mojave Desert, California. In Enzel, Y., Wells, S.G., and Lancaster, N., eds., *Paleoenvironments and paleohydrology of the Mojave and southern Great Basin Deserts*, Boulder, Colorado, Geological Society of America Special Paper 368, p. 189-205.
- Molnar, P., Anderson, R. S., Anderson, S. P., 2007. Tectonics, fracturing of rock, and erosion. *Journal of Geophysical Research*. 112, F03014, doi:10.1029/2005JF000433.
- Moreiras, S.M., 2006. Chronology of a probable neotectonic Pleistocene rock avalanche, Cordón del Plata (Central Andes), Mendoza, Argentina. *Quaternary International* 148, 138-148.
- Moreno, H., Thiele, R., Varela, J., 1991. Estudio Geológico y de Riesgos Volcánico y de Remoción en Masa del Proyecto Hidroeléctrico Alfalfal II y Las Lajas (Technical Report), CHILGENER S.A., Santiago, 78 pp.
- Naranjo, J.A., Varela, J., 1996. Flujos de detritos y barro que afectaron el sector oriente de Santiago el 3 de Mayo de 1993. Servicio Nacional de Geología y Minería, Santiago, 42 pp.
- Nichols, K.K., Bierman, P.R., Foniri, W.R., Gillespie, A.R., Caffee, M., Finkel, R., 2006. Dates and rates of arid region geomorphic processes. *GSA Today*, 16, 4-11.
- Pannatier, Y., 1996. *Variowin: software for spatial data analysis in 2D*. Springer-Verlag, New York.
- Pardo, M., Comte, D., Monfret, T., 2002. Seismotectonic and stress distribution in the central Chile subduction zone. *Journal of South American Earth Sciences* 15, 11-22.
- Philip, H., Ritz, J.-C., 1999. Gigantic paleo-landslide associated with active faulting along the Bogd fault (Gobi-Altay, Mongolia). *Geology* 27, 211-214.
- Ramos, V.A., Cegarra, M.I., Cristallini, E., 1996. Cenozoic tectonics of the High Andes of west-central Argentina (30°–36°S latitude). *Tectonophysics* 259, 185–200.
- Rauld, R., 2002. Analisis morfoestructural del frente cordillerano de Santiago Oriente, entre el río Mapocho y la Quebrada Macul. B. Sc. Thesis, Departamento de Geología, Universidad de Chile, Santiago.

- Rivano, S., Sepúlveda, P., 1986. Hoja Illapel (1:250,000 scale map), IV Región de Coquimbo. Servicio Nacional de Geología y Minería, Santiago, Carta geológica de Chile 69.
- Rivano, S., Sepúlveda, P., Boric, R., Espiñeira, P., 1993. Mapa Geológico de la Hoja Quillota-Portillo (1:250,000 scale map), V Región de Valparaíso. Servicio Nacional de Geología y Minería, Santiago, Carta geológica de Chile 73.
- Rivera, O., Cembrano, J., 2000. Modelo de formación de cuencas volcano-tectónicas en zonas de transferencia oblicuas a la cadena andina: el caso de las cuencas oligomiocenas de Chile central y su relación con estructuras NWW-NW (33°00'-34°30'S). Proc. 9th Congreso Geológico Chileno, Puerto Varas, Chile, Vol. 2, pp. 631-636.
- Rodríguez, C.E., Bommer, J.J., Chandler, R.J., 1999. Earthquake-induced landslides: 1980–1997. *Soil Dynamics and Earthquake Engineering* 18, 325-346.
- Sato, H. P., Hasegawa, H., Fujiwara, S., Tobita, M., Koarai, M., Une, H., Iwahashi, J., 2006. Interpretation of landslide distribution triggered by the 2005 Northern Pakistan earthquake using SPOT 5 imagery. *Landslides*, doi: 10.1007/s10346-006-0069-5.
- Scheidegger, E., 1973. On the prediction of reach and velocity of catastrophic landslides. *Rock Mechanics* 5, 231-236.
- Schuster, R.L., Salcedo, D.A., Valenzuela, L., 2002. Overview of catastrophic landslides of South America in the twentieth century. In: Evans, S. G., DeGraff, J. V. (Eds.), *Catastrophic landslides; effects, occurrence, and mechanisms*. Geological Society of America, *Reviews in Engineering Geology*, Vol. 15, pp. 1-34.
- Sellés, D., 1999. La Formación Abanico en el Cuadrángulo Santiago (33°15'-33°30'S; 70°30'-70°45'O), Chile Central. *Estratigrafía y Geoquímica*. M. Sc. Thesis, Departamento de Geología, Universidad de Chile, Santiago, 154 pp.
- Sellés, D., Gana, P., 2001. Geología del Area Talagante-San Francisco de Mostazal, Región Metropolitana. Servicio Nacional de Geología y Minería, Santiago. Carta Geológica de Chile, *Geología Básica* 74, 30 pp.
- Sepúlveda, S.A., Astroza, M., Kausel, E., Campos, J., Casas, E.A., Rebolledo, S., Verdugo, R., 2008. New findings on the 1958 Las Melosas earthquake sequence, central Chile: implications for seismic hazard related to shallow crustal earthquakes in subduction zones. *Journal of Earthquake Engineering* 12, 432-455.

- Sepúlveda, S.A., Rebolledo, S., Vargas, G., 2006. Recent catastrophic debris flows in Chile: Geological hazard, climatic relationships and human response. *Quaternary International* 158, 83-95.
- SERNAGEOMIN, 2002. Mapa Geológico de Chile (1:1,000,000 scale map), Servicio Nacional de Geología y Minería, Santiago.
- Simonett, D.S., 1967. Landslide distribution and earthquakes in the Bewani and Torricelli Mountains, New Guinea. In Jennings, J.N., Mabbutt, J.A. (eds). *Landform Studies from Australia and New Guinea*, Cambridge University Press, Cambridge, p. 64–84.
- Singer, B.S., Thompson, R.A., Dungan, M.A., Feeley, T.C., Nelson, S.T., Pickens, J.C., Brown, L.L., Wulff, A.W., Davidson, J.P., Metzger, J., 1997. Volcanism and erosion during the past 930 thousand years at the Tatara-San Pedro complex, Chilean Andes. *Geological Society of America Bulletin*, 109, 127-142.
- Stern, C.R., Amini, H., Charrier, R., Godoy, E., Hervé, F., Varela, J., 1984. Petrochemistry and age of rhyolitic pyroclastics flows which occur along the drainage valleys of the Río Maipo and Río Cachapoal (Chile) and the Río Yaucha and Río Papagayos (Argentina). *Revista Geológica de Chile* 23, 39-52.
- Stone, J., 2000. Air pressure and cosmogenic isotope production, *Journal of Geophysical Research* 105 (B10) 23,753–23,759.
- Stuiver, M., Reimer, P. J., Reimer, R. W. 2005. CALIB 5.0. [www program and documentation].
- Thiele, R., 1980. Hoja Santiago (1:250,000 scale map), Región Metropolitana. Instituto de Investigaciones Geológicas, Santiago, Carta geológica de Chile 39.
- von Blanckenburg, F., 2006. The control mechanisms of erosion and weathering at basin scale from cosmogenic nuclides in river sediment. *Earth and Planetary Science Letters* 242, 224–239.
- Wall, R., Sellés, D., Gana, P., 1999. Area Tiltil-Santiago (1:100,000 scale map), Región Metropolitana. Servicio Nacional de Geología y Minería, Mapas Geológicos 11.
- Zech, R., Kull, C., Veit, H., 2006. Late Quaternary glacial history in the Encierro Valley, Northern Chile (29°S), deduced from ¹⁰Be surface exposure dating, *Palaeogeography, Palaeoclimatology, Palaeoecology* 234, 277-286.

CHAPTER 3 Quaternary Denudation Styles and Rates in the Southern Central Andes of Chile Inferred From Cosmogenic ^{36}Cl Inventories in Stream Sediments and Modeled Fluvial Transport Rates

(manuscript in preparation for submission to: Nature Geosciences)

Jose Luis Antinao (1), John Charles Gosse (1), Marc Caffee (2)

(1) Earth Science Department, Dalhousie University, Halifax B3H4J1, Canada

(2) Physics Department, Purdue University, West Lafayette, IN47097, USA

3.1. Introduction

The evolution of mountain landscapes at convergent margins is controlled by the competition between tectonic processes forcing rock uplift and erosional processes dependent on climate and lithology. At steady state conditions and high rock uplift rates, it has been hypothesized (Burbank et al., 1996) that large landslides are the dominant sediment production mechanism required to balance rock uplift. We use for the first time spallogenically produced cosmogenic ^{36}Cl to estimate millennial-scale catchment-wide average erosion rates in small catchments of the tectonically-active southern Central Andes. We estimate present-day total fluvial transport rates for a large catchment including a modeled bedload component. ^{36}Cl erosion rates are generally lower than long term thermochronology exhumation rates (Maksaev et al., 2009), and similar to short term fluvial transport rates and to long term sediment production by large landslides (Antinao and Gosse, 2008). ^{36}Cl sediment yields are uniform throughout the catchments, above and below large Late Pleistocene-Holocene landslides, attesting to how rapidly the landscape re-equilibrates sediment flux after major mass wasting events. A weak but consistent covariance between ^{36}Cl concentration and grain size in the stream sediment further support the hypothesis that deep-seated landslides are a dominant erosional mechanism in this active orogen. However, slopes are not at threshold conditions, suggesting that the southern Central Andes are at a transient stage in their landscape evolution, still not adjusted to rock uplift rates determined by Late Cenozoic tectonics.

Pleistocene to Holocene large deep-seated landslides (area > 0.1 km²) are common (Abele, 1981; Antinao and Gosse, 2008) along the incised valleys of Western Cordillera Principal (WCP) in the southern Central Andes (SCA) of Chile (Fig. 3.1). Their presence, coupled to Pleistocene-Holocene high fluvial incision rates (Fariás et al., 2008), suggests that landslides are producing the sediment required to balance rock uplift in a threshold slopes landscape (Burbank et al., 1996). However, no measurements of sediment flux are available on timescales of 10-10⁴ a, to contrast with e.g. long-term exhumation and sediment production rates (Antinao and Gosse, 2008; Maksaev et al., 2009; Antinao et al., submitted). We selected two small (15 km²) catchments (Quebradas Potrerillos and Macul) that are part of the larger Maipo River catchment (Fig. 3.1 and Supplementary Information Table S1 for details on the catchments) for a terrestrial cosmogenic nuclide (TCN) study which utilizes for the first time cosmogenic ³⁶Cl in stream sediments to estimate catchment-wide average erosion rates. Total fluvial transport estimation on the Maipo River catchment, which is linked to the TCN-studied catchments (Fig. 3.1) was performed by using dissolved and suspended sediment records for the last 15 years, and modeling (Ackers and White, 1973; see Supplementary Information for model description) the bedload for the same gauge station (Fig. 3.1).

Three additional experiments were devised in order to study how landslides may influence the TCN signal in stream sediment, testing if the very process we aim to measure is influencing the procedure. First, a proposed relation linking grain size to concentration in landslide-prone areas (Brown et al., 1995) is assessed. The significant benefits of exploiting this relationship to assess rates of surface processes has generated considerable debate over the past two decades (Frankel et al., 2007; Belmont et al., 2007), mainly trying to evaluate its meaning under different tectonic and climatic settings (Matmon et al., 2005). Second, we compare TCN inventories upstream and downstream of Late Pleistocene to Holocene landslides (Antinao and Gosse, 2008) to determine if a significant amount of sediment from the landslide will bias the TCN method towards higher erosion rates (Brown et al., 1995, 1998). Third, we use the difference in hypsometry between the two catchments to check the sensitivity of the TCN method in landslide-prone areas to record previously recognized relationships between slope and catchment erosion rates (Ahnert, 1970; Montgomery and Brandon, 2002).

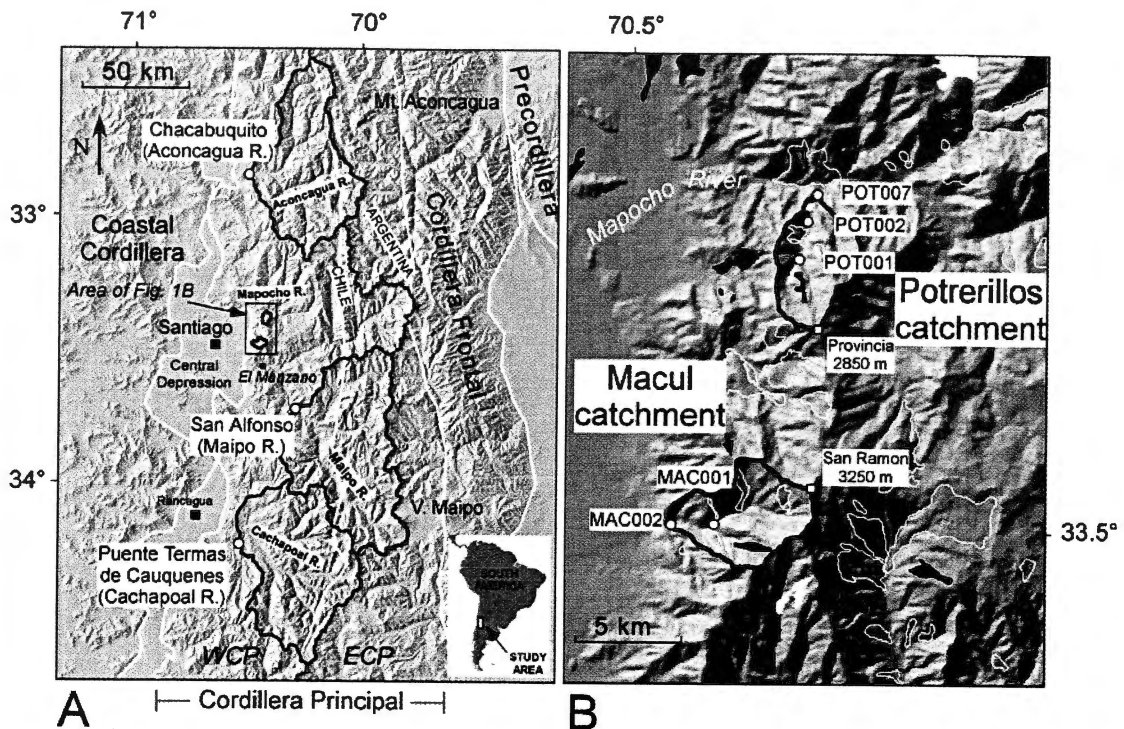


Figure 3.1. A. Shaded Relief Map of the study area and location in central Chile. Morphotectonic units are shown: Cordillera Principal (Western, WCP; Eastern, ECP), Coastal Cordillera, Central Depression, and Cordillera Frontal and Precordillera in Argentina. Upper catchments of the Aconcagua, Maipo and Cachapoal rivers are outlined, with suspended sediment sampling stations as circles (Chacabuquito-Aconcagua, San Alfonso-Maipo, Puente Termas Cauquenes-Cachapoal). Note that the eastern boundaries of these catchments define the continental divide (stippled line which is also the Argentina-Chile border). B. Detail of the area of WCP where Potrerillos and Macul catchments are located. Catchment boundaries are highlighted, and position of sampling points along streams is marked. Landslides of different ages (Antinao and Gosse, 2008) that might affect TCN inventories are shown. Holocene landslides appear in white, Late Pleistocene landslides are marked with a white outline, and Early-Middle Pleistocene landslides are marked in black. Mapocho River runs from east to west in the northern area of the map.

The TCN method for obtaining catchment wide erosion rates is based on the premise that the concentration of a TCN like ^{10}Be or ^{36}Cl in a modern stream sediment sample containing hundreds of thousands of grains eroded from different parts of a catchment at different rates is inversely proportional to the average erosion rate of the entire catchment above the sample point (Granger et al., 1996; Bierman and Steig, 1996). ^{10}Be is the isotope of choice because it is produced via spallation on stoichiometric proportions of Si and O in quartz, a common mineral in the continental crust.

Cosmogenic ^{36}Cl , on the other hand, is produced not only by spallation of ^{40}Ca and ^{39}K (Stone et al., 1998; Evans et al., 1997) but also by thermal neutron absorption by ^{35}Cl (Liu et al., 1994). The latter process is highly dependent on the presence of elements both moderating thermal neutron flux in the subsurface, like hydrogen, and generating neutron flux, like U, Th and Gd. To avoid the difficulties associated with spatial and temporal variation in water content in regolith and in the distribution of the neutron generators, we isolated and used only minerals with a spallogenic component —Ca and K bearing minerals—. We therefore took advantage of the ubiquitous presence of feldspars in the volcanic and volcanoclastic rocks of the catchments (Villarroel and Vergara, 1988; Robinson et al., 2004) to obtain a more precise understanding of the erosion rates and processes. Feldspars were concentrated by density separation of sediment grains (see Supplementary Information on Methods and Table S1), a process which also separated mafic minerals from the analyzed fraction, reducing the total chlorine concentration.

3.2. Results

Our results display a consistent dataset obtained from small, rapidly eroding catchments, extending predictions about the limits of the TCN catchment-wide method (Niemi et al., 2005) and confirming that it is robust enough to appropriately describe tectonically active, landslide-prone areas. ^{36}Cl concentrations in the samples range from $3.03 \cdot 10^4$ to $1.58 \cdot 10^5$ atoms g^{-1} (see Supplementary Information Table S2), and calculated catchment-wide erosion rates vary between 0.20 and 0.66 mm a^{-1} for all samples (Table S2, Fig. 3.2). Weighted averages of the erosion rates are 0.23 ± 0.03 and 0.48 ± 0.09 mm a^{-1} for the Potrerillos and Macul catchments respectively, which represent averaging over a period of ~ 2.6 ka and 1.3 ka (Fig. 2). Inside each catchment, weighted mean erosion rates do not vary downstream (1σ level). Proximity to Late Pleistocene to Holocene landslides does not have any effect on the weighted means (Fig. 3.2). Erosion rates correlate to mean slope (1 km radius window, Fig. 3.3) and relief (see Supplementary Information Table S3).

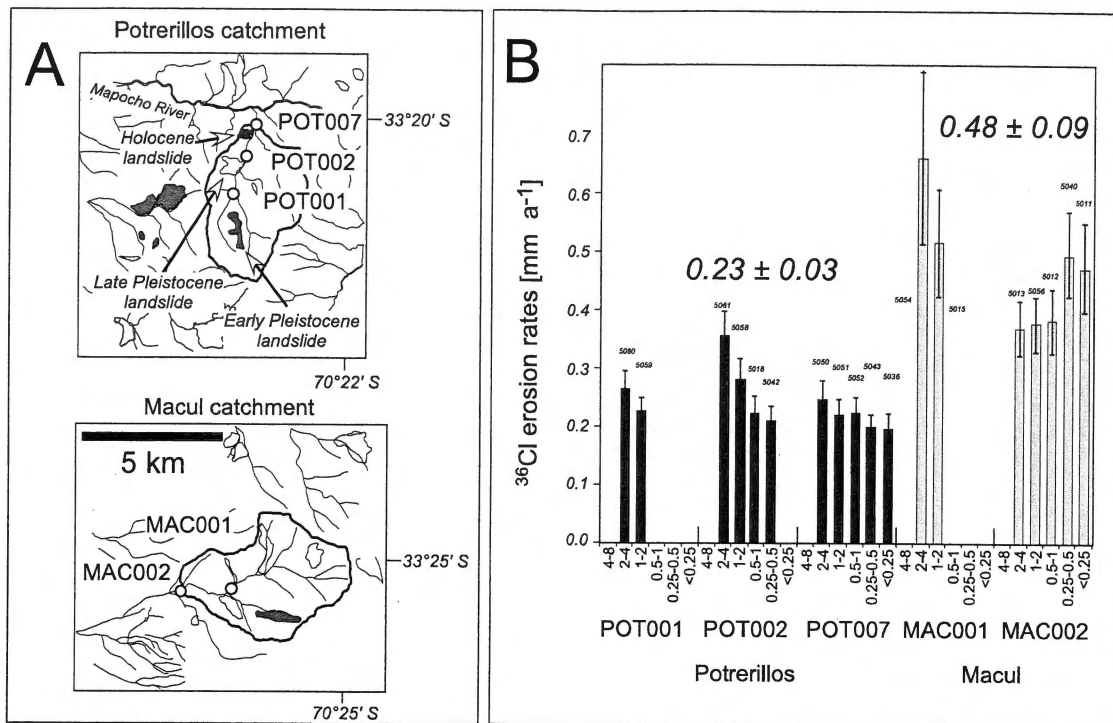


Figure 3.2. A. Detail of the catchments where stream sediment was sampled and analyzed for ^{36}Cl . Landslides are marked and the labeled age is from Antinao and Gosse (2008). Location of samples is marked. B. Catchment-wide average erosion rates derived for each grain size fraction of samples analyzed in this study. Error-weighted means for each catchment are shown at 1σ . Grain size fractions shown in decreasing size for each sample from left to right (compare with Table S2). Error bars correspond to propagated 1σ uncertainties.

Erosion rates appear to vary systematically with grain size within each catchment in all three samples from Quebrada Potrerillos and in one of the Quebrada Macul samples (Fig. 3.2). The increase in average erosion rate (decrease in TCN concentration) with increasing grain size reproduces previous observations (Brown et al., 1998), which are inferred to represent the contribution of deeper rock —with noticeable lower TCN concentration than that at the surface— from deep-seated landslides. Although the trend is barely significant beyond propagated 1σ uncertainties, it supports other evidence that landslides play a significant role in sediment transfer in WCP (Antinao and Gosse, 2008).

Slopes and erosion rates do not change substantially inside each catchment. A correlation between ^{36}Cl erosion rate and slope is evident when both catchments are considered. When ^{36}Cl erosion rate estimates are compared to measurements from other

similar semi-arid areas (Fig. 3.3), they follow the general trend observed by previous studies (Granger et al., 1996; Binnie et al., 2007) appearing at a transitional zone between transport-limited and detachment-limited systems (Binnie et al., 2007).

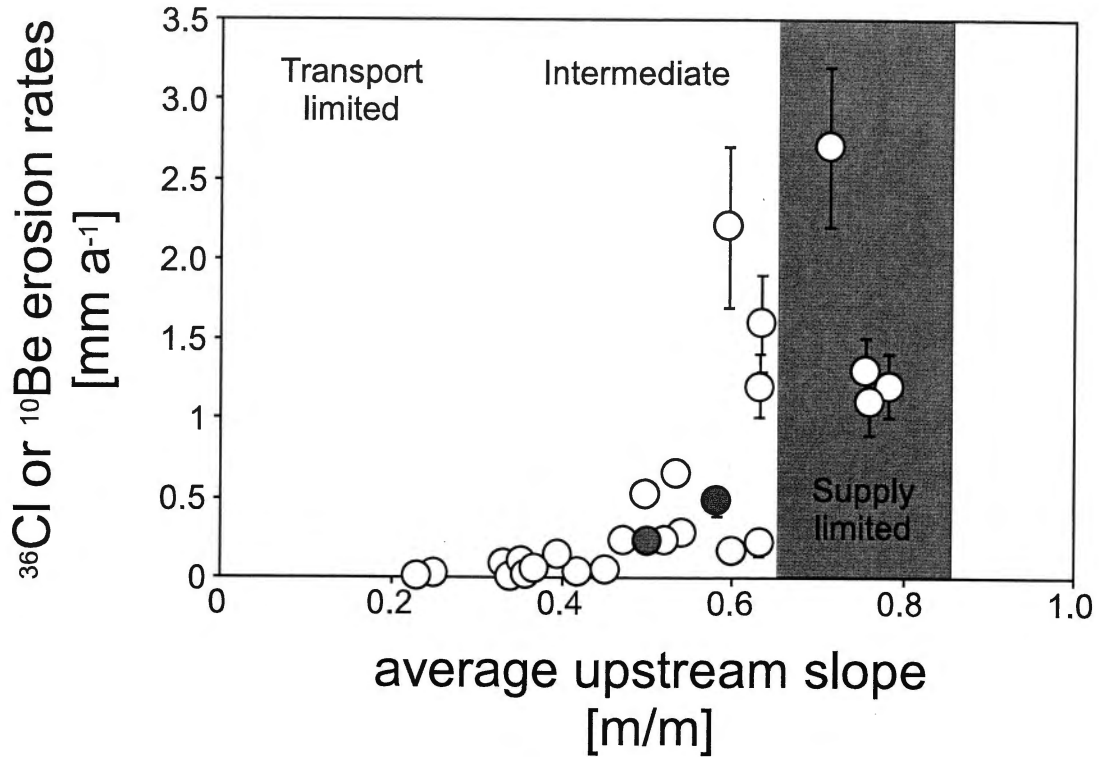


Figure 3.3. Upstream average slope (90 m SRTM data) versus ^{36}Cl erosion rate for the studied catchments (red circles), compared to ^{10}Be erosion rates obtained for areas with similar annual precipitation (yellow circles: measurements at Fort Sage, California, USA, 250 mm a $^{-1}$, Granger et al., 1996; white circles are for the San Bernardino Mountains, USA, 600 mm a $^{-1}$, Binnie et al., 2007).

To compare the Late Holocene ^{36}Cl sediment yields with present-day rates for the larger Maipo catchment, daily solid discharge from suspended sediment data (Fig. 3.4A) was compiled from the closest stream gauge representing similar conditions in the catchment. The suspended load data were compared with bedload estimates modeled for the estimated range of modern day to LGM water discharges. The median values for their distribution were carried over an entire year to obtain total fluvial transport rates (Fig. 3.4B). Bedload transport is estimated to be $\sim 0.03 \text{ mm a}^{-1}$, i.e. $\sim 30\%$ of the suspended sediment load (Table 3.1) for a representative bed sediment grain size and channel properties, considering present day median discharge. To analyze the effect on sediment transport of increased discharges during LGM conditions resulting from increasing

precipitation (Lamy et al., 1999; Hebbeln et al., 2007), we assumed that the distribution of precipitation throughout the year does not change; the same was assumed for the frequency-magnitude distribution of individual events. We assumed that the median discharges doubled the present day value during the LGM or initial deglaciation (i.e., from 60-70 to $\sim 130 \text{ m}^3 \text{ s}^{-1}$), based on paleoclimatic reconstructions (Heusser, 1989, 1990; Lamy et al., 1999; Hebbeln et al., 2007), but without a precise relation between runoff/discharge, it is still highly tentative. Under these conditions and unlimited sediment supply, bedload is estimated to be of the same order or higher than the suspended load, yielding total sediment discharges that are equivalent to maximum denudation rates of $\sim 1.4 \text{ mm a}^{-1}$ (Table 3.1).

Table 3.1. Summary of total fluvial transport load, by component, estimated for present day and Last Glacial Maximum (LGM) water discharge conditions in the Maipo River, San Alfonso station. Bedload calculated according to Ackers and White (1973) model. All transport rates are normalized according to the upstream catchment area and displayed as landscape lowering rates.

Discharge conditions	Bedload [mm a ⁻¹]	Suspended load [mm a ⁻¹]	Dissolved load [mm a ⁻¹]	Total [mm a ⁻¹]
Present day	0.03	0.11	0.06	0.20
LGM	0.7	0.6	0.06 ⁷	1.4

⁷ Assumed to be the same at LGM and present-day conditions.

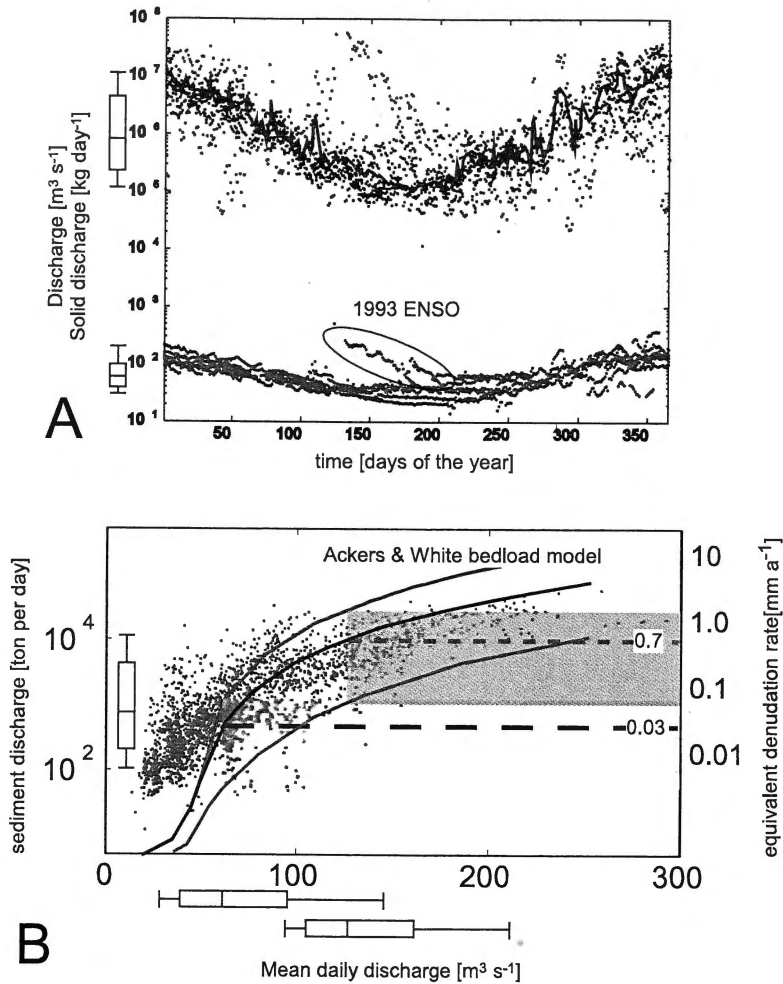


Figure 3.4. A. Mean daily suspended sediment discharge (upper part of diagram, black dots) and water discharge data (red dots) for the Maipo River at the San Alfonso gauging station (Fig. 3.1). Consistent annual periodicity of the data is only interrupted by ENSO years like 1993 (highlighted). A daily average (blue line) has been marked for the suspended sediment record. On the left, outside the graph, box-plots representing the distribution of values (whiskers at 0.09 and 0.91 percentiles). B. Suspended sediment daily discharge (green dots) and bedload estimates according to the Ackers and White (1973) model (red line), versus water discharge data for the Maipo River at the San Alfonso station. Note the dual scale, on the left daily sediment discharges, and, on the right, equivalent landscape lowering rates for the area upstream of the station. Box plots below abscissa show the median values used to estimate bedload contribution at present-day (left) and estimated LGM (lower right) discharge conditions from the models. Range of values are shown by orange bounding lines, the lower one corresponds to finer sediment (mostly sand), and the upper one to coarse sediment (mostly gravel). The central red curve represents the bedload contribution as a function of different water discharges using the present-day measured grain size distribution at the station. Red dashed lines correspond to estimated bedload contribution for modern (long dash) and LGM (short dash).

3.3. Discussion and Conclusion

The TCN results suggest that in this setting, large landslides are quickly cleared from the streams and the sediment flux re-established to the pre-landslide magnitude. This observation is consistent with the lack of lacustrine sediments upstream of most landslide deposits in WCP (Abele, 1981; Antinao and Gosse, 2008), and the noteworthy general lack of alluviation along the major rivers in WCP (Farías et al., 2008). Considering that the duration for averaging the ^{36}Cl -derived rates is ~ 1.3 and 2.6 ka for the Macul and Potrerillos catchments, respectively, they provide a maximum constraint on the time it took the landslide deposits to be sufficiently stable to stop dominating the ^{36}Cl concentration in the sediment immediately downstream the landslide. Our results suggest that the relaxation time for catchments to re-equilibrate in this region is on the order of a few millennia.

We infer from the spatial continuity of the erosion rates along the mainstems that a large proportion of sediment in these catchments is continuously mobilized by large landslides as opposed to regolith generation and export via diffusive hillslope processes. A quick clearing of the landslide dams from the streams is consistent with this effect, which is also evident from the observed correlation of grain-size and TCN concentration or erosion rates, especially along Quebrada Potrerillos. The lack of correlation observed in the lower sample at Quebrada Macul (Fig. 3.2) can be explained by a longer distance from the last landslide generating this trend upstream, the trend being obscured by more homogeneous TCN inventories derived from diffusive hillslope processes (cf. Brown et al., 1995), but that still are transporting sediment at rates similar to the overall landsliding rate.

Although TCN erosion rates appear not to be affected by landslides along a single mainstem, TCN concentration distribution with grain size is a result of landslide influence. We infer that the hillslopes where no landslides have been recorded and those portraying areas of large landslides are eroding approximately at the same rate. Conversely, as diffusive hillslope processes normally have a slower transfer rate than rapid mass-wasting (Brown et al., 1995, 1998; Niemi et al., 2005), we infer that landslide sediment production sets the upper bound for sediment production in the entire catchment, hence dominating denudation. A rapid re-equilibration of the system after a

large landslide event is not only consistent with this inference but necessary to keep denudation at the same level.

The predominance of landslides in denudation inferred here and by other studies (Antinao and Gosse, 2008) appears probably due to particular geologic and tectonic conditions for generation of large landslides in the area, like shallow seismicity (Barrientos et al., 2004), and pervasively fractured volcanoclastic units (Castro et al., 1993), which enhance a static response to base level fall and concomitant fluvial incision throughout WCP (Fariás et al., 2008). In the semi-arid WCP, even the large (2,500 km²) Maipo River catchment appears to be adjusted to hillslope sediment flux today and perhaps also in the Late Holocene (Fig. 3.5). As sediment production by landslides does not appear to be climatically controlled (Antinao and Gosse, 2008), a similar amount of sediment than the one produced and transported at present-day conditions would be available for larger discharges during LGM conditions (Fig. 3.4) and at maximum estimated (LGM-like) discharge conditions the sediment produced will be transported efficiently, in a semi-arid supply-limited system.

In areas of similar climate and total transport and sediment production rates (0.1-1 mm a⁻¹), like the San Gabriel Mountains, California (Lavé and Burbank, 2004), a suite of processes are contributing to the sediment flux. Instead, sediment flux in the SCA appears to be dominated by bedrock landslides, and their volumetric quantification might be enough to quantify total Quaternary sediment flux (Burbank et al., 1996). This conclusion is possible even if a macroscale steady state has not been achieved, suggested by the misfit in long and short-term rates compared here (Fig. 3.5) and the presence of relict Miocene surfaces at high elevations (2500-3000 m) in the landscape (Fariás et al., 2008). Unlike regions where a steady state can be inferred (Hovius et al., 1997, 2000), in this case we propose that rates of landscape denudation from landslides correspond to minimum estimates of Quaternary rock uplift rates in the area. Our results indicate that the presence of large deep-seated landslides dominating denudation in an area of high incision rates is a necessary condition, but not a sufficient one to infer high rock uplift rates, even if the landscape appears to be in an erosional steady state, and more information from independent observations is needed.

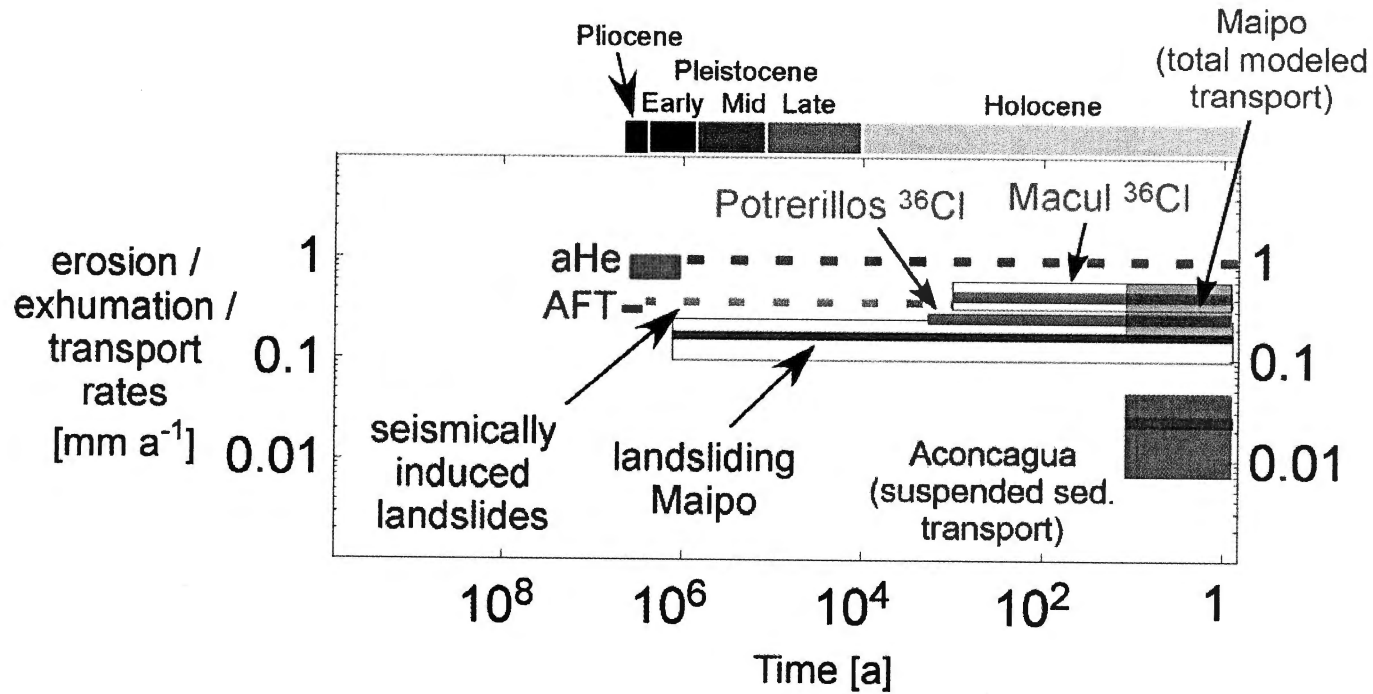


Figure 3.5. Comparison of modeled total transport of sediment for Maipo river at San Alfonso (light blue box bounded by upper and lower limits in the calculated rates according to Table 3.1), suspended sediment transport at Aconcagua river (purple box), ^{36}Cl catchment-wide average erosion rates for Potrerillos and Macul catchments (orange lines with uncertainty box, 1σ), and long-term sediment production by landslides (red and gray lines) from Antinao and Gosse (2008), all plotted against time (log-scale). We also indicate exhumation rates (green) from apatite fission track (AFT) and apatite (U-Th)/He data for WCP (Maksaev et al., 2009; McInnes et al., 2005; Antinao et al., in prep.) (Fig. 3.1).

3.4. References

- Abele, G., 1981. Trockene Massenbewegungen, Schlamstrome und rasche Abflüsse, dominante morphologische Vorgänge in den chilenischen Anden. *Mainzer Geographische Studien* 23, 102.
- Ackers, P., White, W. R., 1973. Sediment transport: New approach and analysis. *J. Hydraul. Div., Am. Soc. Civ. Eng.* 99, 2041-2060.
- Ahnert, F., 1970. Functional relationships between denudation, relief, and uplift in large mid-latitude drainage basins. *American Journal of Science*. 268, 243-263.
- Ali, K. F., De Boer, D. H., 2007. Spatial patterns and variation of suspended sediment yield in the upper Indus River basin, northern Pakistan. *Journal of Hydrology*. 334, 368-387.
- Antinao, J. L., Gosse, J. C., 2008. Large rockslides in the southern Central Andes of Chile (32-34.5 S): Tectonic control and significance for Quaternary landscape evolution. *Geomorphology*, in press, doi:10.1016/j.geomorph.2008.08.008.
- Arcadis, 2008. Estudio de Impacto Ambiental Proyecto Hidroelectrico Alto Maipo, AES GENER S.A, Chapter 5 (baseline), available online at <https://www.e-seia.cl/archivos/20080528.134802.pdf>.
- Ayala, L., López, A., Bzdigian, A., 1984. Producción de sedimento en cuencas andinas de Chile. In: *Programa Hidrológico Internacional, Jornadas de Hidrología de Nieves y Hielos en América del Sur*, 22 pp.
- Bierman, P., Steig, E. J., 1996. Estimating rates of denudation using cosmogenic isotope abundances in sediment. *Earth Surface Processes and Landforms* 21, 125-139.
- Binnie, S. A., Phillips, W. M., Summerfield, M. A., Fifield, L. K., 2007. Tectonic uplift, threshold hillslopes, and denudation rates in a developing mountain range. *Geology*, 35, 743-746.
- Brown, E. T., Stallard, R. F., Larsen, M., Bourles, D. L., Raisbeck, G. M., Yiou, F., 1998. Determination of predevelopment denudation rates of an agricultural watershed (Cayaguas River, Puerto Rico) using in-situ-produced ^{10}Be in river-borne quartz. *Earth and Planetary Science Letters* 160, 723-728.

- Brown, E. T., Stallard, R. F., Larsen, M., Raisbeck, G. M., Yiou, F., 1995. Denudation rates determined from the accumulation of in situ-produced ^{10}Be in the Luquillo Experimental Forest, Puerto Rico. *Earth and Planetary Science Letters* 129, 193-202.
- Burbank, D. W., Leland, J., Fielding, E., Anderson, R. S., Brozovic, N., Reid, M. R., Duncan, C., 1996. Bedrock incision, rock uplift and threshold hillslopes in the northwestern Himalayas. *Nature* 379, 505-510.
- Castro, S., Delucchi F., H., Gausereide, L., Caviedes D., J., Velasco, L., 1993. Ocurrencia de aguas subterráneas a gran presión en el Túnel Común Alfalfal : características, solución adoptada e interpretación. *Revista Geológica de Chile* 20, 85-97.
- Clapp, E. M., Bierman, P. R., Caffee, M., 2002. Using ^{10}Be and ^{26}Al to determine sediment generation rates and identify sediment source areas in an arid region drainage basin. *Geomorphology* 45, 89-104.
- Clapp, E. M., Bierman, P. R., Nichols, K. K., Pavich, M., Caffee, M., 2001. Rates of sediment supply to arroyos from upland erosion determined using in situ-produced cosmogenic ^{10}Be and ^{26}Al . *Quaternary Research* 55, 235-245.
- Clapp, E. M., Bierman, P. R., Schick, A. P., Lekach, J., Enzel, Y., Caffee, M., 2000. Sediment yield exceeds sediment production in arid region drainage basins. *Geology* 28, 995-998.
- Concha, A., 1999. Study of mountain river fluvial mechanics based on physical modeling of a representative prototype. B. Sc. Thesis, Departamento de Ingeniería Civil, Universidad de Chile, Santiago, 105 pp.
- Evans, J. M., Stone, J. O. H., Fifield, L. K., Cresswell, R. G., 1997. Cosmogenic chlorine-36 production in K-feldspar. *Nuclear Instruments and Methods in Physics Research Section B: Beam Interactions with Materials and Atoms* 123, 334-340.
- Farías, M., Charrier, R., Carretier, S., Martinod, J., Fock, A., Campbell, D., Cáceres, J., Comte, D., 2008. Late Miocene high and rapid surface uplift and its erosional response in the Andes of central Chile (33°–35°S). *Tectonics* 27, TC002046.

- Frankel, K. L., Brantley, K. S., Dolan, J. F., Finkel, R. C., Klinger, R. E., Knott, J. R., Machette, M. N., Owen, L. A., Phillips, F. M., Slate, J. L., 2007. Cosmogenic ^{10}Be and ^{36}Cl geochronology of offset alluvial fans along the northern Death Valley fault zone; implications for transient strain in the eastern California shear zone. *Journal of Geophysical Research*. 112, B06407.
- Galy, A., France-Lanord, C., 2001. Higher erosion rates in the Himalaya: Geochemical constraints on riverine fluxes. *Geology* 29, 23-26.
- Granger, D. E., Kirchner, J. W., Finkel, R. C., 1996. Spatially Averaged Long-Term Erosion Rates Measured from In Situ-Produced Cosmogenic Nuclides in Alluvial Sediment. *Journal of Geology* 104, 249-257.
- Hebbeln, D., Lamy, F., Mohtadi, M., Echtler, H., 2007. Tracing the impact of glacial-interglacial climate variability on erosion of the Southern Andes. *Geology* 35, 131-134.
- Heusser, C. J., 1990. Ice age vegetation and climate of subtropical Chile. *Palaeogeography, Palaeoclimatology, Palaeoecology* 80, 107-127.
- Heusser, C. J., 1989. Southern westerlies during the last glacial maximum. *Quaternary Research* 31, 423-425.
- Hovius, N., Stark, C. P., Allen, P. A., 1997. Sediment flux from a mountain belt derived by landslide mapping. *Geology* 25, 231-234.
- Hovius, N., Stark, C. P., Hao-Tsu, C., Jiun-Chuan, L., 2000. Supply and Removal of Sediment in a Landslide-Dominated Mountain Belt: Central Range, Taiwan. *Journal of Geology* 108, 73-89.
- Lamy, F., Hebbeln, D., Wefer, G., 1999. High-resolution marine record of climatic change in mid-latitude Chile during the last 28,000 years based on terrigenous sediment parameters. *Quaternary Research* 51, 83-93.
- Lavé, J., Burbank, D., 2004. Denudation processes and rates in the Transverse Ranges, Southern California; erosional response of a transitional landscape to external and anthropogenic forcing. *Journal of Geophysical Research, F. Earth Surface* 109, F01006, doi: 10.1029/2003JF000023, 31 pp.

- Liu, B., Phillips, F. M., Fabryka-Martin, J. T., Fowler, M. M., Stone, W. D., 1994. Cosmogenic ^{36}Cl accumulation in unstable landforms; 1, Effects of the thermal neutron distribution. *Water Resources Research* 30, 3115-3125.
- Maksaev, V., Munizaga, F., Zentilli, M., Charrier, R., 2009. Fission track thermochronology of Neogene plutons in the high Andes of central Chile: Implications for the tectonic evolution and porphyry Cu-Mo mineralization. *Revista Geológica de Chile*, in press.
- Matmon, A., Bierman, P. R., Larsen, J., Southworth, S., Pavich, M. J., Finkel, R., Caffee, M. W., 2003. Erosion of an ancient mountain range, the Great Smoky Mountains, North Carolina and Tennessee. *American Journal of Science* 303, 817-855.
- Matmon, A., Bierman, P. R., Larson, J., Southworth, S., Pavich, M., Finkel, R. C., Caffee, M., 2005. Grain size dependency of ^{10}Be concentrations in alluvial sediments in the Great Smoky Mountains; Abstracts of the 15th annual V. M. Goldschmidt conference. *Geochimica et Cosmochimica Acta* 69, 160.
- McInnes, B.I.A., Evans, N.J., Fu, F.Q., Garwin, S., Belousova, E., Griffin, W.L., Bertens, A., Sukarna, D., Permanadewi, S., Andrew, R.L., Deckart, K., 2005. Thermal history analysis of selected Chilean, Indonesian, and Iranian porphyry Cu-Mo-Au deposits, in: Anonymous Super Porphyry Copper & Gold Deposits: A Global Perspective. PGC Publishing, Adelaide, Australia, pp. 27-42.
- Montgomery, D. R., Brandon, M. T., 2002. Topographic controls on erosion rates in tectonically active mountain ranges. *Earth and Planetary Science Letters* 201, 481-489.
- Niño, Y., 2002. Simple model for downstream variation of median sediment size in Chilean rivers. *Journal of Hydraulical Engineering* 128, 934-941.
- Pratt-Sitaula, B., Garde, M., Burbank, D. W., Oskin, M., Heimsath, A., Gabet, E., 2007. Bedload-to-suspended load ratio and rapid bedrock incision from Himalayan landslide-dam lake record. *Quaternary Research* 68, 111-120.
- Reinhardt, L. J., Noey, T. B., Barrows, T. T., Dempster, T. J., Bishop, P., Fifield, L. K., 2007. Interpreting erosion rates from cosmogenic radionuclide concentrations measured in rapidly eroding terrain. *Earth Surface Processes and Landforms* 32, 390-406.

- Robinson, D., Bevins, R. E., Aguirre, L., Vergara, M., 2004. A reappraisal of episodic burial metamorphism in the Andes of central Chile. *Contributions to Mineralogy and Petrology* 146, 513-528.
- Ruz, A., 1999. Grain size distributions in Chilean rivers. B. Sc. Thesis, Departamento de Ingeniería Civil, Universidad de Chile, Santiago, 105 pp.
- Stone, J. O., Evans, J. M., Fifield, L. K., Allan, G. L., Cresswell, R. G., 1998. Cosmogenic chlorine-36 production in calcite by muons. *Geochimica et Cosmochimica Acta* 62, 433-454.
- Villarroel, R., Vergara, M., 1988. La Formación Abanico en el área de los cerros Abanico y San Ramón, Cordillera de Santiago, 1, A327-A337.
- Wohl, E., 2000. Mountain rivers. American Geophysical Union, Washington, DC.

3.5. Acknowledgments

JLA was funded by a Dalhousie Graduate Scholarship and a Geological Society of America Student Grant (#7864-05). This research was funded by ACOA-AIF Agreement 100-1052, a CFI Grant, and a NSERC Discovery Grant to JCG. A. Reuther and G. Yang are acknowledged for assistance in establishing the ^{36}Cl lab and protocol at the Dalhousie Geochronology Centre. R. Rauld (Univ. de Chile) provided field assistance to collect the Potrerillos and Macul catchments stream samples; SERNAGEOMIN-Chile provided logistical support for most of the fieldwork. J. Aguirre from Dirección General de Aguas (Chile) kindly facilitated access to digital files of discharge and suspended sediment for the studied stations. John Stone (Univ. of Washington) kindly granted access to A. Reuther and the authors to a Mathematica code used for calculating ^{36}Cl production rates and ages, whose original algorithms were modified to run in Matlab®.

3.6. Methods

3.6.1. Cosmogenic ^{36}Cl in Sediments

Stream sediment sample sites were located in the mainstem of the selected catchments, away from tributary junctions (e.g. Niemi et al., 2005) or active sediment sources like colluvial wedges or recent debris flows deposits, and upstream or downstream from large landslides (Antinao and Gosse, 2008). We obtained 4-5 kg of stream sediment in modern

bars, mainly targeting grain sizes below 5 cm; larger sizes become impractical to sample because the average number of grains needed to make estimations statistically relevant is very large. We aimed to analyze up to seven different grain size fractions: <0.125 mm, 0.125-0.250 mm, 0.25-0.50 mm, 0.5-1 mm, 1-2 mm, 2-4 mm, and 4-8 mm. The fractions were selected based on previous work on the subject (e.g. Clapp et al., 2000, 2001, 2002; Brown et al., 1995, 1998; Reinhardt et al., 2007; Matmon et al., 2003; Frankel et al., 2007; Belmont et al., 2007) and on the grain sizes available from the friable volcanoclastic regolith. Samples were sieved and the different grain size fractions crushed completely to <0.25 mm if necessary. Separation of generally heavier Cl and OH rich phases was performed in LST (Lithium Heteropolytungstate) solution at a density of 2.77 g cm⁻³. Li contamination was carefully monitored before and after LST use with ICP-MS measurements. After the concentration of feldspar-rich phases using LST, the samples were leached 3 times with 2M HNO₃ to remove meteoric ³⁶Cl, rinsed 8x with DIW after each leaching step, dried and subsequently 20-40 g of sample were spiked with 2.0-2.5 g of 1.2399-1.4454 ppm Cl solution (99.999% ³⁵Cl as NaCl). The spiked sample was later dissolved in a mixture of HF and HNO₃ and then Cl as AgCl was extracted at the Dalhousie Geochronology Centre following procedures adapted from Stone et al. (1996), and subsequently analyzed for ³⁶Cl/³⁵Cl and ³⁵Cl/³⁷Cl by AMS at Purdue Rare Isotope Measurement Laboratory (PRIME Lab, Purdue University). Total Cl concentration was determined by isotope dilution with AMS. A complete description of the physical and chemical procedure is presented in the Supplementary Data File. Process chemical blanks were run with the samples in order to correct for ³⁶Cl contamination during chemistry and background and contamination during AMS.

3.6.2. Analysis of Fluvial Records

The gauging stations (Fig. 3.1) have continuous discharge records for at least the last 80 a (Ayala et al., 1984), and daily suspended sediment records span the last 20 years, with variable periods (days to years) displaying no measurements. Although solid discharge vs. water discharge curves might be built to compensate for missing data, we found that the annual averages over all recorded years were very consistent and these figures were used to analyze the sediment transport upstream of the WCP – Central Depression boundary for the three major rivers initially analyzed (Fig. 3.1). Annual

sediment discharges expressed as landscape lowering rates were obtained by multiplying daily sediment concentration by water discharge and then dividing by the area, then by an average density of the rocks in the area.

To estimate mass transfer rates, the dissolved load was added, considering that it is at least of the same order of magnitude as the suspended sediment load (i.e. 1:1 ratio), based on point estimates at El Manzano, Maipo river (e.g., Arcadis, 2008). We purposely did not assume a fixed contribution from bedload (e.g. Galy and France-Lanord, 2001; Wohl, 2000; Pratt-Sitaula et al., 2007; Ali and DeBoer, 2007) and instead explored the contribution through modeling with sediment transport models. We used the bedload transport model of Ackers and White (1973), described in the Supplementary Information, which has been shown to be the best suited to Central Chile bedrock and alluvial/bedrock alpine streams (Concha, 1999; Niño, 2003). Grain size information for the bed sediment and armouring in the area near the San Alfonso gauging station of the Maipo River (Fig. 3.1), was taken from Niño (2002); channel properties were taken from Niño (2002), Ruz (1999) and Arcadis (2008).

3.7. Supplementary Information

3.7.1. Supplementary Data Tables

Table S1. Topography of the catchments selected for the ^{36}Cl and suspended sediment studies.

	average slope [m / m] ([degrees])	min / max slope [m/m]	total catchment relief [m]	maximum elevation [m a.s.l.]	mean annual discharge [m ³ s ⁻¹]	precipitation range [mm a ⁻¹]	mean elevation [m]	total contributing area [km ²]	glacier area (LGM)	Average mean relief ⁸ (5 km)
Macul	0.58±0.04 (29.7)	0.44/0.66	2300	3250	0.5	500-700	2214	16.6	0	2318
Potrerosillos	0.50±0.03 (25.8)	0.42/0.57	1750	2750	0.5 (est)	500-700	1860	13.6	0	1840
Aconcagua	0.51±0.12	0.12/1.24	4920	5865	60	500-1000	3177	2084.6	5	2132
Maipo	0.51±0.13	0.02/0.95	5000	6100	78 ⁹	700-1500	3201	2790.6	10	2130
Cachapoal	0.49±0.15	0.05/1.12	4450	5170	90	1000-2000	2647	2462.2	15	2078

⁸ Obtained from average of pixels inside the catchment for a grid of mean relief over a 5 km circular moving window.

⁹ Discharge in natural stage, before damming of the Yeso River in 1960.

Table S2. Chemical data for sediment and rock samples. Stream sediment sample IDs indicate analyses from this study, rock ID samples are from Antinao and Gosse (2008) and they are used to illustrate bedrock chemistry. Table column Type indicates what processing was done to the sample prior to chemical analysis (BHL: bulk sample, crushed <250 μm , DIW-rinsed, before density separation; HLBL: sample through density separation, before leaching; AL: sample after leaching and before dissolution for ^{36}Cl extraction).

Sample ID	Type	SiO ₂	Al ₂ O ₃	Fe ₂ O ₃	MgO	CaO	Na ₂ O	K ₂ O	TiO ₂	P ₂ O ₅	MnO	Cr ₂ O ₃	V ₂ O ₅	LOI	Sum
		%	%	%	%	%	%	%	%	%	%	%	%	%	%
5011	HLBL	59	16.1	7.58	2.41	4.52	3.62	1.34	0.97	0.2	0.13	< 0.01	0.02	3.94	99.8
5011	AL	67.7	13.9	4.16	0.65	3.37	4.05	1.46	0.9	< 0.01	0.05	< 0.01	0.02	2.75	99.1
5012	AL	67.9	13.8	5.32	0.55	3.11	4	1.57	0.8	0.02	0.06	< 0.01	0.01	2.43	99.5
5013	HLBL	61.8	15.9	6.91	1.79	3.54	4.08	1.71	0.92	0.23	0.12	< 0.01	0.02	3.44	100.4
5013	AL	69.3	13.8	3.31	0.4	2.44	4.16	1.76	0.78	0.02	0.05	0.02	< 0.01	2.73	98.8
5014	BHL	53.2	15.4	11.4	3.37	8.07	2.67	0.93	1.36	0.22	0.21	0.01	0.05	3.66	100.6
5014	AL	66.2	14.3	4.77	1.02	3.69	3.86	1.43	1	< 0.01	0.06	0.01	0.01	2.73	99.1
5015	HLBL	58.9	16.8	7.59	2.26	4.65	3.78	1.41	0.94	0.22	0.13	0.01	0.03	3.87	100.5
5015	AL	66.7	14.5	4.19	0.68	3.42	4.24	1.51	0.88	0.02	0.05	< 0.01	0.01	2.57	98.8
5016	AL	67.7	13.9	4.54	0.62	3	4.24	1.6	0.92	0.02	0.06	< 0.01	0.02	2.64	99.3
5018	AL	61.4	13.8	7.92	1.78	4.85	3.32	1	1.02	0.04	0.11	0.01	0.04	3.71	99
5034	HLBL	60.4	16	6.81	2.32	3.61	3.14	1.96	0.93	0.46	0.13	< 0.01	0.02	4.16	100
5036	AL	58.6	15.4	8.77	2.12	5.43	3.11	0.99	1.13	0.07	0.11	0.01	0.04	4.33	100.1
5039	BHL	54.4	15.4	10.4	3.26	7.87	2.86	1.01	1.18	0.22	0.19	< 0.01	0.04	3.22	100.1
5039	AL	61.70	15.00	6.99	1.84	3.71	3.72	1.38	1.04	0.02	0.11	0.02	0.03	2.69	98.2
5040	AL	62.60	15.20	7.21	1.72	3.59	3.64	1.42	1.12	0.01	0.11	< 0.01	0.03	3.24	99.8
5042	AL	57.2	15.3	9.84	2.54	6.03	3.13	0.95	1.21	0.05	0.14	< 0.01	0.05	3.89	100.3
5043	AL	56.8	16.4	9.33	2.49	6.01	3.22	0.98	1.1	0.05	0.13	< 0.01	0.04	4.03	100.6
5050	BHL	53.1	16.4	9.67	2.99	7.06	3.4	1.08	1.13	0.23	0.17	< 0.01	0.05	5.04	100.3
5050	HLBL	55.7	17.1	8.08	2.45	6.4	3.51	1.22	0.97	0.2	0.13	< 0.01	0.03	5.61	101.4
5050	AL	58.60	15.10	8.47	2.11	4.83	3.29	1.26	1.10	0.02	0.13	0.01	0.03	5.17	100.1
5051	HLBL	53.2	17	9.1	2.93	7.19	3.4	1.05	1.06	0.22	0.15	< 0.01	0.04	5.07	100.4
5051	AL	55.20	15.10	9.95	2.66	5.86	3.33	1.04	1.20	0.06	0.15	< 0.01	0.04	4.55	99.1

Table S2 (continued)

Sample ID	Type	SiO2	Al2O3	Fe2O3	MgO	CaO	Na2O	K2O	TiO2	P2O5	MnO	Cr2O3	V2O5	LOI	Sum
		%	%	%	%	%	%	%	%	%	%	%	%	%	%
5052	AL	55.70	15.20	9.28	2.29	5.64	3.22	1.04	1.18	0.05	0.14	0.02	0.05	4.71	98.5
5054	AL	64.00	14.70	6.29	1.42	3.22	4.05	1.58	1.18	0.02	0.09	0.01	0.02	3.02	99.6
5056	HLBL	59.2	15.8	8.23	2.27	4.24	3.92	1.5	1.05	0.26	0.15	< 0.01	0.03	3.45	100.1
5056	AL	61.90	14.70	7.22	1.65	3.70	3.90	1.47	1.18	0.04	0.11	0.02	< 0.01	2.95	98.8
5058	BHL	50.9	16.8	10.2	3.43	7.89	3.16	0.87	1.18	0.23	0.17	< 0.01	0.05	5.09	100.1
5058	HLBL	52.8	17.8	8.62	2.78	7.14	3.22	0.98	0.99	0.19	0.14	< 0.01	0.04	5.82	100.4
5058	AL	55.90	15.00	9.51	2.37	5.49	3.22	1.04	1.18	0.05	0.14	0.01	0.04	5.09	99.1
5059	HLBL	53.9	16.9	8.96	2.69	6.44	3.47	1.16	1.05	0.23	0.15	< 0.01	0.03	5.2	100.2
5059	AL	56.80	15.10	9.46	2.35	5.33	3.24	1.21	1.20	0.04	0.13	< 0.01	0.02	4.65	99.5
5060	HLBL	54.8	17	8.78	2.6	6.25	3.59	1.24	1.05	0.24	0.15	< 0.01	0.04	5.19	100.9
5060	AL	57.50	14.80	8.67	2.01	4.88	3.48	1.26	1.16	0.05	0.13	< 0.01	0.04	4.70	98.7
5061	HLBL	53.1	17.1	9.07	2.91	6.98	3.4	1.07	1.04	0.22	0.15	< 0.01	0.04	5.57	100.6
5061	AL	55.80	14.80	9.85	2.51	5.36	3.45	1.12	1.23	0.03	0.14	< 0.01	0.03	4.51	98.8
5033		59.40	15.60	7.49	2.87	5.55	2.95	0.86	0.98	0.02	0.11	0.05	0.05	3.19	99.2
5034		60.4	16	6.81	2.32	3.61	3.14	1.96	0.93	0.46	0.13	< 0.01	0.02	4.16	100
5035		67.20	14.20	4.95	0.46	3.48	2.43	1.52	0.99	0.02	0.06	0.02	0.02	2.88	98.2
5127		63.1	15.8	6.82	1.36	2.86	5.72	1.64	1.13	0.05	0.09	< 0.01	0.03	2.44	101
5128		69.4	13.4	5.17	0.83	1.82	5.21	1.84	0.97	0.06	0.09	< 0.01	0.01	1.84	100.7
5129		63.5	15.3	7.48	1.2	2.51	5.65	1.7	1.15	0.05	0.09	< 0.01	0.02	2.24	101

Table S2 (continued).

Sample ID	fieldID	fractionID	Type	U ppm	Th Ppm	Sm ppm	B ppm	Gd ppm	Li ppm	Cl Ppm
5033	PAN001	-	L	<0.01	<0.01	4.1	<40	3.7	20	20.7
5035	PAN003	-	L	<0.01	<0.01	1.8	<40	1.7	20	21.3
5054	MAC001	B	AL	<0.01	<0.01	2.6	<40	2.7	10	11.0
5015	MAC001	C	AL	0.33	0.9	1.9	<4	2	-	20.5
5016	MAC001	D	AL	0.36	0.9	2	<4	2.2	-	12.8
5039	MAC001	E	AL	<0.01	<0.01	2.7	<40	2.8	20	33.7
5039	MAC001	E	BHL	0.74	2.2	5	10	5.66	20	-
5039	MAC001	E	BHL	0.69	2.2	4.5	30	5.09	20	-
5014	MAC001	F	AL	<0.01	<0.01	2.7	<40	2.7	20	21.7
5014	MAC001	F	HL-BL	0.72	2.2	4.8	10	5.62	<10	-
5014	MAC001	F	BHL	0.69	2.3	4.1	<10	4.46	170	-
5013	MAC002	B	AL	<0.01	<0.01	2	<40	2	30	10.5
5056	MAC002	C	AL	<0.01	<0.01	2.7	<40	2.7	30	11.7
5056	MAC002	C	HL-BL	0.84	2.9	4.6	<10	5.44	120	-
5012	MAC002	D	AL	0.34	1	1.8	<4	1.8	-	12.9
5040	MAC002	E	AL	<0.01	<0.01	2.7	<40	2.8	20	13.7
5011	MAC002	F	AL	0.36	1	2.3	<4	2.5	-	17.3
5011	MAC002	F	HL-BL	0.72	2.4	3.8	<10	4.53	260	-
5011	MAC002	F	HL-BL	0.7	2.3	3.9	<10	4.54	260	-
5127	POT008	-	L	0.65	2.1	3.1	20	3.11	10	8.5
5128	POT009	-	L	0.71	2.2	3	10	3.15	20	8.6
5129	POT010	-	L	0.69	2.2	3.3	10	3.3	10	5.6
5060	POT001	B	AL	<0.01	<0.01	1.4	<40	1.5	20	5.8
5060	POT001	B	HL-BL	0.71	2.4	4.4	10	5.13	260	-
5059	POT001	C	AL	<0.01	<0.01	1.9	<40	2	30	6.0
5059	POT001	C	HL-BL	0.65	2.2	4.3	<10	5.12	290	-
5061	POT002	B	AL	<0.01	<0.01	1.7	<40	1.8	30	7.1
5061	POT002	B	HL-BL	0.56	1.9	3.6	<10	4.17	320	-

Table S2 (continued)

Sample ID	fieldID	fractionID	Type	U ppm	Th Ppm	Sm ppm	B ppm	Gd ppm	Li ppm	Cl Ppm
5058	POT002	C	AL	< 0.01	< 0.01	1.7	< 40	1.7	30	5.5
5058	POT002	C	HL-BL	0.56	1.8	3.7	20	4.61	350	-
5058	POT002	C	BHL	0.5	1.7	3.9	<10	4.54	<10	-
5018	POT002	D	AL	0.32	1.5	1.3	<10	1.54	20	4.6
5042	POT002	E	AL	0.42	1.4	1.7	<10	1.95	20	5.6
5050	POT007	B	AL	< 0.01	< 0.01	1.5	< 40	1.6	30	6.6
5050	POT007	B	HL-BL	0.67	2.3	3.9	<10	4.44	220	-
5050	POT007	B	BHL	0.62	2.1	4.3	30	5.14	10	-
5051	POT007	C	AL	< 0.01	< 0.01	1.7	< 40	1.8	40	6.9
5051	POT007	C	HL-BL	0.52	1.9	4	<10	4.63	290	-
5052	POT007	D	AL	< 0.01	< 0.01	1.7	< 40	1.8	40	4.4
5052	POT007	D	HL-BL	0.57	2	3.9	<10	4.54	240	-
5043	POT007	E	AL	0.46	1.7	1.9	<10	2.02	20	6.1
5036	POT007	F	AL	0.46	1.9	1.7	<10	1.98	20	5.1

Table S3a. Summary data for cosmogenic ^{36}Cl measurements. For location of samples refer to Figure 3.2. Suffix after sample code indicate grain size fraction: B: 2-4 mm, C: 1-2 mm, D: 0.5-1 mm, E: 0.25-0.50 mm, F: <0.25 mm. Sample ID refer to Table 2.

Field ID	Sample ID	SLHL production rate [at/g/a] and uncertainty		Catchment averaged production rate [at/g/a] and uncertainty		^{36}Cl concentration [at g ⁻¹ sediment] and uncertainty		Estimated catchment-wide erosion rate [mm/a] and uncertainty		[Cl] ppm and uncertainty	
POT001B	5060	4.10	0.12	17.13	1.00	4.58E+04	2.53E+03	0.27	0.03	5.8	0.3
POT001C	5059	4.21	0.12	17.59	1.02	5.54E+04	2.53E+03	0.22	0.02	6.1	0.4
POT002B	5061	4.14	0.12	15.74	0.91	3.14E+04	2.53E+03	0.36	0.05	7.2	0.3
POT002C	5058	4.01	0.12	15.22	0.88	3.83E+04	2.58E+03	0.28	0.03	5.5	0.3
POT002D	5018	3.65	0.11	13.87	0.80	4.38E+04	3.20E+03	0.22	0.03	4.6	0.3
POT002E	5042	4.09	0.12	15.53	0.89	5.22E+04	3.65E+03	0.21	0.03	5.6	0.4
POT007B	5050	4.11	0.12	14.95	0.87	4.26E+04	2.56E+03	0.25	0.03	6.6	0.3
POT007C	5051	4.20	0.12	15.30	0.88	4.90E+04	2.55E+03	0.22	0.02	6.9	0.3
POT007D	5052	4.01	0.12	14.59	0.84	4.62E+04	2.54E+03	0.22	0.03	4.4	0.3
POT007E	5043	4.13	0.12	15.05	0.87	5.32E+04	2.26E+03	0.20	0.02	6.1	0.2
POT007F	5036	3.89	0.11	14.14	0.82	5.07E+04	3.93E+03	0.20	0.02	5.1	0.4
MAC001B	5054	4.13	0.14	20.45	1.24	2.19E+04	4.31E+03	0.66	0.15	11.1	0.5
MAC001C	5015	4.58	0.17	22.67	1.42	3.11E+04	4.38E+03	0.52	0.09	20.5	0.3
MAC002B	5013	4.07	0.15	17.84	1.12	3.42E+04	2.54E+03	0.37	0.05	10.5	0.3
MAC002C	5056	4.18	0.14	18.31	1.09	3.45E+04	2.61E+03	0.38	0.05	11.7	0.3
MAC002D	5012	4.19	0.15	18.33	1.12	3.39E+04	3.42E+03	0.38	0.05	12.9	0.3
MAC002E	5040	4.15	0.14	18.19	1.09	2.59E+04	2.65E+03	0.50	0.07	13.7	0.3
MAC002F	5011	4.33	0.16	18.97	1.18	2.83E+04	3.44E+03	0.48	0.08	17.3	0.3

Table S3b. Relation between average upstream slope, average relief and erosion rates estimated from ^{36}Cl measurements.

Catchment	Average relief [km]	Average slope [m/m]	Catchment-wide average erosion rate [mm/a]
Macul (all)	2.3	0.58	0.48
Potrerrillos (all)	1.8	0.50	0.23

Table S4. Summary of suspended sediment data for the three major rivers draining Cordillera Principal in the study area, expressed as landscape lowering rates. Gauge points latitudes are quoted. Average lowering rates only contain effective measurements, without extrapolation for missing data along a particular year. Note that for the calculation in the last row, 'normal' years are years having no strong ENSO events, and having a number of days with records > 300. Extreme yields of these years are noted as interval boundaries (bracketed figures); compare these extremes with the box plots for Maipo River data shown in Fig. 3.3A.

Year	Aconcagua (32.8° S)		Maipo (33.5° S)		Cachapoal (34.25° S)	
	Average lowering rate over upstream catchment area [mm a ⁻¹]	Days in record	Average lowering rate over upstream catchment area [mm a ⁻¹]	Days in record	Average lowering rate over upstream catchment area [mm a ⁻¹]	Days in record
1989	0.04	350	0.1391	330	n.a.	n.a.
1990	0.0026	37	0.0384	153	n.a.	n.a.
1991	n.a.	n.a.	n.a.	n.a.	n.a.	n.a.
1992	0.0055	150	n.a.	n.a.	n.a.	n.a.
1993	0.048	237	0.2956	324	n.a.	n.a.
1994	0.03	240	0.1919	324	n.a.	n.a.
1995	0.02	342	0.1021	285	n.a.	n.a.
1996	0.007	359	0.0345	255	n.a.	n.a.
1997	0.037	299	n.a.	n.a.	n.a.	n.a.
1998	0.016	298	n.a.	n.a.	n.a.	n.a.
1999	0.01	265	n.a.	n.a.	n.a.	n.a.
2000	0.05	324	0.1021	324	n.a.	n.a.
2001	0.01	178	n.a.	n.a.	n.a.	n.a.
2002	0.01	145	n.a.	n.a.	n.a.	n.a.
2003	0.01	336	0.0207	50	0.04	304
2004	0.01	353	0.0528	336	0.18	350
2005	0.018	335	0.0845	238	0.16	323
2006	0.031	357	n.a.	n.a.	0.06	322
A. Average of the whole series, and standard deviation	0.020 ± 0.015		0.11 ± 0.09		0.11 ± 0.07	
B. Average annual discharge from 'normal' years	0.028 (0.007 – 0.04)		0.11 (0.05–0.29)		0.14 (0.04–0.18)	

3.7.2. Ackers and White (1973) bedload model description

The Ackers and White (1973) equation as modified by Day (1980) for size-specific transport is

$$q_{bi} = G_{gri} f_i \rho_s d_i V \left(\frac{V}{u^*} \right)^n \quad (\text{A1})$$

where u^* denotes shear velocity

$$u^* = \sqrt{gDS} \quad (\text{A2})$$

and G_{gri} is the dimensionless transport rate of the i th size class, defined as

$$G_{gri} = C \left[\frac{F_{gri}}{A_i} - 1 \right]^m \quad (\text{A3})$$

F_{gri} is the dimensionless particle mobility parameter (analogous to a noncritical Shields stress), A_i is a dimensionless hiding function analogous to a critical Shields stress, and C and m are empirical values. F_{gri} is defined as

$$F_{gri} = \frac{u^{*n}}{\left(gD \frac{\rho_s - \rho}{\rho} \right)^{\frac{1}{2}}} \left[\frac{V}{\sqrt{32} \log \left(\frac{10D}{d_i} \right)} \right]^{1-n} \quad (\text{A4})$$

where n is an empirical parameter that accounts for mobility differences between the fine and coarse components of the bed load (Ackers and White, 1973). A_i , C , m , and n are functions of dimensionless particle size (D_{gri})

$$D_{gri} = d_i [g(\rho_s - \rho) / (\rho \nu^2)]^{1/3} \quad (\text{A5})$$

where ν denotes kinematic viscosity (water temperature assumed 15 C throughout).

For $1 < D_{gri} \leq 60$

$$n = 1 - 0.56 \log(D_{gri}) \quad (\text{A6})$$

$$m = \frac{9.66}{D_{gri}} + 1.34 \quad (\text{A7})$$

$$C = 10^{[2.86 \log(D_{gri}) - (\log(D_{gri}))^2 - 3.53]} \quad (\text{A8})$$

$$A_i = \left[0.4 \left(\frac{d_i}{D_A} \right)^{-1/2} + 0.6 \right] A \quad (\text{A9})$$

where

$$D_A = d_{50ss} \left[1.62 \sqrt{\frac{d_{84ss}}{d_{16ss}}} \right]^{-0.55} \quad (\text{A10})$$

$$A = \left(\frac{0.23}{\sqrt{D_{gri}}} \right) + 0.14 \quad (\text{A11})$$

and d_{84ss} and d_{16ss} are, respectively, the subsurface particle sizes for which 84% and 16% of the sediment sample is finer. Day (1980) defines equation (A10) in terms of grain size percentiles of the unworked laboratory sediment mixture, which we approximate here by the subsurface grain size distribution.

For $D_{gri} > 60$

$$n=0 \quad (\text{A12})$$

$$m=1.5 \quad (\text{A13})$$

$$C=0.025 \quad (\text{A14})$$

$$A_i = \left[0.4 \left(\frac{d_i}{D_A} \right)^{-1/2} + 0.6 \right] A \quad (\text{A15})$$

where

$$A=0.17 \quad (\text{A16})$$

CHAPTER 4 Plio-Pleistocene Exhumation and Surface Uplift of Western Cordillera Principal (33.5°S), Southern Central Andes of Chile

(Manuscript in preparation to be submitted to: Journal of Geophysical Research. Surface Processes)

J.L. Antinao, J.C. Gosse

Dalhousie University

D. Stockli

Kansas University

4.1. Introduction

Erosion and exhumation (Molnar and England, 1990) are linked in tectonically active areas (Burbank et al., 2003), although the extent of the feedback has been difficult to quantify. Erosion can be defined as the removal of rock by surface processes, being a specific way of denudation, and commonly distinguished from tectonic denudation, in which large scale, extensional tectonics account for removal of rock from a region. Exhumation, on the other side, corresponds to the uplift of rocks relative to the local Earth's surface, as measured using geochronology, and is equal to the thickness of rock removed from the Earth's surface (Molnar and England, 1990). Rock uplift is the absolute movement of rock as compared to a fixed datum over the Earth's surface, like the geoid. When rock uplift equals erosion, topography can be said to have reached steady state, with no net change in surface mean elevation (e.g. Montgomery, 2001). Rock uplift is difficult to quantify, as it requires an absolute measure of the position of rocks. It has been suggested (cf. Montgomery, 2001; Dadson et al., 2003; Binnie et al., 2006) that the attainment of exhumational and erosional steady state simultaneously at orogenic timescales (10^6 a) can be used to infer orogenic topographic steady state, although this has been analyzed only for a few orogens (e.g. Montgomery, 2001).

The Andes comprise one of the largest orogens developed in an active, convergent, non-collisional setting. The high relief, high elevation southern Central Andes (SCA) of Chile (Fig. 4.1) have experienced an uninterrupted orogeny since the Miocene (Godoy et al., 1999; Charrier et al., 2002; Fock et al., 2006). During that time and particularly during the Quaternary they have experienced major climatic changes that have had a direct influence on surface processes that cause exhumation (Hebbeln et al., 2007; Aguilar et al., 2008; Antinao et al., 2008). The area is therefore well suited to study the interplay of surface and tectonic processes above a subduction zone. However, detailed erosion and exhumation records suitable for comparison at similar temporal and spatial scales are only now being produced for this area of the orogen. Erosion and incision estimates have been determined for the area (Farías et al., 2008; Antinao and Gosse, 2008; Antinao et al., submitted, §3; Baker et al., 2008), but these records do not overlap much with existent data on exhumation. Apatite and zircon fission track (AFT, ZFT) thermochronology along with scarce apatite and zircon (U-Th)/He data compiled during this decade (Cembrano et al., 2003; McInnes et al., 2005; Fock, 2005; Farías et al., 2008; Maksaev et al., 2009; Spikings et al., 2008) indicate that the Cenozoic exhumational pattern is marked by Miocene to Pliocene exhumation of Cordillera Principal as a separate entity from the Coastal Cordillera (Fig. 4.1), which was exhumed mostly during Late Mesozoic-Early Cenozoic times. However, there are still major issues that remain unclear. For example, the proposed decoupling between Eastern and Western Cordillera Principal (ECP and WCP) or between the Coastal Cordillera (CC) and WCP, suggested by AFT and structural data (Fock, 2005; Fock et al., 2006; Farías et al., 2008) has not yet been temporally constrained. Additionally, the exhumation history of WCP after ca. 5 Ma is not known, except near the porphyry copper systems where (U-Th)/He data provides constraints on cooling up to ~2.5 Ma (McInnes et al., 2005). The knowledge gap is significant because during the last 5 Ma the SCA have experienced major climate changes, a large shift in arc position (50 km to the east, Kay et al., 2005), and a switch in the principal direction of stress patterns (Lavenu and Cembrano, 2008).

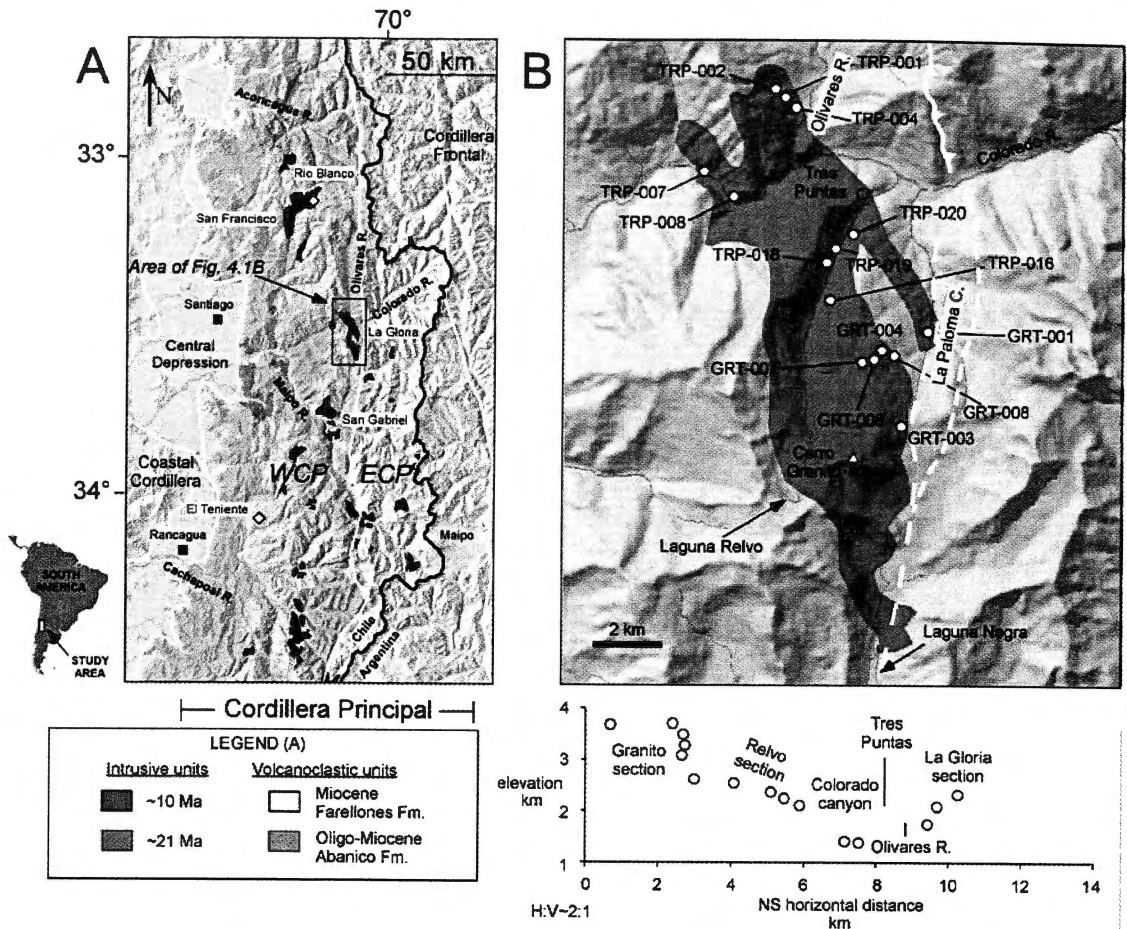


Figure 4.1. A. Shaded Relief Map of the study area and location in central Chile. Morphotectonic units are shown: Cordillera Principal (Western, WCP; Eastern, ECP), Coastal Cordillera, Central Depression, and Cordillera Frontal in Argentina. Cenozoic geology is shown in colors over the shaded relief map. La Gloria, San Gabriel and San Francisco intrusives are shown. The continental divide is marked in black, corresponding also to the Argentina-Chile border. Note the location of El Teniente and Rio Blanco Cu orebodies that have also apatite (U-Th)/He data (McInnes et al., 2005). B. Detail of the area of WCP covered by the present study. The La Gloria Pluton is marked in red above a shaded relief map of the area. Position of sampling points is marked. The lower part of this figure shows the projected sample elevation on a NS transect. The different sections discussed in the text are marked. Colorado River flows from east to west in the northern area of this map; La Paloma creek runs south to north, along the edge of the Coironal-Laguna Negra reverse fault (in white).

We performed an apatite (U-Th-Sm)/He (aHe) thermochronology analysis of a deeply incised granitic pluton in the SCA of central Chile, where high (~2.5 km) relief permitted sampling along a vertical transect to constrain the exhumation history during

the Late Pliocene-Early Pleistocene. To analyze how the erosional system might have responded to temporal changes in exhumation, we compared the aHe derived estimates of exhumation with (i) estimates of sediment production and transport in the area at different timescales (Antinao and Gosse, 2008; Antinao et al., submitted, §3) and (ii) exhumation patterns from other low temperature thermochronometers under similar geological and geomorphological constraints, along the Chilean SCA (Maksaev et al., 2009; Spikings et al., 2008; Farías et al., 2008).

4.2. La Gloria Pluton Area

In the study area, elevations reach up to 4 km, with relief >2 km (Fig. 4.1). A thick (>3000 m) sequence of Oligocene-Miocene volcanic and volcanoclastic rocks is intruded in the study area by the La Gloria plutonic body (Cornejo and Mahood, 1997). The pluton is a NS-oriented isolated granodioritic to quartz-monzonite body emplaced rapidly at a shallow level in the crust (Cornejo and Mahood, 1997). After its emplacement at 9.8 Ma (total fusion biotite K-Ar age by Drake, 1979, unpublished data; cf. Cornejo and Mahood, 1997) the pluton did not develop a long-lived hydrothermal system. Instead it apparently cooled quickly through fissures at the upper levels of emplacement (Cornejo and Mahood, 1997). Total-Al solidification pressures of ~1 kbar determined from hornblende in the wall and roof zones (Cornejo and Mahood, 1997) are consistent with an estimated 4 km of cover at the time of emplacement (Aguirre, 1960). An AFT age of 5.24 ± 0.82 Ma has been determined for the lower part of the pluton, at the Colorado Canyon bottom (Farías et al., 2008).

The north-south Olivares River valley is located mostly to the northeast of the pluton, but over its final reach it incises deeply into the granodiorite (Fig. 4.1). The valley has developed along the Coironal fault, a major reverse fault associated with Late Miocene-Pliocene uplift of the ECP (Ramos et al., 1991; Fock, 2005). The post-Miocene kinematics of the Coironal fault is unknown. Joining the Olivares River at Tres Puntas (Fig. 4.1B), the Colorado River dissects the pluton in two, exposing 2.5 km of vertical section, mainly to the south. Lack of internal deformation in most of the pluton suggests it postdates most of the deformation north of the Colorado River (Cornejo and Mahood, 1997), but according to Fock (2005) the fault cuts dikes that extend south from the pluton

south of it. Lavenu and Cembrano (2008) determined from microtectonic analysis that two compressional events affected the pluton after its emplacement, without large faults developed.

4.3. Methods

Rock samples were taken approximately at 100 m intervals starting from the bottom of the Colorado River canyon, at the locality of Tres Puntas, towards the north (La Gloria section of the profile, 3 km horizontal extension) and the south (Relvo and Cerro Granito sections, 6 km horizontal extension) of the river valley (Fig. 4.1B). Approximately 3 kg of rock were sampled, from which at least 1 kg was crushed completely under 250 μm . After removing the fines, the sample was further separated based on density using LST and on magnetic properties using a Frantz Isomagnetic separator. Between 1 and 5 g of non-magnetic heavy phases (primarily zircon and apatite) were isolated from each sample. Grains were hand picked at 36-106X using a Stemi SV11 Zeiss binocular microscope, giving emphasis to dimensions, overall shape and symmetry of the crystals, along with the presence of inclusions that can be detected at crossed polarizing light. We only processed euhedral grains, mostly $>75 \mu\text{m}$ in width, lacking obvious inclusions or fractures. Grains were measured and photographed using a coupled PaxCAM camera and PaxIt software which enables real time calibrated measurement of crystal dimensions along its axes. For each sample 10 to 20 grain groups (1 to 8 grains each) were assembled, examined and photographed again under 400x magnification using a Zeiss® Axioplan binocular microscope equipped with an Autoscan® AS3000 computer operated stage, searching for smaller (~ 5 micron) bubbles or inclusions of zircon and monazite that remain unidentified after the first stage, specially if their c-axis is parallel to the apatite c-axis.

Between 1-5 grains were loaded into platinum crucibles (0.6 mm diameter by 1.0 mm length) for He gas extraction. The crucibles were mounted in a sample holder (25 samples) where vacuum was established at least 24 h before the measurements. Pt crucibles were heated separately using a Quantronix model 117 YAG laser at 1064 nm operated in continuous mode, 17 W max output. We outgassed apatite for 5 min. at 1050 ± 15 °C, with the output power regulated by a combination of a calcite variable

attenuator and a 2 colour optical pyrometer. The samples were heated in two stages: an initial 5 minute stage for primary degassing, and a 5 minute re-heat to ensure the sample has been completely degassed and as a means to detect higher-T retention phases as inclusions (e.g. House et al., 2000). He data was discarded if they met criteria set e.g. by Farley and Clark (2006), i.e. positive re-extract >0.75% of initial extract and >0.15 fmol ^4He . Hot blanks were run between samples, giving 0.31-0.84 fmol, with a mean of 0.55 fmol, and on average being less than 15% of the sample He. After degassing, gas is H stripped, spiked with 286 fmol of ^3He , and then the ratio $^4\text{He}/^3\text{He}$ is measured along ^2He , Hd and ^2H in a Blazers Prisma QMS-200 quadrupole mass spectrometer at the Dalhousie University Geochronology Centre.

The platinum packets containing apatite grains were retrieved from the vacuum chamber and transferred into teflon beakers. Approximately 1 ml of a 20% HNO_3 spiked solution (containing 0.1 ml of spike with $^{230}\text{Th}/^{232}\text{Th}$, highly enriched $^{235}\text{U}/^{238}\text{U}$, and pure ^{149}Sm) was used for dissolution. The solution was heated to 80°C for 1 hour to ensure complete dissolution. After they cooled to room temperature, 1 ml of milliQ water was added to each beaker. The solutions were then analyzed for U, Th and Sm at the University of Kansas (U-Th)/He Laboratory using a dedicated Fisons/VG PlasmaQuad II+XS Inductively Coupled Plasma Mass Spectrometer (ICP-MS). Data reduction was achieved using an in-house Matlab® routine (Appendix A.3.1) that received He, U, Th and Sm data, along with apatite dimensions, and calculated Ft corrections using procedures outlined by Farley (2002). The uncertainty in the Ft correction was also calculated in accordance with Farley (2002). Analytical errors were propagated throughout the calculations.

In addition to the previous analysis, we used the HeFTy code (Ketcham, 2005) to model existent AFT data from a sample originally taken by Fock (2005) at the bottom of the Colorado River canyon, from the same location where we obtained an aHe cooling age. In this way, we were able to constrain the lower temperature history using two thermochronometers for the same location.

4.4. Results

Arithmetic means of individual cooling ages from single and multiple grain analyses range from 0.6-1.6 Ma for the low elevation samples to ~4-6 Ma for the high ones (Table 4.1, Fig. 4.2). A complete set of analytical results is given in the Appendix (§A.3.2). The simplest way to examine our data would be to analyze cooling rates from individual ages considering that they passed through the aHe closure temperature under a certain geothermal gradient that needs to be assumed. To avoid this assumption, we will examine the cooling ages as a function of depth, using the high relief topography of this section of the Andes to our advantage. The age-elevation relationship (AER) can be interpreted directly as the vertical velocity of rocks relative to the closure isotherm at the time of closure. Changes in the slope of the AER with elevation are typically interpreted to represent temporal evolution of exhumation (Reiners and Brandon, 2006).

A slight break in the slope of the age-elevation is apparent at around 3000 m (Fig. 4.3). Samples above ~3000 m, corresponding to a cooling age of ~2.8 Ma, appear to be very different from the ages at lower elevations, in absolute value and in the relative dispersion shown by the values. A least squares error-weighted regression through the whole dataset yields a slope of 0.77 mm a^{-1} with a correlation coefficient (r^2) of 0.60. Under certain assumptions, this slope may be interpreted as an average exhumation rate between ~1 and 5 Ma. The average exhumation rate is valid only under the assumption of a stable closure isotherm depth and that all samples have the same closure temperature (e.g., Spotila, 2005; Reiners and Brandon, 2006). Therefore, the initial estimate of ~0.77 mm a^{-1} as exhumation rate valid from ~5 to ~1 Ma must be taken with caution. Although the number of data points in the upper part of the profile is not large enough to define a distinct slope of the age-elevation relationship above 3000 m, those points can be differentiated clearly from the lower section of the profile. If the higher elevation samples are left out from the regression analysis, there is no relevant correlation in the data, suggesting that age does not change with elevation in the lower part of the profile, and indicating an event of rapid cooling through the aHe temperature at some point between 2-3 Ma.

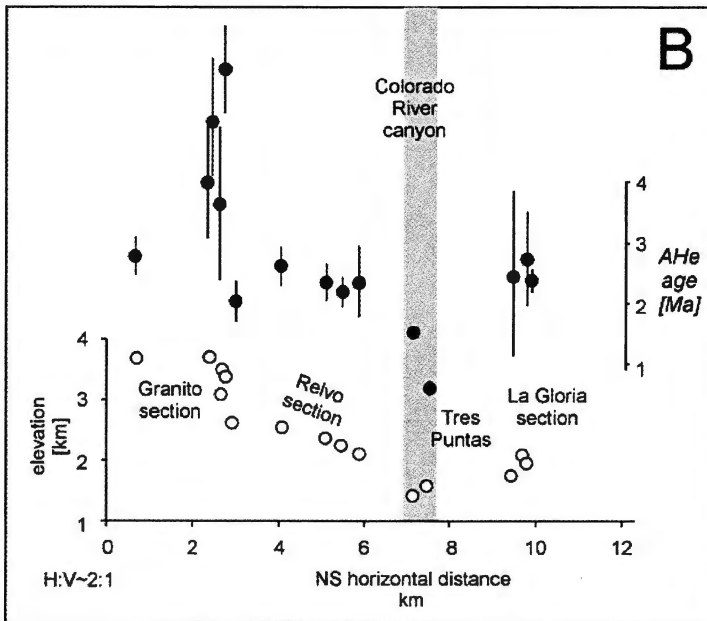
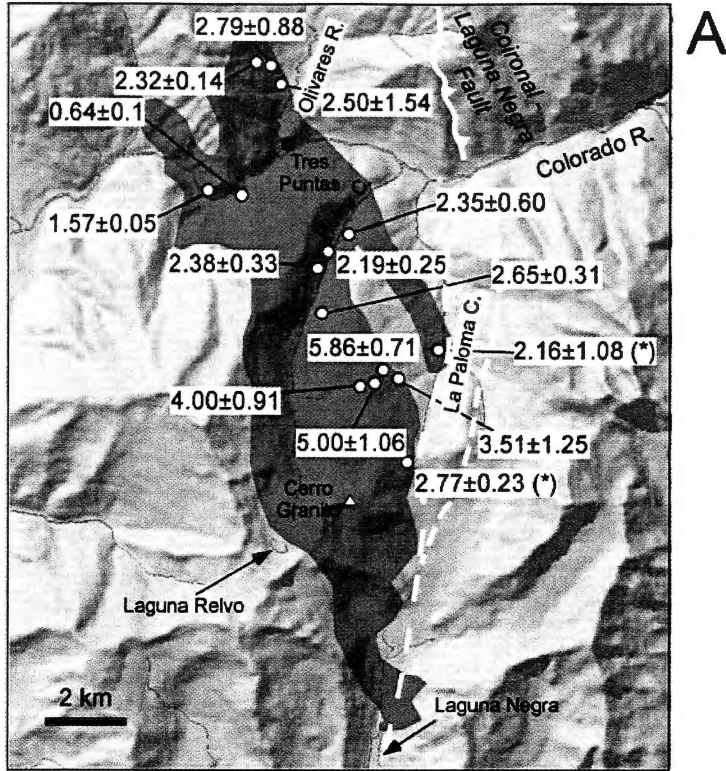


Figure 4.2. A. Apatite (U-Th-Sm)/He (aHe) ages for the La Gloria pluton. Uncertainties displayed are 1σ propagated and individual samples display error-weighted mean. The two ages marked with an asterisk correspond probably to anomalously young ages caused by the Coironal_Laguna Negra Fault (see also Fig. 4.3). B. north-south transect (similar to Fig. 4.1B) with the aHe ages. Note the young ages closer to the bottom of the Colorado River canyon, and older ages along the higher Granito section.

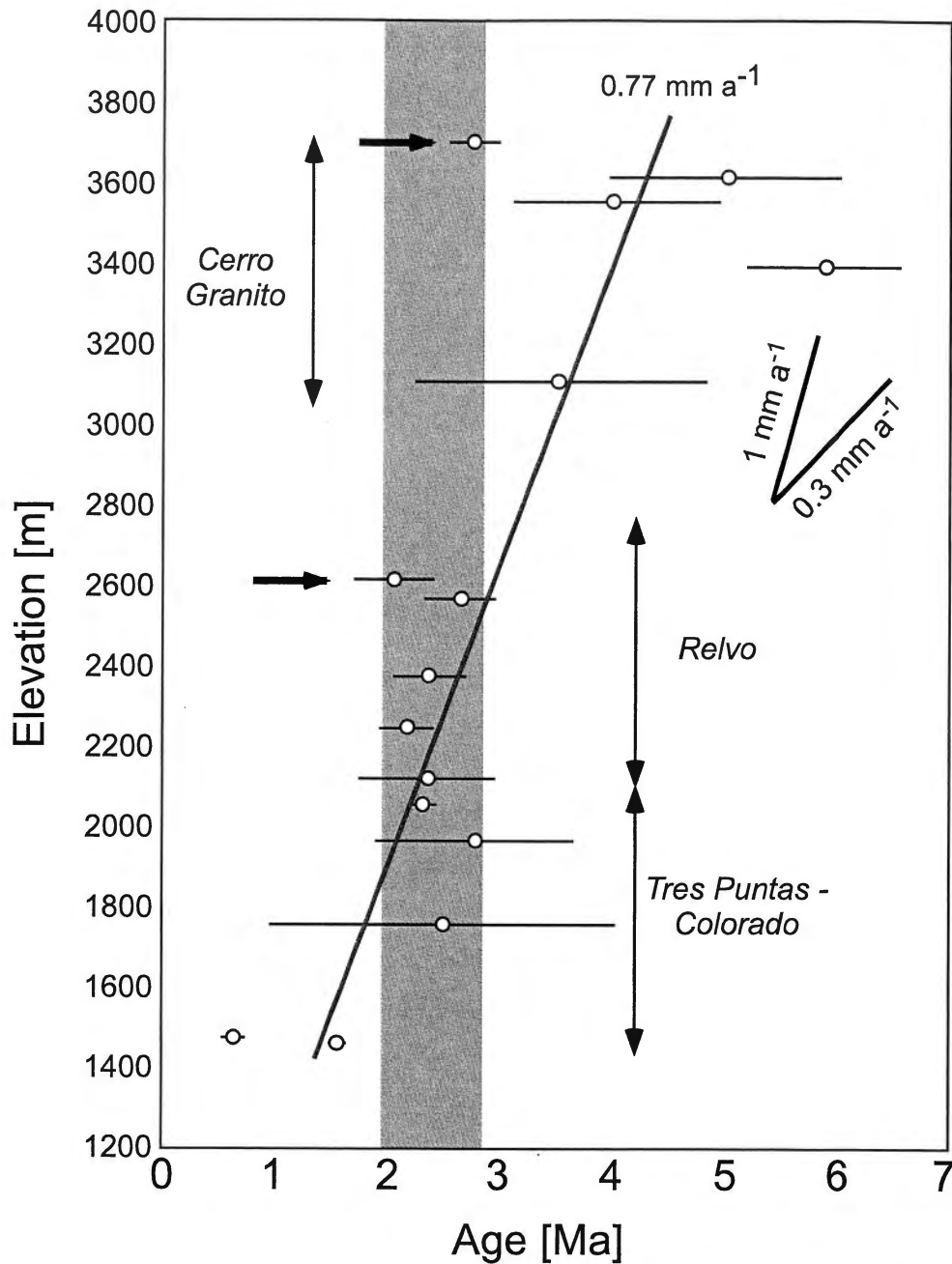


Figure 4.3. Age-elevation relationship for the La Gloria pluton. The two black arrows indicate samples that are anomalously younger, which might have been affected by movement along the Coironal-Laguna Negra fault. They are also marked in the map in Fig. 4.2. The gray line marks the overall trend of 0.77 mm a^{-1} (see text for discussion); also marked are slopes corresponding to 0.3 and 1 mm a^{-1} , which we suggest approach the slopes for the upper (Cerro Granito) and lower (Relvo-Tres Puntas) sections of the profile. A pink band indicates the boundaries of an event of rapid cooling that has been recorded after $\sim 3 \text{ Ma}$, which is responsible for clustering of the $a\text{He}$ ages in the middle portion (1750-2600 m a.s.l.) part of the profile.

Table 4.1. Summary of aHe ages. Uncertainty is 1 standard deviation of the population (with 1 to 8 single to multi grain composites).

Sample	Age [Ma]	Uncertainty [Ma]	Elevation [m]
TRP-008	1.57	0.05	1464
GRT-001	2.07	0.36	2616
TRP-019	2.19	0.25	2248
TRP-002	2.32	0.14	2062
TRP-020	2.35	0.60	2120
TRP-018	2.38	0.33	2374
TRP-004	2.50	1.54	1759
TRP-016	2.65	0.31	2567
GRT-003	2.77	0.23	3699
TRP-001	2.79	0.88	1963
GRT-008	3.51	1.25	3108
GRT-007	4.00	0.91	3550
GRT-006	5.00	1.06	3611
GRT-004	5.86	0.71	3389
TRP-009	0.64	0.10	1477

4.5. Discussion

4.5.1. Interpretation of the Age-Elevation Relationship

The age-elevation relationship (AER) depicted in Fig. 4.3 shows an apparent exhumation rate of 0.77 mm a^{-1} between ~ 5 and ~ 1 Ma, and the apparent break shown at around ~ 2600 m needs to be investigated as it might represent a break in exhumation conditions during cooling of the profile. This possibility will be analyzed in detail in the following section.

Cooling ages from the Tres Puntas and Relvo sections (Fig. 4.3) are indistinguishable under 1σ , showing that there is no obvious interruption of the cooling pattern across the Colorado River valley, and therefore implying that minor faulting that occurred after 2.8 Ma in the lower section of the pluton (Cornejo and Mahood, 1997; Lavenu and Cembrano, 1999, 2008) does not affect the thermochronological data.

The ages of the middle part of the profile (~ 2 -3 Ma, Fig. 4.3) are in agreement with ages determined for areas of the Aconcagua ($\sim 33^\circ$ S, aHe age of 2.4 ± 0.1 Ma, McInnes et al., 2005), Cachapoal (Teniente, 34° S, aHe age of 2.74 ± 0.51 Ma, McInnes et al., 2005), and Teno ($\sim 35^\circ$ S, aHe age of 2.6 ± 1.3 Ma) valleys (Fig. 4.4), all of them along the boundary WCP-ECP. Similar cooling ages for the aHe thermochronometer at

elevations close to the mean elevation of the landscape and in the same structural position along the eastern boundary of WCP indicate a common stage where the cooling rates increased at ~ 2.3 - 2.7 Ma. We will explore further the possibility that increased exhumation is responsible for this observation by using thermal modeling of one sample with two available thermochronometers (see below).

We note that most of the aHe ages discussed in the previous paragraphs are located along a line that is very close to the NS trace of the Coironal-Laguna Negra fault (Ramos et al., 1991; Fock, 2005) or its prolongation (Fig. 4.4). Movement of this fault has been associated with the uplift of Cordillera Frontal in Argentina from 9-6 Ma (Giambiagi et al., 2003; Fock, 2005), an event that developed backthrusts and out-of-sequence thrusts in WCP. Although there is no data on slip rates along the fault, reverse movement along the fault trace is consistent with a regional exhumation event in WCP from 6-3 Ma, caused by E-W compression according to Maksaev et al. (2009). However, after 3 Ma, there is no direct evidence for movement along the fault. Two different scenarios can be envisioned for slip of the fault. In the first scenario, the fault stopped substantial movement before 3 Ma, and therefore no effect would be seen in the thermal structure of the crust during a hypothetical rapid event increasing exhumation between 3 and 2 Ma. The pre-3 Ma slip rates needed to test this hypothesis have not been measured. An alternative scenario is that fault slip continued during the increased exhumation event at ~ 3 - 2 Ma, and then some of the areas closer to the fault were affected by advection of the isotherms which delayed cooling of the rocks and so rocks closer to the fault will yield younger aHe ages. We cannot completely rule out the second scenario, as the two samples closer to the fault showed anomalously lower ages compared to their position along the profile (Fig. 4.3), a situation that can be explained by either tectonic transport along the fault or by the effect of advection of the isotherms that delayed thermal closure.

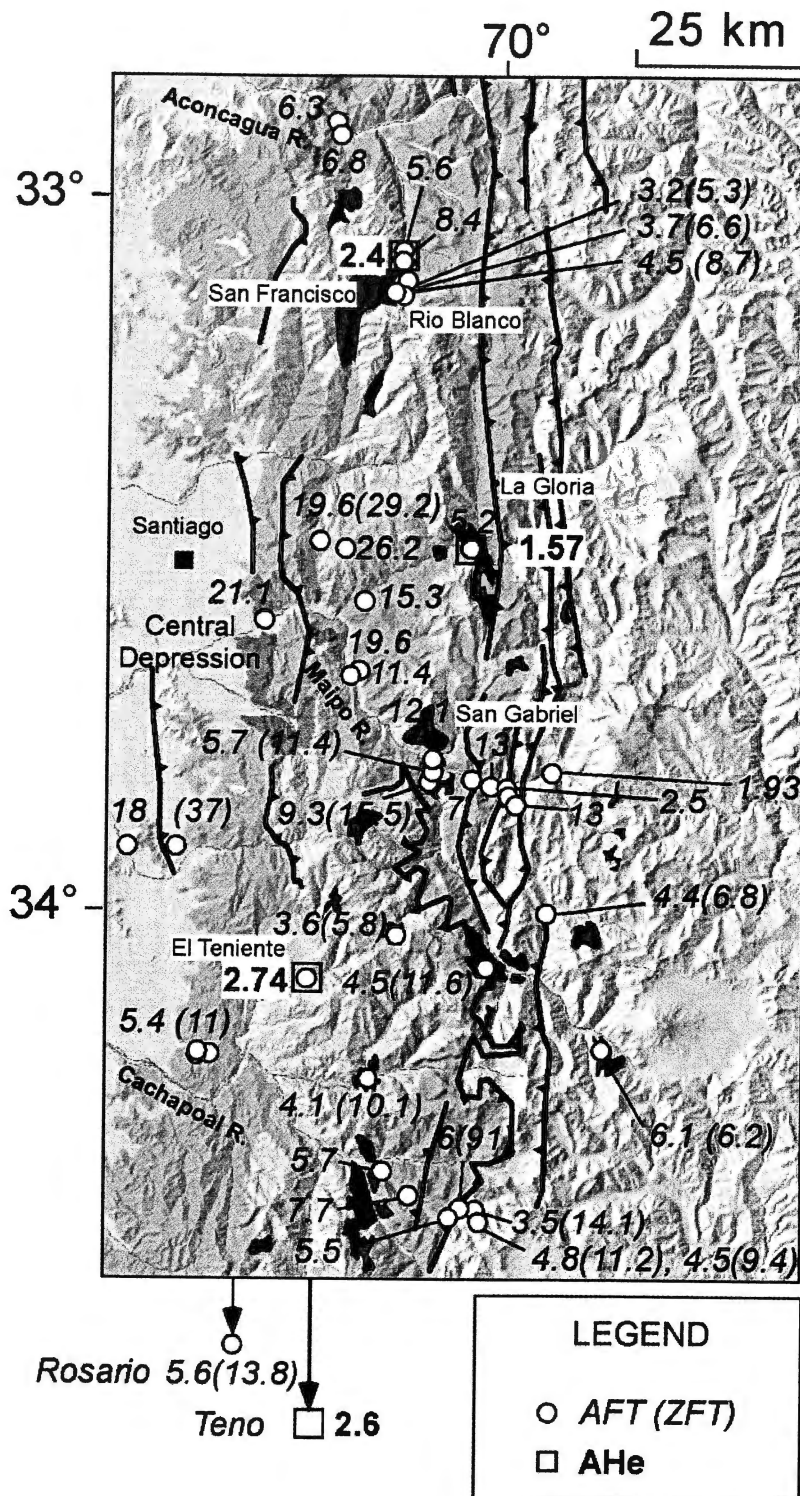


Figure 4.4. Apatite and zircon fission track ages obtained by previous studies in the area, shown in relation to our dataset (La Gloria). The marked sample corresponds to sample TRP009.

We assumed that activity of the Coironal-Laguna Negra fault had an effect on the upper section of the profile, under the second scenario. The simplest interpretation of the uppermost sample (age 2.77 Ma, elevation ~3700 m) is that it was affected by fault slip. Without this sample, we can estimate for the upper part of the profile a lower exhumation rate from ~5 to 3 Ma, of ~0.3 mm a⁻¹ (Fig. 3), similar to what Makshev et al. (2009) estimated regionally and for the San Francisco pluton, 30 km to the north and at a similar timescale, using a vertical profile, i.e. independently from any assumption about the geothermal gradient at the time.

Furthermore, we can perform a simple test (e.g. Spotila, 2005, Reiners and Brandon, 2006) to determine if exhumation remained the same or changed after the time span recorded in our profile. Assuming that exhumation remained at 0.77 mm a⁻¹ (long-term average slope, Fig. 4.3) after ~1.6 Ma (cooling age of the lowermost sample), we can estimate the zero-age intercept, i.e. where rocks are currently at the closure temperature. The estimated depth turns out to be 1.1 km below the surface, which imply a geothermal gradient of ~65 °C/km for the area, higher than any calculation from a known heat flux dataset would suggest (e.g., Hanza and Muñoz, 1996). Assuming that the geothermal gradient has remained approximately constant during the last 2-3 Ma in the region, at about 30±10 °C km (cf. Makshev et al., 2009), the estimated average exhumation for the period would be 1.6±0.6 mm a⁻¹, higher than the 0.77 mm a⁻¹ obtained on average between 5 and 1 Ma. Although an increase in exhumation rate will drive up the geothermal gradient as it adjusts to the new thermal state of the crust (e.g. Reiners and Brandon, 2006), the estimated factor of 2 for the increase would only lower the observed effect but in any case it will not change its sign. Using the RESPTIME code (Ehlers et al., 2005; Reiners and Brandon, 2006) to investigate how long it would take the closure depth to stabilize again after a change of this order, we determined that the transi-snet conditions will only last less than 1 Ma. At that point the closure depth would be moving upwards at less than 10% of the initial velocity immediately after the change.

We conclude that while on average the exhumation rate along the profile can be considered to be 0.77 mm a⁻¹, apparently there is an increase in cooling rate and potentially in the exhumation rate, at some point around 2-3 Ma. In the following

paragraphs we will continue the analysis of the hypothesized increase through the use of two other thermal modeling methods, which in fact do support an increase.

4.5.2. Thermal History Modeling

Apatite fission track data for a sample taken at a location in the bottom of the Colorado River canyon (RCL-02; Fock, 2005; also in Farías et al., 2008) allows us to analyze the thermal history of the sample site because the different thermochronometers date the rock as it ascends through different isotherms. The algorithms for He diffusion use the kinetic data of Farley (2000) and are based around uniform Th and U distribution in the apatite grains. The thermal history solutions were generated using the HeFTy code, which permits thermal history solutions to be found that match the (U-Th)/He (aHe sample TRP-009) and FT data (Ketcham, 2005).

A K-Ar age of 9.8 Ma in biotite (cf. Cornejo and Mahood, 1997), would dictate cooling through the $350\pm 50^\circ\text{C}$ isotherm. However, the modeled thermal history is not sensitive to the early constraints (Fig. 4.5). After rapid cooling from ca. 9 to 8 Ma, which is in agreement with a rapid emplacement and late magmatic cooling of the Miocene granitoids of the area (Cornejo and Mahood, 1997; McInnes et al., 2005; Makshev et al., 2009), the best-fit thermal history suggests a slower cooling rate at $\sim 7.5\text{-}2.5$ Ma, with the rock spending some time in the partial annealing zone, around $140\text{-}120^\circ\text{C}$ (Fig. 4.5). The cooling rate increased rapidly at around 2.5 Ma, indicating fast exhumation of the rocks currently at the bottom of the Colorado River canyon through the aHe closure isotherm.

The cooling rate for the period 6-3 Ma is approximately $9^\circ\text{C}/\text{Ma}$. The proposed thermal evolution is similar to other Late Cenozoic cooling histories for other areas in the SCA. Makshev et al. (2009) obtained a rate of $\sim 0.45\text{ mm a}^{-1}$ from AFT analysis of three samples in an age-elevation profile for the San Francisco pluton (30 km to the north of the location of sample TRP009, and to the west of the Coironal fault, Fig. 4.4). The San Francisco profile gives a denudation rate from 4.5 to 3.2 Ma, and assuming a geothermal gradient of $25^\circ\text{C}/\text{km}$ yields an estimated cooling rate of about $11^\circ\text{C}/\text{Ma}$ for the period, similar to the one obtained in the HeFTy analysis and to the one determined from the AER of the upper part of the profile (Fig. 4.3, 0.3 mm a^{-1}) under the same assumed geothermal gradient ($25^\circ\text{C}/\text{km}$). South of the study area, Spikings et al. (2008) have modeled cooling rates with paired AFT-aHe analysis of a pluton in the Teno valley ($\sim 35^\circ$

S). Their modeling indicates rapid exhumation at ~ 2 Ma through the aHe closure temperature, with modeled cooling rates of $25^\circ\text{C}/\text{Ma}$ from 6 to 2 Ma, higher than the previously discussed cooling rates.

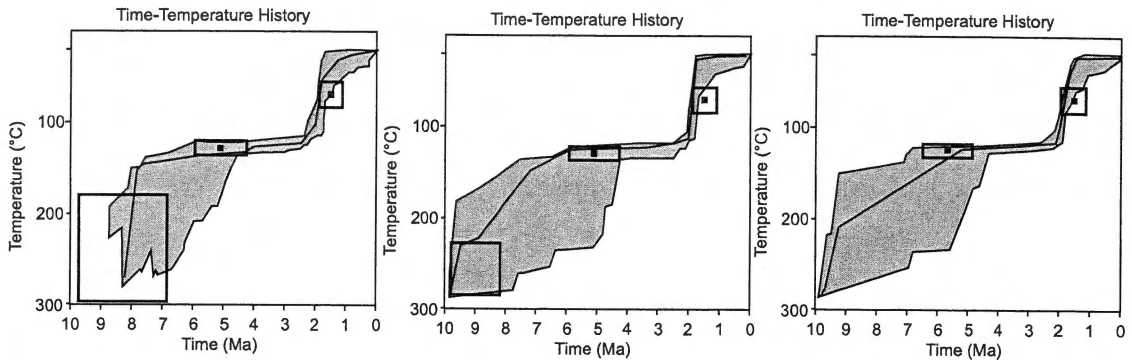


Figure 4.5. Thermal models from the HeFTy code (Ketcham, 2005), using sample TRP009 (apatite Helium) and RCL02 (apatite fission track, Fock, 2005), both taken at the bottom of the Colorado canyon in the Tres Puntas area. The three panels differ in the amount of uncertainty given to the 9.8 Ma K-Ar biotite age used as initial constraint and that has been interpreted as the crystallization age of the pluton. The final time-temperature paths do not differ, showing that they depend mostly on the constraints given by the low temperature chronometers.

As a second check, we used the method developed by Moore and England (2001) to test if our data can be interpreted as a result of a noticeable change in exhumation rate or is only an artifact of a protracted response to exhumation that started at some point in the past (in this case around 6 Ma according to Makshev et al., 2009, and Farias et al., 2008). We first analyze the history of the rocks represented by the sample pair RCL-02/TRP009 explained before. We can safely assume as initial conditions that the rocks were in the partial annealing zone, at $\sim 110^\circ\text{C}$ from 5.2 Ma to ~ 4.0 Ma. After that, the best-fit for the thermal model would be that exhumation resumed at ~ 4.0 Ma, being continuous until today, with a magnitude of $1.2 \pm 0.1 \text{ mm a}^{-1}$.

Using the whole dataset in the aHe profile, and the same modeling scheme already described, the best-fit for the exhumation history, again starting at conditions of $120\text{-}140^\circ\text{C}$ before 4 Ma, is that exhumation has reached $1.1 \pm 0.3 \text{ mm a}^{-1}$, starting at some point ~ 4.0 Ma from the temperatures quoted above. The best-fit solution in this case is not very well constrained but points in the same direction that all previous analyses. Estimated model geothermal gradients for the best-fit modeling schemes are $25\text{-}30^\circ\text{C}/\text{km}$. Comparison of the exhumation rates obtained allows concluding that an

exhumation event that started at rates of less than 1 mm a^{-1} during the Miocene (after 6 Ma) persisted into the Pliocene, and accelerated to rates over $\sim 1 \text{ mm a}^{-1}$ at some point that is after 4 Ma, probably between 3-2 Ma, and that it still occurring during the Pleistocene.

4.5.3. Evolution of Exhumation: Comparison with Other Thermochronometers

McInnes et al. (2005) published aHe data for the Rio Blanco and Teniente porphyry systems, and Farías et al. (2008) and Maksaev et al. (2009) have published AFT and ZFT ages for the area (Fig. 4.4). Our dataset complements the interpretation of Fock (2005) and Maksaev et al. (2009), suggesting that the lower exposed levels of the rocks composing the WCP at the latitude of Santiago (e.g. the lower levels of the Farellones Formation near the confluence of Maipo and Colorado rivers) were at some point in the Partial Annealing Zone for fission tracks on or before $\sim 5 \text{ Ma}$, and that our aHe ages in the Colorado River reflect higher exhumation rates after that time.

An alternate view, suggested by Farías et al. (2008) to explain the 2.74 Ma aHe age near the Teniente porphyry (Fig. 4.4), related these ages to heating by magmatic (subvolcanic) events. Farías et al. (2008) extended this reasoning to conclude that AFT ages cannot be related to exhumation in the WCP between the latitudes of Santiago and Rancagua. However, Maksaev et al. (2009), using AFT data, and earlier Cornejo and Mahood (1997), through petrological analysis, showed that the Late Miocene plutons were emplaced at shallow levels in the crust and that they cooled fast. This conclusion has been also reached by Spikings et al. (2008) for the Late Miocene plutons in WCP between $35\text{-}38^\circ \text{ S}$, and is valid even for the hydrothermal systems at the porphyry copper areas, where cooling rates have been proposed as extremely high (McInnes et al., 2005). The AFT ages at most places therefore can be reasonably interpreted as cooling through closure isotherms and hence they validate an interpretational scheme for the aHe ages in WCP involving exhumation, not magmatic cooling (cf. Fock, 2005). Another possible source of non-exhumation heating could be non-exposed unrecognized Pliocene plutons in the study area, but the large influence needed to have an impact in our data is unlikely considering the small size of the rather isolated bodies located mostly outside of WCP, to the east.

In summary, the thermal history of the La Gloria pluton is consistent with exhumation cooling after ~6 Ma, which increased at ~2-3 Ma, and which continues at similar rates in the region of the Colorado canyon. This exhumation event can be observed as far north as the Aconcagua Valley (6.3-6.5 Ma AFT; Farías et al., 2008; 2.4 Ma aHe, McInnes et al., 2005), and as far south as the upper Cachapoal (5.6-3.2 Ma, AFT, Maksaev et al., 2009) and Teno valleys (5.8 Ma ZFT, 2.6 Ma aHe, Spikings et al., 2008). In a NS longitudinal swath (Fig. 4.6) extending in the high relief area from the Aconcagua River valley in the north (~33° S) to the Teno River valley in the south (~35° S), aHe ages at the mean elevation are approximately the same (~2.2-2.6 Ma). We can include also an area of subdued relief, still obvious in the topography, in the Teniente area, that presents an aHe age of 2.74 Ma. The spatial correlation of the former ages with the boundary of WCP and ECP suggests that the exhumation was associated with structures along this boundary. We hypothesize that the western boundary of WCP might have also experienced exhumation at around the same time, based on the Teniente data of McInnes et al. (2005), although more research in western WCP is necessary to test this.

In summary, based on the combined AFT-aHe dataset (Fig. 4.4), we conclude that a period of slow exhumation prevailed after final deposition of the last volcanic sequences of Farellones Formation inside an area roughly defined by the Aconcagua and Cachapoal river valleys (Fig. 4.6A), and by the Coironal-Laguna Negra and San Ramón-Pocuro fault systems (Rauld, 2002; Fock, 2005; Farías et al., 2008). We determined above that rapid exhumation has occurred in the eastern edge of this block. The outstanding question now is whether or not the entire WCP between the Aconcagua and Cachapoal valleys experienced this rapid exhumation, influencing erosion rates and styles.

4.5.4. Overall erosional response to rapid incision and exhumation along WCP boundaries

To analyze whether all sections of WCP evolved following a similar exhumation history than the eastern area, we explore the possible responses of the system during the Quaternary, by analyzing other datasets. Sediment production rates in the Maipo catchment (WCP) during the Pleistocene have been estimated to be ~0.2 mm a⁻¹ (Antinao and Gosse, 2008), which are similar to short term (30 a) sediment transport estimates

(total transport including suspended, dissolved and bedload, 0.25 mm a^{-1} for Maipo River, Antinao et al., submitted), and intermediate timescales (Holocene) cosmogenic basin wide erosion rates of $0.25\text{-}0.5 \text{ mm a}^{-1}$ (Antinao et al., submitted), for small catchments draining to Maipo River.

If we assume that exhumation has remained at $\sim 1 \text{ mm a}^{-1}$ in the eastern side of WCP since the beginning of the Pleistocene, there is an important discrepancy between it and the Pleistocene landslide sediment production rates estimated by Antinao and Gosse (2008) for the entire WCP block or the sediment yield in western WCP during the Holocene (Antinao et al., submitted). Exhumation rates determined here show an increase during the Late Pliocene, similar to the one determined by McInnes et al. (2005) for the Río Blanco and Teniente systems. Assuming that in the boundary WCP-ECP exhumation has been caused by removal of rock by erosion in response to tectonic uplift, the evolution of the difference between exhumation and erosion estimates along the Pliocene-Pleistocene give us an important indication regarding estimation of the response time for equilibration of erosion with tectonic uplift (cf. Kooi and Beaumont, 1996; Hooke, 2003). Although there is empirical evidence for an increase in erosion rates with time during Pliocene to Pleistocene, a more precise temporal evolution characterization is warranted. Estimation of the response time from numerical and analytical models (Kooi and Beaumont, 1996; Hooke, 2003) applied to transient conditions like those present in the SCA can therefore be compared with datasets from studies like the one depicted here and their comparison will improve the modeling schemes.

The significant difference observed suggests that the response of surface processes in the whole WCP area to the Late Pliocene exhumation acceleration at its boundaries still might continue in the future. As sediment is not contained inside WCP, and assuming that there is no flux towards the Atlantic basins from the Olivares area during the Pleistocene, incision in WCP should have followed a base level fall developed at least on the western side of WCP (Figs. 4.6, 4.7). Simultaneous uplift of the whole block is supported by the lack of regional tilting of the Farellones sequences (Thiele, 1980; Fock, 2005).

Although a possible local effect of the movement of the Coironal fault and its southern prolongation might contribute to an apparent increase in exhumation rates

during Late Pliocene, independent constraints on the slip rate of this fault are not available. The evolution of the thermal field in this area is not known and hence it is very difficult to perform estimates or to obtain a model of the slip to investigate thermal effects on the aHe system, as performed e.g. by Whipp et al. (2007). Additionally, the thermal field might have been perturbed by the activity of low enthalpy springs driving fluids from areas closer to the present day volcanic arc. Until these effects are more constrained by further research, there is no reason to assume a higher geothermal gradient for the area at least until the AFT thermochronometer was closed (Maksaev et al., 2009).

4.5.5. Surface Uplift Linked to Exhumation

We hypothesize that after a slow exhumation of WCP during the Late Miocene (6-5 Ma), which allowed the 10 Ma plutons, like La Gloria and their host rocks (Farellones Formation) to sit undeformed in the PRZ at a geothermal gradient not much larger than $30^{\circ} \text{C km}^{-1}$, the whole area experienced a renewed surface uplift between 2-3 Ma, developing relief mainly due to base level fall along the boundaries between WCP and both the Central Depression and ECP. The latter has remained a constrained boundary, and the relief has been created along a fault zone, where the Olivares river valley, the Yeso valley, and then the Upper Maipo river valley have been carved (Fig. 4.6).

The hypothesized Pliocene evolution is not similar to earlier trends in exhumation, as suggested by the AFT ages along the Colorado and Maipo River valleys (Fock, 2005; Farías et al., 2008; Maksaev et al., 2009). AFT ages are older as they are closer to the Central Depression, and they suggest a depositional pattern, without thermal resetting in the volcanic sequences on top of the pile (Fock, 2005), opposite to the exhumational pattern in the central and eastern side (Maksaev et al., 2009). Exhumation during the Late Miocene might be higher in the eastern side, while almost zero in the Pocuro-San Ramon Fault Zone (PSRFZ) until the Pliocene at least. This exhumation pattern was possibly caused by the initial propagation of erosion after base level fall caused by the inversion (20-16 Ma) of the normal faults bounding the Abanico Basin, recorded in AFT decreasing ages towards the upper reaches of the valleys (Fig. 4.4). One notable exception is the valley of the Maipo and Volcán rivers, where a pattern with younger ages towards the center of WCP suggest i) an old, large valley existed there

during the Miocene, and ii) that exhumation proceeded from both sides towards the center of WCP, implying that drainages partially flowed towards the Atlantic.

A high (2.6-3.5 km) relief fringe that approximately marks the boundary between WCP and ECP, and that can be traced as far north as the Aconcagua river (Fig. 4.6), extending through the above mentioned areas, is interrupted only by a region where Pleistocene large scale landslides appear at the Upper Maipo river valley (Antinao and Gosse, 2008). This high relief fringe reappears south, at the headwaters of the Cachapoal and Pangal rivers (Fig. 4.6). We hypothesize that surface uplift in the area occurred in a block whose eastern boundary corresponds to the mentioned high relief area, and that in the western side was bounded by either NS reverse, west-vergent systems like the PSRFZ (Rauld, 2002) or WNW fault systems (Fig. 4.7). A minimum of 2 km has been suggested by Pons and Vicente (1985) based on reconstructed environmental conditions (altitude) for growth of vegetation fossil remains in the Miocene Farellones sequences of the Aconcagua valley area. Both east and west boundaries are affected by massive landsliding of Late Pliocene-Early Pleistocene age (Godoy et al., 1994; Antinao and Gosse, 2008), in sets that appear successively younger towards the inner part of the uplifted block (Fig. 4.6), towards the headwaters of southwest-flowing rivers. Particularly notable are the NW-WNW set of rockslides that extend from the Central Depression towards the San Francisco – Olivares plateau and the fringe of rockslides widening the Colorado Canyon immediately downstream of La Gloria Pluton (Fig. 4.6C). The area of the Colorado-Maipo junction probably at 1.5 Ma looked similar to the Tres Puntas area today, then later widening via large scale landsliding that started propagating from a NW fringe following the Maipo valley, then propagating upwards. Areas where apparently a higher relief developed at some point, for example the NW trend between Colina and the Mapocho River, or between Codegua and El Teniente (Fig. 4.6), display the above mentioned landslide trends that can be followed towards the highlands. The higher elevation plateaus at La Olla, Los Azules, Extravio (Fig. 4.6), the last one with AFT ages reflecting depositional ages (Fig. 4.4), sit relatively undeformed, and they must have experienced surface uplift with an erosional response that has not yet reached the upper part of the plateaus.

The uplifted blocks must correspond to high mechanical strength packages of cover and basement. The presence inside these blocks of 2-3 km thick packages of the ignimbrite-bearing Farellones Formation might explain the mechanical behavior of the entire block, although also they include large plutons that supply increased strength. This behavior has already been imaged using refraction and gravity data in the area of the Teniente orebody (Godoy et al., 1999), and it is explained by a weaker package of volcanoclastic Abanico Fm. rocks being deformed in front or below a stronger cover of Farellones Fm. ignimbrites. The deformation needed to uplift these blocks was accommodated along the edges through tight folds and thrust faults (Rauld, 2002; Fock, 2005) that must have at least Pliocene slip.

Figure 4.6. (next page). Summary interpretation of thermochronological data shown here and by other studies. A. Shaded relief map of the SCA showing summary aHe ages from this study, McInnes et al. (2005), and Spikings et al. (2008), along hypothesized eastern and western boundaries of a WCP block rapidly uplifted during the Late Pliocene. Note the coincidence of this block with a zone of high relief (in yellow, >2000 m over 5 km window, gray axis marks the boundary ECP-WCP) and high elevation (>3000 m), that are not EW boundaries but rather NW. Note that south of 35°S, areas of similar high relief or elevation only are associated with volcanic centers. The blue line marks the southernmost occurrence of widespread shallow seismicity and large landslides (Cipreses boundary, Antinao and Gosse, 2008). Other NW landslide trends are marked in green lines. B. Change in morphometric parameters (McIntosh, 2005) pointing to a change in morphology at 35° S. C. Detail of the area between 33-34 °S. Note the high relief zone marked with a dashed line at the boundary ECP-WCP, where hypothesized Late Pliocene enhanced exhumation has occurred. Outside this area, relief in excess of 2.6 km mostly occurs at the arc. aHe ages are marked for points along this fringe (marked by a dashed line). On the western WCP, areas northeast of Santiago and at El Teniente might also mark areas of former high relief that at the present display landslides that are younger towards the headwaters of the catchments draining the area towards the Central Depression. These lines mark areas of hypothesized high denudation on the western WCP. The arrows indicate temporal evolution of landslide triggering points as high angle slopes are flattened by mass wasting. D. Sketch showing how base level for WCP streams fell during the hypothesized Late Pliocene to recent activity of the two fault systems bounding WCP (shown with black arrows). Earlier movement of the Coironal fault is shown with a gray arrow.

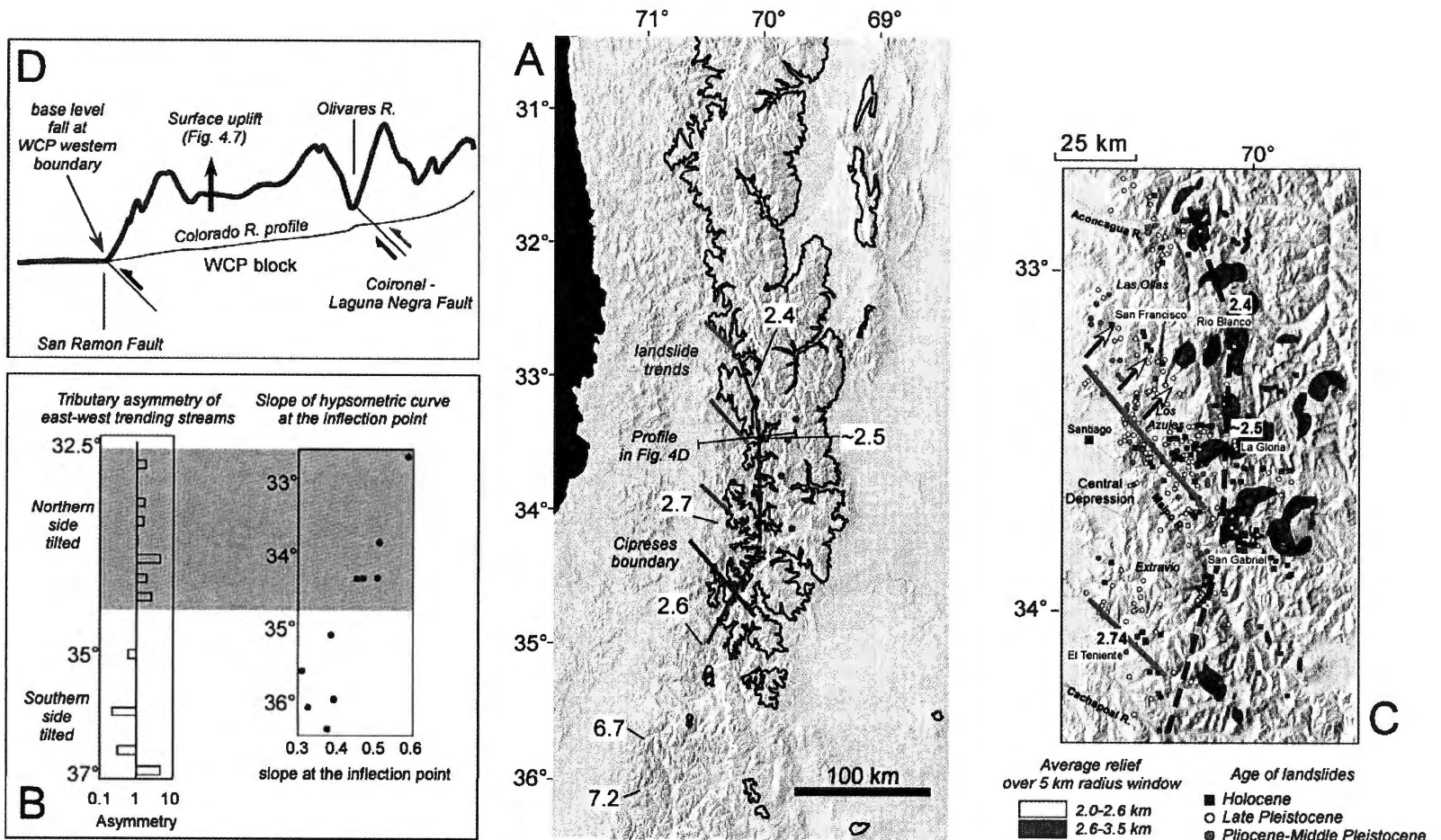


Figure 4.6. (Caption in previous page).

Our interpretation of exhumation for the edges of this area complements the one by Farías et al. (2008) and Makshev et al. (2009) of a high surface uplift at the end of the Miocene for WCP. The surface uplift persisted and it was enhanced during the Late Pliocene into the Pleistocene. The erosional response to the rapid surface uplift at this period was marked by the occurrence of large scale landslides coupled to river incision. However, these processes have been highly localized because their occurrence is closely linked to shallow seismicity (Antinao and Gosse, 2008), and in many places headward incision has not reached the original depositional surfaces of the Farellones Fm, preserving a Late Miocene low relief landscape at elevations of 2500-3000 m (Farías et al., 2008).

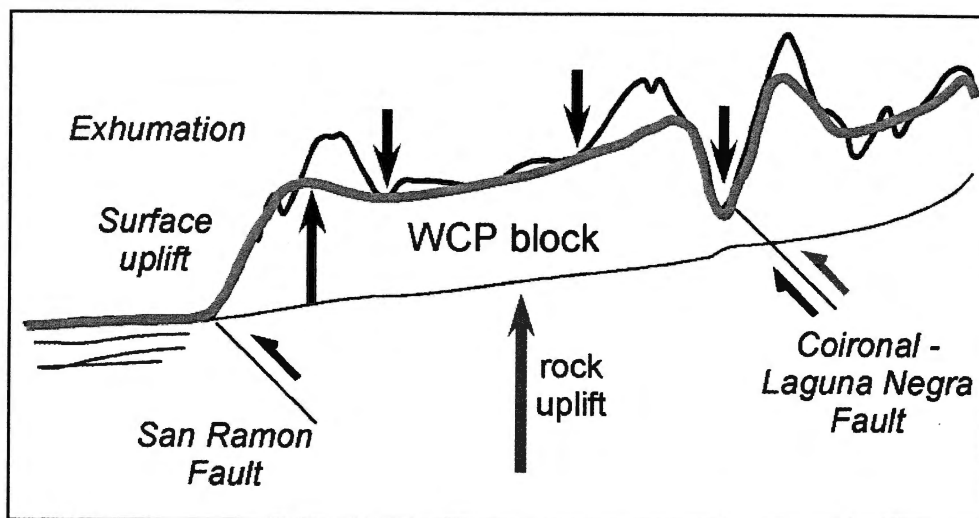


Fig. 4.7. Sketch of relation between hypothesized rock uplift in the WCP block at the latitude of the Colorado River valley (discussed in the text), surface uplift, and recorded exhumation between 2-3 Ma. The exhumation must have concentrated mostly along major valleys and the NS boundaries of the block. Mean elevation should have increased at that point. After that, some original Miocene depositional surfaces are still untouched by erosional processes, and remain as high elevation features on the landscape. In green, mean elevation; in blue, approximate Colorado River long profile.

We predict that young (<3 Ma) aHe cooling ages should appear along major valleys across WCP, if our proposed hypothesis of WCP uplift as a block is true. If the WCP uplifted as a single block, the valleys of the Aconcagua, Mapocho, Maipo-Colorado and Cachapoal rivers should show also a pattern of younger ages towards the headwaters,

as a result of propagation of erosion. Across Cordillera Principal, a nested pattern in cooling ages should appear, with aHe ages getting younger towards the boundary ECP-WCP and the present-day drainage divide (which probably is in a similar place to where it was positioned after 2 Ma). The AFT pattern, although generally should follow the aHe trend, it might show young (~up to 6 Ma) ages towards the center of WCP (e.g. the Maipo-Volcan rivers, Fig. 4.4), delimiting an older drainage divide position.

4.5.6. Climatic or Tectonic Trigger for Enhanced Surface Uplift and Exhumation at the End of the Pliocene

We have determined that exhumation and surface uplift developed during the Pliocene in WCP. However, the trigger for these effects has yet to be determined. A climatic trigger for the Late Pliocene rapid exhumation cannot be discarded, as climatic records point to the beginning of global cooling at this time (e.g. Lunt et al., 2008). The most important glaciation-induced exhumation event that has been determined for the Andes south of 38°S occurred between 7 to 5 Ma (Thompson et al., 2008). As the Pliocene global cooling at 3 Ma was a larger event at a global scale than the onset of the Patagonian ice caps, it must have been recorded also in the previously mentioned record, an effect which is not observed, suggesting that global climate was probably not as important as local conditions for triggering exhumation in the Andes.

Alternatively, tectonically induced rock uplift might be responsible for the enhanced Late Pliocene exhumation. If so, we should observe other common effects around this time. Indeed, several effects have been documented. Eastward migration of the volcanic arc occurred after 4 to 2 Ma (depending on the position along strike, cf. Kay et al., 2005), concomitant with a change in geochemistry of volcanic products around 3 Ma (Lara et al., 2006). In addition, a change at around 2.8 Ma in the stress state as observed by microtectonic analysis (Lavenu and Cembrano, 1999, 2008), from a predominant EW Pliocene compression to a NS compression, consistent with right lateral transpressional systems that dominate the Quaternary in this area of the orogen, north of 37.5° S. At that location, there is a change to a purely transpressional system to the south (e.g. Melnick et al., 2006).

We follow Lavenu and Cembrano (2008) to hypothesize that enhanced exhumation can be explained by the presence of a rigid block beneath WCP, which is

being slowly moved northwards in the forearc, being buttressed against a buoyant recently subducted Juan Fernandez Ridge (JFR). The subducted JFR impedes movement and induces NS to NE shortening, which we hypothesize is starting to be accommodated along WNW and NW structures that are still nucleating into major faults, causing shallow seismicity in the WCP block of the orogen between 32.5° and 35°S. Changes in morphology as recorded by several indices (McIntosh, 2005), and in regional-scale relief and elevation (Fig. 4.6), not straight along a NS direction but following a NW boundary centered around 35° S (Fig. 4.6) all support the hypothesis of a tectonic against a pure climatic trigger for Pliocene exhumation of WCP. Furthermore, recent and ongoing geophysical investigations (e.g., Pardo et al., 2008; Yáñez et al., 2008) support this idea, suggesting that the Late Miocene-Pliocene tectonomagmatic evolution of the area has been controlled by the presence of a deep Paleozoic basement block (Fig. 4.8) in the overriding plate interacting with the subducted plate. Further research is warranted to clarify its structure, extent and impact on tectonic and landscape evolution of the SCA.

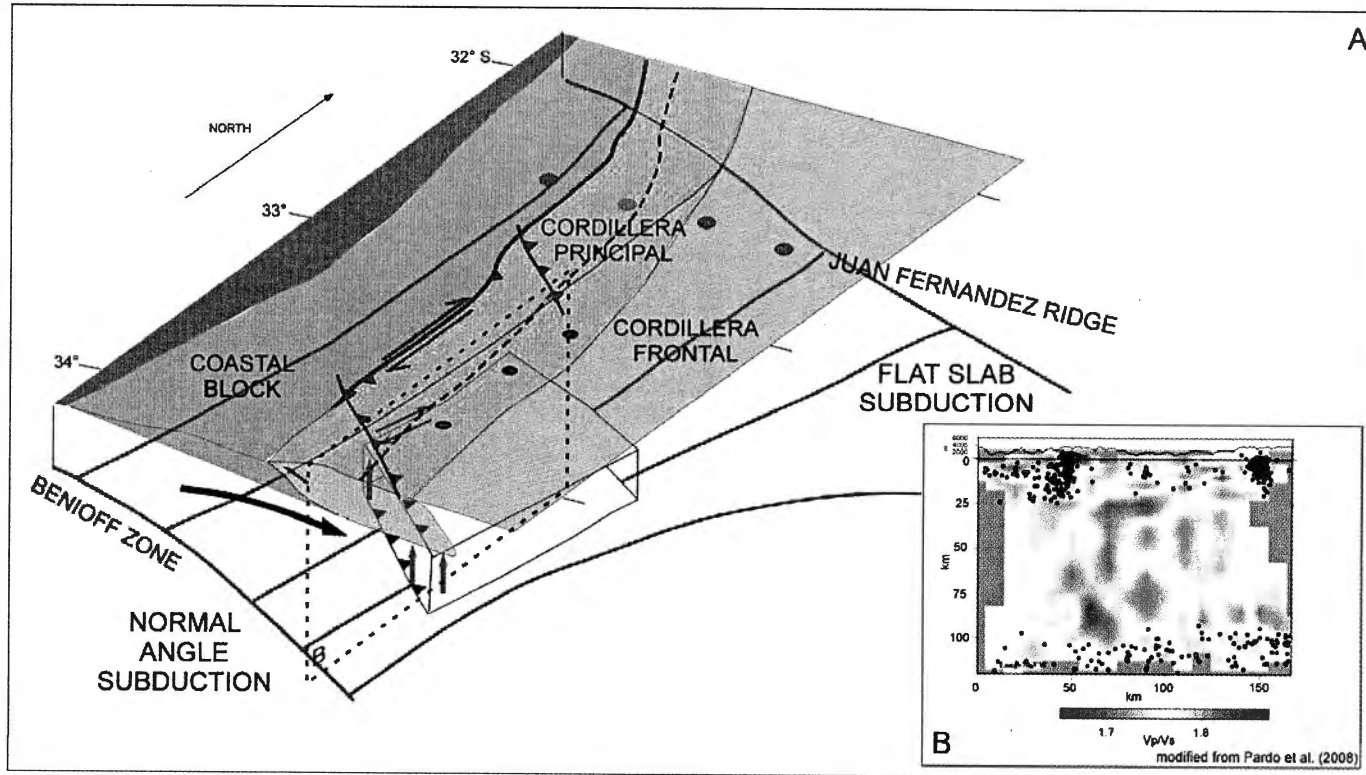


Figure 4.8. Sketch of the hypothesized mid-crustal block affecting tectonic evolution of the area after 2-3 Ma. A. Oblique subduction (black arrow) against the denser crustal block beneath CP induces SW-NE compression and might induce development of strike-slip structures (from stress partitioning) that might be reflected at the surface (red lines indicate active faults; note that SW vergent thrusts are inferred based on landslide trends and relation with shallow seismicity or are based on mapped faults at El Teniente). The block is a rigid structure that is being buttressed against the flat slab portion of the subducted Nazca plate (Lavenu and Cembrano, 2008). The net effect is to generate uplift of the Cordillera Principal rocks directly above the block. B. Shallow seismicity patterns and seismic tomography (Pardo et al., 2008) might reflect the north and south boundaries of the block at intermediate depth. Red circles depict Quaternary volcanoes.

4.6. Conclusions

Apatite He ages in the area of La Gloria Pluton, SCA of central Chile, represent cooling of rocks through the 75 °C isotherm between ~6.0-1.5 Ma. The obtained ages, when plotted against their elevation in a vertical profile, suggest an apparent average exhumation rate of 0.77 mm a⁻¹ for the age range quoted above. Thermal history modeling for one of the lowermost samples in the profile along with other considerations for thermal structure and kinematics of major faults in the region allow determining that the exhumation was not constant over the period, but that two different rates can be differentiated.

A first period between ~6-2.5 Ma has a exhumation rate of ~0.3 mm a⁻¹, which was followed by an acceleration of exhumation after ~2-3 Ma, which is not consistent with estimates of erosion for the same area and time, reflecting transient conditions for orogenic evolution. Although a more accurate thermal state of the crust is needed to state exhumation rates, considering possible recent activity of faults in the area, current estimates indicate that there is still a delay of the erosional signal after enhanced exhumation started.

Late Pliocene exhumation and surface uplift have been most probably caused by local tectonic activity of a deeper crustal block which is interacting with a recently subducted oceanic ridge, generating rock uplift and shortening of the WCP between 32.5° and 35° S. Mechanical properties of the volcanoclastic cover of exhumed block and the seismically induced erosional pattern are affecting the way erosion propagates inside it, indicating that even in this high relief range, a time response of erosion of at least 2 Ma can be estimated after the change in exhumation conditions related to tectonic uplift.

4.7. References

Antinao, J. L. and Gosse, J. C., 2008. Large rockslides in the southern Central Andes of Chile (32-34.5 S): Tectonic control and significance for Quaternary landscape evolution. *Geomorphology*. in press, doi:10.1016/j.geomorph.200.08.008.

- Binnie, S. A., Phillips, W. M., Summerfield, M. A., Fifield, L. K., 2007. Tectonic uplift, threshold hillslopes, and denudation rates in a developing mountain range. *Geology*, 35, 743-746.
- Burbank, D. W., Blythe, A. E., Putkonen, J., Pratt-Sitaula, B., Gabet, E., Oskin, M., Barros, A., Ojha, T. P., 2003. Decoupling of erosion and precipitation in the Himalayas. *Nature*. 426, 652-655.
- Burbank, D. W., Leland, J., Fielding, E., Anderson, R. S., Brozovic, N., Reid, M. R., Duncan, C., 1996. Bedrock incision, rock uplift and threshold hillslopes in the northwestern Himalayas. *Nature*. 379, 505-510.
- Cembrano, J., Zentilli, M., Grist, A., Yáñez, G., 2003. Nuevas edades de trazas de fisión para Chile Central (30-34°S): Implicancias en la exhumación y alzamiento de los Andes desde el Cretácico. Congreso Geológico Chileno, X, Actas.
- Charrier, R., Baeza, O., Elgueta, S., Flynn, J. J., Gans, P., Kay, S. M., Muñoz, N., Wyss, A. R., Zurita, E., 2002. Evidence for Cenozoic extensional basin development and tectonic inversion south of the flat-slab segment, southern Central Andes, Chile (33°-36° S.L.). *Journal of South American Earth Sciences*. 15, 117-139.
- Cornejo, P. C. and Mahood, G. A., 1997. Seeing past the effects of re-equilibration to reconstruct magmatic gradients in plutons; La Gloria Pluton, central Chilean Andes. *Contributions to Mineralogy and Petrology*. 127, 159-175.
- Dadson, S. J., Hovius, N., Chen, H., Dade, W. B., Hsieh, M. L., Willett, S. D., Hu, J. -, Horng, M. -, Chen, M. -, Stark, C. P., Lague, D., Lin, J., 2003. Links between erosion, runoff variability and seismicity in the Taiwan orogen. *Nature*. 426, 648-651.
- Farías, M., Charrier, R., Carretier, S., Martinod, J., Fock, A., Campbell, D., Cáceres, J., Comte, D., 2008. Late Miocene high and rapid surface uplift and its erosional response in the Andes of central Chile (33°-35°S). *Tectonics*. 27.
- Farley, K.A., 2002. (U-Th)/He dating: Techniques, calibrations, and applications, in: Porcelli, P. D., Ballentine, C. J., Wieler, R. (Eds.), *Noble Gas Geochemistry, Reviews in Mineralogy and Geochemistry*. 47, 819-843.
- Farley, K. A., Helium diffusion from apatite: General behavior as illustrated by Durango fluorapatite. *Journal of Geophysical Research*. 105, 2903-2914.

- Farley, K. A., Clark, M. K., 2006. Progress and problems with apatite (U–Th)/He dating. *Geochimica et Cosmochimica Acta*. 70, A166.
- Fock, A., 2005. Cronología y tectónica de exhumación en el Neógeno de los Andes de Chile Central entre los 33° y los 34° S. Universidad de Chile, Departamento de Geología,. M.Sc. Thesis, unpublished, 178 pp.
- Fock, A., Charrier, R., Farías, M., Muñoz, M., 2006. Fallas de vergencia oeste en la Cordillera Principal de Chile Central: Inversión de la cuenca de Abanico (33°-34°S). *Revista De La Asociación Geológica Argentina, Serie D, Publicación Especial*. 10, 48-55.
- Giambiagi, L. B., Ramos, V. A., Godoy, E., Alvarez, P., Orts, S., 2003. Cenozoic deformation and tectonic style of the Andes between 33° and 34° south latitude. *Tectonics*. 22, 1041.
- Godoy, E., Lara, L., Burmester, R., 1994. El 'lahar' cuaternario de Colon-Coya: Una avalancha de detritos pliocena. *Congreso Geológico Chileno, VIII, Actas, Vol. 1*, 305-309.
- Godoy, E., Yáñez, G., Vera, E., 1999. Inversion of an Oligocene volcano-tectonic basin and uplifting of its superimposed Miocene magmatic arc in the Chilean Central Andes: first seismic and gravity evidences. *Tectonophysics*. 306, 217-236.
- Hanza, V., Muñoz, M., 1996. Heat flow map of South America. *Geothermics*. 25, 599-646.
- Hebbeln, D., Lamy, F., Mohtadi, M., Echtler, H., 2007. Tracing the impact of glacial-interglacial climate variability on erosion of the Southern Andes. *Geology*. 35, 131-134.
- House, M. A., Farley, K. A., Stockli, D., 2000. Helium chronometry of apatite and titanite using Nd-YAG laser heating. *Earth and Planetary Science Letters*. 183, 365-368.
- Hovius, N., Stark, C. P., Allen, P. A., 1997. Sediment flux from a mountain belt derived by landslide mapping. *Geology*. 25, 231-234.
- Hovius, N., Stark, C. P., Hao-Tsu, C., Jiun-Chuan, L., 2000. Supply and Removal of Sediment in a Landslide-Dominated Mountain Belt: Central Range, Taiwan. *Journal of Geology*. 108, 73-89.

- Kay, S. M., Godoy, E., Kurtz, A., 2005. Episodic arc migration, crustal thickening, subduction erosion, and magmatism in the south-central Andes. *Geological Society of America Bulletin*. 117, 67-88.
- Ketcham, R., 2005. Forward and Inverse modeling of low-temperature thermochronometry data, in: Reiners, P. W., Ehlers, T. A. (Eds.), *Noble Gas Geochemistry, Reviews in Mineralogy and Geochemistry*, 58, 275-314.
- Lara, L., Lavenu, A., Stern, C., 2006. Plio-Pleistocene eastward migration of the arc front in Southern Andes (33-35° S): Tectonic regimes and volcanism south of the Pampean flat-slab segment. *Geological Society of America Specialty Meetings*, 2, paper 3-33.
- Lavenu, A. and Cembrano, J., 1999. Compressional and transpressional stress pattern for Pliocene and Quaternary brittle deformation in fore-arc and intra-arc zones (Andes of Central and Southern Chile). *Journal of Structural Geology*. 21, 1669-1691.
- Lavenu, A. and Cembrano, J., 2008. Deformación compresiva cuaternaria en la Cordillera Principal de Chile central (Cajón del Maipo, este de Santiago). *Revista Geológica De Chile*. 35, 233-252.
- Lunt, D. J., Foster, G. L., Haywood, A. M., Stone, E. J., 2008. Late Pliocene Greenland glaciation controlled by a decline in atmospheric CO₂ levels. *Nature* 454, 1102-1105.
- Maksaev, V., Munizaga, F., Zentilli, M., Charrier, R., 2009. Fission track thermochronology of Neogene plutons in the high Andes of central Chile: Implications for the tectonic evolution and porphyry Cu-Mo mineralization. *Revista Geológica de Chile*, in press.
- Maksaev, V., Zentilli, M., Munizaga, F., Charrier, R., 2003. Denudación/alzamiento del Mioceno Superior-Plioceno Inferior en la Cordillera de Chile Central (33-35 S) inferida por dataciones por trazas de fisión en apatito de plutones miocenos. *Congreso Geológico Chileno, X, Actas*.
- McInnes, B.I.A., Evans, N.J., Fu, F.Q., Garwin, S., Belousova, E., Griffin, W.L., Bertens, A., Sukarna, D., Permanadewi, S., Andrew, R.L., Deckart, K., 2005. Thermal history analysis of selected Chilean, Indonesian, and Iranian porphyry Cu-Mo-Au deposits, in: *Anonymous Super Porphyry Copper & Gold Deposits: A Global Perspective*. PGC Publishing, Adelaide, Australia, pp. 27-42.

- McIntosh, J., 2004. Analysis of range-scale topographic changes from digital topography in the southern-central Andes (latitudes 32° to 39°S). B. Sc. Thesis, Dalhousie University, Earth Sciences Department, Halifax, 121 pp.
- Melnick, D., Folguera, A., Ramos, V. A., 2006. Structural control on arc volcanism: The Caviahue–Copahue complex, Central to Patagonian Andes transition (38°S). *Journal of South American Earth Sciences*. 22, 66-88.
- Ramos, V. A., Godoy, E., Lo Forte, G. L., Aguirre-Urreta, M. B., 1991. La franja plegada y corrida del norte del Río Colorado, Región metropolitana, Chile central. *Congreso Geológico Chileno V, Actas, Vol. 1(6)*, 323-327.
- Rauld, R. A., 2002. Analisis morfoestructural del frente cordillerano de Santiago Oriente, entre el rio Mapocho y la Quebrada Macul. Universidad de Chile, Departamento de Geología,. M.Sc. Thesis, unpublished, 57 pp.
- Reiners, P. W. Brandon, M. T., 2006. Using thermochronology to understand orogenic erosion. *Annual Review of Earth and Planetary Sciences* 34, 419-466.
- Spikings, R., Dungan, M., Foeken, J., Carter, A., Page, L., Stuart, F., 2008. Tectonic response of the central Chilean margin (35-38 degrees S) to the collision and subduction of heterogeneous oceanic crust; a thermochronological study. *Journal of the Geological Society of London* 165, 941-953.
- Spotila, J.A., 2005. Applications of Low-Temperature thermochronometry to quantification of recent exhumation in mountain belts. In: Reiners, P. W., Ehlers, T. A. (Eds.), *Noble Gas Geochemistry, Reviews in Mineralogy and Geochemistry*, 58, 449-466.
- Thiele, R., 1980. Hoja Santiago, Región Metropolitana. 1:250,000 scale sheet, Servicio Nacional de Geología y Minería, Santiago, Geological Maps 10.
- Thomson, S. N., Brandon, M. T., Vásquez, C., Reiners, P. W., Tomkin, J. H., 2008. Thermochronologic evidence for a poleward transition from destructive to constructive glacial control on mountain building: An example from the Patagonian Andes. *In* Garver, J.I., and Montario, M.J. (eds.), *Proceedings from the 11th International Conference on thermochronometry*, Anchorage, Alaska, Sept. 2008, pp. 232-235.

Whipp, D.M., Jr., Ehlers, T.A., Blythe, A.E., Huntington, K.W., Hodges, K.V., Burbank, D., 2007. Plio-Quaternary exhumation history of the central Nepalese Himalaya; 2; Thermokinematic and thermochronometer age prediction model. *Tectonics*. 26, 23.

Yáñez, G., Rivera, O., Comte, D., Pardo, M., Baeza, L., Vera, E., 2008. Damage zone and the occurrence of world-class porphyry copper deposits in the active margin of Chile: Geophysical signatures and tectonomagmatic inferences. 7th International Symposium on Andean Geodynamics (ISAG 2008, Nice), Extended Abstracts, 592-593.

CHAPTER 5 Discussion

5.1. Introduction

The main objectives of this study are: a) to analyze long term landscape evolution of an active non-collisional convergent margin like the southern Central Andes (SCA) of Chile, documenting quantitatively the effect that landslides have on it, and identifying conditions under which this effect is present, and b) to establish a conceptual landscape evolution model for the Quaternary in this region, which takes into account the tectonic and climatic factors that might have influenced this area of the Andes and that should include estimates of sediment production and exhumation at timescales of 10^0 - 10^6 a. In *Chapters 2, 3 and 4*, I discuss these estimates for surface and tectonic processes mainly for western Cordillera Principal (WCP) at different timescales. Useful information was also extracted about the relative activity of different surface processes (e.g. production by landslides and fluvial transport) that affect landscape evolution of the southern Central Andes.

In the present chapter, I summarize the main findings of the different component studies already described. I proceed to discuss them in the context of other previously published and unpublished data, drawing conclusions that are relevant to the hypotheses and objectives stated in *Chapter 1*. The discussion starts with specific ideas regarding evolution of this particular portion of the Andes, continues by introducing a landscape evolution model for the area, and ends with general implications that can be extracted from the study.

The hypotheses stated in *Chapter 1* to be tested can be restated here:

1. Landslides contribute a large proportion of the sediment that is being fed to the stream network in the southern Central Andes over the long term (10^6 a).
2. Fluvial transport outpaces sediment production on hillslopes on long term (10^6 a) timescales along Cordillera Principal, maintaining bedrock reaches and avoiding extensive alluviation inside the range.

5.2. Synthesis of Results

In *Chapter 2*, I present and analyze the distribution and age of large ($>0.1 \text{ km}^2$) Pliocene to recent rockslides (bedrock involved landslides) in Cordillera Principal to determine triggering mechanism and relation to landscape evolution of the area. Key findings are:

- a) The rockslide triggering mechanism is most likely shallow seismicity occurring in association with but not completely related to mapped faults and major NS structures in the area.
- b) A relative chronosequence of rockslide occurrence was calibrated with existing absolute dates and new cosmogenic nuclide exposure ages for selected rockslides. The chronosequence suggests that the record spans the Late Pliocene-Holocene, and that most of the slope failures occurred during Late Pleistocene times. Erosion by streams and debris flows (and minor burial by younger landslides) has led to the removal of a large fraction of the older landslide deposits from the surface inventory.
- c) In the SCA, the distribution of landslide areas follows an inverse power-law relation similar to the one observed by authors elsewhere, which is independent of the triggering mechanism. The observed distribution reflects loss of smaller landslides mainly by erosion. Reconstruction of the smaller components of the population is possible by using the larger elements to define the complete distribution. Rockslide-induced sediment yield was therefore calculated by using the chronosequence to estimate a recurrence time and the reconstructed landslide distributions to obtain volumes of sediment. Throughout the Quaternary, rockslides have delivered sediment to streams at rates equivalent to landscape denudation rates of $0.10 \pm 0.06 \text{ mm a}^{-1}$.
- d) Following another line of reasoning, by assuming that all the landslides have been generated by earthquakes, and taking into consideration volumes derived from shallow earthquakes that have their own frequency-magnitude distribution, already determined for the study area, estimates of landscape denudation are $0.3_{-0.2}^{+0.6} \text{ mm a}^{-1}$.

- e) Based on comparison with published data referring to other surface processes (suspended sediment transport, glacial erosion, fluvial incision) in the area, I conclude that the estimates of sediment transfer and the spatial distribution of rockslides reflect a landscape in which tectonic and geological controls on denudation are more significant than climate.

In *Chapter 3*, I analyze catchment-wide average Late Holocene erosion rate estimates from cosmogenic ^{36}Cl measurements on stream sediment for two small ($\sim 15 \text{ km}^2$) catchments (Potrerillos and Macul creeks) in the central part of the study area (Fig. 5.1). The catchments are representative of lithological, elevation, slope, and relief conditions in WCP; they also display Late Pleistocene to Holocene rockslides that might affect sediment flux. The catchment-wide erosion rates were compared with the sediment production from landslides in the entire WCP between the Choapa and Cachapoal rivers (*Chapter 2*) and with sediment transport in three major rivers in the area (Aconcagua, Maipo, Cachapoal rivers, all with drainage areas $\sim 2,500 \text{ km}^2$, Fig. 5.1.), calculated from discharge and suspended sediment records. In the case of the Maipo River, total sediment transport was modeled for present day and for hypothetical LGM runoff conditions, incorporating a bedload and a dissolved load component. Potrerillos and Macul catchments drain into the Maipo River, therefore the comparison with it is the most relevant. Key findings are:

- f) Middle-Late Holocene-recent erosion rates at Potrerillos and Macul catchments are 0.23 ± 0.03 and $0.48 \pm 0.09 \text{ mm a}^{-1}$, which represent averaging periods of ~ 2.6 and 1.5 ka respectively.
- g) There is a weak but consistent grain size dependence of the TCN inventories in stream sediment, developed in this landslide-affected terrain, which implies that large landslides do affect the TCN signal in the way predicted by some researchers. The results also suggest that there is a dilution of this effect downstream.
- h) Inside a catchment, Late Pleistocene and Holocene landslides do not have an effect on ^{36}Cl derived erosion rates based on comparison of error weighted means for the estimated rates upstream and downstream large landslides. I interpret this as reflecting that landslides act coupling hillslopes to overall long-term stream

sediment flux in areas where the stream sediment flux is not supported by hillslope diffusive-type processes.

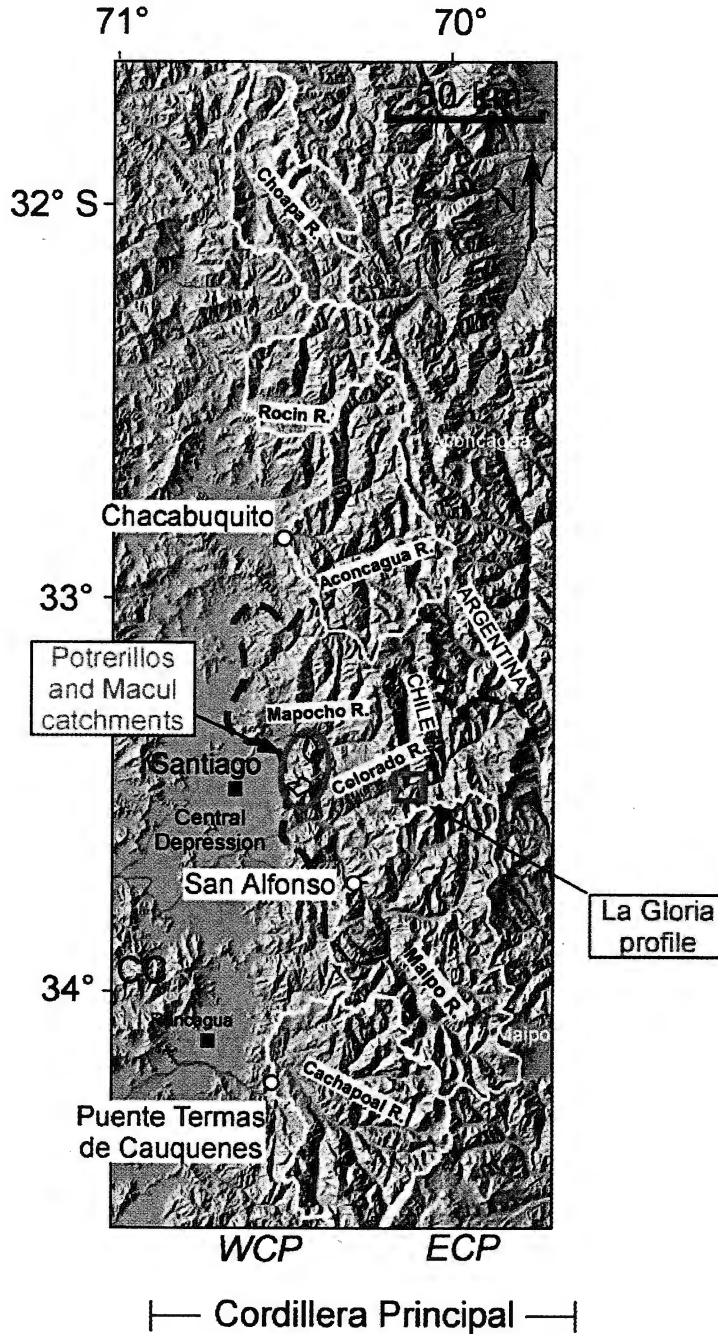


Figure 5.1. The study area, showing the distribution of the different studied catchments or component areas of the study. Main WCP catchments in the study area marked in yellow. Suspended sediment stations are marked in blue. In red, Maipo, Mapocho and Colina area used for derivation of landslides sediment production in the Maipo catchment (Table 5.1, §5.3.1).

- i) When plotted against mean slope upstream of the sampling point, the catchment-wide average ^{36}Cl erosion rates follow a trend observed in previous studies for similar climatic conditions (e.g. Granger et al., 1996; Binnie et al., 2007). The studied catchments appear as transitional between transport-limited and detachment-limited systems (Binnie et al., 2007).
- j) Estimates for sediment transport in the three major rivers analyzed (Maipo, Aconcagua, and Cachapoal) at present-day discharges vary between 0.02 and 0.14 mm a^{-1} just for suspended sediment transport. When bedload and dissolved load are considered, up to 0.25 mm a^{-1} has been obtained as total transport rates for the Maipo river.
- k) Tentative figures for total sediment transport at LGM discharges reach $\sim 1.4 \text{ mm a}^{-1}$ for the Maipo river, larger than the late Holocene ^{36}Cl rates, and are consistent fluvial geomorphology of the Maipo and other rivers throughout the western Cordillera Principal, especially along its eastern boundary, which indicate that removal of sediment may be relevant to avoid extensive alluviation. This result is speculative and it must be used with caution until better estimates for total runoff, and for the response of hillslopes to increased runoff are developed for the area.
- l) The SCA in the Maipo catchment area is better envisaged as a tectonically enabled, climatically driven system that in present-day conditions is transitional or transport-limited.
- m) The presence of large deep-seated landslides dominating denudation in an area of high incision rates is a necessary condition, but not a sufficient one to infer high rock uplift rates as suggested previously for landscapes that appear to be in erosional steady state (constant erosion rates with time), and more information from independent observations is needed.

In *Chapter 4*, the Plio-Pleistocene cooling history of La Gloria pluton in the central part of Cordillera Principal is analyzed using Apatite (U-Th-Sm)/He (aHe) thermochronology. The key findings are:

- n) The pattern of ages and geological constraints allow inferring that cooling can be interpreted as exhumation of rock through the aHe closure temperature of 75°C.

- o) The aHe age vertical profile performed at La Gloria pluton in the Colorado Canyon (Maipo catchment) renders ages between 1.5 and 6.4 Ma. Ages correlate with elevation along most of the vertical profile. On average the exhumation rate was determined to be 0.77 mm a^{-1} , between ~ 1.5 to ~ 5 Ma, with an episode of rapid ($> \sim 1 \text{ mm a}^{-1}$) exhumation that started between ~ 2 -3 Ma.
- p) An AFT age of 5.24 ± 0.82 Ma (Fock, 2005) and the aHe age of 1.57 ± 0.05 Ma obtained in this study for samples taken at the bottom of the Colorado Canyon allowed modeling of their thermal history using HeFTy (Ketcham, 2005). Results of the modeling indicate that after rapid cooling from ca. 9 to 8 Ma, which might be only related to cooling of the pluton after its intrusion, a relatively slow cooling rate proceeded at ~ 7.5 -2.5 Ma, with the rock spending some time in the fission track partial annealing zone. The cooling rate increased rapidly at around 2.5 Ma, indicating fast exhumation of the rocks currently at the bottom of the Colorado River canyon through the aHe closure isotherm. The history is consistent with the interpretation of the age-elevation relationship.
- q) The exhumation event that has been detected probably was coeval with surface uplift, and apparently it is related to a major tectonic event, which is also related to changes in the arc configuration, chemistry of the arc, and stress conditions in the arc and forarc region during the Late Pliocene.
- r) Through comparison with other published thermochronological data, it can be concluded that even though exhumation proceeded at high ($\sim 1 \text{ mm a}^{-1}$) rates in the boundaries of WCP blocks, it did not affect the rocks in the central part of them, suggesting an important lag between incision in the boundaries and erosion in the center of WCP that allowed preservation of Late Miocene surfaces in the center of WCP.

5.3. Pliocene to Quaternary Landscape Evolution of Cordillera Principal Between the Choapa and Cachapoal Rivers

The results obtained in chapters 2-4 can be used to postulate a general landscape evolution model for the area. The discussion starts with a compilation of sediment

production and transport rates at different spatial and time scales, ending with an interpretation of dominant tectonic and surface processes in the area.

5.3.1. Holocene Sediment Production by Landslides in the Maipo Catchment

The Maipo catchment (and inside it the Colorado river catchment, Fig. 5.1) holds a larger number of rockslides that any of the other large catchments involved in the study (Choapa, Rocín, Aconcagua, Cachapoal, Fig. 5.1). To check if this catchment indeed has more participation in the sediment production of WCP, sediment production was recalculated with the same analysis used for the whole area (32-34.5° S) in Chapter 2, but using only Holocene landslides occurring in the Maipo catchment (including those contributing to the Mapocho river, Fig. 5.1).

The Maipo catchment gives rates of about 0.16 mm a^{-1} (Table 5.1), mainly because of the smaller area considered when compared to the whole landslide inventory, whereas the averaged WCP (and partially ECP) gives us a contribution of 0.1 mm a^{-1} . The reconstruction of sediment production from landslide inventories is less feasible in the Aconcagua and Cachapoal rivers. Although they follow in number of landslides inside their catchments, they do not have a number large enough to avoid high uncertainties in modeling their distributions (see §2.9.2), and only a differential rate can be estimated, which is on average for both $\sim 0.04 \text{ mm a}^{-1}$. (Table 5.1, Fig. 5.2).

Table 5.1. Calculation of landscape lowering rates for the Maipo and integrated Cachapoal, Aconcagua, and Choapa catchments.

Region	Total landslide volume [km ³]	Area [km ²]	Landscape lowering rate [mm a ⁻¹]
All study area	2880	14,000	0.10±0.06
Maipo catchment (including Colina and Mapocho, Fig. 5.1)	2390	~7,000	0.16±0.07
Choapa, Aconcagua and Cachapoal	~600	~7,000	0.04±0.03

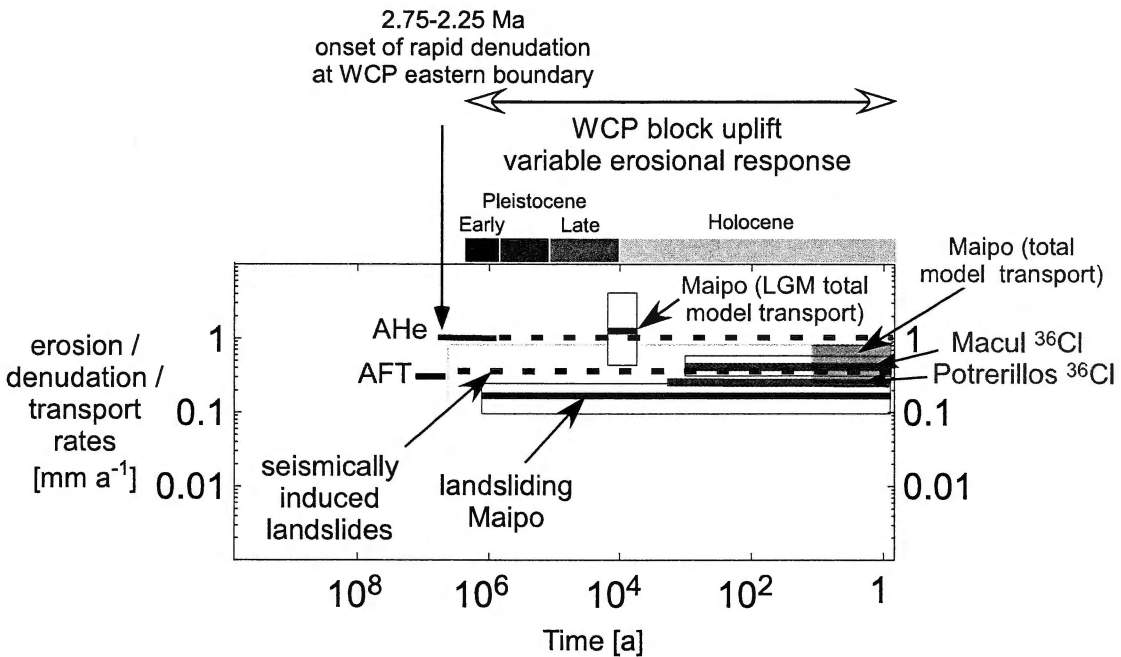


Figure 5.2. Temporal evolution of exhumation, denudation and transport rates at different scales in the Southern Central Andes. The same data displayed in Fig. 3.5 is shown here, but adding the thermochronology data for the last 6 Ma in the middle reach of the Colorado River (La Gloria Pluton), and adding sediment production rates derived from seismically triggered landslides (§2.5.2), and the recalculated figure for Maipo catchment landslides (§5.3.1).

5.3.2. Supply and Transport of Sediment at Different Time and Spatial Scales

After the specific production of sediment by large rockslides in the Maipo catchment has been calculated, sediment production (supply) and transport rates can be compared for the different timescales involved (Table 5.2). At present-day conditions, major rivers in the area transport a total amount of sediment of the same order of magnitude that the total estimated sediment yield from landslides (Fig. 5.2, Table 5.2) during the Holocene, a figure that was extrapolated to the entire Quaternary using assumptions discussed in Chapter 2.

Table 5.2. Comparison of sediment production and transport rates at different timescales in the Chilean southern Central Andes.

Estimate	Rate and uncertainty [mm a ⁻¹] ¹⁰	Timescale [ka]	Involved area [km ²]
Model total load, Maipo	0.20±0.10	0.02	2500
Model mechanical load, Maipo	0.14±0.10	0.02	2500
Model total load, LGM conditions, Maipo	1.4±1.0		2500
Model mechanical load, LGM conditions	1.3±1.0		2500
Cosmogenic inventory, Potrerillos	0.22±0.03	2.6	15
Cosmogenic inventory, Macul	0.48±0.09	1.25	15
(U-Th)/He denudation, La Gloria pluton, eastern boundary of WCP	1.0±0.3	2.5-1.5 10 ³ (3.0-0 10 ³)	?
Landslide inventory, total for western SCA	0.10±0.06	Up to 1.8 10 ³ ?	10,000
Seismically triggered landslide volume, SCA (33-34.5°)	0.3 (+0.2/-0.3)	Up to when seismicity started	4,500
Landslide inventory, Maipo catchment (including Colina, Mapocho catchments)	0.16±0.10	Up to 1.8 10 ³ ?	7,000

¹⁰ All transport and total volume estimations have been converted into mean landscape lowering rates by considering the upstream area for which these estimates are valid.

Considering only the sediment that can be produced from mechanical weathering (suspended sediment and bedload) from river data, landslides supply most of the produced sediment under conditions similar to today. It is apparent also from the sediment transport modeled under LGM conditions that the major rivers are able to transport amounts in excess of what is being produced in the long-term by landsliding only.

Large landslides can remain in the landscape for a long time without being removed by erosion (Korup, 2005a, 2006a; Strasser and Schlunegger, 2005; Ouimet et al., 2007; Korup et al., 2007). However, sediment storage in the study area that can be attributed to landslides older than Late Pleistocene-Holocene times is minor. The few landslides that remain are located mostly in areas of increased slope by presence of faults, without major rivers eroding their deposits. The proposed fluvial transport modeled for LGM conditions of runoff and associated stream discharge (Table 5.3) suggest that Maipo and perhaps all major rivers in WCP have had the capacity to remove most of the sediment that was stored along their valleys previous to Late Pleistocene-Holocene times, breaching any landslide dams along the streams.

Table 5.3. Estimated water and sediment discharge (from mechanically weathered rock) by major rivers at present day conditions and during LGM, compared to hypothetical sediment production by landslides.

Process	Rate [mm a⁻¹]
Landslide-derived sediment production, overall Holocene rate, Maipo catchment	0.16±0.07
Transport of mechanically weathered rock, Maipo River, present day.	0.14±0.10
Transport of mechanically weathered rock, Maipo River, LGM	1.0±1.0

5.3.3 Plio-Pleistocene Exhumation Compared to Erosion Rates

Several erosion and incision estimates have been compiled at different size and timescales for WCP and neighboring areas (Fig. 5.3). There is a consistent pattern of incision and erosion in WCP, distinct from the one at Cordillera Frontal or Coastal Cordillera. Lower erosion rates in areas of WCP south of 35° S are also evident, despite the increase in precipitation rates. The spatial pattern of erosion and incision along the southern Central Andes, indicates that all process rates tend to be higher towards the axis of the orogen, marked by the continental divide in this case (Fig. 5.3).

There is an appreciable difference between exhumation rates of $\sim 1 \text{ mm a}^{-1}$ in the eastern areas of WCP at the Plio- Pleistocene boundary, given by the aHe data in Chapter 4, and lower erosion or transport rates ($0.1\text{-}0.5 \text{ mm a}^{-1}$) during the Pleistocene and later at the Holocene, at different catchment sizes and timescales across WCP (Chapters 2 and 3). The different exhumation levels suggested by thermochronometers in different positions across the landscape (Cembrano et al., 2003; McInnes et al., 2005; Farías et al., 2008; Maksaev et al., 2009) and also the different sediment production and transport rates across WCP, ECP and the Coastal Cordillera (Fig. 5.3) suggest that the orogen is at a transient stage of landscape evolution, and that the drainage network is still adjusting to a base level fall caused by tectonic activity along WCP boundaries that started in the Late Miocene and accelerated during the Pliocene.

At the latitude of Santiago, in the Maipo catchment, an increase in sediment transport and local incision rates is clear from west to east. Holocene sediment yield rates of 0.15 mm a^{-1} in the central part of the Coastal Cordillera (unpublished ^{10}Be erosion rates data from J. Gosse, Fig. 5.3), to $0.25\text{-}0.48 \text{ mm a}^{-1}$ of ^{36}Cl averaged erosion rates in westernmost WCP catchments (Fig. 5.3), similar to the 0.25 mm a^{-1} that the Maipo River is exporting outside CP, and approaching the $0.3\text{-}2.0 \text{ mm a}^{-1}$ of incision that have been determined for some reaches inside Cordillera Principal (e.g. Stern et al., 1984; Farías et al., 2008).

This increase is consistent with the tectonic and landscape evolution model proposed by Farías et al. (2008). However, they envisaged Cordillera Principal and Coastal Cordillera responding to the same order of magnitude of total uplift, without emphasizing on the amount of denudation accomplished at the boundaries of a

differentially uplifted CP block. Lower erosion rates in the Coastal Cordillera even in the high relief slopes of the range northwest of Santiago (unpublished data by Gosse, Fig. 5.3) coupled to the large amount of colluvial and alluvial sediment present in the area west of the PSRFZ, are suggestive of a waning landscape that has not been affected by recent base level changes.

Miocene to Pliocene marine deposits (Encinas et al., 2006a) now in the westernmost Coastal Cordillera have been uplifted from 1-2 km deep (Late Miocene) to shallow (Pliocene) marine environments to ~100-200 m a.s.l. at 33° S today. However, the lack of good chronological control on gravels that might be their continental equivalents on western Coastal Cordillera precludes accurate inferences about the age of eventual rock uplift and concomitant erosion due to base level fall. Spatially variable Pliocene to recent uplift conditions in the Coastal Cordillera compared to Cordillera Principal can be reconciled assuming that some of the differential movement occurred along structures oblique to the arc, not parallel to it (cf. Encinas et al., 2006a; Godoy et al., 1999). This assumption does not void the conclusion that there is a differential uplift of WCP respect to the Coastal Cordillera (CC) since the Late Pliocene, but it allows for a more heterogeneous contrast between both landscape units.

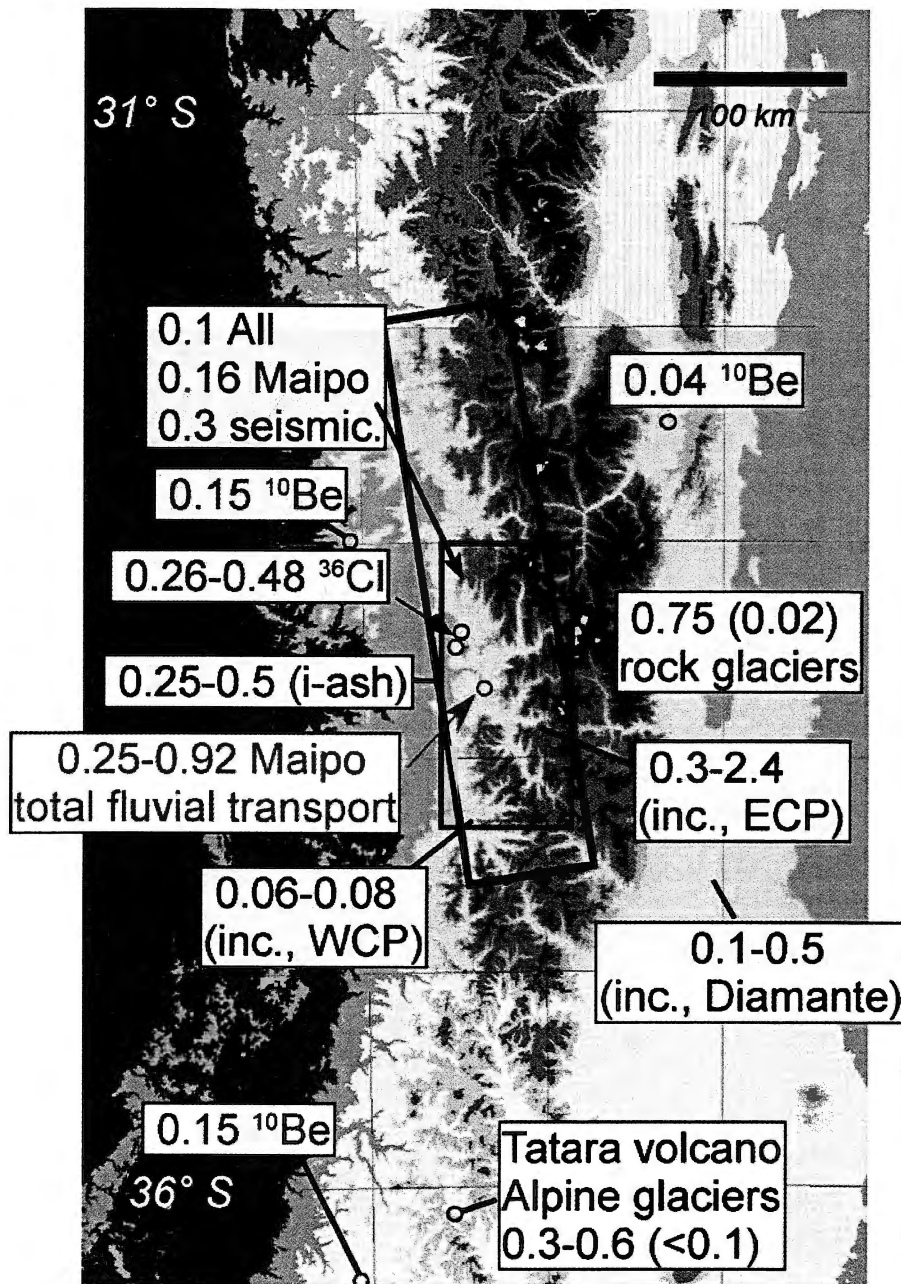


Figure 5.3. Distribution of local fluvial incision and erosion rates in the vicinity of the study area for a time window between 5 Ma and the present. In red: unpublished TCN catchment-wide ^{10}Be data (Gosse). Fluvial incision (inc.) rates are marked in black. Included in the same set are erosion rates by glaciers (Singer et al., 1997) and rock glaciers (Brenning and Trombotto, 2006; specific rates for the areas where the processes have been measured are displayed first; normalized rates, to account for the specific regions where these processes operate, are displayed in parentheses). The black rectangle indicates area covered by the study depicted in Chapter 2. The purple rectangle indicates distribution of 0.45 Ma ash level (Stern et al., 1984), with estimated incision rates. In light blue, fluvial transport rates. In blue, ^{36}Cl sediment yield rates.

5.3.4 Differential Block Uplift inside WCP

I propose that not only WCP has uplifted differentially from CC since the Late Pliocene (~3 Ma), but also different blocks inside WCP might have been subject to different rates of uplift. The presence of oblique-to-the-orogen erosional boundaries is marked by linear groups of landslides (Fig. 4.6). I hypothesize these erosional remains mark zones of block boundaries that have been the locus of active subsurface deformation in the recent past. NS to NE shortening (Lavenu and Cembrano, 1999, 2008) is hypothesized to be accommodated along WNW and NW structures that are still nucleating into major faults, an effect which is probably reflected by the occurrence of shallow seismicity in WCP between 32.5° and 35°S.

Coexistence of rugged topography in the areas of high relief inside WCP with areas of subtle topography, low relief, and low slopes, suggest that the relict Late Miocene surfaces are preserved due to heterogeneities in the propagation of erosion through Cordillera Principal. In WCP, where denudation by surface processes has not yet reached the same rate than exhumation captured in the record of major valleys since the Pliocene (Fig. 5.2), transient conditions have developed during the Quaternary, and net surface uplift is probably still occurring.

5.3.5. Controls on Landscape Evolution

5.3.5.1. Inherited Structures in WCP

Rivera and Cembrano (2000), and Rivera and Falcon (2000) have shown that NW trending structures in WCP have influenced the formation of Oligo-Miocene volcanotectonic basins. These inherited structures might correspond to reactivated NNW-NW trending Paleozoic basement structures. In the present study, the pattern of occurrence of large rockslides (e.g. Fig. 4.6) suggests the presence of a common factor that can be related to these structures. I follow Pardo et al. (2008) to hypothesize that a strong structural control over the behavior of entire blocks of WCP is present, controlling their uplift (and partially their associated denudation) at higher rates since at least 3-4 Ma, until the present. The most evident block appears to be located bounded in the south

by the Maipo River valley from San Gabriel to the Central Depression outlet, the Yeso valley-Laguna Negra-Coironal fault system in the east, the Aconcagua River in the north, and the Pocuro-San Ramon Fault zone (PSRFZ) to the west (Fig. 4.6C). This region behaves as a block of contrasting higher mechanical rigidity than the rocks around it. The rocks in the inner part of it have been hardly deformed at all (Fock, 2005), except for the area close to the PSRFZ, where tight folding is present (e.g. Fock, 2005; Fock et al., 2006; Farías et al., 2008; Rauld, 2002; Godoy et al., 1999). AFT ages in units of the central part of this block have hardly entered the PAZ, and AFT ages in rocks of the top of the sequence are in practice depositional ages (Farías et al., 2008).

Other of these hypothesized blocks is located bounded in the north and east by the Maipo River, then in the west by the set of reverse faults that appear near El Teniente (Fig. 1.5, 4.6C), and in the south bounded by the Cachapoal River valley. In the central regions of these blocks, only highly canyonized river systems (like Rocin, Mapocho, Colorado and Codegua rivers) appear incising the landscape. Where the canyons cross intrusive rocks, for example, the landscape displays the highest relief in this zone of the Andes. At the edges of these zones, for example at the Codegua and Colorado rivers, where the canyons cut through fractured volcanic rocks, large landslides dominate the landscape, being driven by shallow seismicity, occurring in a NW trend (Fig. 4.6C). In the case of the Mapocho River, the lack of seismicity apparently plays a major role in keeping the canyon morphology even when the river valley has been incised into volcanoclastic rocks.

Rigid, dense ($\sim 3 \text{ g cm}^{-3}$), impervious, deep (20-25 km) structures that control shallow seismicity patterns have been recently imaged in this area with gravity analysis and seismic tomography (Pardo et al., 2008; Yáñez et al., 2008). The correlation between the effects of these structures both in stress field and surface processes can be seen for example in a 10-20 km deep seismicity trend that can be followed from the southwest of the study area (Codegua) towards the center of it (the Maipo river valley, Fig. 2.7), ending at a boundary that has a surface expression in multiple landslides (Fig. 2.7, 4.6). The area to the north of this trend of landslides correspond with the above mentioned Maipo-Aconcagua block, which hosts most of major Quaternary and present-day glaciers

in the region, in a highly canyonized landscape, different from the landscape to the southwest.

It has been hypothesized that these pre-Cenozoic blocks in the subsurface (20-30 km deep, Yáñez et al., 2008) might affect the lithological distribution of the Miocene units hence affecting surface processes via the control on lithology dependent hillslope processes, like large landslides. Despite this, a spatial covariance is observed between these hypothesized deep structures and: a) the distribution of Quaternary landslides; b) the shallow seismicity distribution; c) the post-3 Ma high exhumation rates at points along the eastern boundary of these areas. The canyonized, high relief landscape yields to a landslide-dominated landscape in the areas where shallow seismicity appear concomitant to incision in the weaker levels of the Oligocene-Miocene volcanoclastic rocks. In contrast, where less seismicity coupled with strong 2-3 km of Farellones Formation rocks occur, very few landslides appear, and mean elevation in this area increases (Fig. 4.6C), with reduced relief.

5.3.5.2. The Onset of Shallow Seismicity

I have proposed that shallow seismicity strongly conditions large landslides in the SCA. If large landslides are helping propagation of denudation to the upper reaches of the catchments, then the onset of shallow seismicity critically determines when erosional response might have actually started its present-day development. In the study area, in addition to the state of stress in a compressive setting, that normally would contribute to slope instability (cf. Lavenu and Cembrano, 1999; McKinnon and Garrido, 2003), strength reduction of slopes can be caused by vibration during seismic events (Murphy, 2006; Sepúlveda et al., 2008). The landscape in WCP without the occurrence of seismically-triggered landslides might look similar to areas like La Olla, the upper Mapocho River valley or the Extravío area (Fig. 4.6C), where canyons do exist with vertical walls almost 1 km high in mostly Farellones Fm. rocks, and where large (>500 m) knickpoints in low-order streams deter incision from reaching the upper slopes and further propagating denudation to the higher, low-relief relict Late Miocene surfaces.

There is no direct evidence for the actual onset of shallow seismicity. However, Lavenu and Cembrano (2008) have determined that the last compressional event in Cordillera Principal at the latitude 34° S can be constrained to have happened at some

time after 2.8 Ma. Exhumation at Pluton La Gloria reached a peak after that time (2.25-2.75 Ma). One way to export mass outside the orogen at that time to explain the increased exhumation under no particular increase in sediment transport by any climatic change, is to increase sediment production in the hillslopes. As I am not aware of any climatic change at that particular time in the area that increased sediment production via increase of rates of mechanical or chemical weathering, the onset of shallow seismicity allowing landslide-produced sediment to reach rapidly the streams, might be considered to be a necessary factor to enhance denudational response to a hypothetical increase in rock uplift.

5.3.5.3. Role of Climate Change in the Late Pliocene Tectonic and Landscape Evolution of the Southern Central Andes

The Pliocene has more precipitation and increased temperatures respect to the Quaternary, determined by global records. In addition, permanent El Niño weather has also been determined for the area of the central Pacific during the Late Pliocene, implying stormier conditions. An increased runoff and discharge of rivers might have enhanced exhumation, coupling it better to already existing rock uplift which might have been result of the initial inversion of the Abanico basin during the Miocene. However, both conditions have ended at ~3Ma, and they indicate less favorable conditions for erosion, hence reduced possibilities for exhumation.

Another factor that might be related to climate change is the onset of glaciation. An event of Late Miocene - Early Pliocene glaciation has been inferred using exhumation records in the southern Andes (Thomson et al., 2008); this event has been determined as reflecting exhumation from 5 to 7 Ma (Thomson et al., 2008), a period which is older than the aHe exhumation record determined in this study for the southern Central Andes (Fig. 4.6C). The aHe record of Thomson et al. (2008) does not show any spatial pattern and it happened along a large portion of the Andes at essentially the same time, therefore it is not expected that the southern Central Andes behave differently. The terrestrial records for this portion of the Andes do not show evidence for glacial or glaci-fluvial deposits in the foreland or forearc sequences for the period 5-2 Ma. More detailed studies regarding records of early glaciation are needed before discarding or confirming its relative role as a factor for exhumation in the area, compared to tectonic processes.

5.3.5.4. Role of the Absolute Motion of the South American Plate in the Late Pliocene Tectonic and Landscape Evolution of the Southern Central Andes

Increase in exhumation has been detected at around 2-3 Ma along the eastern area of WCP, and specifically in area of La Gloria pluton. This event might be linked to other tectonic effects occurring approximately at the same time, which have already been described in Chapter 4 (e.g. arc migration to the east, geochemistry changes in arc magmatism, contractional style and direction changes). I hypothesize that they are genetically related to changes in the absolute movement of South America plate.

There is growing evidence supporting the effect that the upper plate has in contractional styles along the Andean continental margin as an example of a subduction zone with a high topography developed (e.g. Hampel and Pfiffner, 2006). The most evident test of a relation between upper plate absolute motion and deformation corresponds to the one derived from kinematic analyses of fault populations in the central Andes, including the study area. Temporal changes in the contraction directions reflect the absolute South American plate motions during the last 20.5 Ma (e.g., Marrett and Strecker, 2000; Lavenu and Cembrano, 1999, 2008) rather than the Nazca-South American relative motion, which has remained relatively constant (e.g. Hindle et al., 2002). From 20.5 to 3.2 Ma, South America moved west-northwestward (Pardo-Casas and Molnar, 1987). At 3.2 Ma, South America changed to the west-southwestward direction still maintained today (Pardo-Casas and Molnar, 1987; DeMets et al., 1990; Norabuena et al., 1998). There is a correlation observed between the evolution of contraction in southern Bolivia and northwestern Argentina, with WNW-ESE shortening which ended during the Pliocene. Since 2-3 Ma, ENE-WSW shortening predominates (Marrett and Strecker, 2000). Similarly, in central Chile, Lavenu and Cembrano have indicated that a change in the main stress direction is observed at ~2.8 Ma, with EW shortening giving place to NS shortening. Currently, NS strike-slip fault mechanisms for shallow earthquakes along the boundary WCP-ECP (Fig. 2.7) seem to indicate also the stress pattern, although there is a complete range of partitioning of the deformation indicated by absolute GPS measurements (Allmendinger et al., 2006).

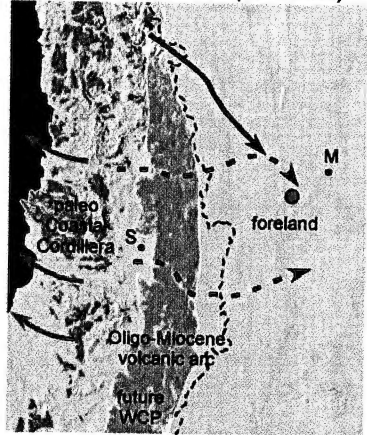
Marrett and Strecker (2000) suggested that there is a causative relation between intraplate contraction and the westward advance of the South American plate. This advance has been faster than the rollback of the Nazca plate. The effects of the faster advance are consistent with the landscape evolution determined for our study area. Although probably locally influenced by the presence of old inherited structures and pieces of accreted basement composing the upper plate along the continental margin (Fig. 4.8), the effects of the push caused by the South Atlantic ridge apparently extend over a large portion of the continental margin and represent a first order control in the tectonic and landscape evolution of it at the timescales analyzed here.

5.3.6. A General Model for Plio–Pleistocene Landscape Evolution of Cordillera Principal between 32° and 35° S

Cordillera Principal in the Late Miocene was probably not a high relief, high elevation area (e.g. Fock, 2005, Farías et al., 2008). Indeed, Ramos et al. (2008) have shown that the Late Miocene foreland basins developed in Cordillera Frontal, Argentina, incorporated Jurassic to Cretaceous zircons that were derived from Coastal Cordillera plutonic units (Fig. 5.4A). The involvement of sediments derived from present-day Coastal Cordillera in the foreland units implies that an uplifted, higher elevation coastal block was present at the time, and that the continental divide was located much closer to the coast than now, at least around the latitude 33° S, leaving all CP at that latitude as a bypass area where rivers mostly flowed eastward towards the foreland (Fig. 5.4A).

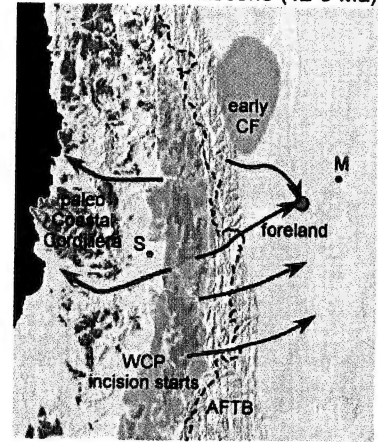
Figure 5.4. (next page). Conceptual sketch of landscape evolution for the Southern Central Andes since the Miocene (see text for explanation). The green circle indicates location of foreland deposits studied by Ramos et al. (2008). Purple circles indicate volcanic centers in panels D and E. Black arrows indicate drainage flow towards the Atlantic. Blue arrows indicate flow towards the Pacific. Numbers in panels C and D indicate time (Ma) for uplift and exhumation of Cordillera Frontal and Precordillera, respectively.

A. Middle Miocene (16-12 Ma)



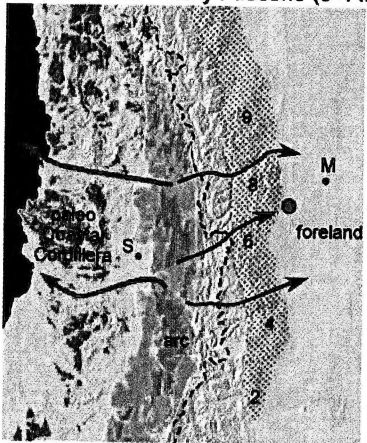
Abanico inversion starts
 Farellones Fm. is deposited in
 compressive setting
 thickened crust
 early stages of the AFTB (not shown)

B. Middle - Late Miocene (12-9 Ma)



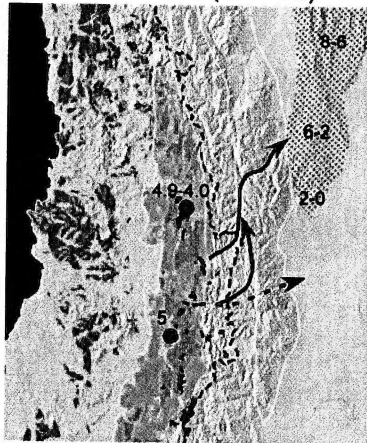
inversion slowed
 AFTB and northern CF exhumation
 arc and divide in WCP
 incision starts in WCP
 along with exhumation of
 Oligo-Miocene sequences

C. Late Miocene - Early Pliocene (9-4 Ma)



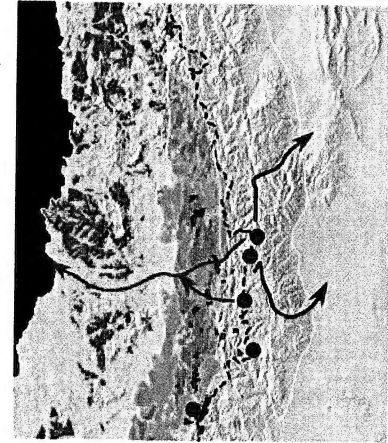
arc has reduced activity
 incision towards both Atlantic and Pacific
 out-of-sequence thrusts
 Teniente Volcanics 9-7 Ma

D. Pliocene (4-2.5 Ma)



10 Ma plutons unroofed at ~3 Ma
 slow exhumation 0.3-0.45 mm a⁻¹
 CF blocks streams; some preserved as antecedent,
 some streams turn north, others to the Pacific

E. Late Pliocene-Pleistocene (2.5-0 Ma)



reactivation of W-vergent faults
 causes base level fall in WCP
 rapid exhumation in WCP,
 2.5 km exposed in 2 Ma,
 ~1 mm a⁻¹
 onset of shallow seismicity?
 change in stress (EW to NS)
 arc shifted/ changed geochemistry
 landslides in NW trends

Figure 5.4. (Caption in previous page).

CP was not a lowlands area either, because the Early to Middle Miocene volcanic rocks of CP were never buried by Late Miocene sediments, from field and thermochronology data (e.g., Godoy et al., 1999; Charrier et al., 2002, 2005, 2007; Giambiagi et al., 2003a) and at some point in the Middle to Late Miocene (~16 Ma), the entire WCP block started to uplift by inverting the normal faults that formed once the original boundaries of the Oligocene-Miocene volcanotectonic basins (Godoy et al., 1999; Charrier et al., 2002). Probably at that point, drainage coming from CC stopped flowing towards the east (Fig. 5.4B), and since then, CC drained completely towards the Pacific. The abandoned valleys coming from the Coastal Cordillera now were occupied by streams that originated in WCP, and that continued partially their flow towards the eastern area. Oligocene-Early Miocene AFT ages at the Rocín and Maipo river valleys in western WCP (Fig. 4.5) suggest that large Miocene valleys existed at the time of basin inversion, and that probably some of them remained flowing towards the Atlantic from WCP until at least Middle Miocene (12 Ma). The upper levels of the Early Pliocene foreland units (Fig. 5.4A-C) display progressively larger components of Oligocene-Miocene volcanic and volcanoclastic rocks of the Abanico and Farellones Formations (Giambiagi et al., 2003a; Ramos et al., 2008), as these units started slow exhumation (Fig. 5.4B-C).

Denudation associated with base level fall along the boundaries of WCP and possible surface uplift of this block between 9 and 4 Ma is recorded by thermochronology of plutonic and volcanic sequences (Farías et al., 2008; Maksaev et al., 2009) and by deposition of synorogenic strata in Argentina (Fig. 5.4B-C). However, the eastern boundary of WCP was not deeply exhumed at least until ~3 Ma, when the upper levels of the La Gloria pluton were unroofed by a proto-Olivares river running NS along a major bounding structure, active in the region after 10 Ma (Fig. 5.4D).

Between 2.75-2.25 Ma, rapid denudation developed along the eastern boundary of WCP (Figures 5.4D-E). This episode of rapid denudation is associated with rapid base level fall for the rivers in WCP, driving incision and drainage reorganization towards the Pacific (Figs. 4.6, 4.7). The episode is a major tectonic event that might be also associated with movement of the volcanic arc to the present-day position (Lara et al., 2006), and continuing reorganization of continental scale drainage, as hypothesized

above. Architecture of valleys in ECP between 33°-34° S still reflects partially flow towards the east (especially junction angles of river valleys), although at present day most flow is towards the west. This observation might reflect rapid propagation of incision through headwaters retreat, along with capture of drainages going to the Atlantic. Specific examples of remains of this progression of captured Atlantic drainages can be seen in the upper Choapa, and the upper Yeso and Maipo river valleys. Since 2.75-2.25 Ma, shallow seismicity has allowed enhanced sediment production in the hillslopes of WCP, which removes mass from it towards the Central Depression. Steep topography and shallow seismicity generates large bedrock-involved landslides, which stay in the landscape until removed by the action of increased discharge during glacial stages. A model of landscape evolution can be suggested for the Quaternary in the area (Figure 5.4E), in which sediment is fed to the system via seismically triggered landslides, and it is routed efficiently at glacial stages, when enhanced precipitation acts to remove the sediment from WCP. The estimates for increase in discharge are tentative, driven by the analysis mentioned in Heusser (1989, 1990) using palinological data for central Chile. Hebbeln et al. (2007) has suggested that the amount of precipitation change during full glacial stages might reach a 5-fold increase. This would not only drain but completely empty most of the 10^4 - 10^5 a accumulation as suggested by the Holocene rates (Chapter 2). It is interesting to note also that the predicted change is most noticeable north of 35° S (figure 2c in Hebbeln et al., 2007), but this is only due to the assumed 5 degrees north of translation of the frontal precipitation, an amount that might be excessive (cf. Heusser, 1989). During interglacial stages, runoff apparently does not remove efficiently sediment from the hillslopes and valleys areas, and there is an accumulation of sediment which is partially removed by debris flows to the lowlands (e.g. Naranjo and Varela, 1996). This effect implies that there is still a lack of equilibrium in denudation on shorter versus intermediate timescales in WCP, but that reaches long-term erosional equilibrium at 100 ka timescales. From the previous observations it is possible to infer that neither topographic nor erosional steady state have been reached yet in the SCA after the last (apparently dominant) tectonic forcing at ~3 Ma.

5.5 General Implications of the Study

This thesis presents for the first time a quantitative comparison of the role of landslides in landscape evolution of an active subduction margin. The following paragraphs discuss broad implications that the results portrayed in this thesis have for landscape evolution and geomorphic analysis.

5.5.1. Power Law Relations for Landslide Inventories

The results of this study confirm that the general power-law distribution observed for landslide sizes in small area ($< 10^5 \text{ m}^2$) landslide inventories (Malamud et al., 2004a,b; Turcotte et al., 2006) is also valid for landslides larger than 10^5 m^2 , and that is even valid for sizes up to 10^2 km^2 . Although the distribution observed in the historical inventory analyzed in Chapter 2 can be explained by a simple power law or a Pareto distribution (e.g. Stark and Hovius, 2001; Malamud et al., 2004a), the slope can fit very well into the general gamma distribution proposed by Malamud et al. (2004a).

5.5.2. Landslides in Landscape Evolution

Equivalence of fluvial transport rates and landslide sediment generation rates on the long term indicate that landslides are able to generate most of the sediment exported from certain areas of an active orogen, as predicted by Burbank et al. (1996) when bedrock uplift rates reach a threshold. However, they apparently dominate sediment production at net flux rates of $0.1\text{-}0.5 \text{ mm a}^{-1}$, lower than the $>0.5 \text{ mm a}^{-1}$ suggested by Burbank et al. (1996), and similar to the range ($0.1\text{-}1.0 \text{ mm a}^{-1}$) of rates that Lavé and Burbank (2004) mentioned as rates whose erosional response is dominated by mixed supply due to shallow mass wasting and slow colluvial processes, in a similar climate.

Two caveats must be stated in relation to this conclusion. First, the southern Central Andes, and particularly WCP, are a transient orogen, probably still in its waxing stage, where there is a clear disequilibrium between tectonic and surface processes. The hypothesized surface uplift needs to be confirmed and supported by more independent data to derive rock uplift rates. This situation is different from what has been hypothesized for the NW Himalayas by Burbank et al. (1996) and for the Transverse Ranges by Lavé and Burbank (2004). Indications of a lack of steady state come from the

convex hillslopes that appear inside WCP, for example, or from the dependence of erosion rates with slope and relief detected in the ^{36}Cl study. Second, an issue that might be relevant for orogen evolution numerical modeling, it is that landslide participation in mass transfer is strongly determined by the genesis of the mass wasting; in this case the presence of shallow seismicity over homogeneous lithologies. I hypothesize that in absence of seismicity, a low relief, high elevation Cordillera Principal will be the most prominent feature in the region. These constraints preclude the generalization of the rates obtained in this study to threshold values to be used in landscape evolution models, and they also impose a strong caution against the use of extrapolated rates for modeling areas without specific restrictions regarding the mode of occurrence of surface processes.

5.5.3 Methodological Implications for Cosmogenic Basin-Wide Erosion Rates

In Chapter 3, cosmogenic ^{36}Cl inventories in stream sediment were used to estimate basin-wide average erosion rates, using the spallogenically produced ^{36}Cl . Several methodological implications can be extracted from this experiment.

The methodology proposed here can be easily adapted to the study of depth profiles to study erosion rates at periods not ending at present-day conditions, because it is based on the accumulation of a spallogenic isotope, similar to the well known ^{10}Be depth profile methodology (Bierman and Nichols, 2004; Braucher et al., 2009). The removal of the thermal neutron capture component is even more relevant in the analysis of depth profiles in depositional terraces, because it relaxes the need for estimation of water content in the vadose zone, especially in shallow (1-10 m) water table conditions which are normally found in alluvial reaches. The presence of water even in amounts of 2% weight might imply large uncertainties in the final determination of cosmogenic chlorine production rate determination and final concentration estimates, and normally it carries a non-tractable temporal evolution which might complicate or void most conclusions derived from the analysis of affected samples (e.g. Frankel et al., 2007).

The presence of large landslides does not affect cosmogenically measured rates. Although in general it can be stated that in a tectonically active area, landslides that are older than the period of averaging of the cosmogenic signal should not affect the

estimates of erosion rates, the results of this study allow reaching even more robust conclusions. In this case, the relaxation time depends on the style of denudation inside the catchments. If landslides dominate denudation compared to other slower processes (e.g. diffusional processes), the relaxation time will be very short compared to the case where landslides are not predominant part of the overall denudation signal.

The method proved to be robust enough to be applied even in small catchments under the presence of landslides, a result that confirms and expands the prediction of Niemi et al. (2005), and that gives access to study tectonically active regions with high erosion rates and recurrent landslides, with a large flexibility in the type of lithologies under analysis.

5.6. Further Questions to Be Addressed

Sediment production and transport rates for present day conditions in the Cordillera Principal portion of the Maipo catchment were estimated. It was inferred that large landslides might contribute a high proportion (~20->50% depending on bedload estimates). However, a large uncertainty is still apparent from the calculations, and the remaining portion of sediment production is not well defined. A better understanding of the other contributing processes, especially in the higher altitude areas of the catchment, is essential to discriminate from the landslide component. Absolute quantification is required not only at a regional scale, but to help into the analysis of general erosion by mountain glaciers and other hillslope processes in tectonically active regions.

It is evident also from the analysis that a more thorough understanding of the structural geology of the area is warranted. The inferred faults on WNW trends where landslides appear (Figs. 4.6 and 4.8) have been described only in the southernmost areas. More low temperature thermochronology specific and regional studies linked with specific mapping may help to identify structures and determine slip rates in this highly dynamic environment.

The catchment wide ^{36}Cl method was only tested for two catchments inside the study area. The tectonic blocks inferred from this study might have had differential erosional response to tectonic and climatic factors during the Quaternary, and erosion rates could be investigated using cosmogenic studies and through comparison with other

procedures to estimate sediment yield at different timescales. Application of the technique to older deposits (paleo-erosion rates) and in different regions of the landscape would not only be beneficial for Andean studies but to improve the technique itself. There is a critical need for this improvement, as the methodology has a high potential to study regions where lithologies with low content or uneven quartz distribution preclude the use of ^{10}Be as the cosmogenic isotope of choice.

5.7. Conclusions

The Cordillera Principal, in the southern Central Andes of Chile, between 32°-34.5° S, has been investigated in terms of processes and rates shaping Plio-Quaternary landscape evolution, focusing on large landslides. The main conclusions of the research are:

- The orogen is highly segmented, with inherited pre-Cenozoic structures and domains that define not only the distribution of tectonic processes but also denudational styles in response to stress and deformation.
- During the Quaternary, sediment produced by shallow seismicity-induced large landslides, has been exported efficiently from Cordillera Principal towards the Central Depression. A hypothetical increase of discharge at full glacial conditions might have supported efficient sediment transport.
- Exhumation, being a relatively slow steady process since the Late Miocene as product of east-west shortening, accelerated in the Late Pliocene, generated surface uplift of the Western Cordillera Principal block, creating a high elevation area that still persists until today. Over this region, Quaternary sediment production and transport rates appear to be consistently higher than areas in the surrounding Coastal Cordillera, to the west, and areas of Cordillera Principal to the south.
- The difference between erosion and exhumation estimates and the variability of these estimates on 10^6 a timescales imply that the Southern Central Andes are a transient orogen and have not reached a topographic steady state, which is consistent with geologic and geomorphic evidence across the study area.

References

- Abele, G., 1974. Bergsturze in den Alpen, ihre Verbreitung, Morphologie und Folgeerscheinungen. *Wiss. Alpeinvereinshefte* 25, 230 pp.
- Abele, G., 1981. Trockene Massenbewegungen, Schlamstrome und rasche Abflüsse, dominante morphologische Vorgänge in den chilenischen Anden. *Mainzer Geographische Studien* 23, 102 pp.
- Abele, G., 1984. Derrumbes de montaña y morrenas en los Andes chilenos. *Revista de Geografía Norte Grande*, 11, 17-30.
- Ackers, P., White, W. R., 1973. Sediment transport: New approach and analysis. *J. Hydraul. Div., Am. Soc. Civ. Eng.* 99, 2041-2060.
- Adams, J., 1980. Contemporary uplift and erosion of the Southern Alps, New Zealand. *Geological Society of America Bulletin*, 91, 12-14.
- Aguilar, G., Riquelme, R., Flores, P., Lohse, P., 2008. Glacial and paraglacial process in the semiarid of the Central Andes (29°S-30°S): Implication on the climate condition and the glacial denudation during the Late Pleistocene-Holocene; 33rd international geological congress; Abstracts, 1204771.
- Aguirre, L., 1960. *Geología de los Andes de Chile Central, provincia de Aconcagua*. Boletín 9, Instituto Investigaciones Geológicas, 70 pp.
- Ahnert, F., 1970. Functional relationships between denudation, relief, and uplift in large mid-latitude drainage basins. *American Journal of Science* 268, 243-263.
- Ali, K. F., De Boer, D. H., 2007. Spatial patterns and variation of suspended sediment yield in the upper Indus River basin, northern Pakistan. *Journal of Hydrology* 334, 368-387.
- Alvarado, P., Beck, S., Zandt, G., Araujo, M., Triep, E., 2005. Crustal deformation in the south-central Andes backarc terranes as viewed from regional broad-band seismic waveform modeling. *Geophysical Journal International* 163, 580-598.
- Antinao, J. L., Gosse, J.C., 2008. Large rockslides in the southern Central Andes of Chile (32-34.5 S): Tectonic control and significance for Quaternary landscape evolution. *Geomorphology*, *In press*, doi:10.1016/j.geomorph.2008.08.008.

:

- Arcadis, 2008. Estudio de Impacto Ambiental Proyecto Hidroeléctrico Alto Maipo, AES GENER S.A, Chapter 5 (baseline), available online at <https://www.e-seia.cl/archivos/20080528.134802.pdf>.
- Ayala, L., López, A., Bzdigian, A., 1984. Producción de sedimento en cuencas andinas de Chile. In: *Programa Hidrológico Internacional, Jornadas de Hidrología de Nieves y Hielos en América del Sur*, 22 pp.
- Balco, G., Stone, J. O., Lifton, N. A., Dunai, T. J., 2008. A complete and easily accessible means of calculating surface exposure ages or erosion rates from ^{10}Be and ^{26}Al measurements. *Quaternary Geochronology* 3, 174-195.
- Ballantyne, C. K., Stone, J. O., 2004. The Beinn Alligin rock avalanche, NW Scotland: cosmogenic ^{10}Be dating, interpretation and significance. *The Holocene* 14, 448-453.
- Barnard, P. L., Owen, L. A., Sharma, M. C., Finkel, R. C., 2001. Natural and human-induced landsliding in the Garhwal Himalaya of northern India. *Geomorphology* 40, 21-35.
- Barrientos, S., Vera, E., Alvarado, P., Monfret, T., 2004. Crustal seismicity in central Chile. *Journal of South American Earth Sciences* 16, 759-768.
- Beck, S., Barrientos, S., Kausel, E., Reyes, M., 1998. Source characteristics of historic earthquakes along the central Chile subduction zone. *Journal of South American Earth Sciences* 11, 115-129.
- Belmont, P., Pazzaglia, F. J., Gosse, J.C., 2007. Cosmogenic ^{10}Be as a tracer for hillslope and channel sediment dynamics in the Clearwater River, western Washington State. *Earth and Planetary Sciences Letters* 264, 123-135.
- Bierman, P. R., Nichols, K.K., 2004. Rock to sediment, slope to sea with (super ^{10}Be); rates of landscape change. *Annual Review of Earth and Planetary Sciences* 32, 215-255.
- Bierman, P., Steig, E.J., 1996. Estimating rates of denudation using cosmogenic isotope abundances in sediment. *Earth Surface Processes and Landforms* 21, 125-139.
- Binnie, S. A., Phillips, W. M., Summerfield, M. A., Fifield, L. K., 2007. Tectonic uplift, threshold hillslopes, and denudation rates in a developing mountain range. *Geology* 35, 743-746.

- Binnie, S. A., Phillips, W. M., Summerfield, M. A., Fifield, L. K., 2006. Sediment mixing and basin-wide cosmogenic nuclide analysis in rapidly eroding mountainous environments. *Quaternary Geochronology* 1, 4-14.
- Blodgett, T. A., Blizard, C., Isacks, B. L., 1998. Andean Landslide Hazards. In: *Geomorphological Hazards in High Mountain Areas*, J. Kalvoda and C. L. Rosenfeld (eds.), Kluwer Academic Publishers, pp. 211-227.
- Braucher, R., Del Castillo, P., Siame, L., Hidy, A. J., Bourlés, D. L., 2009. Determination of both exposure time and denudation rate from an in situ-produced ^{10}Be depth profile: A mathematical proof of uniqueness. Model sensitivity and applications to natural cases. *Quaternary Geochronology* 4, 56-67.
- Brenning, A., Trombotto, D., 2006. Logistic regression modeling of rock glacier and glacier distribution: Topographic and climatic controls in the semi-arid Andes. *Geomorphology* 81, 141-154.
- Brown, E. T., Stallard, R. F., Larsen, M., Bourles, D. L., Raisbeck, G. M., Yiou, F., 1998. Determination of predevelopment denudation rates of an agricultural watershed (Cayaguas River, Puerto Rico) using in-situ-produced ^{10}Be in river-borne quartz. *Earth and Planetary Science Letters* 160, 723-728.
- Brown, E. T., Stallard, R. F., Larsen, M., Raisbeck, G. M., Yiou, F., 1995. Denudation rates determined from the accumulation of in situ-produced ^{10}Be in the Luquillo Experimental Forest, Puerto Rico. *Earth and Planetary Science Letters* 129, 193-202.
- Brüggen, J., 1950. *Fundamentos de la Geología de Chile*. Instituto Geográfico Militar, 378 pp.
- Bull, W., 1991. *Geomorphic responses to climatic change*. Oxford University Press, 326 pp.
- Burbank, D. W., Blythe, A. E., Putkonen, J., Pratt-Sitaula, B., Gabet, E., Oskin, M., Barros, A., Ojha, T.P., 2003. Decoupling of erosion and precipitation in the Himalayas. *Nature* 426, 652-655.
- Burbank, D. W., Leland, J., Fielding, E., Anderson, R. S., Brozovic, N., Reid, M. R., Duncan, C., 1996. Bedrock incision, rock uplift and threshold hillslopes in the northwestern Himalayas. *Nature* 379, 505-510.

- Cahill, T. A., Isacks, B.L., 1992. Seismicity and shape of the subducted Nazca Plate. *Journal of Geophysical Research* 97, 503-517.
- Campbell, D., 2005. Termocronología del sector comprendido entre los ríos Rocin y Aconcagua: Implicancias en la evolución Meso-Cenozoica de la Zona. M. Sc. Thesis, Departamento de Geología, Universidad de Chile, Santiago, 113 pp.
- Castro, S., Delucchi, H., Gauseide, L., Caviedes J., Velasco, L., 1993. Ocurrencia de aguas subterráneas a gran presión en el Túnel Común Alfalfal: características, solución adoptada e interpretación. *Revista Geológica de Chile* 20, 85-97.
- Caviedes, C., 1972. Geomorfología del Cuaternario del valle de Aconcagua, Chile Central. *Freiburger Geographische Hefte* 11, 153 pp.
- Cembrano, J., Zentilli, M., Grist, A., Yáñez, G., 2003. Nuevas edades de trazas de fisión para Chile Central (30-34°S): Implicancias en la exhumación y alzamiento de los andes desde el Cretácico. *Congreso Geológico Chileno - X*, Concepción, CD.
- Chang, K., Taboada, A., Chan, Y., Dominguez, S., 2006. Post-seismic surface processes in the Jiufengershan landslide area, 1999 Chi-Chi earthquake epicentral zone, Taiwan. *Engineering Geology* 86, 102-117.
- Charrier, R., Baeza, O., Elgueta, S., Flynn, J.J., Gans, P., Kay, S. M., Muñoz, N., Wyss, A. R., Zurita, E., 2002. Evidence for Cenozoic extensional basin development and tectonic inversion south of the flat-slab segment, southern Central Andes, Chile (33°-36° S.L.). *Journal of South American Earth Sciences* 15, 117-139.
- Charrier, R., Bustamante, M., Comte, D., Elgueta, S., Flynn, J.J., Iturra, N., Muñoz, N., Pardo, M., Thiele, R., Wyss, A. R., 2005. The Abanico extensional basin: Regional extension, chronology of tectonic inversion and relation to shallow seismic activity and Andean uplift. *N. Jb. Geol. Palaont. Abh.* 236, 43-77.
- Charrier, R., 1983. *Carta geológica de Chile, Escala 1:250.000, Hoja El Teniente*. Carta geológica de Chile, Universidad de Chile, 155 pp.
- Charrier, R., Munizaga, F., 1979. Edades K-Ar de volcánicas Cenozoicas del sector cordillerano del río Cachapoal, Chile (34° 15' de Latitud Sur). *Revista Geológica de Chile* 7, 41-51.

- Charrier, R., Pinto, L., Rodríguez, M.P., 2007. Tectonostratigraphic evolution of the Andean orogen in Chile. In: *The Geology of Chile*, T. Moreno and W. Gibbons (eds.), Geological Society, pp. 21-114.
- Chen, R., Chang, K., Angelier, J., Chan, Y., Deffontaines, B., Lee, C., Lin, M., 2006. Topographical changes revealed by high-resolution airborne LiDAR data: The 1999 Tsaoling landslide induced by the Chi-Chi earthquake. *Engineering Geology* 88, 160-172.
- Chiu, D., 1991. Geología del relleno Cuaternario de las hoyas de los ríos Yeso, Volcán y Maipo, este último entre las localidades de Guayacán y los Queltehues, Región Metropolitana, Chile. M. Sc. Thesis, Departamento de Geología, Universidad de Chile, Santiago, 111 pp.
- Clapp, E. M., Bierman, P. R., Schick, A. P., Lekach, J., Enzel, Y., Caffee, M., 2000. Sediment yield exceeds sediment production in arid region drainage basins. *Geology* 28, 995-998.
- Clapp, E. M., Bierman, P. R., Caffee, M., 2002. Using ^{10}Be and ^{26}Al to determine sediment generation rates and identify sediment source areas in an arid region drainage basin. *Geomorphology* 45, 89-104.
- Clapp, E. M., Bierman, P. R., Nichols, K. K., Pavich, M., Caffee, M., 2001. Rates of sediment supply to arroyos from upland erosion determined using in situ-produced cosmogenic ^{10}Be and ^{26}Al . *Quaternary Research* 55, 235-245.
- Concha, A., 1999. Study of mountain river fluvial mechanics based on physical modeling of a representative prototype. B. Sc. Thesis, Departamento de Ingeniería Civil, Universidad de Chile, Santiago, 105 pp.
- Cornejo, P. C., Mahood, G.A., 1997. Seeing past the effects of re-equilibration to reconstruct magmatic gradients in plutons; La Gloria Pluton, central Chilean Andes. *Contributions to Mineralogy and Petrology* 127, 159-175.
- Crozier, M., 1986. *Landslides: causes, consequences & environment*. Croom Helm, 252 pp.
- Cruden, D. M., Varnes, D.J., 1996. Landslide types and processes. In: *Special report 247: Landslides: Investigation and Mitigation*, A. K. Turner and R. L. Schuster (eds.), Transportation and Road Research Board, National Academy of Science, pp. 36-75.

- Cruden, D. M., Hu, X. Q., 1993. Exhaustion and steady state models for predicting landslide hazards in the Canadian Rocky Mountains. *Geomorphology* 8, 279-285.
- Cuadra, P., 1986. Geocronología K-Ar del yacimiento El Teniente y áreas adyacentes. *Revista Geológica de Chile* 27, 3-26.
- Dadson, S. J. and coauthors, 2003. Links between erosion, runoff variability and seismicity in the Taiwan orogen. *Nature* 426, 648-651.
- Davis, W. M., 1899. The geographical cycle. *Geography Journal* 14, 481-504.
- DeMets, C., Gordon, R. G., Argus, D. F., Stein, S., 1990. Current plate motions. *Geophysical Journal International* 101, 425-478.
- Densmore, A. L., Anderson, R. S., McAdoo, B. G., Ellis, M.A., 1997. Hillslope evolution by bedrock landslides. *Science* 275, 369-372.
- Desilets, D., Zreda, M., Prabu, T., 2006. Extended scaling factors for in situ cosmogenic nuclides: New measurements at low latitude. *Earth and Planetary Science Letters* 246, 265-276.
- Dodson, M. H., 1973. Closure Temperature in Cooling Geochronological and Petrological Systems. *Contributions to Mineralogy and Petrology* 40, 259-274.
- Dramis, F., Blumetti, A.M., 2005. Some considerations concerning seismic geomorphology and paleoseismology. *Tectonophysics* 408, 177-191.
- Dunai, T. J., Gonzalez Lopez, G. A., Juez-Larre, J., 2005. Oligocene-Miocene age of aridity in the Atacama Desert revealed by exposure dating of erosion-sensitive landforms. *Geology* 33, 321-324.
- Dunai, T., 2001. Influence of secular variation of the magnetic field on production rates of in situ produced cosmogenic nuclides. *Earth and Planetary Science Letters* 193, 197-212.
- Eaton, L. S., Morgan, B. A., Kochel, R. C., Howard, A.D., 2003. Role of debris flows in long-term landscape denudation in the central Appalachians of Virginia. *Geology* 31, 339-342.
- Encinas, A., Le Roux, J.P., Buatois, L. A., Nielsen, S. N., Finger, K. L., Fourtanier, E., Lavenu, A., 2006a. Nuevo esquema estratigráfico para los depósitos marinos mio-pliocenos del área de Navidad (33°00'-34°30'S), Chile central. *Revista Geológica de Chile* 33, 221-246.

- Encinas, A., MaksaeV, V., Pinto, L., Le Roux, J. P., Munizaga, F., Zentilli, M., 2006b. Pliocene lahar deposits in the Coastal Cordillera of central Chile: Implications for uplift, avalanche deposits, and porphyry copper systems in the Main Andean Cordillera. *Journal of South American Earth Sciences* 20, 369-381.
- Erikson, I., Högstedt, J., 2004. Landslide hazard assessment and landslide precipitation relationship in Valparaiso, central Chile. Ph.D. dissertation, Department of Physical Geography, Earth Sciences Centre, Göteborg University., 88 pp.
- Erismann, T. H., Abele, G., 2001. *Dynamics of rockslides and rockfalls*. First ed. Springer, Berlin. 316 pp.
- Espizua, L. E., 1993. Quaternary glaciations in the Rio Mendoza valley, Argentina Andes. *Quaternary Research* 40, 150-162.
- Espizua, L. E., 1999. Chronology of late Pleistocene glacier advances in the Rio Mendoza Valley, Argentina; Glaciers of the Southern Hemisphere. *Global Planetary Change* 22, 193-200.
- Espizúa, L. E., Bengochea, J. D., Aguado, C., 1993. Mapa de riesgo de remoción en masa en el valle del Río Mendoza. *XII Congreso Geológico Argentino y II Congreso de Exploración de Hidrocarburos*, pp. 323-332.
- Evans, J. M., Stone, J., Fifield, L. K., Cresswell, R. G., 1997. Cosmogenic chlorine-36 production in K-feldspar. *Nuclear Instruments and Methods in Physics Research Section B: Beam Interactions with Materials and Atoms* 123, 334-340.
- Farías, M., Charrier, R., Fock, A., Campbell, D., Martinod, J., Comte, D., 2005. Rapid Late Cenozoic surface uplift of the central Chile Andes (33°-35° S). In: *6th International Symposium on Andean Geodynamics (ISAG 2005), Extended Abstracts*, Barcelona, IRD, pp. 261-265.
- Farías, M., Charrier, R., Carretier, S., Martinod, J., Fock, A., Campbell, M., Cáceres, L., Comte, D., 2006. Late Miocene regional surface uplift and slow response of erosion in the Andes of central Chile: Implications for the geodynamics in subduction zones. *EOS Trans. Am. Geophys. Union*, 87, T11A-0411.
- Farías, M., Charrier, R., Carretier, S., Martinod, J., Fock, A., Campbell, D., Cáceres, J., Comte, D., 2008. Late Miocene high and rapid surface uplift and its erosional response in the Andes of central Chile (33°–35°S). *Tectonics* 27

- Farley, K. A., 2000. Helium diffusion from apatite: General behavior as illustrated by Durango fluorapatite. *Journal of Geophysical Research* 105, 2903-2914.
- Farley, K. A., 2002. (U-Th)/He dating: Techniques, calibrations, and applications. In: *Noble Gas Geochemistry, Reviews in Mineralogy and Geochemistry* 47, P. D. Porcelli, C. J. Ballentine and R. Wieler (eds.), pp. 819-843.
- Farley, K. A., Clark, M.K., 2006. Progress and problems with apatite (U-Th)/He dating. *Geochimica et Cosmochimica Acta*, 70, A166.
- Fauque, L. E., Cortes, J. M., Folguera, A., Etcheverria, M., 2000. Avalanchas de roca asociadas a neotectónica en el valle del río Mendoza, al sur de Uspallata. *Revista de la Asociación Geológica Argentina* 55, 419-423.
- Fock, A., 2005. Cronología y tectónica de exhumación en el Neógeno de los Andes de Chile Central entre los 33° y los 34° S. M. Sc. Thesis, Departamento de Geología, Universidad de Chile, Santiago, 178 pp.
- Fock, A., Charrier, R., Farías, M., Muñoz, M., 2006. Fallas de vergencia oeste en la Cordillera Principal de Chile Central: Inversión de la cuenca de Abanico (33°-34°S). *Revista de la Asociación Geológica Argentina, Serie D, Publicación Especial*, 10, 48-55.
- Frankel, K. L., Brantley, K. S., Dolan, J. F., Finkel, R. C., Klinger, R. E., Knott, J. R., Machette, M. N., Owen, L. A., Phillips, F. M., Slate, J. L., 2007. Cosmogenic ¹⁰Be and ³⁶Cl geochronology of offset alluvial fans along the northern Death Valley fault zone; implications for transient strain in the eastern California shear zone. *Journal of Geophysical Research* 112, B06407.
- Galy, A., France-Lanord, C., 2001. Higher erosion rates in the Himalaya: Geochemical constraints on riverine fluxes. *Geology* 29, 23-26.
- Giambiagi, L. B., Ramos, V. A., Godoy, E., Alvarez, P., Orts, S., 2003a. Cenozoic deformation and tectonic style of the Andes between 33° and 34° south latitude. *Tectonics* 22, 1041.
- Giambiagi, L. B., Alvarez, P. P., Godoy, E., Ramos, V.A., 2003b. The control of pre-existing extensional structures on the evolution of the southern sector of the Aconcagua fold and thrust belt, southern Andes. *Tectonophysics* 369, 1-19.

- Gilbert, G. K., 1877. *Geology of the Henry Mountains (Utah): U.S. Geographical and Geological Survey of the Rocky Mountains Region*. U.S. Government Printing Office, 170 pp.
- Godoy, E., Yáñez, G., Vera, E., 1999. Inversion of an Oligocene volcano-tectonic basin and uplifting of its superimposed Miocene magmatic arc in the Chilean Central Andes: first seismic and gravity evidences. *Tectonophysics* 306, 217-236.
- Godoy, E., Lara, L., Burmester, R., 1994a. El 'lahar' cuaternario de Colon-Coya: Una avalancha de detritos pliocena. In: *VII Congreso Geológico Chileno*, pp. 305-309.
- Godoy, E., Lara, L., Ugalde, I., 1994b. Derrumbes de cerro holocenos en los Andes Centrales de Chile. In: *VII Congreso Geológico Chileno*, pp. 310-314.
- Godoy, E., Navarro, M., Rivera, O., 1996. Zonas Triangulares en el borde occidental de la Cordillera Principal (32° 30'-34° 30'), Chile: una solución a la paradoja Abanico-Farellones. In: *XIII Congreso Geológico Argentino y III Congreso de Exploración de Hidrocarburos, Actas*, pp. 373-381.
- Gomez, B., Page, M., Bak, P., Trustrum, N., 2002. Self-organized criticality in layered, lacustrine sediments formed by landsliding. *Geology* 30, 519-522.
- Gosse, J. C., Phillips, F.M., 2001. Terrestrial in situ cosmogenic nuclides; theory and application. *Quaternary Science Reviews* 20, 1475-1560.
- Granger, D. E., Kirchner, J.W., Finkel, R.C., 1996. Spatially Averaged Long-Term Erosion Rates Measured from In Situ-Produced Cosmogenic Nuclides in Alluvial Sediment. *Journal of Geology* 104, 249-257.
- Guthrie, R. H., Evans, S.G., 2004. Analysis of landslide frequencies and characteristics in a natural system, coastal British Columbia. *Earth Surface Processes and Landforms* 29, 1321-1339.
- Hack, J. T., 1960. Interpretation of erosional topography in humid temperate regions. *American Journal of Science*, 258A, 80-97.
- Hampel, A., Pfiffner, A., 2006. Relative importance of trenchward upper plate motion and friction along the plate interface for the topographic evolution of subduction-related mountain belts. In: *Analogue and numerical modelling of crustal-scale processes*. Geological Society Special Publications 253, pp. 105-115.

- Hanza, V., Muñoz, M., 1996. Heat flow map of South America. *Geothermics* 25, 599-646.
- Hauser, A., 1985. Flujos de barro en la zona preandina de la Región Metropolitana : características, causas, efectos, riesgos y medidas preventivas. *Revista Geológica de Chile* 24, 75-92.
- Hauser, A., 2000. *Remociones en masa en Chile*. Servicio Nacional de Geología y Minería, *Boletín*, 59, second edition, 89 pp.
- Hauser, A., 2002. Rock avalanche and resulting debris flow in Estero Parraguirre and Rio Colorado, Region Metropolitana, Chile. In: *Catastrophic landslides; effects, occurrence, and mechanisms*, S. G. Evans and J. V. DeGraff (eds.), Geological Society of America, Reviews in Engineering Geology, Vol. 15, pp. 135-148.
- Hebbeln, D., Lamy, F., Mohtadi, M., Echtler, H., 2007. Tracing the impact of glacial-interglacial climate variability on erosion of the Southern Andes. *Geology* 35, 131-134.
- Hermanns, R. L., Trauth, M. H., Niedermann, S., McWilliams, M., Strecker, M.R., 2000. Tephrochronologic Constraints on Temporal Distribution of Large Landslides in Northwest Argentina. *Journal of Geology* 108, 35-52.
- Hermanns, R. L., Niedermann, S., Villanueva Garcia, A., Schellenberger, A., 2006. Rock avalanching in the NW Argentine Andes as a result of complex interactions of lithologic, structural and topographic boundary conditions, climate change and active tectonics. In: *Landslides from Massive Slope Failures*, S. G. Evans, G. Scarascia-Mugnozza, A. Strom and R. L. Hermanns (eds.), Kluwer, pp. 497-520.
- Hermanns, R. L., Niedermann, S., Villanueva Garcia, A., Sosa Gomez, J., Strecker, M.R., 2001. Neotectonics and catastrophic failure of mountain fronts in the southern intra-Andean Puna Plateau, Argentina. *Geology* 29, 619-623.
- Heusser, C. J., 1989. Southern westerlies during the last glacial maximum. *Quaternary Research* 31, 423-425.
- Heusser, C. J., 1990. Ice age vegetation and climate of subtropical Chile. *Palaeogeography, Palaeoclimatology, Palaeoecology* 80, 107-127.
- Hewitt, K., 1999. Quaternary moraines vs. catastrophic rock avalanches in the Karakoram Himalaya, Northern Pakistan. *Quaternary Research* 51, 220-237.

- Hewitt, K., 2002. Styles of rock avalanche depositional complexes conditioned by very rugged terrain, Karakoram Himalaya, Pakistan. In: *Catastrophic landslides: effects, occurrence, and mechanisms*, S. Evans and J. V. DeGraff (eds.), Geological Society of America, Reviews in Engineering Geology, Vol. 15, pp. 345-377.
- Hewitt, K., 2006. Disturbance regime landscapes: mountain drainage systems interrupted by large rockslides. *Progress in Physical Geography* 30, 365-393.
- Hindle, D., Kley, J., Klosko, E., Stein, S., Dixon, T., Norabuena, E., 2002. Consistency of geologic and geodetic displacements during Andean orogenesis. *Geophysical Research Letters* 29, 4.
- Hooke, R. L., 2003. Time constant for equilibration of erosion with tectonic uplift. *Geology* 31, 621-624.
- House, M. A., Farley, K. A., Stockli, D., 2000. Helium chronometry of apatite and titanite using Nd-YAG laser heating. *Earth and Planetary Sciences Letters* 183, 365-368.
- Hovius, N., 2000. Macroscale process systems of mountain belt erosion. In: *Geomorphology and Global Tectonics*, M. Summerfield (ed.), pp. 78-105.
- Hovius, N., C. P. Stark, and P. A. Allen, 1997. Sediment flux from a mountain belt derived by landslide mapping. *Geology* 25, 231-234.
- Hovius, N., Stark, C. P., Hao-Tsu, C., Jiun-Chuan, L., 2000. Supply and Removal of Sediment in a Landslide-Dominated Mountain Belt: Central Range, Taiwan. *Journal of Geology* 108, 73-89.
- Hungr, O., 2006. Rock avalanche occurrence, process and modeling. In: *Landslides from massive rock slope failure. NATO Science Series. Series IV, Earth and Environmental Sciences* 49, pp. 243-266.
- Huntington, K. W., Blythe, A. E., Hodges, K.V., 2006. Climate change and late Pliocene acceleration of erosion in the Himalaya. *Earth and Planetary Sciences Letters* 252, 107-118.
- Isaaks, E. H., Srivastava, R. M., 1989. *An introduction to applied geostatistics*. Oxford University Press, 561 pp.

- Ivy-Ochs, S., Poschinger, A. V., Synal, H. -, Maisch, M. 2008. Surface exposure dating of the Flims landslide, Graubünden, Switzerland. *Geomorphology*, in press, doi:10.1016/j.geomorph.2007.10.024.
- Jarman, D., 2006. Large rock slope failures in the Highlands of Scotland: Characterisation, causes and spatial distribution. *Engineering Geology* 83, 161-182.
- Jibson, R. W., Harp, E. L., Schulz, W., Keefer, D.K., 2006. Large rock avalanches triggered by the M 7.9 Denali Fault, Alaska, earthquake of 3 November 2002. *Engineering Geology* 83, 144-160.
- Kay, S. M., Godoy, E., Kurtz, A., 2005. Episodic arc migration, crustal thickening, subduction erosion, and magmatism in the south-central Andes. *Geological Society of America Bulletin* 117, 67-88.
- Keaton, J. R., Rinne, R., 2002. Engineering-geology mapping of slopes and landslides. In: *Geoenvironmental mapping; methods, theory and practice*, P. T. Bobrowsky (ed.), Balkema, pp. 230-245.
- Keefer, D. K., 1984. Landslides caused by earthquakes. *Geological Society of America Bulletin* 95, 406-421.
- Keefer, D. K., 1994. The importance of earthquake-induced landslides to long-term slope erosion and slope-failure hazards in seismically active regions. *Geomorphology*. 10, 265-284.
- Ketchum, R., 2005. Forward and Inverse modeling of low-temperature thermochronometry data. In: *Noble Gas Geochemistry, Reviews in Mineralogy and Geochemistry* 58, P. W. Reiners and T. A. Ehlers (eds.), pp. 275-314.
- Kirchner, J. W., Finkel, R. C., Riebe, C. S., Granger, D. E., Clayton, J. L., King, J. G., Megahan, W. F., 2001. Mountain erosion over 10 yr, 10 k.y., and 10 m.y. time scales. *Geology* 29, 591-594.
- Kober, F., Ivy-Ochs, S., Schlunegger, F., Baur, H., Kubik, P. W., Wieler, R., 2007. Denudation rates and a topography-driven rainfall threshold in northern Chile; multiple cosmogenic nuclide data and sediment yield budgets. *Geomorphology* 83, 97-120.
- Korup, O., 2005a. Geomorphic imprint of landslides on alpine river systems, southwest New Zealand. *Earth Surface Processes and Landforms* 30, 783-800.

- Korup, O., 2005b. Large landslides and their effect on sediment flux in South Westland, New Zealand. *Earth Surface Processes and Landforms* 30, 305-323.
- Korup, O., 2006a. Effects of large deep-seated landslides on hillslope morphology, western Southern Alps, New Zealand. *Journal of Geophysical Research* 111, F01018.
- Korup, O., 2006b. Rock-slope failure and the river long profile. *Geology* 34, 45-48.
- Korup, O., Clague, J. J., Hermanns, R.L., Hewitt, K., Strom, A. L., Weidinger, J.T., 2007. Giant landslides, topography, and erosion. *Earth and Planetary Science Letters* 261, 578-589.
- Korup, O., McSaveney, M. J., Davies, T.R.H., 2004. Sediment generation and delivery from large historic landslides in the Southern Alps, New Zealand. *Geomorphology* 61, 189-207.
- Kurtz, A., Kay, S. M., Charrier, R., Farrar, E., 1997. Geochronology of Miocene plutons and Andean uplift history in the El Teniente region, central Chile (34° - 35° S). *Revista Geológica de Chile* 24, 75-90.
- Lal, D., 1991. Cosmic ray labeling of erosion surfaces; in situ nuclide production rates and erosion models. *Earth Planetary Science Letters* 104, 424-439.
- Lamy, F., Hebbeln, D., Wefer, G., 1999. High-resolution marine record of climatic change in mid-latitude Chile during the last 28,000 years based on terrigenous sediment parameters. *Quaternary Research* 51, 83-93.
- Lara, L., Lavenu, A., Stern, C., 2006. Plio-Pleistocene eastward migration of the arc front in Southern Andes (33-35° S): Tectonic regimes and volcanism south of the Pampean flat-slab segment. *Backbone of the Americas*, Mendoza, Geological Society of America - Asociación Geológica Argentina, Paper 3-33.
- Lave, J., Burbank, D., 2004. Denudation processes and rates in the Transverse Ranges, Southern California; erosional response of a transitional landscape to external and anthropogenic forcing. *Journal of Geophysical Research, F. Earth Surface* 109, F01006, doi: 10.1029/2003JF000023, 31 pp.
- Lavenu, A., 2006. Neotectónica de los Andes entre 1°N y 47°S (Ecuador, Bolivia y Chile): una revisión. *Revista de la Asociación Geológica Argentina* 61, 504-524.

- Lavenu, A., Cembrano, J., 1999. Compressional and transpressional stress pattern for Pliocene and Quaternary brittle deformation in fore-arc and intra-arc zones (Andes of Central and Southern Chile). *Journal of Structural Geology* 21, 1669-1691.
- Lavenu, A., Cembrano, J., 2008. Deformación compresiva cuaternaria en la Cordillera Principal de Chile central (Cajón del Maipo, este de Santiago). *Revista Geologica de Chile* 35, 233-252.
- Liu, B., Phillips, F. M., Fabryka-Martin, J. T., Fowler, M. M., Stone, W. D., 1994. Cosmogenic ^{36}Cl accumulation in unstable landforms; 1, Effects of the thermal neutron distribution. *Water Resources Research* 30, 3115-3125.
- Lunt, D. J., Foster, G. L., Haywood, A. M., Stone, E. J., 2008. Late Pliocene Greenland glaciation controlled by a decline in atmospheric CO_2 levels. *Nature* 454, 1102-1105.
- Maksaev, V., Munizaga, F., Zentilli, M., Charrier, R., 2009. Fission track thermochronology of Neogene plutons in the high Andes of central Chile: Implications for the tectonic evolution and porphyry Cu-Mo mineralization. *Revista Geológica de Chile*, in press.
- Maksaev, V., Zentilli, M., Munizaga, F., Charrier, R., 2003. Denudación/alzamiento del Mioceno Superior-Plioceno Inferior en la Cordillera de Chile Central (33-35° S) inferida por dataciones por trazas de fisión en apatito de plutones miocenos. In: *X Congreso Geológico Chileno, Actas*, Concepción, CD.
- Malamud, B., Turcotte, D., Guzzetti, F., Reichenbach, P., 2004. Landslide Inventories and their statistical properties. *Earth Surface Processes and Landform*, 29, 687-711.
- Malamud, B., Turcotte, D., Guzzetti, F., Reichenbach, P., 2004. Landslides, earthquakes, and erosion. *Earth and Planetary Science Letters* 229, 45-59.
- Marangunic, C., Thiele, R., 1971. Procedencia y determinaciones gravimétricas de espesor de la morena de la Laguna Negra, Provincia de Santiago [Origin and gravimetric surveys of the thickness of the moraine of the Laguna Negra, Santiago Province]. *Comunicaciones* 38, 1-25.
- Marrett, R., Strecker, M., 2000. Response of intracontinental deformation in the Central Andes to late Cenozoic reorganization of South American Plate motions. *Tectonics* 19, 452-467.

- Martin, Y., Rood, K., Schwab, J.W., Church, M., 2002. Sediment transfer by shallow landsliding in the Queen Charlotte Islands, British Columbia. *Canadian Journal of Earth Sciences* 39, 189-205.
- Mather, A. E., Griffiths, J. S., Stokes, M., 2003. Anatomy of a 'fossil' landslide from the Pleistocene of SE Spain. *Geomorphology* 50, 135-149.
- Matheron, G., 1962. *Traité de Géostatistique appliquée, Tome I*. Editions Technip, 334 pp.
- Matmon, A., P. R. Bierman, J. Larsen, S. Southworth, M. J. Pavich, R. Finkel, and M. W. Caffee, 2003: Erosion of an ancient mountain range, the Great Smoky Mountains, North Carolina and Tennessee. *American Journal of Science* 303, 817-855.
- Matmon, A., Bierman, P., Larson, J., Southworth, S., Pavich, M., Finkel, R., Caffee, M., 2005. Grain size dependency of ^{10}Be concentrations in alluvial sediments in the Great Smoky Mountains; Abstracts of the 15th annual V. M. Goldschmidt conference. *Geochimica et Cosmochimica Acta* 69, 160.
- McDonald, E.V., McFadden, L.D., Wells, S.G., 2003, Regional response of alluvial fans to the Pleistocene-Holocene climatic transition, Mojave Desert, California. In Enzel, Y., Wells, S.G., and Lancaster, N., eds., *Paleoenvironments and paleohydrology of the Mojave and southern Great Basin Deserts*, Boulder, Colorado, Geological Society of America Special Paper 368, p. 189-205.
- McInnes, B.I.A., Evans, N.J., Fu, F.Q., Garwin, S., Belousova, E., Griffin, W.L., Bertens, A., Sukarna, D., Permanadewi, S., Andrew, R.L., Deckart, K., 2005. Thermal history analysis of selected Chilean, Indonesian, and Iranian porphyry Cu-Mo-Au deposits. In: *Super Porphyry Copper & Gold Deposits: A Global Perspective*, PGC Publishing, pp. 27-42.
- McIntosh, J., 2004. Analysis of range-scale topographic changes from digital topography in the southern-central Andes (latitudes 32° to 39°S). B. Sc. Thesis, Dalhousie University, Earth Sciences Department, Halifax, 121 pp.
- McKinnon, S., Garrido, I., 2003. Stress field analysis at the El Teniente Mine: evidence for N-S compression in the modern Andes. *Journal of Structural Geology* 25, 2125-2139.

- Melnick, D., 2007. Neogene seismotectonics of the south-central Chile margin : subduction-related processes over various temporal and spatial scales. Ph.D. dissertation, Univ., Mathemat.-Naturwiss. Fak., Potsdam,
- Molnar, P., England, P., 1990. Late Cenozoic uplift of mountain ranges and global climate change: chicken or egg? *Nature* 346, 29-34.
- Molnar, P., Anderson, R. S., Anderson, S.P., 2007. Tectonics, fracturing of rock, and erosion. *Journal of Geophysical Research* 112, F03014, doi:10.1029/2005JF000433.
- Montgomery, D. R., 2001. Slope distributions, threshold hillslopes, and steady-state topography. *American Journal of Science* 301, 432-454.
- Montgomery, D. R., Brandon, M.T., 2002. Topographic controls on erosion rates in tectonically active mountain ranges. *Earth and Planetary Science Letters* 201, 481-489.
- Moreiras, S. M., 2006. Chronology of a probable neotectonic Pleistocene rock avalanche, Cordon del Plata (Central Andes), Mendoza, Argentina. *Quaternary International* 148, 138-148.
- Moreno, H., Thiele, R., Varela, J., 1991. Estudio Geológico y de Riesgos Volcánico y de Remoción en Masa del Proyecto Hidroeléctrico Alfalfal II y Las Lajas, CHILGENER S.A., 98 pp.
- Mpodosis, C., Ramos, V.A., 1989. The Andes of Chile and Argentina. In: *Geology of the Andes and its relation to Hydrocarbon and Mineral Resources*, G. E. Ericksen, M. T. Cañas and J. A. Reinemud (eds.), pp. 59-90.
- Murphy, W., 2006. The role of topographic amplification on the initiation of rock slopes failures during earthquakes. In: *Landslides from Massive Rock Slope Failure*, Stephen G. Evans, Gabriele Scarascia-Mugnozza, Alexander Strom and Reginald L. Hermanns (eds.), Springer, pp. 139-154.
- Naranjo, J. A., Varela, J., 1996. *Flujos de detritos y barro que afectaron el sector oriente de Santiago el 3 de Mayo de 1993*. Boletín, 47, Servicio Nacional de Geología y Minería, 42 pp.
- Nichols, K. K., Bierman, P. R., Foniri, W. R., Gillespie, A. R., Caffee, M., Finkel, R., 2006. Dates and rates of arid region geomorphic processes. *GSA Today* 16, 4-11.

- Niemi, N. A., Oskin, M., Burbank, D. W., Heimsath, D. W., Gabet, E. J., 2005. Effects of bedrock landslides on cosmogenically determined erosion rates. *Earth and Planetary Science Letters* 237, 480-498.
- Niño, Y., 2002. Simple model for downstream variation of median sediment size in Chilean rivers. *J. Hydr. Engrg.* 128, 934-941.
- Norabuena, E., Leffler-Griffin, L., Mao, A., Dixon, T., Stein, S., Sacks, I.S., Ocola, L., Ellis, M., 1998. Space geodetic observations of Nazca-South America convergence across the Central Andes. *Science* 279, 358-362.
- Ouimet, W. B., Whipple, K. X., Royden, L. H., Zhiming, Sun, Zhiliang, Chen, 2007. The influence of large landslides on river incision in a transient landscape; eastern margin of the Tibetan Plateau (Sichuan, China). *Geological Society of America Bulletin* 119, 1462-1476.
- Pannatier, Y., 1996. *Variowin: software for spatial data analysis in 2D*. Springer-Verlag, 91 pp.
- Pardo, M., Comte, D., Monfret, T., 2002. Seismotectonic and stress distribution in the central Chile subduction zone. *Journal of South American Earth Sciences* 15, 11-22.
- Pardo, M., Vera, E., Monfret, T., Yáñez, G., 2008. Damage zone and the occurrence of world-class porphyry copper deposits in the active margin of Chile: Geophysical signatures and tectonomagmatic inferences. In: *7th International Symposium on Andean Geodynamics (ISAG 2008), Extended Abstracts*, Nice, IRD, pp. 377-380.
- Pardo-Casas, F., Molnar, P., 1987. Relative motion of the Nazca (Farallon) and South American plates since Late Cretaceous time. *Tectonics* 6, 233-248.
- Pazzaglia, F. J., 2003. Landscape evolution models. In: *Developments in Quaternary Science*, A.R. Gillespie, S.C. Porter, and B.F. Atwater (eds.), Elsevier, pp. 247-274.
- Peizhen, Z., Molnar, P., Downs, W.R., 2001. Increased sedimentation rates and grain sizes 2-4 Myr ago due to the influence of climate change on erosion rates. *Nature* 410, 891-897.
- Penck, W., 1924. *Die Morphologische Analyse (Morphological Analysis of Landforms)*. J. Engelhorn's Nachfolger, 283 pp.

- Philip, H., Ritz, J., 1999. Gigantic paleolandslide associated with active faulting along the Bogd fault (Gobi-Altay, Mongolia). *Geology* 27, 211-214.
- Pratt-Sitaula, B., Garde, M., Burbank, D. W., Oskin, M., Heimsath, A., Gabet, E., 2007. Bedload-to-suspended load ratio and rapid bedrock incision from Himalayan landslide-dam lake record. *Quaternary Research* 68, 111-120.
- Ramos, V. A., Godoy, E., Lo Forte, G.L., Aguirre-Urreta, M.B. 1991. La franja plegada y corrida del norte del río Colorado, Región Metropolitana, Chile central. In: VI Congreso Geológico Chileno, 1991, Volumen 1, *Resúmenes Presentados*, pp. 323-327.
- Ramos, V.A., Cegarra, M., Cristallini, E., 1996. Cenozoic tectonics of the High Andes of west-central Argentina (30-36°S latitude). *Tectonophysics* 259, 185-200.
- Ramos, V., Mahoney, J. B., Kimbrough, D., Grove, M., 2008. Miocene synorogenic deposits: provenance and uplift history based on detrital zircons of the Aconcagua region, Argentina. In: South American Symposium on Isotope Geology, Bariloche, Argentina, *Proceedings*, pp. 48.
- Rauld, R. A., 2002. Análisis morfoestructural del frente cordillerano de Santiago Oriente, entre el río Mapocho y la Quebrada Macul. M. Sc. Thesis, Departamento de Geología, Universidad de Chile, Santiago, 57 pp.
- Reid, L. M., Page, M.J., 2003. Magnitude and frequency of landsliding in a large New Zealand catchment. *Geomorphology* 49, 71-88.
- Reiners, P. W., Brandon, M.T., 2006. Using thermochronology to understand orogenic erosion. *Annual Reviews Earth and Planetary Sciences* 34, 419-466.
- Reinhardt, L. J., Noey, T. B., Barrows, T. T., Dempster, T. J., Bishop, P., Fifield, L. K., 2007. Interpreting erosion rates from cosmogenic radionuclide concentrations measured in rapidly eroding terrain. *Earth Surface Processes and Landforms* 32, 390-406.
- Riquelme, R., Darrozes, J., Maire, E., Hérail, G., Soula, J.C., 2008. Tasas de denudación de largo tiempo en los Andes Centrales, Chile, estimadas a partir de un modelo digital de elevación usando la función 'Top Hat' por cierre y la interpolación ponderada por el inverso de la distancia: implicancias del clima Neógeno del Desierto de Atacama. *Revista Geológica de Chile* 35, 105-121.

- Rivano, S., Sepúlveda, P., 1986. Hoja Illapel (1:250,000 scale map), IV Región de Coquimbo. Servicio Nacional de Geología y Minería, Santiago, Carta geológica de Chile 69.
- Rivano, S., Sepúlveda, P., Boric, R., Espiñeira, P., 1993. Mapa Geológico de la Hoja Quillota-Portillo (1:250,000 scale map), V Región de Valparaíso. Servicio Nacional de Geología y Minería, Santiago, Carta geológica de Chile 73.
- Rivera, O., and J. Cembrano, 2000: Modelo de formación de cuencas volcano-tectónicas en zonas de transferencia oblicuas a la cadena andina: el caso de las cuencas oligo-miocenas de Chile central y su relación con estructuras NWW-NW (33°00'-34°30'S). In: *IX Congreso Geológico Chileno*, Puerto Varas, pp. 631-636.
- Rivera, O., Falcón, F. 2000. Secuencias de relleno de cuencas volcano-tectónicas transversales oligo-miocenas en los alrededores del yacimiento El Teniente (33°45'-34°30'). In: *IX Congreso Geológico Chileno*, Puerto Varas, pp. 819-823.
- Robinson, D., Bevins, R., Aguirre, L., Vergara, M., 2004. A reappraisal of episodic burial metamorphism in the Andes of central Chile. *Contributions to Mineralogy and Petrology* 146, 513-528.
- Rodríguez, C. E., Bommer, J. J., Chandler, R. J., 1999. Earthquake-induced landslides: 1980–1997. *Soil Dynamics and Earthquake Engineering* 18, 325-346.
- Roering, J. J., Kirchner, J. W., Dietrich, W.E., 2005. Characterizing structural and lithologic controls on deep-seated landsliding; implications for topographic relief and landscape evolution in the Oregon Coast Range, USA. *Geological Society of America Bulletin* 117, 654-668.
- Ruz, A., 1999. Grain size distributions in Chilean rivers. M. Sc. Thesis, Departamento de Ingeniería Civil, Universidad de Chile, Santiago, 105 pp.
- Sato, H. P., Hasegawa, H., Fujiwara, S., Tobita, M., Koarai, M., Une, H., Iwahashi, J., 2006. Interpretation of landslide distribution triggered by the 2005 Northern Pakistan earthquake using SPOT 5 imagery. *Landslides*,
- Scheidegger, E., 1973. On the prediction of reach and velocity of catastrophic landslides. *Rock Mechanics* 5, 231-236.

- Schildgen, T. F., Hodges, K. V., Whipple, K. X., Reiners, P.W., Pringle, M.S., 2007. Uplift of the western margin of the Andean Plateau revealed from canyon incision history, southern Peru. *Geology* 35, 523-526.
- Schuster, R. L., Salcedo, D. A., Valenzuela, L., 2002. Overview of catastrophic landslides of South America in the twentieth century. In: *Catastrophic landslides: Effects, occurrence, and mechanisms*, S. G. Evans and J. V. DeGraff (eds.), Geological Society of America, pp. 1-34.
- Sellés, D., Gana, P., 2001. Geología del Area Talagante-San Francisco de Mostazal, Región Metropolitana. Servicio Nacional de Geología y Minería, Santiago. Carta Geológica de Chile, Geología Básica 74, 30 pp.
- Sellés, D., 1999. La Formación Abanico en el Cuadrángulo Santiago (33°15'-33°30'S; 70°30'-70°45'O), Chile Central. Estratigrafía y Geoquímica. M. Sc. Thesis, Departamento de Geología, Universidad de Chile, Santiago, 154 pp.
- Sepúlveda, S. A., Astroza, M., Kausel, E., Campos, J., Casas, E. A., Rebolledo, S., Verdugo, R., 2008. New findings on the 1958 Las Melosas earthquake sequence, central Chile: implications for seismic hazard related to shallow crustal earthquakes in subduction zones. *Journal of Earthquake Engineering* 12, 432-455.
- Sepúlveda, S. A., Rebolledo, S., Vargas, G., 2006. Recent catastrophic debris flows in Chile: Geological hazard, climatic relationships and human response. *Quaternary International*, 158, 83-95.
- SERNAGEOMIN, 2002. Mapa Geológico de Chile (1:1,000,000 scale map), Servicio Nacional de Geología y Minería, Santiago.
- Simonett, D. S., 1967. Landslide distribution and earthquakes in the Bewani and Torricelli Mountains, New Guinea. In: *Landform Studies from Australia and New Guinea*, J. N. Jennings and J. A. Mabbutt (eds.), Cambridge University Press, pp. 64-84.
- Singer, B.S., Thompson, R.A., Dungan, M.A., Feeley, T.C., Nelson, S.T., Pickens, J.C., Brown, L.L., Wulff, A.W., Davidson, J.P., Metzger, J., 1997. Volcanism and erosion during the past 930 thousand years at the Tatara-San Pedro complex, Chilean Andes. *Geological Society of America Bulletin*, 109, 127-142.

- Spikings, R., Dungan, M., Foeken, J., Carter, A., Page, L., Stuart, F., 2008. Tectonic response of the central Chilean margin (35-38 degrees S) to the collision and subduction of heterogeneous oceanic crust; a thermochronological study. *Journal of the Geological Society of London* 165, 941-953.
- Spotila, J.A., 2005. Applications of Low-Temperature thermochronometry to quantification of recent exhumation in mountain belts. In: P. W. Reiners and T. A. Ehlers (eds.), *Noble Gas Geochemistry, Reviews in Mineralogy and Geochemistry* 58, pp. 449-466.
- Stark, C.P., Hovius, N. 2001. The characterization of landslide size distributions. *Geophysical Research Letters* 28, 1091-1094.
- Stern, C.R., Amini, H., Charrier, R., Godoy, E., Hervé, F., Varela, J., 1984. Petrochemistry and age of rhyolitic pyroclastics flows which occur along the drainage valleys of the Río Maipo and Río Cachapoal (Chile) and the Río Chaucha and Río Papagayos (Argentina). *Revista Geológica de Chile* 23, 39-52.
- Stone, J. O., Evans, J. M., Fifield, L. K., Allan, G.L., Cresswell, R.G., 1998. Cosmogenic chlorine-36 production in calcite by muons. *Geochimica et Cosmochimica Acta* 62, 433-454.
- Stone, J., 2000. Air pressure and cosmogenic isotope production. *Journal of Geophysical Research* 105 (B10), 23753-23759.
- Strasser, M., Schlunegger, F., 2005. Erosional processes, topographic length-scales and geomorphic evolution in arid climatic environments; the "Lluta collapse", northern Chile. *Geologische Rundschau = International Journal of Earth Sciences* (1999), 94, 433-446.
- Strom, A., Korup, O., 2006. Extremely large rockslides and rock avalanches in the Tien Shan Mountains, Kyrgyzstan. *Landslides* 3, 125-136.
- Stuiver, M., Reimer, P. J., Reimer, R. W. 2005. CALIB 5.0. [www.calib.org: program and documentation].
- Thiele, R., 1980. Hoja Santiago (1:250,000 scale map), Región Metropolitana. Instituto de Investigaciones Geológicas, Santiago, Carta geológica de Chile 39.

- Thomson, S. N., Brandon, M. T., Vásquez, C., Reiners, P. W., Tomkin, J.H., 2008. Thermochronologic evidence for a poleward transition from destructive to constructive glacial control on mountain building: An example from the Patagonian Andes. In: Garver, J.I., and Montario, M.J. (eds.), *Proceedings from the 11th International Conference on thermochronometry*, Anchorage, Alaska, Sept. 2008.
- Turcotte, D. L., Malamud, B. D., Guzzetti, F., Reichenbach, P., 2006. A general landslide distribution applied to a small inventory in Todi, Italy; Fractal analysis for natural hazards. *Geological Society Special Publications* 261, 105-111.
- Villarroel, R., Vergara, M., 1988. La Formación Abanico en el área de los cerros Abanico y San Ramón, Cordillera de Santiago. In: *V Congreso Geológico Chileno*, Sociedad Geologica de Chile, A327-A337.
- von Blanckenburg, F., 2005. The control mechanisms of erosion and weathering at basin scale from cosmogenic nuclides in river sediment. *Earth and Planetary Science Letters*, 237, 462-479.
- Wall, R., Sellés, D., Gana, P., 1999. Area Tiltill-Santiago (1:100,000 scale map), Región Metropolitana. Servicio Nacional de Geología y Minería, Mapas Geológicos 11.
- Whipp, D.M., Jr, Ehlers, T., Blythe, A., Huntington, K., Hodges, K., Burbank, D., 2007. Plio-Quaternary exhumation history of the central Nepalese Himalaya; 2; Thermokinematic and thermochronometer age prediction model. *Tectonics* 26, 23.
- Whipple, K., Kirby, E., Brocklehurst, S., 1999. Geomorphic limits to climate-induced increases in topographic relief. *Nature* 401, 39-43.
- Wobus, C., Whipple, K., Hodges, K., 2006. Neotectonics of the central Nepalese Himalaya; constraints from geomorphology, detrital $^{40}\text{Ar}/^{39}\text{Ar}$ thermochronology, and thermal modeling. *Tectonics* 25, 18.
- Wobus, C., Heimsath, A., Whipple, K., Hodges, K., 2005. Active out-of-sequence thrust faulting in the central Nepalese Himalaya. *Nature* 434, 1008-1011.
- Wobus, C., Pringle, M., Whipple, K., Hodges, K., 2008. A late Miocene acceleration of exhumation in the Himalayan crystalline core. *Earth and Planetary Science Letters* 269, 1-10.
- Wohl, E., 2000. *Mountain rivers*. American Geophysical Union, 320 pp.

- Yáñez, G., Rivera, O., Comte, D., Pardo, M., Baeza, L., Vera, E., 2008. Damage zone and the occurrence of world-class porphyry copper deposits in the active margin of Chile: Geophysical signatures and tectonomagmatic inferences. In: *7th International Symposium on Andean Geodynamics (ISAG 2008), Extended Abstracts*, Nice, IRD, pp. 592-593.
- Zech, R., Kull, C., Veit, H., 2006. Late Quaternary glacial history in the Encierro Valley, Northern Chile (29°S), deduced from ^{10}Be surface exposure dating. *Palaeogeography, Palaeoclimatology, Palaeoecology* 234, 277-286.

Appendices

A.1. Supplementary Data File of Antinao and Gosse (2008): Large rockslides in the Southern Central Andes of Chile (32-34.5°S): Tectonic Control and Significance for Quaternary Landscape Evolution.

A.1.1. Inventory Data

The complete rockslide inventory is stored in a shapefile named *inventory.shp* (ESRI format), along with auxiliary files.

A.1.2. Detailed Examples of Rockslide-Bearing Areas in the Southern Central Andes

The following paragraphs enhance the contents of Tables 2 and 3, offering detailed descriptive information for selected areas where rockslides concentrate. Fig. SDF2-1 shows location of individually studied areas.

1. Rocín-Pelambres-Choapa (Fig. SDF2-2). Some of the rockslides in this area appear depicted in the map by Rivano et al. (1993). Lithologies are dominated in this area by the Oligocene-Miocene Abanico Formation (previously thought Cretaceous, cf. Rivano et al., 1993; Charrier et al., 2005; Campbell, 2005), covered by Miocene rocks of the Farellones Formation. Both units are thrust to the west along the Pocuro fault, over Cretaceous rocks. Rockslides appear aligned with the northernmost expression of the PSR fault system (Fig. SDF2-1a). In the area of the Pelambres copper mine, younger landslides are close to areas with older rockslides, suggesting a common, repeating cause. Presence of lakes and meadows (Conchuca Meadows, Lagunas El Sobrante, the latter south of the area shown in Fig. SDF2-2) and lacustrine sediments over and upstream the landslides, specifically at Jorquera and Pelambres (Fig. SDF2-2) suggest Upper Pleistocene to Recent activity of these features, according to the chronosequence developed. Regional observations north of 31° S, although not as detailed as inside the study area (Paskoff, 1970), indicate that occurrence of rockslides is apparently lower north of Pelambres area, marking a contrast with the region to the south.

2. Aconcagua River (Fig. SDF2-3). Already recognized by Abele (1984), the more prolific section of the river in terms of landslide occurrence can be assigned to the

area upstream of the Colorado river junction with the Aconcagua River up to the Juncalillo river area, near Portillo (see paragraph 3). In this section, lithology is dominated by the Abanico Formation, and rockslides are common, occurring along steep topography (Fig. SDF2-3). The Salto del Soldado landslide dominates the valley river downstream the junction of the Aconcagua and the Riecillos rivers, together with the steep gorge associated with it (Fig. SDF2-4). On the western portion of this section, a larger, older rockslide is barely visible from the valley (Cerro Negro, Fig. SDF2-4a). Colluvial aprons that descended from its escarpment and secondary slides that were removed from the toe and middle portion of this old slide are apparent (Fig. SDF2-3). The main toe has been eroded by the Aconcagua River. The landslides in this section appear to have been caused by discontinuities between the Miocene granodioritic intrusives and the volcanic units of Abanico Formation. The Salto del Soldado rockslide has three identified sliding surfaces. The deepest one is now exposed at about 1500 m asl (Fig. SDF2-4c), with associated slickensides and fault gauge. It exposes bedrock, showing that the detachment in the upper part of the landslide occurred partially on intrusive rock only. Another surface exposed on a cut for an irrigation ditch and on the main International road shows highly fractured volcanic and intrusive rocks, separated by a surface with fault gauges and minor slickensides (Fig. SDF2-4b). The higher degree of fracturing can be explained as this surface acted as a secondary sliding surface as the deposit was stopped progressively at higher levels when the toe reached the opposite slope.

Shortly after the Salto del Soldado slide event, deduced from the lack of extensive lacustrine deposits upstream, the dam created by the slide on the Aconcagua River collapsed, sending debris over the lower portion of the valley. Deposits of this catastrophic event are preserved in the area called Los Espinos (Fig. SDF2-3). Caviedes (1972) identified the terrace but assigned all the sediments to a glaciofluvial stage. Grain size and sedimentary structures indicate a high flow rate during a very short lived event that acted on top of a glaciofluvial terrace, in a section studied by Caviedes (1972) and now partially covered by a retaining wall (Fig. SDF2-4d). The presence of this glaciofluvial terrace constrains the age of the landslide to Upper Pleistocene at least and no earlier than Middle Pleistocene, according to the age that Caviedes (1972) assigned to

the glacial deposits found in the Aconcagua valley upstream. A few meters of lacustrine deposits –devoid of organic matter- crop closely upstream of the rockslide, and suggest that the obstruction was short lived.

Directly on top of the gorge, striations that were interpreted as glacial and that suggested that the entire deposit was a moraine complex (Caviedes, 1972), are interpreted here as caused by erosive action of blocks being removed by the river during the breaching of the dam caused by the slide on the Aconcagua River . Similar features were found during this study in the Colorado valley (La Paloma creek) downstream a large middle Pleistocene rockslide that has been reworked. Only at Potrero Alto (Fig. SDF2-3), 5 km upstream of Salto del Soldado, diamictons that can be interpreted as glacial in origin appear on the northern side of the Aconcagua valley. They are generally on top of colluvial deposits, with sharp contacts and faceted and striated boulders.

3. Jahuel – San Francisco (Fig. SDF2-5). Northwest of Los Andes, an interesting cluster of landslides organized in a NW-WNW pattern can be recognized. No fault or structure has been mapped that explains this pattern, but sharp lines can be traced joining the upper part of all failures. On the Co. San Francisco range, two steps that topographically face southwest are easily recognizable in the DEMs looking from the SFLA basin. One is present at 2800 m a.s.l., the other at 3200 m a.s.l., and while their origin may be related to a lithological or a structural discontinuity, they appear to control the landslides, although it might be argued that the rockslide sources also follow closely the line of peaks, indicating a possible seismic amplification trigger (in absence of erosive control, cf. Sepulveda et al., 2005).

The westernmost slides from this cluster appear with a subtle morphology, being parched onto bedrock. In some places, they appear to be highly oxidized, brown-reddish debris flow deposits, clast- to matrix-supported, with angular to subrounded clasts, polyolithological, and with 'ghost' clasts, very friable. The upper section of one of them in Quebrada El Arpa has a layer of 50 cm of tephra overlying it. The tephra itself has been reworked, with fluvial gravels and minor boulders occurring at the very top of the sequence. The appearance of the tephra layer has more resemblance to the tephra layers that Espizua (1993, 1998) and Moreiras (2006) have found in the Upper Mendoza river valley, and that they dated as ~ 360 ka. A rough correlation can be made, consistent with

morphology, soils development, and deposit weathering, to interpret these features as Lower-Middle Pleistocene in age.

It is interesting to note that in the case of the slides coming from Cerro El Cobre, streams incised rockslide deposits following their shape and after eroding the slide boundary itself, they kept eroding in the same place but onto bedrock apparently due to the low strength of the highly fractured and deeply weathered rock of the Abanico Formation along the PSR fault zone. The drainage network seems to be incising unconsolidated deposits, but they are actually incising bedrock.

4. Portillo (Fig. SDF2-6). This area features a rockslide event covering glacial deposits from a receding glacier in the Juncalillo area, similar to the case of landslides in other areas (e.g. junction of Colina and Volcán rivers, and Yeso-Mesón Alto landslide). Although already identified by Abele (1984) and Rivano et al. (1993), Godoy et al. (1994b) presented the first comprehensive description of the slide deposits, assigning them to the Holocene. The rockslides appear to have occurred immediately after ice started recession towards the upper valley now occupied by Laguna del Inca. A lateral moraine is the only visible portion of the moraine complex, with good exposures of till at around 2900 m on road cuts west of the Portillo ski resort. Partially covered on the west side by a younger, small landslide and in the east side by the Portillo main rockslide, this moraine has been already described by Brügger (1950) and Caviedes (1972). Its altitudinal position matches deposits on the other side of the continental divide, that have been dated as MOIS2 (Almacenes drift, < 15 000 yr BP, or Horcones drift, LGM, 22 800 – 15 000 yr BP, Espizúa 1999; Espizúa et al., 1993, 2000). Whether the Portillo deposits correlate to one or the other of the two events recorded in Argentina depends on the position of the former ELA. Assuming tilting of the ELA towards the Chilean side of the divide, as it is today (Lliboutry, 1956; Hastenrath, 1970), these deposits could be correlated with Almacenes drift, and the main rockslide might be Holocene in age, as Godoy et al. (1994b) suggested.

The main unit of the rockslide deposit fell from about 3500-3750 m a.s.l. on the eastern side of the Laguna del Inca, where a steeply (70° to the W) tilted sequence of Mesozoic andesites and tuffs crops. The rockslide did not find any obstacle on their descent, except for the opposite slope, travelling down valley towards the area of Llano

Juncalillo and then continuing farther to the area where Juncal river joins with Ojos de Agua, a small creek draining from the north. The deposit itself can be characterized by large mono-lithologic boulders 5-15 m size of epidote bearing andesites. Matrix is almost absent in the upper deposit (close to Laguna del Inca and in the upper set of switchbacks of the International Route). Boulders are fractured and it is frequent to observe striae on some of them, probably reflecting movement along shearing planes before or during the rockslide event. On the lower part (Juncal River valley), the large boulders diminish in size to 2-10 m (rare), and the deposit is dominated by a clast- to matrix-supported diamicton, monolithologic with epidote and chlorite bearing andesites, and a matrix of granule, sand and silt in the distal (Ojos de Agua) areas.

There are associated smaller landslides that probably occurred after or simultaneously with the main event, and cover its deposits. The southwestern part of the main body in the Juncalillo valley appears to have collapsed shortly after the event. This secondary failure was probably induced by elevated pore pressures in the obstructed outlet of the Juncalillo-Laguna del Inca glacial system, which still had not been attained an equilibrium with the rockslide. Lacustrine deposits crop at elevations higher than the present lake in the southeastern area of Laguna del Inca and also just below the level of the Customs Complex. A small escarpment on the deposit is left of that secondary event, and a small flat surface is still visible, and attributable to a second, lower lake now gone. Besides that event, three landslides have fallen on top of the main body. The first one, described by Godoy et al (1994b) as unit II, fell from the same area than the main body, taken some remaining material of the escarpment area shortly after the main event, and is more equate to a rockfall or a sequence of them, due to the distribution of sizes of boulders found in the area immediately close to the escarpment. The second event is a rockslide from the southern area, where also steep slopes appear, the deposit being composed of andesitic boulders up to 2 m, which cover the main body and apparently are also on top of the above mentioned eastern slide. A third landslide fell partially on top of the lower portion of the deposit, overlooking the Juncal valley, and it is composed mostly of diorite boulders.

In the lower part, the deposit has been covered with a thin mantle of a yellow-brown diamicton, matrix-supported, with subangular to subrounded clasts, polyolithologic,

mostly gravels and minor boulders. On the junction of Juncalillo and Juncal rivers, the mantle of this deposit marks a well defined terrace on top of the rockslide, and farther downstream on the Juncal valley, near Ojos de Agua, appears bearing subrounded, faceted clasts.

The lake impounded by the combined landslide and morainic complex apparently has attained equilibrium, draining underground towards Juncal River, following the west boundary of the moraine-landslide deposit. The outlet emerges at an elevation of 2800 m a.s.l., this being probably the location of the former outlet or spillway over the moraine system. Discharge in the Laguna del Inca catchment is not as variable as in areas where other landslide-dammed lakes have been described as collapsing shortly (days to years) after the landslide event (e.g., Ermini and Casagli, 2003). Reduced glacial activity after deposition of the rockslide and stabilization of the valley infilling induced by the presence of the glacial deposit, had lead to preservation of the lake and the landslide deposit. This effect might be present also in the Laguna Negra-Yeso Reservoir areas and it has consequences for hazards assessment.

5. Lower Colorado River (Fig. SDF2-7). The lower portion of Colorado River valley, before the junction with Maipo River, displays three generations of rockslides. The oldest ones, Quebrada El Laurel and Alfalfal, apparently deflected the river to the south; there are diamicton deposits on the southern area near the town of Los Maitenes which apparently have been transported from the northern slopes of the valley. After this event, the landslides at El Cinco Mil and Cuesta Maitenes blocked the river, creating a lake whose sediments are still visible on a roadcut east of the Cuesta Los Maitenes slide. The last generation involved the small rockslides at Quebrada Seca and Morro Bandurrias, and the remobilized I-IV from the main El Laurel deposit.

6. El Ingenio (Fig. SDF2-8). Following the Maipo valley, between the Yeso and Colorado rivers, appears one of the most impressive examples of rocksliding in the Southern Central Andes. Hardly seen from the route along the river, the El Ingenio rockslide (Chiu, 1991; Godoy et al 1994b) developed from nearby Cerro San Sebastián, in the north. Almost horizontally stratified rocks cut by an escarpment 500 m high give the deposit its northern, sharp boundary. On the southern sector, apparently tectonic drag folds (Fock, 2005) allow to distinguish highly fractured bedrock from the shattered

rockslide deposit. From the main route, the central part of the deposit and two upper flood terraces can be seen. Apparently this landslide is older than Upper Pleistocene, because there has been incision on the rock below the lowest altitude where deposits can be found, at Tinoco Gorge. Erosion of the main body of the rockslide can not be explained just by thinning and collapse of the deposit crossing the Maipo valley, and it may be possible that a good amount of the central part of the deposit has already been eroded downstream. The nearby Coyanco deposit (southwestern corner, Fig. SDF2-8) apparently displaced the course of the Coyanco Creek, and generated sediments 50-75m thick in the distal part after collapse of the related dam. At the junction of Coyanco and Maipo rivers, the Diamante Ignimbrite (Chiu, 1981; Stern et al., 1984; Stern, 2004) has been found on top of the (mostly) flood deposits for both of them, constraining their age to Mid Pleistocene (older than 0.45 Ma).

7. Yeso River – Mesón Alto area (Fig. SDF2-9). In the Yeso River Valley, an area covered in debris almost 10-15 km along the valley and around 20 km², represents one or more events coming from the nearby Mesón Alto Massif (peak at 5257 m a.s.l.). Marangunic and Thiele (1971) attributed these deposits to a frontal moraine complex, with a thickness up to 400 m and 4.5 km³ in volume. Abele (1984) estimated the volume in 4.3 km³. The landslide deposits, crossing the Yeso River from east to west, ended at the Laguna Negra area (Fig. SDF2-10a), bringing almost pure granodiorite boulders (Fig. SDF2-10b) from a nearby intrusive body (Moreno et al., 1991) to an otherwise predominantly andesitic area.

The Yeso slide is useful to constrain the mechanism of emplacement of rockslides in this sector of the Southern Central Andes. As Abele (1984) pointed out, the sequence granodiorite-andesite from bottom to top present in the cliffs to the southeast of the Yeso reservoir, is repeated on the landslide outcrops from west to east on the south coast of the reservoir (Fig. SDF2-10a). The movement must have been translational mostly, to explain the observed lithological distribution with minor disruptions. A translational movement matches also observations made on other slides in the area (Potrero Alto, in the Aconcagua River valley, and Potrerillos, in the Mapocho River valley) at different size scales. The volume of sediment and vertical height could easily be the origin of a rock avalanche or sturzstrom (cf. Abele 1974, Erismann and Abele, 2001) as in the case

of the Placetas Amarillas rock avalanche, in Argentina ($\sim 10^9 \text{ m}^3$, Moreiras, 2006). In the Yeso event, as in many other examples in the Southern Central Andes, the deposit remained as a rather cohesive unit and the travel distance compared to the fall height, is not large, which suggest a 'dry' trigger, with a small volume of water involved.

An explanation of the damming mechanism for Laguna Negra and former Laguna Azul (now Yeso Reservoir) must consider till deposits damming the northern and western catchments, with a rockslide event falling on top of the glacial morphology in the late stages of the local LGM ice advance. This explains the minimal reworking of the landslide deposits as well as the apparent stability of the lakes, a situation similar to the one present in the Portillo area. However, consideration of the deposit as glacial in origin can be discarded by several reasons. The large volume of homogeneous lithology material accumulated on what is now the outlet of the Yeso reservoir works against glacial processes, which will tend to mix lithologies. There is no similar volume of glacial deposits stored as a single moraine sequence in the nearby valleys of Mapocho, Colorado, Maipo and Volcán Rivers (not considering as glacial deposits the Engorda rockslides, see section 8). There is no prolongation of the frontal complex as lateral moraines towards the upper Yeso River valley, and on the eastern side of Laguna Negra, a clear lateral moraine is truncated by the landslide (Fig. SDF2-9).

The western side of the deposit, however, can be interpreted as glacial in origin. Till deposits crop in the western margin of the valley downstream, in the area of San Nicolás, and lateral moraines can be followed from the upper section of Portezuelo La Paloma – Laguna Negra to the deposits damming Laguna Negra. According to this, the Yeso- Mesón Alto rockslide was deposited on top of an already large morainic complex coming from the present Echaurren and former Laguna Negra and Laguna Encañado glaciers.

South of the Mesón Alto complex, the Cortaderas rockslide appears blocking also the Yeso River valley near San Nicolás. It is composed of purely andesitic volcanoclastic rocks and sandstones that failed from the same regional structure that the Yeso-Mesón Alto rockslide. The Cortaderas rockslide toe (Fig. SDF2-10c) was remobilized during the M=6.9 1958 Las Melosas earthquake (Sepúlveda et al., 2007), and this area sustains continuous debris flows that are removing slowly the rockslide material.

8. Morales – La Engorda (Fig. SDF2-11). In the Volcán River valley, rockslide deposits appear linked with glacial deposits in a way such that it is possible to estimate the age of rockslide deposits in the area. Three rockslides have data constraining their age. The oldest one, falling northwards from the slopes of Jurassic sedimentary rocks, fell probably on top of recessional ice, covering a moraine that has a well developed arcuate morphology, and that obstructed the drainage of Colina River just below the junction with Volcán River (Fig. SDF2-12). Organic material in the lacustrine sediments from this obstructed drainage has been dated as 24.51 ± 0.41 ^{14}C ka (uncalibrated ages from Moreno et al., 1991; to see calibrated ages, see Table 4 in the main text). The rockslide event probably happened after the ice started to reced, as the rockslide deposit has not been reworked by ice. Lower sections, close to the Colina River, show till deposits being overlain by rockslide deposits that show a configuration similar to a large rockfall (Hauser, 2000). Downstream the Volcán River, two other organic bearing layers have been dated by Moreno et al. (1991), but their stratigraphic position is not clear. They are located upstream junction with Quebrada Morales, showing 9.24 ± 0.11 ^{14}C ka the upper and 15.73 ± 0.17 ^{14}C ka the lower (Moreno et al., 1991). At the road cuts in the junction between the Volcán River and Quebrada Morales, till outcrops are mixed with rockslide debris from Quebrada Morales. As this subsidiary valley also has a glacier on its headwaters, the data can be interpreted, as it has been done in other areas, as a rockslide event coming on top of a glacial deposit. In this case, however, the two ages may represent either two ice advances blocking the mainstem, or an earlier advance followed by the rockslide event blocking the valley at 9.24 ± 0.11 ^{14}C ka. It can be assumed that these are close maximum ages, as the rockslides in this reach are always directly on top of other relevant deposits. This assumption puts them in the Upper Pleistocene-Holocene age range. It must be emphasized that these data was used to tune the relative chronosequence developed for the entire study area.

9. Colón-Coya rock and debris avalanche composite deposit (Fig. SDF2-13). In the area of the Teniente copper mine, the Colón-Coya Formation has been described by Godoy et al. (1994a) and Gómez (2001), and interpreted as a series of mass movement events Pliocene to Pleistocene in age (4.9-1.8 Ma). This unit is relevant as it might represent the largest rock avalanche deposit present in the study area. The Colón -Coya

Formation was originally defined by Cuadra (1986) as the equivalent to the Alto Colón 'complex' first described by Camus (1977). Cuadra (1986) and Gómez (2001) described the unconformable relation between these deposits and the Farellones Formation. These deposits cover an area of approximately 150 km², and their present volume has been estimated as 7.3 km³ (Gómez, 2001). Godoy et al. (1994a) discriminated two main units based on the consolidation of the deposits and the position related to the source (Fig. SDF2-13). The main body of the avalanche came from the western slopes of the Farellones Fm. outcrops, from the area of Olla Blanca and Cerro Montura, in the north, and from Matancilla, in the east. The age relationships are somewhat difficult to decipher due to the difficulties posed by correlation between volcanic units highly variable in space, deposited over a preexistent topography of north-south valleys and ridges in the former Abanico-Farellones contact. Despite that, a general model for the age of the deposit is shown in Fig. SDF2-13, and sets the age for the deposition of the main body before 4.6, and ca. 4.9 Ma, being later covered and/or intruded by volcanic rocks whose age is variable between 3.8-1.8 Ma.

Although the age is relatively clear, the main problem of Colón -Coya deposit continues being its genesis. The main unit of Godoy et al (1994a) was interpreted as an avalanche deposit, but it is not clear if it is a dry, cold rock avalanche (Godoy et al., 1994a; Encinas et al., 2006) or a combination of hot debris avalanches, landslides, lahars and volcanic eruptive products generated during a period of enhanced volcanic activity in the area (Gómez, 2001; Camus, 1977). Geochronologic data of the El Teniente area shows a continuous succession of hydrothermal events starting at 6.3 Ma, which concluded in the formation of the Braden breccia body at 4.8 Ma. This sequence may have had an extrusive expression in the form of volcanic explosive eruptions, especially the 4.8 Ma, also being bracketed by two apatite ages in ash inside the main deposit (Encinas et al., 2006). Godoy et al (1994a) suggested that more than one event of mass wasting is recorded in the deposit, based on cross-cutting relations and development of oxidized depositional surfaces. They also suggested that the events were short-lived and close in time (hundreds of thousands of years). Thus, at least part of the main unit was formed in the presence of the active volcanic system which hosted the hydrothermal complex developing El Teniente (e.g., Makshev et al., 2003). Due to this long-lived

activity, the Colón -Coya deposit will be used only for certain purposes; and as it is probably a composite deposit, its use in area-frequency relation analysis is precluded.

A.1.3. Cosmogenic Isotope Sample Preparation and Additional Data

A.1.3.1. Beryllium-10

All samples were cleaned, crushed and sieved to sand size grains, before concentration of quartz was accomplished at the Dalhousie Geochronology Centre. We obtained 20-50 g (Table SDF3-1) of pure quartz (250–355 μm fraction) following chemical treatment procedures described by Kohl and Nishiizumi (1992) at the Dalhousie Geochronology Centre. Approximately 0.2 mg of Be carrier (produced by J. Klein from a shielded beryl crystal extracted from the Homestake gold mine in South Dakota) was added to the purified quartz (< 50 ppm Al), the quartz was digested with HF-HClO₄, and using controlled precipitations and anion and cation exchange chromatography the Be was extracted with 99.999% ammonia and converted to BeO. The oxide was mixed proportionately with niobium metal powder and packed in stainless steel target cathodes (e.g., Gosse and Phillips, 2001). The targets underwent AMS measurement at Lawrence Livermore National Laboratory (LLNL) under the supervision of Dr. Robert Finkel.

The average $^{10}\text{Be}/^9\text{Be}$ ratio of the process blank with this carrier at LLNL is 4×10^{-15} and for these samples the blank correction was less than 2%. The AMS standard used for all samples was KNSTD3110. The ^{10}Be half life assumed for these 2007 analyses was 1.36 Ma.

Surface production rates at all ^{10}Be sample sites were calculated using four different time-dependent scaling schemes (Balco et al., 2008). Uncertainties included in the error propagation include the AMS analytical uncertainty, a 3% error in the decay constant of ^{10}Be (1.36 Ma, Nishiizumi, 2007), and production rate errors in the ^{10}Be production rate calculations, which are embedded in the procedure by Balco et al.(2008).

Table SDF3-1. Carrier amount, carrier concentration, mass of sample and topographical shielding factor used in ^{10}Be and ^{36}Cl production rate scaling.

Sample	Isotope	Sample Mass [g]	Carrier Mass [g]	Carrier Concentration ^9Be or ^{35}Cl [g g^{-1}]	Shielding Factor
MAQ002	^{10}Be	21.6723	0.2402	9.950E-4	0.9956
MES001	^{10}Be	37.7801	0.2372	9.950E-4	0.9959
MES002	^{10}Be	48.4200	0.2343	9.950E-4	0.9976
MES003	^{10}Be	47.1604	0.2358	9.950E-4	0.998
PAN001	^{36}Cl	40.0004	2.4461	1.45E-03	0.9766
PAN003	^{36}Cl	40.0003	2.3735	1.45E-03	0.9792
SOLD004	^{36}Cl	40.2223	1.9788	1.24E-03	0.8869
SOLD006	^{36}Cl	40.0557	1.9969	1.24E-03	0.9640
MAC004	^{36}Cl	50.9668	1.3364	1.45E-03	0.4436
MAC005	^{36}Cl	49.9974	1.1012	1.45E-03	0.9427
MAC006	^{36}Cl	50.1357	1.2706	1.45E-03	0.9613
POT008	^{36}Cl	50.8511	1.1092	1.45E-03	0.9822
POT009	^{36}Cl	50.0503	1.1611	1.45E-03	0.9803
POT010	^{36}Cl	50.1857	1.0558	1.45E-03	0.9834

A.1.3.2. Chlorine-36

Samples were crushed completely below 250 μm at the Dalhousie Geochronology Centre, and aliquots of the sample were sent to the SGS Laboratory in Ontario, Canada, for XRF and ICP-MS determination of major and trace elements, and gamma emission spectrometry analysis of B and Gd (see Table SDF3-2). 40 g of the 125-250 μm fraction were dissolved and chemical separation of chlorine was achieved by precipitation of silver chloride by standard procedures (e.g., Zreda, 1994) that involved the addition of ^{35}Cl enriched carrier (99.9% pure ^{35}Cl carrier as NaCl salt from Oak Ridge National Lab standard batch 150301, dissolved in ultrapure water). Samples were then sent to PRIME Lab at Purdue University for accelerator mass spectrometry analysis of the $^{36}\text{Cl}/\text{Cl}$ ratio and the $^{35}\text{Cl}/^{37}\text{Cl}$ ratio, under the supervision of Dr. Marc Caffee. Uncertainties on ^{36}Cl concentration were propagated throughout the entire calculations and involve analytical uncertainties in XRF, ICP-MS and AMS data, historical blank correction uncertainties, and production rate uncertainties. ^{36}Cl production rates from Ca according to Stone et al. (1998), the rest according to Phillips et al. (2001). Production rates and ages were derived

according to a MATLAB algorithm, based on an original Mathematica® code by John Stone (unpublished).

Table SDF3-2. Chemical data used in determination of production rates for ³⁶Cl data reduction.

Sample ID	SiO ₂	Al ₂ O ₃	Fe ₂ O ₃	MgO	CaO	Na ₂ O	K ₂ O	TiO ₂	P ₂ O ₅	MnO	Cr ₂ O ₃	V ₂ O ₅	LOI	Sum
	%	%	%	%	%	%	%	%	%	%	%	%	%	%
SOLD004	68.8	14.8	2.39	0.15	3.68	3.57	3.63	0.45	<0.01	0.06	<0.01	<0.01	1.1	98.6
SOLD006	70.2	14.0	3.39	0.36	1.83	4.33	3.34	0.36	<0.01	0.07	<0.01	<0.01	0.34	98.2
PAN001	59.4	15.6	7.49	2.87	5.55	2.95	0.86	0.98	0.02	0.11	0.05	0.05	3.19	99.2
PAN003	67.2	14.2	4.95	0.46	3.48	2.43	1.52	0.99	0.02	0.06	0.02	0.02	2.88	98.2
POT008	63.1	15.8	6.82	1.36	2.86	5.72	1.64	1.13	0.05	0.09	<0.01	0.03	2.44	101
POT009	69.4	13.4	5.17	0.83	1.82	5.21	1.84	0.97	0.06	0.09	<0.01	0.01	1.84	100.7
POT010	63.5	15.3	7.48	1.2	2.51	5.65	1.7	1.15	0.05	0.09	<0.01	0.02	2.24	101
MAC001	58.4	14.9	9.55	2.24	6.07	3.32	1.06	1.37	0.04	0.15	<0.01	0.04	3.54	100.7
MAC002	59.6	15.2	8.92	1.72	6.09	3.44	1.46	1.31	0.04	0.12	<0.01	0.04	3.02	100.9
MAC003	58.6	14.7	9.34	1.94	6.29	3.69	1.26	1.36	0.05	0.13	<0.01	0.04	3.02	100.4

Table A3-2, continued.

Sample ID	U	Th	Sm	B	Gd
	ppm	ppm	ppm	ppm	ppm
SOLD004	1.7	6.6	3.2	<4	3.3
SOLD006	0.69	2.4	1.4	<4	1.5
PAN001	<1	<1	4.1	<40	3.7
PAN003	<1	<1	1.8	<40	1.7
POT008	0.65	2.1	3.1	20	3.11
POT009	0.71	2.2	3	10	3.15
POT010	0.69	2.2	3.3	10	3.3
MAC001	0.56	1.8	3.1	<10	3.59
MAC002	0.61	2	3.2	<10	3.56
MAC003	0.55	1.6	2.8	<10	3.1

A.1.4. References

- Abele, G., 1974. Bergsturze in den Alpen, ihre Verbreitung, Morphologie und Folgerscheinungen. Wissenschaftliche Alpeinvereinshefte 25, 230 pp.
- Abele, G., 1984. Derrumbes de montaña y morrenas en los Andes chilenos. Revista de Geografía Norte Grande 11, 17-30.
- Balco, G., Stone, J. O., Lifton, N. A., Dunai, T. J., 2008. A complete and easily accessible means of calculating surface exposure ages or erosion rates from ¹⁰Be and ²⁶Al measurements. Quaternary Geochronology. 3, 174-195.

- Brüggen, J., 1950. Fundamentos de la Geología de Chile. Editorial Nascimento, Santiago, 378 pp.
- Campbell, D., 2005. Termocronología del sector comprendido entre los ríos Rocín y Aconcagua: Implicancias en la evolución Meso-Cenozoica de la zona. M. Sc. Thesis, Departamento de Geología, Universidad de Chile, Santiago.
- Caviedes, C., 1972. Geomorfología del Cuaternario del valle de Aconcagua, Chile Central. *Freiburger Geographische Hefte* 11, 153 pp.
- Caviedes, C., Paskoff, R., 1975. Quaternary Glaciations in the Andes of North Central Chile. *Journal of Glaciology* 14, 155-169.
- Charrier, R., Bustamante, M., Comte, D., Elgueta, S., Flynn, J.J., Iturra, N., Muñoz, N., Pardo, M., Thiele, R., Wyss, A. R., 2005. The Abanico extensional basin: Regional extension, chronology of tectonic inversion and relation to shallow seismic activity and Andean uplift. *N. Jb. Geol. Palaont. Abh.* 236, 43-77.
- Chiu, D., 1991. Geología del relleno Cuaternario de las hoyas de los ríos Yeso, Volcán y Maipo, este último entre las localidades de Guayacán y los Queltehues, Región Metropolitana, Chile. B. Sc. Thesis, Departamento de Geología, Universidad de Chile, Santiago.
- Cuadra, P., 1986. Geocronología K-Ar del yacimiento El Teniente y áreas adyacentes. *Revista Geológica de Chile* 27, 3-26.
- Encinas, A., MaksaeV, V., Pinto, L., Le Roux, J.P., Munizaga, F., Zentilli, M., 2006. Pliocene lahar deposits in the Coastal Cordillera of central Chile: Implications for uplift, avalanche deposits, and porphyry copper systems in the Main Andean Cordillera. *Journal of South American Earth Sciences* 20, 369-381.
- Erismann, T.H., Abele, G., 2001. Dynamics of rockslides and rockfalls. Springer, Berlin, 316 pp.
- Ermini, L., Casagli, N., 2003. Prediction of the behaviour of landslide dams using a geomorphological dimensionless index. *Earth Surface Processes and Landforms* 28, 31-47.
- Espizúa, L., 2000. Quaternary glacial sequence in the Rio Mendoza valley, Argentina. In: Smolka, P.P., Volkheimer, W. (Eds) Southern hemisphere paleo and neoclimates: Key Sites, Methods, Data and Models, Springer, Berlin, pp. 287-293.

- Espizúa, L., Bigazzi, G., 1998. Fission-track dating of Punta de Vacas glaciation in the Rio Mendoza valley, Argentina. *Quaternary Science Reviews* 17, 755–760.
- Espizúa, L.E., 1993. Quaternary glaciations in the Rio Mendoza valley, Argentina Andes. *Quaternary Research* 40, 150-162.
- Espizúa, L.E., 1999. Chronology of late Pleistocene glacier advances in the Rio Mendoza Valley, Argentina; Glaciers of the Southern Hemisphere. *Global and Planetary Change* 22, 193-200.
- Espizúa, L.E., Bengochea, J.D., Aguado, C.J., 1993. Mapa de riesgo de remoción en masa en el valle del Río Mendoza. In: XII Congreso Geológico Argentino y II Congreso de Exploración de Hidrocarburos, Actas, VI, pp. 323-332.
- Fock, A., 2005. Cronología y tectónica de exhumación en el Neógeno de los Andes de Chile Central entre los 33° y los 34° S. M. Sc. Thesis, Departamento de Geología, Universidad de Chile, Santiago.
- Godoy, E., Lara, L., Burmester, R., 1994a. El 'lahar' cuaternario de Colon-Coya: Una avalancha de detritos pliocena. *Proc. 7th Congreso Geológico Chileno, Concepción, Chile, Vol. 1*, pp. 305-309.
- Godoy, E., Lara, L., Ugalde, I., 1994b. Derrumbes de cerro holocenos en los Andes Centrales de Chile. *Proc. 7th Congreso Geológico Chileno, Concepción, Chile, Vol. 1*, pp. 310-314.
- Gómez, R., 2001. Geología de las unidades volcanogenicas cenozoicas del área industrial de la mina El Teniente, entre Colón y Coya, Cordillera Principal de Rancagua, VI Región. B. Sc. Thesis, Departamento de Geología, Universidad de Chile, Santiago.
- Gosse, J., Phillips, F.M., 2001. Terrestrial in situ cosmogenic nuclides: theory and applications, *Quaternary Science Reviews* 20, 1475-1560.
- Hastenrath, S. L., 1971. On the Pleistocene snow-line depression in the arid regions of the South American Andes, *Journal of Glaciology* 10, 255–267.
- Hauser, A., 2000. Remociones en masa en Chile, Servicio Nacional de Geología y Minería, Santiago, Boletín 59.
- Kohl, C.P., Nishiizumi, K., 1992. Chemical isolation of quartz for measurement of in situ-produced cosmogenic nuclides. *Geochimica et Cosmochimica Acta* 56, 3583–3587.

- Lliboutry, L., 1956. Nieves y glaciares de Chile. Fundamentos de glaciología. Ediciones de la Universidad de Chile, Santiago.
- Maksaev, V., Zentilli, M., Munizaga, F., Charrier, R., 2003. Denudación/alzamiento del Mioceno Superior-Plioceno Inferior en la Cordillera de Chile Central (33-35° S) inferida por dataciones por trazas de fisión en apatito de plutones miocenos. Proc. 10th Congreso Geológico Chileno, Concepción, Chile.
- Marangunic, C., Thiele, R., 1971. Procedencia y determinaciones gravimétricas de espesor de la morena de la Laguna Negra, Provincia de Santiago, Comunicaciones 38, 25 pp.
- Moreiras, S.M., 2006. Chronology of a probable neotectonic Pleistocene rock avalanche, Cordón del Plata (Central Andes), Mendoza, Argentina. Quaternary International 148, 138-148.
- Moreno, H., Thiele, R., Varela, J., 1991. Estudio Geológico y de Riesgos Volcánico y de Remoción en Masa del Proyecto Hidroeléctrico Alfalfal II y Las Lajas (Technical Report), CHILGENER S.A., Santiago, 78 pp.
- Nishiizumi, K., Imamura, M., Caffee, M. W., Southon, J. R., Finkel, R. C., McAninch, J., 2007. Absolute calibration of ^{10}Be AMS standards. Nuclear Instruments and Methods in Physics Research Section B: Beam Interactions with Materials and Atoms. 258, 403-413.
- Paskoff, R. 1970. Recherches géomorphologiques dans le Chili semi-aride. Biscaye Frères, Bordeaux, 420 pp.
- Phillips, F. M., W. D. Stone, Fabryka-Martin, J., 2001. An improved approach to calculating low-energy cosmic-ray neutron fluxes near the land/atmosphere interface, Chemical Geology 175, 689–701.
- Rivano, S., Sepúlveda, P., Boric, R., Espiñeira, P., 1993. Mapa Geológico de la Hoja Quillota-Portillo (escala 1:250.000), V Región de Valparaíso. Servicio Nacional de Geología y Minería, Santiago, Carta geológica de Chile 73.
- Sepúlveda, S.A., Astroza, M., Kausel, E., Campos, J., Casas, E.A., Rebolledo, S., Verdugo, R., 2007. New findings on the 1958 Las Melosas earthquake sequence, central Chile: implications for seismic hazard related to shallow crustal earthquakes in subduction zones. Accepted for publication, Journal of Earthquake Engineering.

- Sepúlveda, S.A., Murphy, W., Jibson, R. W., Petley, D. N., 2005. Seismically induced rock slope failures resulting from topographic amplification of strong ground motions: The case of Pacoima Canyon, California. *Engineering Geology* 80, 336-348.
- Stern, C.R., 2004. Active Andean volcanism: its geologic and tectonic setting. *Revista Geológica de Chile* 31, 161-206.
- Stern, C.R., Amini, H., Charrier, R., Godoy, E., Hervé, F., Varela, J., 1984. Petrochemistry and age of rhyolitic pyroclastics flows which occur along the drainage valleys of the Río Maipo and Río Cachapoal (Chile) and the Río Chaucha and Río Papagayos (Argentina). *Revista Geológica de Chile* 23, 39-52.
- Stone, J., 2000. Air pressure and cosmogenic isotope production, *Journal of Geophysical Research* 105 (B10) 23,753–23,759.
- Stone, J., Evans, J., Fifield, L., Allan, G., Cresswell, R., 1998. Cosmogenic chlorine-36 production in calcite by muons. *Geochimica et Cosmochimica Acta* 62, 433–454.
- Zreda, M. G., 1994. Development and calibration of the cosmogenic ^{36}Cl surface exposure dating method and its applications to the chronology of late Quaternary glaciations, Ph.D. thesis, N. M. Inst. of Min. and Technol., Socorro, 318 pp.

A.1.5. Figure captions for the Supplementary Data File (Appendix A.1)

Figure SDF2-1. Location map, showing location of figures SDF2-2,3,5,6,7,8,9,11.

Figure SDF2-2. Rocín-Pelambres-Choapa area. Note location of Conchuca Meadows, probably a result of damming Choapa River with Jorquera rockslide.

Figure SDF2-3. Aconcagua River Valley, upper reach. Note the ubiquity of gorges across different catchments and in the mainstem of the Aconcagua River; numbers refer to location of photographs depicted in Fig. SDF2-4.

Figure SDF2-4. Salto del Soldado rockslide: **a.** view of the older landslides hanging on the northern slopes, downvalley of the Salto del Soldado area; **b.** Salto del Soldado Gorge and perched rockslide-colluvial deposits on the opposite slope; **c.** View of upper sliding surface, most of the light coloured rock is monzodiorite intruding the dark-coloured Oligo-Miocene volcanic rocks, the arrow indicates location of surfaces where apparently rockslide-related slickensides appear; and **d.** Los Espinos terrace. The picture shows a detail of the massive deposit overlying the glaciofluvial terrace.

Figure SDF2-5. Los Andes area. Note the WNW pattern on the ridge NE of the city, that can be followed from the northwest to the southeast corner of the map (dashed lines).

Figure SDF2-6. Portillo Area.

Figure SDF2-7. Lower Colorado River valley area.

Figure SDF2-8. El Ingenio area.

Figure SDF2-9. Yeso Reservoir - Laguna Negra Area. Yeso- Mesón Alto and Quebrada Las Cortaderas rockslides, showing their spatial relation with fluvial and glacial deposits. Till deposits, mostly along lateral moraines, are truncated by landslide deposits. Overtopping of landslide-dam lakes caused large events of flooding that left impressive landforms. Most of the left alluvial terraces have a slope exceeding 1-2 degrees with boulders up to 5 m size.

Figure SDF2-10. **a.** Orthophoto showing textural features of the Yeso-Mesón Alto rockslide; **b.** Yeso Rockslide. The view is front point e on the previous photograph. The scarpment is conspicuous, the highest peak is Cerro Mesón Alto (5257 m a.s.l.); **c.** Las Cortaderas rockslide, with the 1958 Las Melosas earthquake-triggered small debris slide.

Figure SDF2-11. Morales-La Engorda area, Upper Volcán River valley.

Figure SDF2-12. Junction of Colina and Volcán Rivers. The arrow indicates where organic-rich sediments record blockage of Colina River by the advancing ice (from the point of view of the observer flowing to the SSW). Shortly after deglaciation, the rockslide covered the moraine.

Figure SDF2-13. **a.** Oblique composition of a Landsat image of the Colón-Coya area, with generalized units and escarpments; **b.** Chronostratigraphic sketch of units for the Colón -Coya composite deposit.

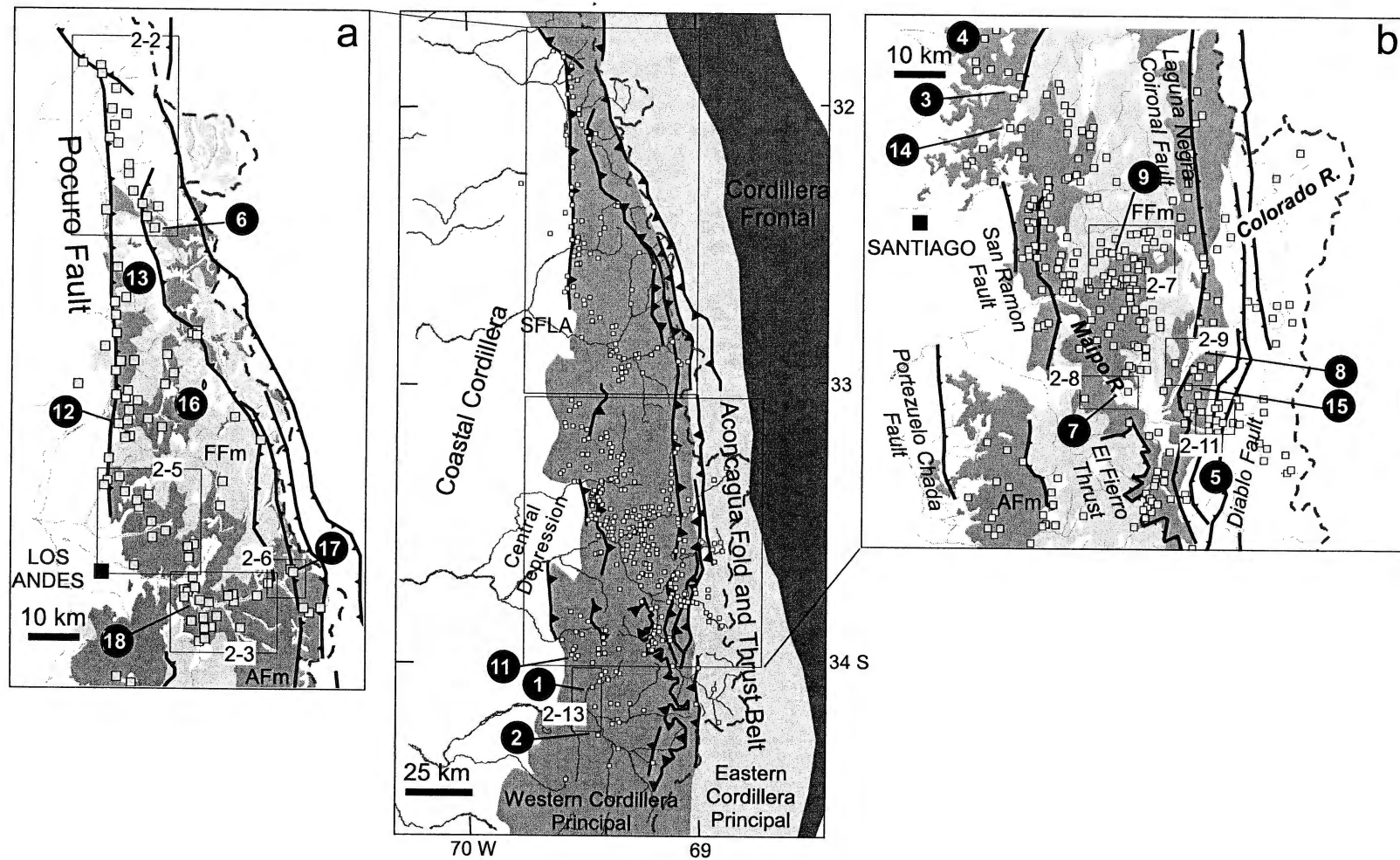
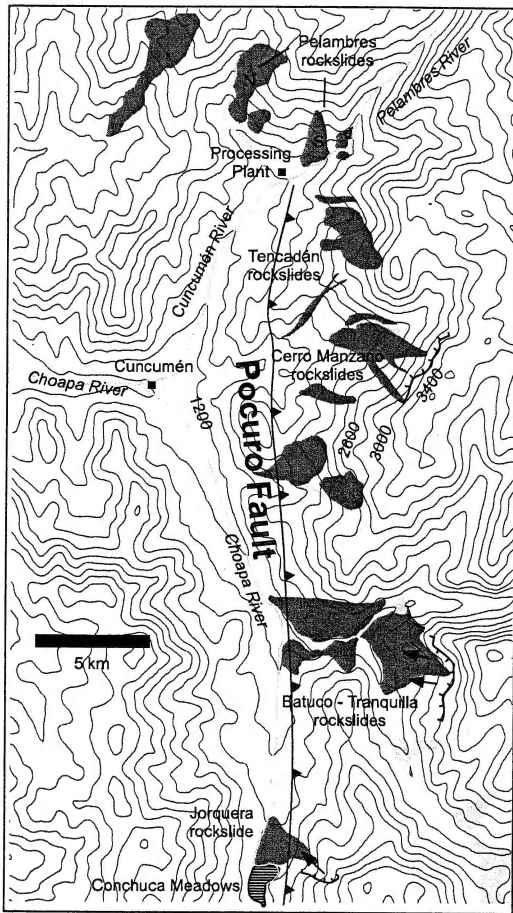


Figure SDF2-1



LEGEND


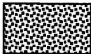





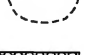

-  Lacustrine terrace, deposits
-  Till deposits
-  Fluvial, glaciofluvial, outburst deposits, terraces
-  Rockslides: a. main body, b. smaller subsidiary slide
-  scarpment and sense of movement for rockslide
-  fault
-  gorge
-  ice extent
-  unclassified deposits

Figure SDF2-2

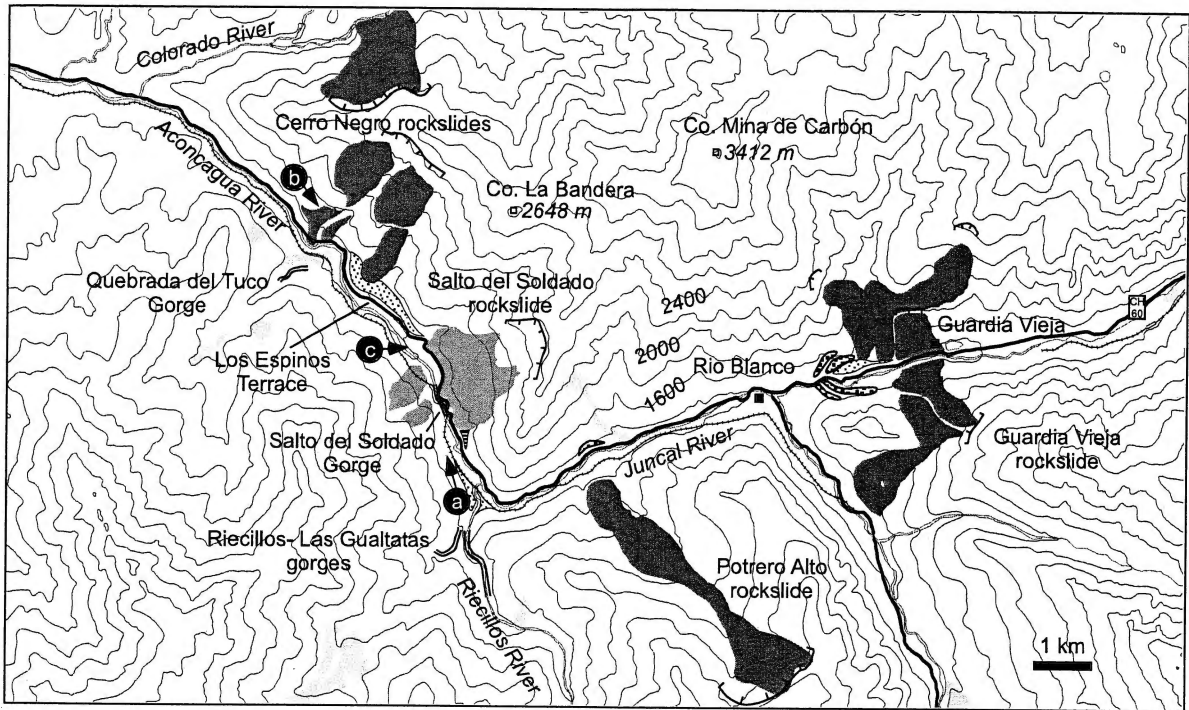


Figure SDF2-3

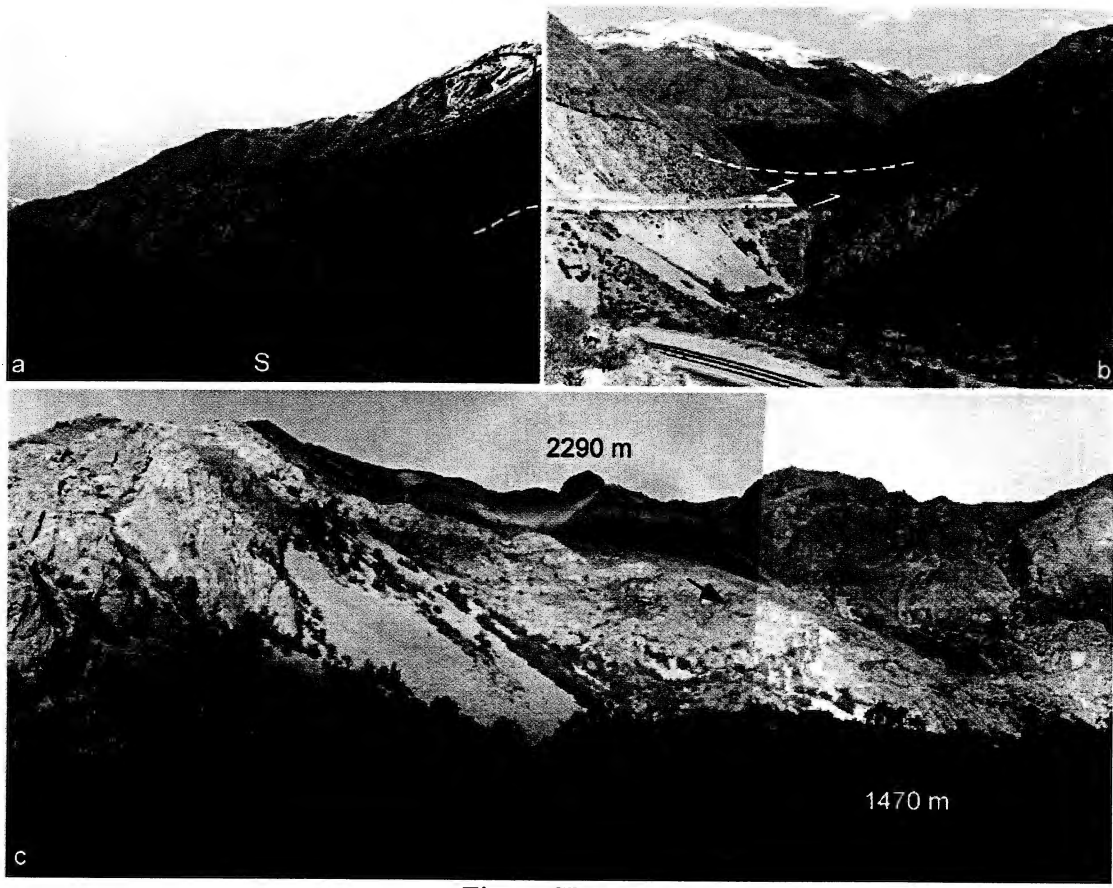


Figure SDF2-4.

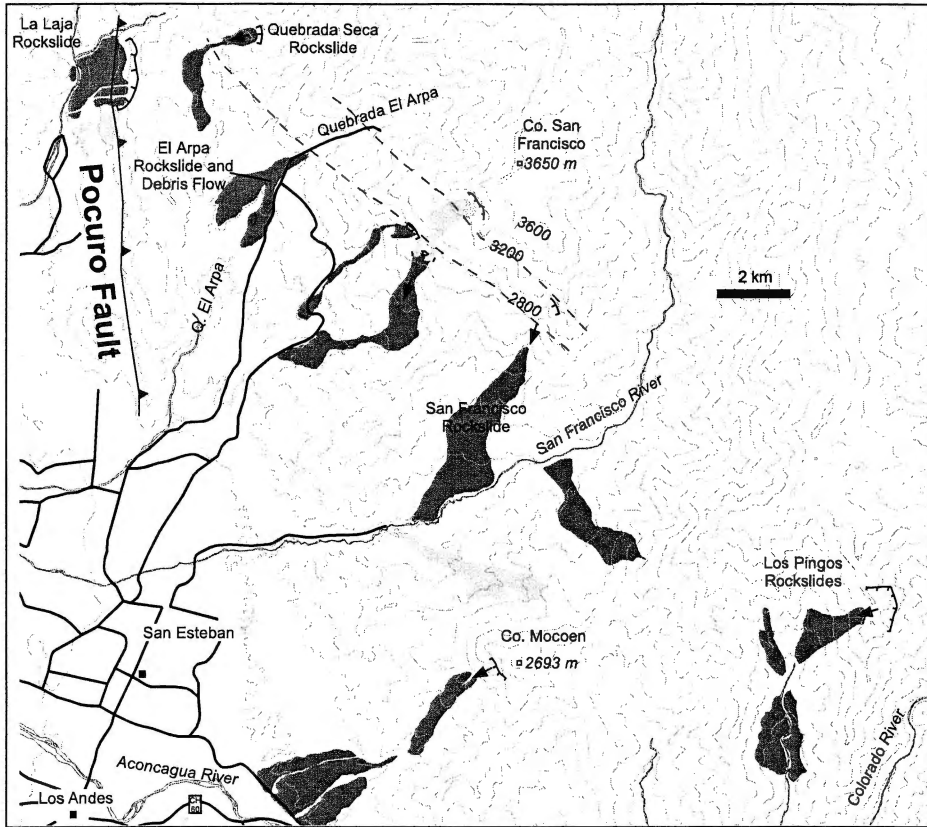


Figure SDF2-5

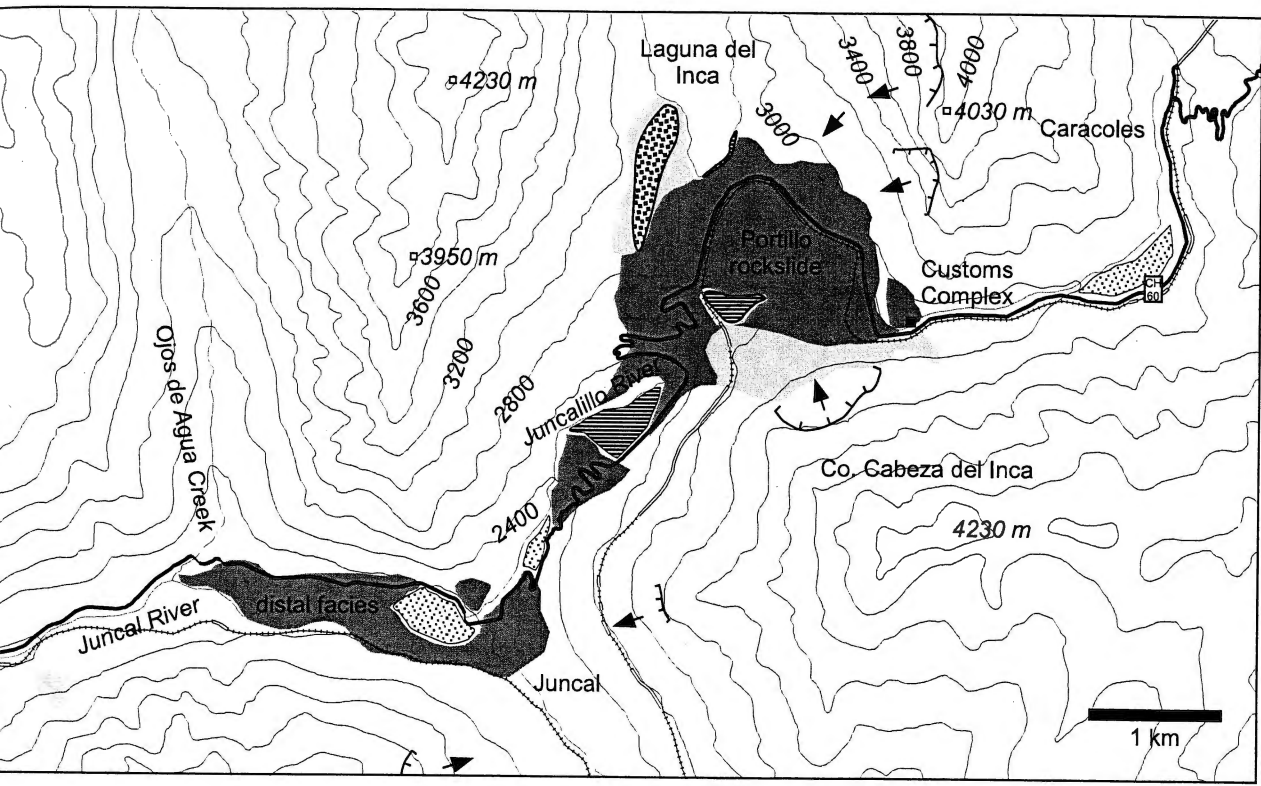


Figure SDF2-6

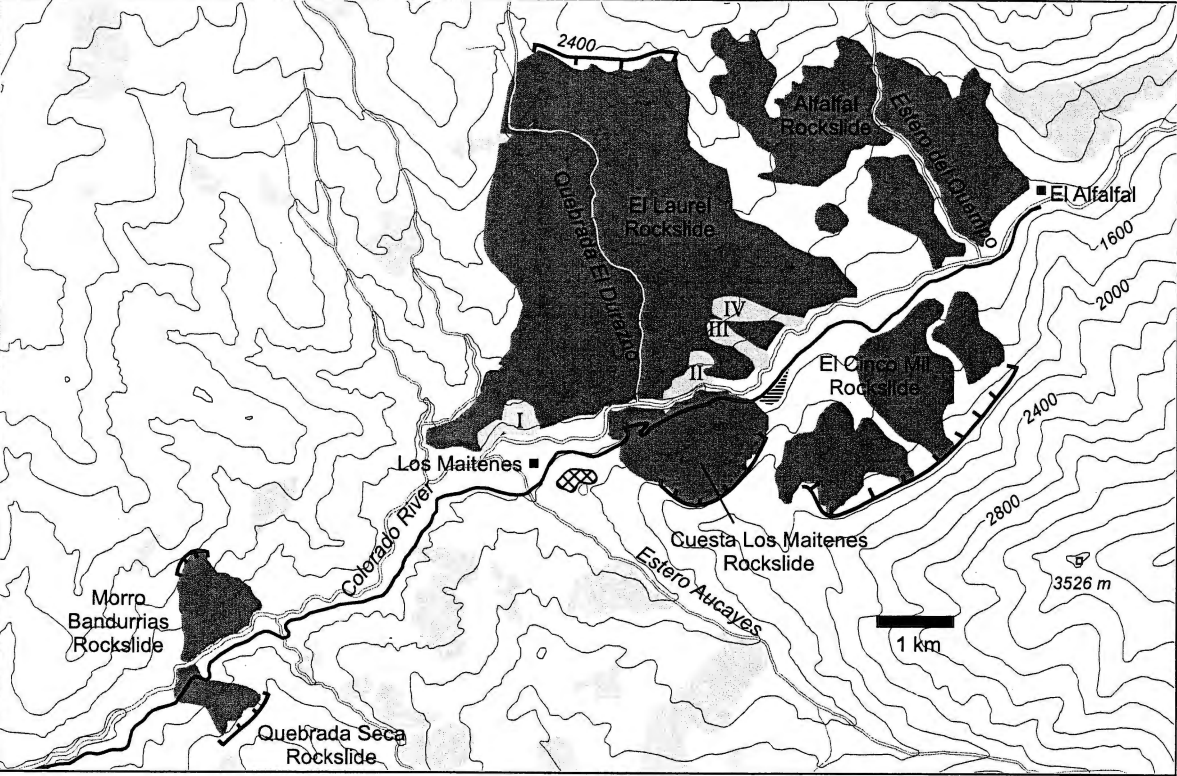


Figure SDF2-7

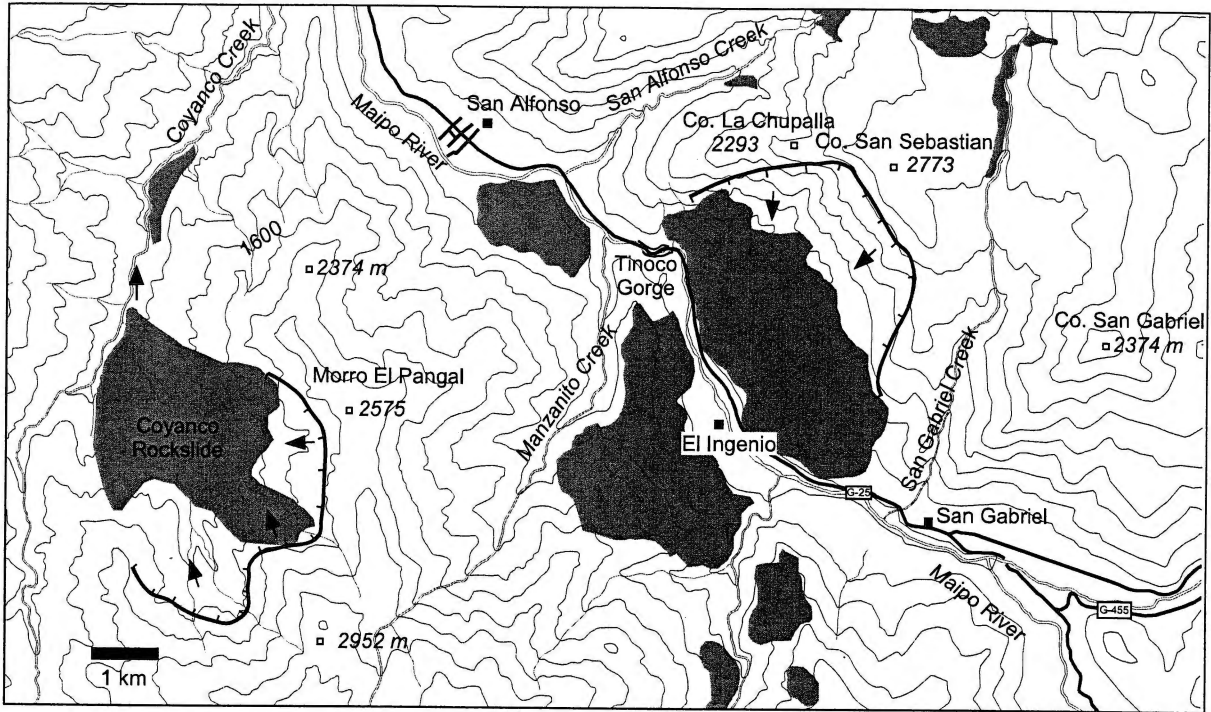


Figure SDF2-8

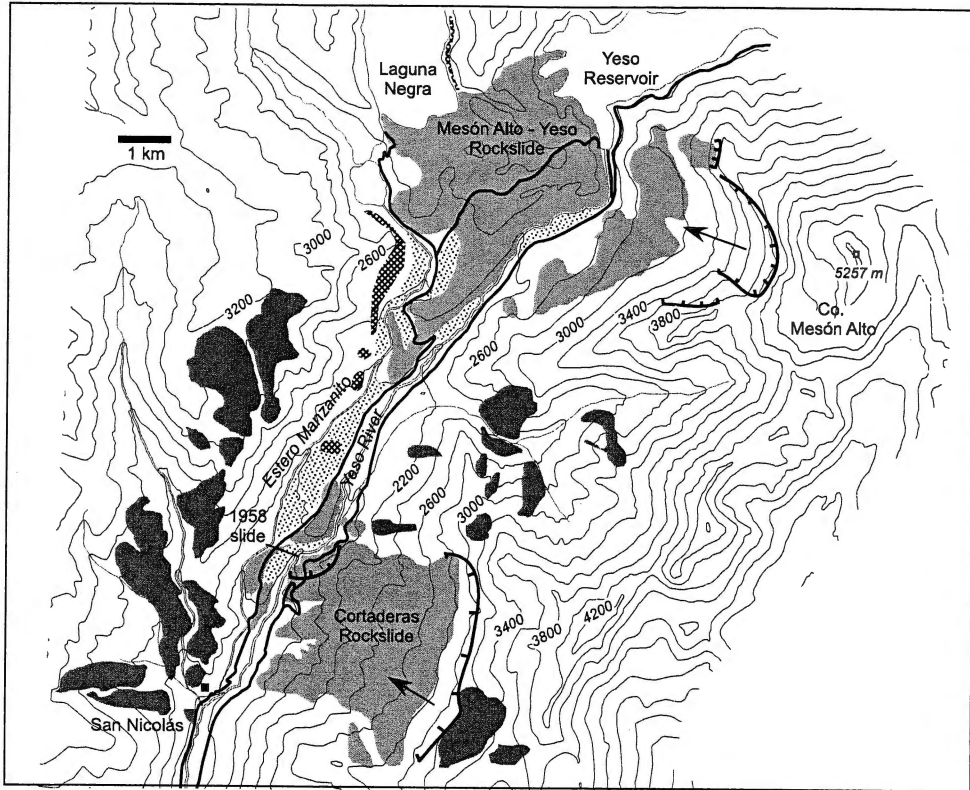


Figure SDF2-9

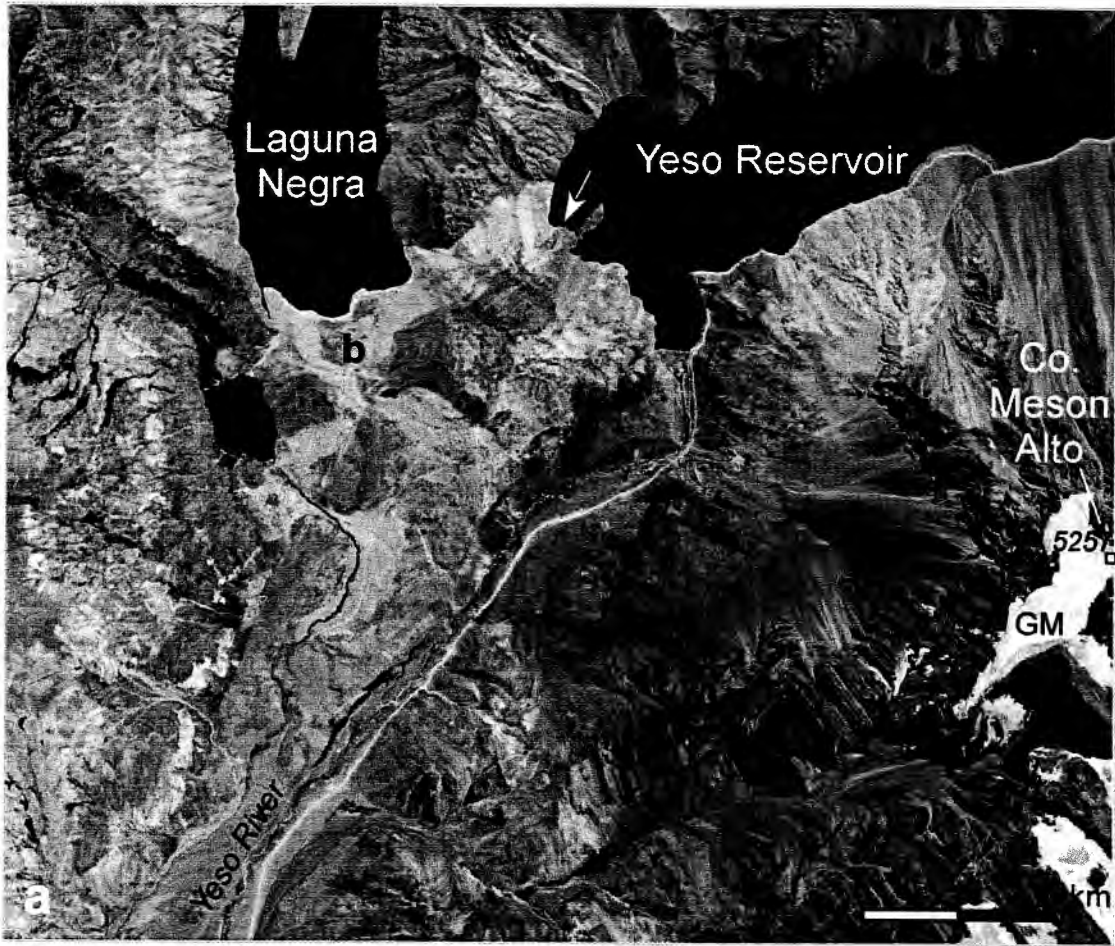


Figure SDF2-10

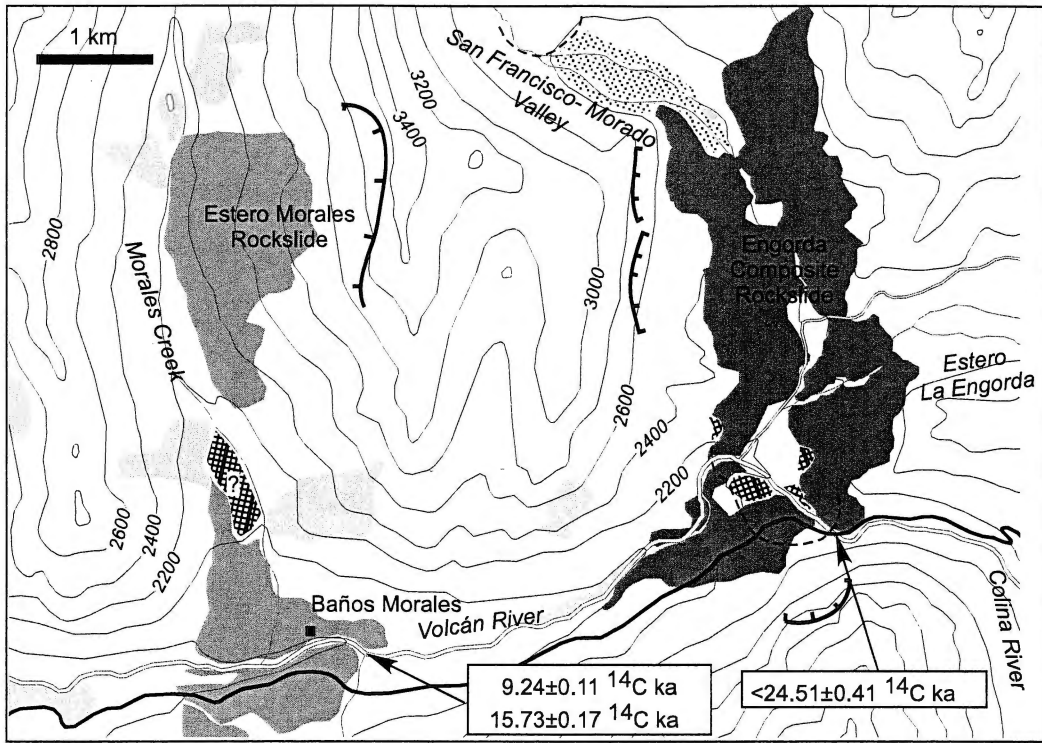


Figure SDF2-11



Figure SDF2-12

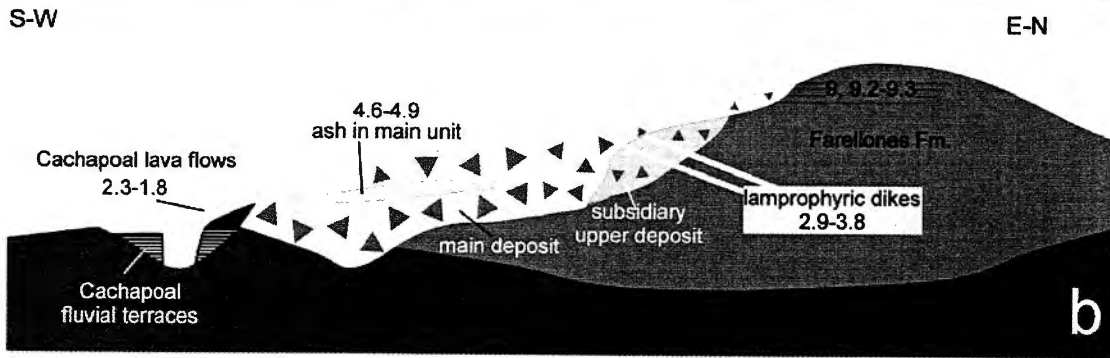
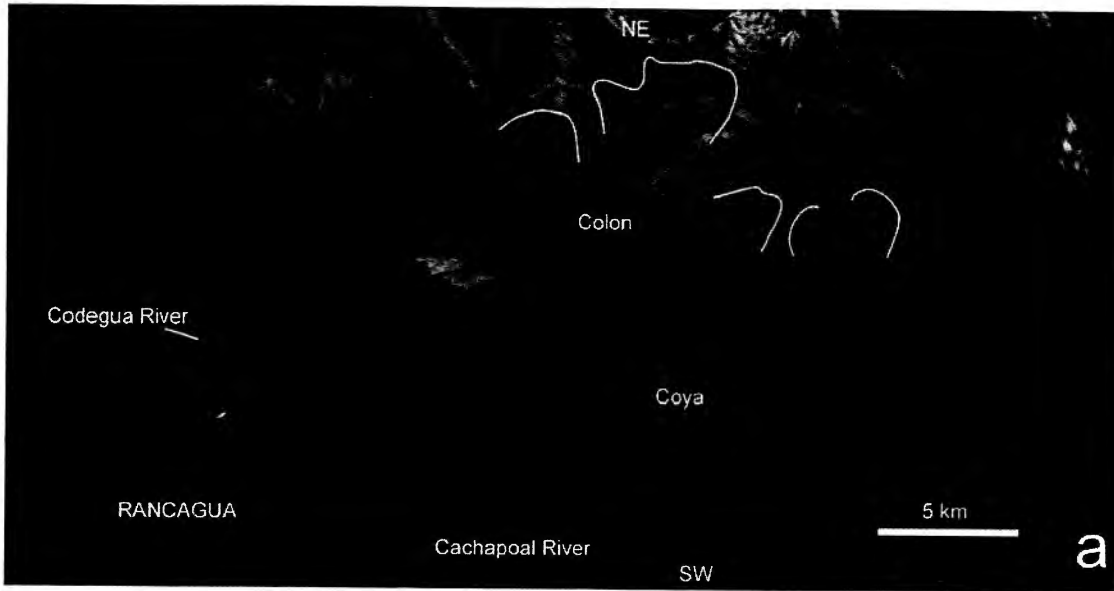


Figure SDF2-13.

A.2. Supplementary Information for Antinao et al.: Quaternary Denudation Styles and Rates in the Southern Central Andes of Chile Inferred From Cosmogenic ³⁶Cl Inventories in Stream Sediments and Modeled Fluvial Transport Rates

A.2.1. Matlab Code for Calculating ³⁶Cl Concentration, Exposure Ages, and Erosion Rates

```
clear;
MISSING='MISSING';
for i=1:3
    figure(i);clf;
end; %clear the figures

%Production Rates%

Pf0          = 626;
pfaststddvn = 40;
%from Phillips et al. (GRL, 1996)

caspsall     = 0.3485; %atom Cl36 / g / y %CaO
caspsallstddvn= 0.01215;
%From Tabernacle Hill (includes +-3.4% 1sigma uncertainty)
%From Stone et al. 1996 GeoCosmoActa, 48.8 at/gCa/y
%caspsall=48.8*0.01*molwtca/molwtca0

camu         = 0.03439; %atom Cl36 /g / y CaO
camustddvn  = 0.00688;
% from Wombeyan (uncertainty set at +-25%)
% set at 20% from the number in Stone's mathematica code

kspall       = 1.337; %atom Cl-36 /g / y %K20
kspallstddvn = 0.075;
%from J. Evans thesis (includes +-5.6% 1 sigma uncertainty)

kmu          = 0.0847; %atom Cl-36 g / y %K20 muon capture properties of K-feldspar
kmustddvn    = 0.0108;
%from J. Evans thesis (includes 12.7% uncertainty)

tispall      = 0.03;% atom Cl36 /% TiO2/yr
tispallstddvn= 0.015; %assumed 50%
%adapted from Fe data and Josef Masarik's GEANT calculations. Uncertainty
%set at +-50% level

timu         = 0.0003; %set to 1% of Ti spall rate
timustddvn   = 0.0003; % assumed 100%
fespall      = 0.0133; %0.6994*1.9021*0.01
%i.e. Fe/Fe2O3 * assumed PFe in atom/gFe/y*0.01, giving P in atom/%Fe2O3/y

fespallstddvn= 0.00133; %assumed 10%
femu         = 0.000133; %set at 1% of the Fe spall rate
femustddvn   = 0.000133; %assumed 100%

%Avogadro Number%
NA           = 6.02214e23;
%lambda - decay constant of Cl36, a^-1%
lambda       = 2.303e-6;
%list of elements%
elements     = {'H' 'Li' 'B' 'C' 'N' 'O' 'Na' 'Mg' 'Al' 'Si' 'P' 'S' 'Cl' 'Ar' 'K' 'Ca'
'Ti' 'Cr' 'Mn' 'Fe' 'Sm' 'Gd' 'Th' 'U'};
```

```

%Neutron parameters%
%all lists below are according to the list of elements in line 56

%atomic weights%
Ak=[1.0 6.94 10.81 12.01 14.01 16.00 22.99 24.31 26.98 28.09 30.97 32.07 35.45 39.94 39.10
40.08 47.88 52.00 54.94 55.85 150.36 157.25 232.05 238.07];
%scattering cross sections in barns per atom%
sigmasck=1e-24.*[20.5 0.95 4.27 4.74 10.0 3.76 3.025 3.42 1.41 2.04 5.0 1.1 15.8 1.5 2.04
2.93 4.09 3.38 2.20 11.35 38 172 12.6 8.3];
%Dilute resonance integrals for absorption in the epithermal region, probably including
thermal abs. in some cases: U-Th%
Iabsk=1e-24.*[0.0 32 1722 0.0016 0.88 0.0004 0.311 0.038 0.17 0.127 0.08 0.25 13.7 0.42
1.0 0.235 3.1 1.6 14 1.39 1400 390 85 278];
Iabs35=15e-24; %Cl-35%
%average log decrement in E per neutron collision
Elossk=[1.0 0.264 0.174 0.158 0.136 0.12 0.084 0.08 0.072 0.07 0.063 0.061 0.055 0.0492
0.05 0.049 0.041 0.038 0.036 0.035 0.013 0.013 0.0086 0.0084];
%elemental cross sections for thermal neutron absorption in barns per atom%
sigmathermal=1e-24.*[0.333 70.5 765 0.0035 1.91 0.00028 0.53 0.063 0.233 0.171 0.18 0.52
33.5 0.66 2.1 0.43 6.1 3.1 13.3 2.56 9640 41560 7.56 7.68];
sigma35 = 43e-24; %Cl35%
sigma39alpha=0.0043e-24; %K39(n,alpha)%
%cross sections for thermal neutron absorption by trace elements in barns
%per atom; order: Li B Cl Cr Sm Gd Th U
sigmathermaltrace=1e-24.*[70.5 765 33.5 3.1 9640 41560 7.56 7.68];
postrace=[0 1 1 0 0 0 0 0 0 0 0 0 1 0 0 0 0 0 1 0 0 1 1 1 1];

%Neutron yields from U- and Th-induced alpha reactions%
%neutron yield per g oxide per year per ppm U and per ppm Th for
%(alpha,n) reactions with rock-forming oxides
sio2yieldu = 0.45 ; sio2yieldth = 0.20;
tio2yieldu = 0.09 ; tio2yieldth = 0.03;
al2o3yieldu = 2.81 ; al2o3yieldth = 1.41;
fe2o3yieldu = 0.20 ; fe2o3yieldth = 0.17;
feoyieldu = 0.20 ; feoyieldth = 0.18;
mnoyieldu = 0.05 ; mnoyieldth = 0.02;
mgoyieldu = 3.59 ; mgoyieldth = 1.60;
caoyieldu = 0.07 ; caoyieldth = 0.02;
na2oyieldu = 10.82 ; na2oyieldth = 5.07;
k2oyieldu = 0.41 ; k2oyieldth = 0.27;
p2o5yieldu = 0.13 ; p2o5yieldth = 0.04;
h2oyieldu = 0.20 ; h2oyieldth = 0.07;
co2yieldu = 0.29 ; co2yieldth = 0.11;

%combine into a matrix, with oxides in the same order as list 'majorelts'
%defined in neutron calculations below%

nyields=[sio2yieldu sio2yieldth; tio2yieldu tio2yieldth; al2o3yieldu al2o3yieldth;
fe2o3yieldu fe2o3yieldth; feoyieldu feoyieldth; mnoyieldu mnoyieldth; mgoyieldu
mgoyieldth; caoyieldu caoyieldth; na2oyieldu na2oyieldth; k2oyieldu k2oyieldth; p2o5yieldu
p2o5yieldth; h2oyieldu h2oyieldth; co2yieldu co2yieldth];

%SAMPLE INFO

load('sx.mat');
%this variable must be available in the local directory

%general data
samplename= sx(1);% eg from 'CNEF5033' only id ...5033 in this case
samplewt = sx(35);%40.0004; %correct for real value of sample dissolved%
density = sx(55);%2.6 ; % assume a slightly higher value - granitoid
top = sx(56);%0 ; %depth to top in cm
bottom = sx(57);%3 ;
latitude = sx(58);%35; %aprox, correct if it is negative, and improve pos data
longitude = sx(59);%70; %the same that above but irrelevant as geomagnetic not impl
altitude = sx(60);%1500; %this in meters

```

```

horizonfactor = sx(61);%1; %it must be calculated using cellshield.m before spreadsheet

%following numbers are manually adapted to each sample
totalerosion = sx(62);% 1; %estimated depth eroded in cm
if sx(63)==1
    initcl36='steadystate';
end; %enter 'steadystate' if surface was created from an old rock mass, 0 if fresh - lava
flow
carriercl = sx(36)*1000; %2373.5; %not this sample correct it !! %weight carrier Cl in
mg
clrunblank = sx(41);%15; %blank cl [in g]
clrunblank2 = 1e-5; %this is rather arbitrary, but it refers to a longterm blank
uncertainty.
cl36ratio(1) = sx(31);%12.67; %Cl36/Cl and uncertainty below 1e-15 atom/atom
cl36ratio(2) = sx(32);%3.43;
cl36runblank(1)=sx(43);
cl36runblank(2)=1e5;%blank and uncertainty -approx. in atoms long term uncert.?
flag=sx(64); %isotopic dilution activated if 1... this will be most of the cases
cl3537ratio(1)= sx(33);%24.29; %Cl35/Cl37 ratio if it is a cl35, it must be more than 3.12
cl3537ratio(2)= sx(34);%0.1;%error

%isotopic dilution calc
weight35=34.9688; %g/mol atomic weight Cl-35
weight36=35.968 ; %g/mol atomic weight Cl-36
weight37=36.9659; %g/mol atomic weight Cl-37
weightcl=35.453; %g/mol atomic weight Cl
if flag==1
    factorw=weight35./weight37.*cl3537ratio(1);
    spikewt=sx(36); % 4.025 (previous) ;%g Cl-35 spike, previously sample wt was
displayed;
    spikect=sx(37);%Conc spike in ppm
    aspike=0.999; %abundance of 35 in spike solution... checked on Oak Ridge NL bottle
    anormal=0.7578; %normal abundance 35-37 check that...
    %isotope dilution calc
    %old calc... samplect=spikewt./samplewt.*spikect.*(aspikes-factorw.*(1-
aspikes))./(factorw.*(1-anormal)-anormal);
    samplect=1./samplewt.*(((factorw+1).*aspikes-
factorw).*spikewt*spikect+((factorw+1).*anormal-factorw).*clrunblank)./(factorw-
(1+factorw).*anormal);
    dclratio=spikewt.*spikect./samplewt.*weight35./weight37.*((aspikes-1).*(factorw-
(1+factorw).*anormal)+(1-anormal).*((factorw+1).*aspikes-factorw))./(factorw-
(1+factorw).*anormal).^2;
    samplectstdvnsqrt=(cl3537ratio(2).^2*dclratio.^2+clrunblank2.^2/samplewt.^2)
    %sample concentration in [g/g]
    %old calc cl36clsample=cl36ratio.*(1+(spikect.*spikewt./samplewt./samplect)); %ratio
real
    %cl36ratio=cl36clsample;%replace the value
    cl(1)=samplect*1000000; %cl in ppm
    cl(2)=samplectstdvnsqrt*1e6; %std dev
end;
%extra solo para figura

%Whole rock composition%
%oxide wt% then relative standard deviation assigned to each%
sio2 =[sx(2) 0.01];
tio2 =[sx(9) 0.01];
al2o3=[sx(3) 0.01];
fe2o3=[sx(4) 0.01];
feo =[0 0.01]; %actually not reported%
mno =[sx(11) 0.01];
mgo =[sx(5) 0.01];
cao =[sx(6) 0.01];
na2o =[sx(7) 0.01];
k2o =[sx(8) 0.01];
p2o5 =[sx(10) 0.01]; %<0.01 reported%
h2o =[sx(13) 0.1]; %reported as LOI - unknown temp assumed 110 C % uncertainty!!
co2 =[0 0]; %may be included in the LOI assumed 0%

%trace elements ppm then absolute - ppm uncertainty%

```

```

%these are affecting neutron flux then they need to be measured in original
%whole rock
li=[sx(27) 0]; %reported sometimes, if %, factor 1e4 must be used sx(27)*1e4 ppm=nofactor
b=[sx(19) 0]; %<4% should be in ppm... check which one is used
clwr=[5 10]; %unrep, repeat of the values above!%
cr=[sx(12)*1e4*104/152 0]; %actually reported as % oxide Cr2O3
%v2O5 is reported but never used sx(33);
sm=[sx(18) 0.1]; %if not available value for rock unit can be used all ppm%
gd=[sx(20) 1]; %if not available value for rock unit can be used%
u=[sx(16) 0.1]; %if not available value for rock unit can be used%
th=[sx(17) 0.1]; %if not available value for rock unit can be used%
so4=[0 0]; %to compile -not used- there is similar code in the mathematica version%
s=so4; %idem%

```

```

spallationcontributorsanalysedafterleaching=1;
if spallationcontributorsanalysedafterleaching
% the following is if the spallation components were measured after
% leaching (which normally is)
caomin(1)=cao(1); caomin(2)=cao(2);
k2omin(1)=k2o(1); k2omin(2)=k2o(2);
tio2min(1)=tio2(1); tio2min(2)=tio2(2);
fe2o3min(1)=fe2o3(1); fe2o3min(2)=fe2o3(2);
else
%otherwise these numbers have to be provided independently as here
caomin(1)=3.68; caomin(2)=0.01;
k2omin(1)=0.21; k2omin(2)=0.01;
tio2min(1)=2.11; tio2min(2)=0.01;
fe2o3min(1)=14.39; fe2o3min(2)=0.01;
end;

```

```

if flag~=1
cl(1)=clwr(1); %this will assign cl composition of target as whole rock cl
cl(2)=clwr(2); %
end;
N35=(NA.*samplect./weightcl).*anormal;

```

```

% CALCULATIONS
% Preliminary calculations
% 1.- Cl-36 concentration

```

```

cl36concentration=((cl36ratio(1))*1e-
15*NA*((samplewt.*(samplect)+clrunblank)./weightcl+spikewt.*spikect./weight35)-
(cl36runblank(1)))./samplewt;
%it needs samplect in [g/g] or cl(1)/1e6
%cl36concentration=(cl36ratio(1).*1e-
15.*1.698635e16.*(samplewt.*cl(1)+1000*carriercl+1e6*clrunblank)-
cl36runblank(1))./samplewt;
%extra step really needed... caocarb=caomin? then caocarb was used...

```

```

cl36concentrationstdv=NA.*1e-
15./samplewt./weightcl.*sqrt((samplewt.*samplect+clrunblank).^2.*cl36ratio(2).^2+samplewt.
^2*samplectstdv.^2+clrunblank2.^2+weightcl.^2./(NA*1e-15).^2.*cl36runblank(2).^2);
caocarb=caomin;
clcaratio=cl36concentration./caocarb(1)/(NA./56.0774/100);
clcaratiostdv=clcaratio.*sqrt((cl36concentrationstdv./cl36concentration).^2+caocarb(2)
.^2);

```

```

% 2.- Neutrons

```

```

if abs(latitude)>60
LAMBDAF=150;
elseif abs(latitude)<=60 && abs(latitude)>20
LAMBDAF=160;
else LAMBDAF=170;
end;

```

```

gamma=LAMBDAF; %attenuation length in g/cm^2 see mathematica code

```

```

if flag~=1
    wholerockcl=clwr; %reassignment%
else
    wholerockcl=cl; %reassignment of the calculated value
end;

%Neutron calculations%

%takes oxides and trace elem data, converts them into wt. fractions (g/g)
%of each of the 24 elements%

Wkrock=0.01*[0.1111.*h2o(1) 1e-4.*li(1) 1e-4.*b(1) 0.2729.*co2(1) 0.0
0.8888.*h2o(1)+0.7271.*co2(1)+0.2581.*na2o(1)+0.3970.*mgo(1)+0.4708.*al2o3(1)+0.5326.*sio2
(1)+0.5636.*p2o5(1)+0.6662.*so4(1)+0.1699.*k2o(1)+0.2853.*cao(1)+0.4006.*tio2(1)+0.2255.*mno
(1)+0.3006.*fe2o3(1)+0.2227.*feo(1) 0.7419.*na2o(1) 0.6030.*mgo(1) 0.5292.*al2o3(1)
0.4674.*sio2(1) 0.4364.*p2o5(1) 0.3338.*so4(1)+1.0.*s(1) 1e-4.*wholerockcl(1) 0.0
0.8301.*k2o(1) 0.7147.*cao(1) 0.5994.*tio2(1) 1e-4.*cr(1) 0.7745.*mno(1)
0.6694.*fe2o3(1)+0.7773.*feo(1) 1e-4.*sm(1) 1e-4.*gd(1) 1e-4.*th(1) 1e-4.*u(1)];
%converts Wk into mol fractions mol k/mol rock of each of the 24 elements;
%dot product in the denominator sums up all molar abundances to give the
%total mol/g rock%
fkrock=(Wkrock.*Ak.^-1)/(Wkrock*(Ak.^-1));
%mean atomic weight of the rock%
Arock=fkrock*Ak';
%atom abundances atom k/g rock%
Nkrock=NA.*(Wkrock.*Ak.^-1);
%now compares all indices%
display('comparison ');
sum(Wkrock) %close to 1.00 %
(Wkrock*(Ak.^-1)).^-1
Arock

%Uncertainties
Wkrockstddvn=0.01*[0.1111*h2o(1)*h2o(2) 1e-4*li(2) 1e-4*b(2) 0.2729*co2(1)*co2(2) 0.0
sqrt((0.8888*h2o(1)*h2o(2)).^2+(0.7271*co2(1)*co2(2)).^2+(0.2581.*na2o(1).*na2o(2)).^2+(0.3970*mgo(1)*mgo(2)).^2+(0.4708*al2o3(1)*al2o3(2)).^2+(0.5326*sio2(1)*sio2(2)).^2+(0.5636*p2o5(1)*p2o5(2)).^2+(0.1699*k2o(1)*k2o(2)).^2+(0.2853*cao(1)*cao(2)).^2+(0.4006*tio2(1)*tio2(2)).^2+(0.2255*mno(1)*mno(2)).^2+(0.3006*fe2o3(1)*fe2o3(2)).^2+(0.2227*feo(1)*feo(2)).^2+(0.7419*na2o(1)*na2o(2) 0.6030*mgo(1)*mgo(2) 0.5292*al2o3(1)*al2o3(2)
0.4674*sio2(1)*sio2(2) 0.4364*p2o5(1)*p2o5(2) 0.3338.*so4(2)+1.0.*s(2) 1e-4*wholerockcl(2)
0.0 0.8301*k2o(1)*k2o(2) 0.7147*cao(1)*cao(2) 0.5994*tio2(1)*tio2(2) 1e-4*cr(2)
0.7745*mno(1)*mno(2) sqrt((0.6694*fe2o3(1)*fe2o3(2)).^2+(0.7773*feo(1)*feo(2)).^2) 1e-4*sm(2) 1e-4*gd(2) 1e-4*th(2) 1e-4*u(2)];
Arockstddvn=sqrt(sum(Wkrockstddvn.^2.*Ak.^2));
Nkrockstddvn=NA./Ak.*Wkrockstddvn;

%Air calculations%
%start with the mol fractions%
fkair=[0.0 0.0 0.0 0.0 0.78 0.21 0.0 0.0 0.0 0.0 0.0 0.0 0.0 0.0 0.0 0.0 0.0 0.0 0.0 0.0 0.0 0.0 0.0 0.0];
%Aair is given by the dot product with Ak%
Aair=dot(fkair,Ak);
%abundances in air%
Nkair=NA.*fkair./Aair;
%Macroscopic scattering cross section of the rock%
SIGMAscrock=dot(sigmatck,Nkrock);
%Macroscopic scattering cross-section of air%
SIGMAscair=dot(sigmatck,Nkair);

%Uncertainties
SIGMAscrockstddvn=NA.*sqrt(sum(Wkrockstddvn.^2.*sigmatck.^2./Ak.^2));

%Epithermal Neutron transport properties%
Dethrock = (3.*SIGMAscrock.*(1-2.*(3.*Arock).^-1)).^-1;
Dethair = (3.*SIGMAscair.*(1-2.*(3.*Aair).^-1)).^-1;
Ieffrock = dot(Iabsk,Nkrock);
Ieffair = dot(Iabsk,Nkair);
AVGELOSSrock = sum(Elossk.*sigmatck.*Nkrock)./SIGMAscrock;

```

```

AVGELOSSair = sum(Elossk.*sigmasck.*Nkair)./SIGMAScair;
LAMBDAethrock= (AVGELOSSrock.*(Ieffrock+SIGMAScrock)).^-1;
LAMBDAethair = (AVGELOSSair.*(Ieffair+SIGMAScair)).^-1;
SIGMAethrock = (LAMBDAethrock).^-1;
SIGMAethair = (LAMBDAethair).^-1;
Rethrock = (Arock./Aair).^0.5;
Rethair = 1.0;
Lethrock = (Dethrock./SIGMAethrock).^0.5;
Lethair = (Dethair./SIGMAethair).^0.5;
cl35epicapturefrn = Iabs35.*N35./Ieffrock; %N35 must be defined before this line%

%Uncertainties
Ieffrockstddvn=NA*sqrt(sum(Wkrockstddvn.^2.*Iabsk.^2./Ak.^2));

%Thermal neutron transport properties%

Dthermalrock = (3.*SIGMAScrock.*(1-2.*(3.*Arock).^-1)).^-1;
Dthermalair = (3.*SIGMAScair.*(1-2.*(3.*Aair).^-1)).^-1;
pEthermalrock = exp(-(Ieffrock./SIGMAScrock));
pEthermalair = exp(-(Ieffair./SIGMAScair));
Rthermalrock = pEthermalrock./pEthermalair;
Rthermalair = 1;
SIGMAthermalrock = dot(sigmathermalk,Nkrock);
SIGMAthermalair = dot(sigmathermalk,Nkair);
LAMBDAthermalrock = SIGMAthermalrock.^-1;
LAMBDAthermalair = SIGMAthermalair.^-1;
lthermalrock = (Dthermalrock./SIGMAthermalrock)^0.5;
lthermalair = (Dthermalair./SIGMAthermalair)^0.5;
cl35capturefrn= cl(1).*43.6e-24.*1.6986e16.*0.7577./SIGMAthermalrock; %fraction of
thermalized neutrons captured by Cl-35
absorb=NA.*Wkrock.*sigmathermalk./Ak;majorabsorber=elements(find(absorb==max(absorb)));
%find the major absorber
SIGMAthermaltr=dot(sigmathermalk.*postrace,Nkrock); %cross section for
absorption by trace elem. only
stopping=[1-SIGMAthermaltr/SIGMAthermalrock SIGMAthermaltr/SIGMAthermalrock]; %fraction of
thermal n capture by major,trace

%Uncertainties
SIGMAthermalrockstddvn=NA.*sqrt(sum(sigmathermalk.^2.*Wkrockstddvn.^2./Ak.^2));
cl35capturefrnstdvnc=cl35capturefrn.*sqrt((cl(2)/cl(1)).^2+(SIGMAthermalrockstddvn./SIGMA
thermalrock).^2);
Dthermalrockstddvn=((-1/(3*(1-2/(3*Arock)))*SIGMAScrock.^2).*SIGMAScrockstddvn).^2+(-
2/(9.*(1-2/(3*Arock))).^2.*Arock.^2.*SIGMAScrock).*Arockstddvn).^2).^0.5;
lthermalrockstddvn=1/2.*sqrt(Dthermalrockstddvn.^2./SIGMAthermalrock./Dthermalrock+Dtherma
lrock.*SIGMAthermalrockstddvn.^2./SIGMAthermalrock.^3);
N35stdvn=NA.*samplectstddvn.*anormal./weightcl;
cl35epicapturefrnstdvnc=Iabs35./Ieffrock.*sqrt(N35stdvn.^2+N35.^2.*Ieffrockstddvn.^2./Ief
frock.^2);

%extra factors only for uncertainty estimation
%resonance escape ratio (ref. page 23 mathematica code by Stone
AVGELOSSrockstddvn=1./SIGMAScrock.*sqrt(sum(Elossk.^2.*sigmasck.^2.*Nkrockstddvn.^2)+AVGEL
OSSrock.^2.*SIGMAScrockstddvn.^2);
pEthermalrockstddvn=((-
(1/(exp(Ieffrock./AVGELOSSrock).*AVGELOSSrock)).*Ieffrockstddvn).^2+(Ieffrock./exp(Ieffro
ck./AVGELOSSrock).*AVGELOSSrock.^2).*AVGELOSSrockstddvn).^2).^0.5;
r=(pEthermalrock/0.56).* (Arock./14.675).^0.5;
rstddvn=((0.466147.*Arock.^0.5.*pEthermalrockstddvn).^2+((0.23307.*pEthermalrock)/Arock.^
0.5.*Arockstddvn).^2).^0.5;
repi=((1-pEthermalrock)/0.44).* (Arock./14.675).^0.5;
repistddvn=((-0.593278.*Arock.^0.5.*pEthermalrockstddvn).^2+((0.29664.*(1-
pEthermalrock)/Arock.^0.5).*Arockstddvn).^2).^0.5;
phistar=0.56.*r./SIGMAthermalrock;
phistarstddvn=((0.56.*rstddvn./SIGMAthermalrock).^2+((-
0.56.*r).*SIGMAthermalrockstddvn./SIGMAthermalrock.^2).^2).^0.5;
deltaphi=0.56.*(16.611-(r./SIGMAthermalrock));
deltaphistddvn=((( -
0.56)/SIGMAthermalrock).*rstddvn).^2+(((0.56.*r)/SIGMAthermalrock.^2).*SIGMAthermalrocks
tddvn).^2).^0.5;

```

```

fthermal=((0.915./(3.9.*Dthermalrock)) + gamma.^-
1)./((0.915./(3.9.*Dthermalrock))+Lthermalrock.^-1);
fthermalstdvsn=((0.234615.*(0.234615./Dthermalrock + gamma.^-
1))/(Dthermalrock.^2.*(0.234615./Dthermalrock+Lthermalrock.^-1).^2) -
0.234615./(Dthermalrock.^2.*(0.234615./Dthermalrock + Lthermalrock.^-
1))).^2.*Dthermalrockstdvsn.^2 + ((0.234615./Dthermalrock + gamma.^-
1)/(0.234615./Dthermalrock + Lthermalrock.^-
1).^2.*Lthermalrock.^2).^2.*Lthermalrockstdvsn.^2).^0.5;
fepi=cl35epicapturefrn;
fepistddvn=cl35epicapturefrnstdvsn;

%3.- PRODUCTION RATES

%SCALING
%the following calls a function to scale...
%input may be vectors but usually will be scalars

smfactor          = scale(latitude,altitude);
muonfactor        = smfactor(2,:);
spallationfactor  = smfactor(1,:);

%no antarctica still, easy to implement, see mathematica code

%note calculation for horizon-shielding in cellshield

depthfactor       = (gamma./(density.*(bottom-top)))*(exp(-density.*top./gamma)-exp(-
density.*bottom./gamma));
depthfactormuons  = (1500./(density.*(bottom-top)))*(exp(-density.*top./1500)-exp(-
density.*bottom./1500));
surfacefactor     = horizonfactor.*depthfactor;
surfacefactormuons=horizonfactor.*depthfactormuons;
% N35             = (NA.*1e-6*cl(1)./35.453).*0.7577; %changed up to improve matlab code
N39               = k2omin(1).*1.2787e20.*0.93258; %first number is atoms K per % k2o
second is k-39/k ratio
k39capturefrn    = sigma39nalpha.*N39./SIGMathermalrock;

%Epithermal neutron flux

phistarethrocks  =
(0.8.*spallationfactor+0.2.*muonfactor).*horizonfactor.*Pf0.*Rethrock./(SIGMAethrock-
Dethrock./LAMBDAF.^2);
phistarethairs   =
(0.8.*spallationfactor+0.2.*muonfactor).*horizonfactor.*Pf0.*Rethair./(SIGMAethair-
Dethair./LAMBDAF.^2);
faux1            = (Dethrock./LAMBDAF).*(phistarethrocks-
(Dethair/Dethrock).*(phistarethairs)); %auxiliary to clean code
faux2            = Dethrock./Lethrock+Dethair./Lethair; %auxiliary to clean code - not in
Mathematica code
FDELTAphistarethrocks= ((Dethair./Lethair).*(phistarethairs-phistarethrocks)-faux1)./faux2;
FDELTAphistarethairs = ((Dethrock./Lethrock).*(phistarethrocks-phistarethairs)-faux1)./faux2;

%pass on 4 values to function phieth(z)

phistarthermalrock=
pEthermalair.*Rthermalrock.*phistarethrocks./(LAMBDAethrock.*(SIGMathermalrock-
Dthermalrock./LAMBDAF.^2));
phistarthermalair =
pEthermalair.*Rthermalair.*phistarethairs./(LAMBDAethair.*(SIGMathermalair-
Dthermalair./LAMBDAF.^2));
FcursDELTAphistarethrocks =
pEthermalair.*Rthermalrock.*FDELTAphistarethrocks./(LAMBDAethrock.*(SIGMathermalrock-
Dthermalrock./Lethrock.^2));
FcursDELTAphistarethairs =
pEthermalair.*Rthermalair.*FDELTAphistarethairs./(LAMBDAethair.*(SIGMathermalair-
Dthermalair./Lethair.^2));
faux3=(Dthermalrock./Lthermalrock + Dthermalair./Lthermalair).^-1;

```

```

faux4=(Dthermalair.*(phistarthermalair./LAMBDAF-FcursDELTAphistarethair./Lethair))-
(Dthermalrock.*(phistarthermalrock./LAMBDAthermalrock +
FcursDELTAphistarethrook./Lethrock));
faux5=(phistarthermalrock-phistarthermalair+FcursDELTAphistarethrook-
FcursDELTAphistarethair);
FcursDELTAphistarthermalair = faux3.*(faux4+(Dthermalrock./Lthermalrock.*faux5));
FcursDELTAphistarthermalrock = faux3.*(faux4-(Dthermalair./Lthermalair.*faux5));

%pass on 6 values to function phithermal(z)

%matrices to pass on variables

Methrock = [phistarethrook LAMBDAF FDELTAphistarethrook Lethrock];
Mthermalrock = [phistarthermalrock LAMBDAF FcursDELTAphistarethrook Lethrock
FcursDELTAphistarthermalrock Lthermalrock];
Methair = [phistarethair LAMBDAF FDELTAphistarethair Lethair ];
Mthermalair = [phistarthermalair LAMBDAF FcursDELTAphistarethair Lethair
FcursDELTAphistarthermalair Lthermalair];

% z presentation of thermal and eth neutron flux
%red epith blue thermal

figure(1);
[x,y]=fplot(@phieth,[0 350],1e-3,1,[],Methrock,Methair);
plot(x,y,'-r');
[x1,y1]=fplot(@phithermal,[0 350],1e-3,1,[],Mthermalrock,Mthermalair);
hold on;
plot(x1,y1,'-b');
hold off;
xlabel('Depth [cm]');
ylabel('Neutron Flux [n g cm-2]');
title('Neutron Flux with Depth');

% to obtain production rates vs. z, new functions are defined outside, multiplying...

% peth(z)=phieth(z)*Iabs35*N35 ... from Mathematica code
% p35th(z)=phithermal(z)*sigma35*N35 ...
% p39th(z)=phithermal(z)*sigma39alpha*N39...

% the following values are useful and are computed directly...

peth0=phieth(0.0,Methrock, Methair).*Iabs35.*N35;
p35th0=phithermal(0.0,Mthermalrock, Mthermalair).*sigma35.*N35;

% also they can be calculated using the functions:
% peth0=peth(0.0,Methrock, Methair,Iabs35,N35)
% p35th0=p35th(0.0,Mthermalrock, Mthermalair,sigma35,N35)
%

%Plot of production rates - n derived
figure(2);
[x,y]=fplot(@peth,[0 350],1e-3,1,[],Methrock,Methair,Iabs35,N35);
plot(x,y,'-r');
[x1,y1]=fplot(@p35th,[0 350],1e-3,1,[],Mthermalrock,Mthermalair,sigma35,N35);
hold on;
plot(x1,y1,'-b');
[x2,y2]=fplot(@p39th,[0 350],1e-3,1,[],Mthermalrock,Mthermalair,sigma39alpha,N39);
hold on;
plot(x2,y2,'-g');
xlabel('Depth [cm]');
ylabel('Production rate [atom g-1 year-1]');
title('Production Rate with Depth');

display('production rates');

```



```

%integration over depth

pnepithermal = quad(@(z) phieth(z, Methrock,
Methair), density*top, density*bottom) .* Iabs35.*N35./ (density*bottom-density*top);
p35nthermal = quad(@(z) phithermal(z, Mthermalrock,
Mthermalair), density*top, density*bottom) .* sigma35.*N35./ (density*bottom-density.*top);
p39nthermal = p35nthermal.*(sigma39alpha.*N39) ./ (sigma35.*N35);

%depth and thickness corrections for thermal and epithermal n capture (by
%integration)

nepizcorrection=pnepithermal/peth00;
nthermalzcorrection=p35nthermal/p35th00;

%uncertainties on local prod. rates
p35nthermalstdvvn=((p35nthermal.*pfaststdvvn./Pf0).^2+(p35nthermal.*cl(2)./cl(1)).^2+((0.8
.*spallationfactor+0.2.*muonfactor).*Pf0.*horizonfactor.*nthermalzcorrection.*5.6614e-
7.*cl(1).*phistarstdvvn).^2+((0.8.*spallationfactor+0.2.*muonfactor).*Pf0.*horizonfactor.*
nthermalzcorrection.*5.661e-
7.*cl(1).*deltaphi.*fthermalstdvvn).^2+((0.8.*spallationfactor+0.2.*muonfactor).*Pf0*horiz
onfactor.*nthermalzcorrection.*5.6614e-7.*cl(1).*fthermal.*deltaphistddvvn).^2).^0.5;
pnepithermalstdvvn=pnepithermal.*((fepistddvvn./fepi).^2+(pfaststdvvn./Pf0).^2+(repistddvvn.
/rep1).^2).^0.5;

%finish integration over depth, local prod rates given
% other local Production rates and uncertainties

pcaspall= surfacefactor.*spallationfactor.*casvall.*caomin(1);
pcamu = depthfactormuons.*horizonfactor.*muonfactor.*camu.*caomin(1);
pkspall = surfacefactor.*spallationfactor.*kspall.*k2omin(1);
pkmu = depthfactormuons.*horizonfactor.*muonfactor.*kmu.*k2omin(1);
ptispall= surfacefactor.*spallationfactor.*tispall.*tio2min(1);
ptimu = depthfactormuons.*horizonfactor.*muonfactor.*timu.*tio2min(1);
pfespall= surfacefactor.*spallationfactor.*fespall.*fe2o3min(1);
pfemu = depthfactormuons.*horizonfactor.*muonfactor.*femu.*fe2o3min(1);
pmuneutrons = depthfactormuons.*horizonfactor.*muonfactor.*175.*0.5.*cl35capturefrn;

pcaspallstdvvn=surfacefactor.*spallationfactor.*((casvall.*caocarb(2)).^2+(caocarb(1).*cas
pallstdvvn).^2).^0.5;
pcamustddvn
=surfacefactormuons.*muonfactor.*((camu.*caocarb(2)).^2+(caocarb(1).*camustddvn).^2).^0.5;
pkspallstdvvn
=surfacefactor.*spallationfactor.*((kspall.*k2omin(2)).^2+(k2omin(1).*kspallstdvvn).^2).^0
.5;
pkmustddvn
=surfacefactormuons.*muonfactor.*((kmu.*k2omin(2)).^2+(k2omin(1).*kmustddvn).^2).^0.5;
ptispallstdvvn=surfacefactor.*spallationfactor.*((tispall.*tio2min(2)).^2+(tio2min(1).*tisp
allstdvvn).^2).^0.5;
ptimustddvn
=surfacefactormuons.*muonfactor.*((timu.*tio2min(2)).^2+(tio2min(1).*timustddvn).^2).^0.5;
pfespallstdvvn=surfacefactor.*spallationfactor.*((fespall.*fe2o3min(2)).^2+(fe2o3min(1).*f
espallstdvvn).^2).^0.5;
pfemustddvn
=surfacefactormuons.*muonfactor.*((femu.*fe2o3min(2)).^2+(fe2o3min(1).*femustddvn).^2).^0.
5;
p39nthermalstdvvn=p39nthermal.*((pfaststdvvn/Pf0).^2+k2omin(2).^2).^0.5;
%above is simplified. Assumes major contributions from Pf0 and [K]
k39capturefrnstdvvn=((k39capturefrn.*k2omin(2)).^2+(-
k39capturefrn.*SIGMathermalrockstdvvn./SIGMathermalrock).^2).^0.5;
pmuneutronsstdvvn=0.3.*pmuneutrons;

%Plotting Production Rates versus depth

%matrices to pass values

```

```

Mspall=[density gamma horizonfactor spallationfactor caspall caomin(1) kspall k2omin(1)
tis pall tio2min(1) fespall fe2o3min(1)];

[x3,y3]=fplot(@Pspall,[0 350],1e-3,1,[],Mspall);
hold on;
plot(x3,y3(:,1),'-m',x3,y3(:,2),'c--',x3,y3(:,3),'y-',x3,y3(:,4),'k--');

Mmuon =[density 1500.0 horizonfactor muonfactor camu caomin(1) kmu k2omin(1) timu
tio2min(1) femu fe2o3min(1)];

[x4,y4]=fplot(@Pmuon,[0 350],1e-3,1,[],Mmuon);
hold on;
plot(x4,y4(:,1),':m',x4,y4(:,2),'c:',x4,y4(:,3),'y:',x4,y4(:,4),'k:');

legend('Epithermal N','Thermal 35Cl','Thermal 39K','Spallation Ca','Spallation
K','Spallation Ti','Spallation Fe','Muon Ca','Muon K','Muon Ti','Muon Fe');

% ptotal
ptotal=p35nthermal+pnepithermal+pcaspall+pcamu+pkspall+pkmu+p39nthermal+ptispall+ptimu+pfes
pall+pfemu+pmuneutrons;
ptotalstddvn=(p35nthermalstddvn.^2+pnepithermalstddvn.^2+pcaspallstddvn.^2+pcamustddvn.^2+
pkspallstddvn.^2+pkmustddvn.^2+p39nthermalstddvn.^2+ptispallstddvn.^2+ptimustddvn.^2+pfes
allstddvn.^2+pfemustddvn.^2+pmuneutronsstddvn.^2).^0.5;

muratio =
((p35nthermal+pnepithermal).*(0.2.*muonfactor)/(0.8.*spallationfactor+0.2.*muonfactor))+p
camu+pkmu+pfemu+ptimu)/((p35nthermal+pnepithermal).*(0.8.*spallationfactor)/(0.8.*spallatio
nfactor+0.2.*muonfactor))+pcaspall+pkspall+ptispall+pfespall);
muratiostddvn=0;%error in muratio must include spallation and mu prod. by Fe and Ti
factors

ufissionneutrons=0.427.*u(1);
%n production by U238 fission; constant= U atm/ppm* Usf*n yield per fission
if ufissionneutrons==0
    ufissionneutronsstddvn=0;
else
    ufissionneutronsstddvn=ufissionneutrons.*((4.973e-4+(u(2)./u(1)).^2).^0.5);
end;
%error in above, assumes 2.23% combined error in Usf and n yield per
%fission

majorelts=[sio2(1) tio2(1) al2o3(1) fe2o3(1) feo(1) mno(1) mgo(1) cao(1) na2o(1) k2o(1)
p2o5(1) h2o(1) co2(1)];
rsdmajorelts=[sio2(2) tio2(2) al2o3(2) fe2o3(2) feo(2) mno(2) mgo(2) cao(2) na2o(2) k2o(2)
p2o5(2) h2o(2) co2(2)];

alphaneutryields=(majorelts./100)*nyields; %verificar orden!!!
alphaneutryieldsstddvn=((rsdmajorelts.*majorelts./100).^2)*(nyields.^2).^0.5;

ualphaneutrons=u(1)*alphaneutryields(1);
thalphaneutrons=th(1)*alphaneutryields(2);

ualphaneutronsstddvn=(u(2).^2.*alphaneutryields(1).^2+u(1).^2.*alphaneutryieldsstddvn(
1).^2).^0.5;
thalphaneutronsstddvn=(th(2).^2.*alphaneutryields(2).^2+th(1).^2.*alphaneutryieldsstdd
vn(2).^2).^0.5;

bckgdneutrons=ufissionneutrons+ualphaneutrons+thalphaneutrons;
bckgdneutronsstddvn=(ufissionneutronsstddvn.^2+ualphaneutronsstddvn.^2+thalphaneutronsstdd
vn.^2).^0.5;
%combined uncertainties in background neutron production rates

pbckgd=bckgdneutrons.*(c135capturefrn+k39capturefrn);
pbckgdstddvn=(bckgdneutrons.^2.*(c135capturefrnstddvn.^2+k39capturefrnstddvn.^2)+bckgdneut
ronsstddvn.^2.*(c135capturefrn+k39capturefrn).^2).^0.5;

```

```

%Cl-36 from intrinsic neutron production and uncertainty
if strcmp(initcl36, 'steadystate')
    cl36bckgd=pbckgd/lambda;
    cl36bckgdstdvvn=pbckgdstdvvn/lambda;
else
    cl36bckgd=c136concentration.*pbckgd./(ptotal+pbckgd);

cl36bckgdstdvvn=(c136concentrationstdvvn.^2.*pbckgd.^2.*(pbckgd+ptotal).^2+c136concentrati
on.^2.*(pbckgdstdvvn.^2.*ptotal.^2+pbckgd.^2.*ptotalstdvvn.^2)).^0.5/(pbckgd+ptotal).^2;
end;

cosmoc136=c136concentration-cl36bckgd;
cosmoc136stdvvn=(c136concentrationstdvvn.^2+c136bckgdstdvvn.^2).^0.5;

% 4.- Age and erosion rate trade-offs

psp=horizonfactor.*spallationfactor.*(casvall.*caomin(1)+kspall.*k2omin(1)+tispall.*tio2mi
n(1)+femu.*fe2o3min(1));
pmu=horizonfactor.*muonfactor.*(camu.*caomin(1)+kmu.*k2omin(1)+timu.*tio2min(1)+femu.*fe2o
3min(1)+175*0.5*c135capturefrn);
k1 =phistarthermalrock.*(sigma35.*N35+sigma39alpha.*N39);
k2 =FcursDELTAphistarthermalrock.*(sigma35.*N35+sigma39alpha.*N39);
k3 =phistarethrocl.*Iabs35.*N35;
k4 =FDELTAphistarethrocl.*Iabs35.*N35;
k5 =FcursDELTAphistarethrocl.*(sigma35.*N35+sigma39alpha.*N39);
tzeroerosion=-lambda.^-1.*log(1-lambda.*cosmoc136./ptotal);
tzeroerosionstdvvn=(cosmoc136stdvvn.^2.*(ptotal-lambda.*cosmoc136).^-
2+cosmoc136.^2*ptotalstdvvn.^2/(cosmoc136.*lambda.*ptotal-ptotal.^2).^2).^0.5;
tzeroerosioninternalerror=(ptotal-cosmoc136.*lambda).^2.*(cosmoc136stdvvn.^2).^0.5;

%parameters to solve the equation...

plist(6,1)=top;
plist(6,2)=bottom;
plist(1,1)=psp+k1+k3;
plist(1,2)=density/gamma;
plist(2,1)=k2;
plist(2,2)=density/Lthermalrock;
plist(3,1)=k4+k5;
plist(3,2)=density/Lethrock;
plist(4,1)=pmu;
plist(4,2)=density/1500.0;
plist(5,1)=cosmoc136;
plist(5,2)=totalerosion;
plist(7,1)=lambda;
plist(7,2)=0; %marker to indicate how the equation is going to be solved
% 0=both t,e unknown 1=t known, e unknown,2=t unknown,e known
% 0 --> plist(5,2) is totalerosion then t is replaced as
% Teros/eros
% 1 --> t is replaced with the number in plist(5,2), look for erosionrate
% 2 --> erosionrate (from a list) is replaced with the number in plist(5,2)

specifiederosionpair(2) = fzero(@(x) myfun(x,plist),totalerosion/tzeroerosion); %erosion
rate
specifiederosionpair(1) = totalerosion / specifiederosionpair(2); %age

%jo que se cae si le pones 0 a totalerosion

plist(7,2)=1;
plist(5,2)=100000; %to replace t in the function... the lower the ratio the lower this
number normally between 1e4 to 1e6

maxerosionrate = fzero(@(x) myfun(x,plist),0.01); %max erosion rate pasa t=4e4 (linea
anterior), start e=0.001

```

```

%create tvserosionlist
plist(7,2)=2;

for i=1:41
    erosionrate = 0.995 * (i-1) * maxerosionrate / 40;
    plist(5,2) = erosionrate;
    t = fzero(@(x) myfun(x,plist),tzeroerosion);
    tvserosionlist(i,1)=t;
    tvserosionlist(i,2)=erosionrate;
end;

%PLOT of EROSION RATE - AGE TRADEOFF

figure(3);
plot(tvserosionlist(:,1),tvserosionlist(:,2),'g');
axis([0 min(3e6,12*tzeroerosion) 0 1.2*maxerosionrate]);
xlabel('Age [years]');
ylabel('Erosion rate [cm/y]');
title('Age/Erosion Rate Trade-off plot');
text(tzeroerosion,maxerosionrate.*1.1, strcat('age for no erosion =
',num2str(tzeroerosion,'%2.4g'),' years'),'FontSize',10)
line([tzeroerosion tzeroerosion],[0 maxerosionrate],'Color','b','LineStyle','--');
line([tzeroerosion 12*tzeroerosion],[maxerosionrate
maxerosionrate],'Color','b','LineStyle','--');

% end of Calculations

% Display
disp(' ');
display('-----');
display('Final Results');
display(datestr(now));
display(strcat('ID : ',num2str(samplename)));
display('Neutron Capture Results');
display('-----');
disp(' ');display('Thermal Neutrons');
disp(' ');
disp(strcat('Fraction stopped by Cl-35 =
',num2str(cl35capturefrn,'%2.4g'),char(177),num2str(cl35capturefrnstdvvn,'%2.4g')));
disp(strcat('Fraction stopped by major elements = ',num2str(stopping(1),'%2.3f')));
disp(strcat('Fraction stopped by trace elements = ',num2str(stopping(2),'%2.3f')));
disp(strcat('Macroscopic cross section (cm^2/g) = ',num2str(SIGMAscrock,'%2.3f')));
disp(strcat('Mean Free Path (g/cm^2) = ',num2str(LAMBDAthermalrock,'%2.3f')));
disp(strcat('major absorber : ',majorabsorber));

display('Epithermal Neutrons');
disp(' ');
disp(strcat('Fraction captured by Cl-35 =
',num2str(cl35epicapturefrn,'%2.4g'),char(177),num2str(cl35epicapturefrnstdvvn,'%2.4g')));
disp(strcat('Macroscopic resonance Integral (cm^2/g) = ',num2str(Ieffrock)));

disp(' ');display('Radiogenic Neutrons');
disp(' ');
disp(strcat('[U] = ',num2str(u(1),'%2.4g'),char(177),num2str(u(2),'%2.4g'),' [Th] =
',num2str(th(1),'%2.4g'),char(177),num2str(th(2),'%2.4g')));
disp(strcat('Intrinsic Neutron production (n/g/y)=
',num2str(bckgdneutrons,'%2.4g'),char(177),num2str(bckgdneutronsstdvvn,'%2.4g')));
disp(strcat('Background Neutron flux (n/cm^2/y) = ',MISSING));
disp(' ');
display('Scaling Results');
display('-----');
disp(' ');display('Altitude/latitude scaling based on standard atmosphere (ICAO Lal
fit)');
disp(' ');disp(strcat('Altitude/Latitude scaling (spallation) =
',num2str(spallationfactor,'%2.4g')));
disp(' ');disp(strcat('Altitude/Latitude scaling (muons) =
',num2str(muonfactor,'%2.4g')));

```

```

disp(' ');disp(strcat('Fraction of 2Pi flux                               =
',num2str(horizonfactor,'%2.4g')));
disp(' ');disp(strcat('Depth/thickness correction (spallation) =
',num2str(depthfactor,'%2.4g')));
disp(' ');disp(strcat('Depth/thickness correction (thermal n) =
',num2str(nthermalzcorrection,'%2.4g')));
disp(' ');disp(strcat('Depth/thickness correction (epithermal
n)=' ,num2str(nepizcorrection,'%2.4g')));
disp(' ');
display('Production rate Results');
display('-----');
disp(' ');
disp(strcat('Cosmogenic Cl-36 (atom/g) =
',num2str(cosmoc136,'%2.4g'),char(177),num2str(cosmoc136stddvn,'%2.4g')));
disp(strcat('Background Cl-36 (atom/g) =
',num2str(cl36bckgd,'%2.4g'),char(177),num2str(cl36bckgdstddvn,'%2.4g')));
disp(' ');
disp(strcat('Ca spallation rate (atom/g/yr) =
',num2str(pcasvall,'%2.4g'),char(177),num2str(pcasvallstddvn,'%2.4g')));
disp(strcat('K spallation rate (atom/g/yr) =
',num2str(pkspall,'%2.4g'),char(177),num2str(pkspallstddvn,'%2.4g')));
disp(strcat('Ti spallation rate (atom/g/yr) =
',num2str(ptispall,'%2.4g'),char(177),num2str(ptispallstddvn,'%2.4g')));
disp(strcat('Fe spallation rate (atom/g/yr) =
',num2str(pfespall,'%2.4g'),char(177),num2str(pfespallstddvn,'%2.4g')));
disp(strcat('K (n,alpha) (atom/g/yr) =
',num2str(p39nthermal,'%2.4g'),char(177),num2str(p39nthermalstddvn,'%2.4g')));
disp(strcat('Ca (mu, alpha) (atom/g/yr) =
',num2str(pcamu,'%2.4g'),char(177),num2str(pcamustddvn,'%2.4g')));
disp(strcat('K (mu, p2n) (atom/g/yr) =
',num2str(pkmu,'%2.4g'),char(177),num2str(pkmustddvn,'%2.4g')));
disp(' ');
disp(strcat('Thermal n Cl35 capture (atom/g/yr) =
',num2str(p35nthermal,'%2.4g'),char(177),num2str(p35nthermalstddvn,'%2.4g')));
disp(strcat('Epithermal n Cl35 capture (atom/g/yr) =
',num2str(pnepithermal,'%2.4g'),char(177),num2str(pnepithermalstddvn,'%2.4g')));
disp(strcat('Muon induced n capture (atom/g/yr) =
',num2str(pmuneutrons,'%2.4g'),char(177),num2str(pmuneutronsstddvn,'%2.4g')));
disp('----- ');
disp(strcat('Total production (atom/g/yr) =
',num2str(ptotal,'%2.4g'),char(177),num2str(ptotalstddvn,'%2.4g')));
disp(' ');
disp(strcat('Ratio muon/nucleon production = ',num2str(muratio)));
disp(' ');
disp(strcat('[Cl] (ppm) =
',num2str(cl(1),'%2.1f'),char(177),num2str(cl(2),'%2.1g')));
disp(' ');
disp('Age results ');
disp(' ');disp(strcat('age for no erosion =
',num2str(tzeroerosion,'%2.4g'),char(177),num2str(tzeroerosionstddvn,'%2.4g'), ' years'));
disp(strcat('Internal error ...',num2str(tzeroerosioninternalerror)));

```

A.3. Supplementary Information for Antinao et al.: Plio-Pleistocene Exhumation and Surface Uplift of Western Cordillera Principal (33.5°S), Southern Central Andes of Chile

A.3.1. Analytical Results

Table A. U, Th, Sm, He, and Ft correction results

Duluthian Sample ID												grain dimension information										He spectrometry										U, Th, Sm ICP-MS										Ft										Uncertainty (%)										Field sample		Sample age (t)	
RunID	batch	SampleID	grID	w1	w2	w3	wavg	lvsdvd	length	4He(fmol)	Blk(fmol)	Blk. (%)	Re-ext.(fmol)	Re-ext.(%)	238U/235U	%RSD	232Th/232Th0	%RSD	47Sm/149Sm	%RSD	Ft factor	Ft	U	Th	Sm	He	Total	Age (Ma)	Age (gram)	uncert.	ID	Mean	Std. Dev.																																
171	2	GRT-001-1	a	90	90	90	90	256	3.56	0.36	0.53	59.58	0.020	5.55	0.0690	0.3930	0.4675	0.9110	0.0301	1.0920	0.7184	6.43	0.39	0.91	1.09	1.50	6.76	0.69	0.05	GRT-001-1	2.07	0.36																																	
180	2	GRT-001-2	a	82	82	82	82	295	1.04	0.58	35.80										0.6920	7.97	0.97	0.97	1.20	1.50	8.25	1.77	0.15	GRT-001-15																																			
172	2	GRT-001-2	a	105	105	105	105	5	265	4.04	0.52	51.80	0.044	9.05	0.1332	0.5470	0.8584	0.7420	0.0635	0.5930	0.7520	4.50	0.55	0.74	0.50	1.50	4.87	3.97	0.19	GRT-001-2																																			
173	2	GRT-001-3	a	104	104	104	104	5	196	4.91	0.54	8.60	0.420	8.60	0.2637	0.5300	1.6493	0.6390	0.1313	0.5430	0.7304	4.92	0.53	0.64	0.54	1.50	5.24	2.02	0.11	GRT-001-3																																			
173	2	GRT-001-3	b	104	104	104	104	5	185												0.7338	4.60	0.53	0.64	0.54	1.50	4.94	2.01	0.10																																				
173	2	GRT-001-3	c	122	122	122	122	5	199												0.7664	3.18	0.53	0.64	0.54	1.50	3.66	1.92	0.07																																				
173	2	GRT-001-3	d	107	107	107	107	5	191												0.7406	4.31	0.53	0.64	0.54	1.50	4.67	1.99	0.09																																				
173	2	GRT-001-3	e	95	95	95	95	5	195												0.7175	5.67	0.53	0.64	0.54	1.50	5.95	2.06	0.12																																				
175	2	GRT-001-4	a	103	103	103	103	5	222	1.94	0.50	20.60	0.313	15.55	0.1039	0.6370	0.7352	0.3580	0.0540	0.6110	0.7387	4.71	0.64	0.36	0.61	1.50	5.03	2.00	0.10	GRT-001-4																																			
176	2	GRT-001-5	a	84	84	84	84	5	181	2.56	0.66	20.50	0.126	5.08	0.1415	0.3440	1.2628	0.6030	0.1156	0.2880	0.8872	7.54	0.34	0.60	0.29	1.50	7.72	1.79	0.14	GRT-001-5																																			
176	2	GRT-001-5	b	83	83	83	83	5	176												0.8830	7.75	0.34	0.60	0.29	1.50	7.93	1.80	0.14																																				
176	2	GRT-001-5	c	81	81	81	81	5	189												0.6805	8.20	0.34	0.60	0.29	1.50	8.37	1.81	0.15																																				
176	2	GRT-001-5	d	87	87	87	87	5	178												0.6845	6.95	0.34	0.60	0.29	1.50	7.15	1.77	0.13																																				
176	2	GRT-001-5	e	94	94	94	94	5	185												0.7135	5.81	0.34	0.60	0.29	1.50	6.05	1.72	0.10																																				
177	2	GRT-001-6	a	103	103	103	103	5	233	1.61	0.81	33.30	0.004	0.02	0.0667	0.5480	0.5530	0.5410	0.0513	0.6430	0.7418	4.71	0.55	0.54	0.64	1.50	5.04	2.49	0.13	GRT-001-6																																			
177	2	GRT-001-6	b	102	102	102	102	5	239												0.7408	4.81	0.55	0.54	0.64	1.50	5.14	2.49	0.13																																				
177	2	GRT-001-6	c	90	90	90	90	5	240												0.7143	6.43	0.55	0.54	0.64	1.50	6.67	2.58	0.17																																				
178	2	GRT-001-9	a	72	72	72	72	5	190	1.91	0.41	17.60	0.210	10.81	0.1033	0.7840	0.7362	0.7340	0.0566	0.6820	0.6800	10.76	0.78	0.73	0.88	1.50	10.94	2.25	0.25	GRT-001-9																																			
178	2	GRT-001-9	b	79	79	79	79	5	201												0.6763	8.68	0.78	0.73	0.88	1.50	8.90	2.16	0.19																																				
178	2	GRT-001-9	c	69	69	69	69	5	217												0.6438	11.87	0.78	0.73	0.88	1.50	12.03	2.27	0.27																																				
209	3	GRT003-1	a	118	113	102	111	8	250	3.25	0.69	17.50	0.016	0.49	0.1258	1.0480	0.7649	0.5040	0.0744	0.4090	0.7584	3.96	1.05	0.50	0.41	1.50	4.41	2.76	0.12	GRT003-1	2.77	0.23																																	
196	3	GRT003-3	a	101	112	112	108	6	259	6.69	0.74	9.93	0.025	0.38	0.2766	0.4570	1.3609	0.9380	0.1280	0.3470	0.7541	4.22	0.46	0.94	0.35	1.50	4.61	2.72	0.13	GRT003-3																																			
196	3	GRT003-3	b	114	117	109	113	4	263												0.7632	3.80	0.46	0.94	0.35	1.50	4.23	2.69	0.11																																				
223	3	GRT003-4	a	112	120	123	118	6	216	17.17	0.59	3.33	0.031	0.18	0.7891	0.3750	3.3715	0.7150	0.2262	0.3730	0.7634	3.44	0.37	0.71	0.27	1.50	3.85	2.48	0.10	GRT003-4																																			
223	3	GRT003-4	b	122	113	126	120	6	232												0.7893	3.31	0.37	0.71	0.27	1.50	3.73	2.46	0.09																																				
223	3	GRT003-4	c	103	106	108	106	3	227												0.7454	4.40	0.37	0.71	0.27	1.50	4.73	2.54	0.12																																				
223	3	GRT003-4	d	118	115	119	117	2	228												0.7642	3.51	0.37	0.71	0.27	1.50	3.91	2.48	0.10																																				
205	3	GRT003-6	a	115	126	116	119	9	360	5.53	0.69	11.08	0.059	1.07	0.1564	1.4500	1.2633	0.3070	0.1230	0.3270	0.7784	3.58	1.45	0.31	0.33	1.50	4.16	3.14	0.13	GRT003-6																																			
210	3	GRT003-7	a	159	163	163	162	2	407	11.83	0.86	5.26	0.049	0.42	0.4165	0.2860	2.1968	0.6710	0.2258	0.1220	0.8334	1.65	0.29	0.67	0.12	1.50	2.36	2.77	0.07	GRT003-7																																			
220	3	GRT004-10	a	112	107	101	107	6	190	1.63	0.90	28.77	0.004	0.26	0.0323	1.3110	0.3095	0.2880	0.0314	0.7200	0.7404	4.31	3.13	0.29	0.72	1.50	5.56	5.36	0.30	GRT004-10	5.88	0.71																																	
215	3	GRT004-7	a	106	104	107	106	2	246	4.87	0.65	11.84	0.015	0.31	0.0530	1.0620	0.7860	0.6090	0.4255	0.6010	0.7505	4.40	1.06	0.61	0.60	1.50	4.85	6.37	0.31	GRT004-7																																			
214	3	GRT006-1	a	116	105	117	113	7	388	3.86	0.66	14.57	0.001	0.02	0.1109	1.0490	0.8734	0.5390	0.1999	0.4400	0.7752	3.80	1.05	0.54	0.44	1.50	4.27	3.20	0.14	GRT006-1	5	1.06																																	
203	3	GRT006-10	a	100	109	107	105	5	246	7.18	0.75	9.43	0.039	0.53	0.1210	0.4130	0.8258	0.8240	0.1208	0.5910	0.7474	4.50	0.41	0.82	0.59	1.50	4.87	6.06	0.30	GRT006-10																																			
203	3	GRT006-10	b	103	101	99	101	2	218												0.7350	4.92	0.41	0.82	0.59	1.50	5.26	6.16	0.32																																				
204	3	GRT006-11	b	114	110	127	117	9	219	6.15	0.77	11.14	0.008	0.13	0.1505	0.9590	0.9480	0.4770	0.1377	0.4630	0.7831	3.51	0.96	0.48	0.46	1.50	3.99	4.18	0.17	GRT006-11																																			
204	3	GRT006-11	a	115	114	125	118	8	219												0.7631	3.44	0.96	0.48	0.46	1.50	3.93	4.18	0.16																																				
199	3	GRT006-12	b	137	123	116	125	11	262	9.07	0.75	7.61	0.000	0.2029	0.8330	1.0480	0.8610	0.1563	0.3770	0.7811	3.01	0.83	0.86	0.38	1.50	3.59	4.80	0.17	GRT006-12																																				
199	3	GRT006-12	a	122	120	103	115	10	249												0.7646	3.65	0.83	0.86	0.38	1.50	4.14	4.90	0.20																																				
208	3	GRT006-2	a	148	148	159	155	12	380	13.21	0.70	5.05	0.002	0.01	0.2270	0.5530	1.6756	0.7860	0.2103	0.1930	0.8261	1.83	0.55	0.79	0.19	1.50	2.56	4.98	0.13	GRT006-2																																			
206	3	GRT006-3	a	119	136	143	133	12	409	75.75	0.71	0.92	0.141	0.19	0.2278	0.4720	1.2907	0.5270	0.1915	0.1740	0.8043	2.61	0.47	0.53	0.17	1.50	3.09	33.04	1.02	GRT006-3																																			
213	3	GRT006-4	a	107	113	121	114	7	305	5.35	0																																																						

Table A. U, Th, Sm, He, and Fc correction results (continued)

Dalhousie Sample Id		grain dimension information						He spectrometry						U, Th, Sm ICP-MS						Ft						Uncertainty (%)						Age [Ma]		Field sample		Sample age (1)	
Runid	batch	SampleID	grid	lwt	w2	w3	wavg	lwt/idev	length	4He(fmol)	Blk(fmol)	Blk %	Re-ext(fmol)	Re-ext (%)	238U/235U	%RSD	232Th/230Th	%RSD	47Sm/149Sm	%RSD	Ft factor	Ft	U	Th	Sm	He	Total	Age (grain)	uncert.	ID	Mean	Std. Dev.					
222	3	TRP004-10	a	113	113	118	115	3	295	3.25	0.58	15.20	0.012	0.35	0.0812	0.5740	0.3548	0.5230	0.0455	0.7640	0.7475	3.65	0.57	0.52	0.76	1.50	4.09	4.19	0.17	TRP004-10	2.5	1.54					
225	3	TRP004-16	a	107	112	99	106	7	233	3.07	0.62	16.73	0.010	0.32	0.1412	0.7660	1.0344	0.4780	0.0807	0.6320	0.7473	4.40	0.77	0.48	0.63	1.50	4.78	2.14	0.10	TRP004-16							
225	3	TRP004-16	a	109	109	106	108	2	212												0.7473	4.22	0.77	0.48	0.63	1.50	4.61	2.14	0.10								
225	3	TRP004-16	a	109	100	91	100	9	241												0.7371	5.04	0.77	0.48	0.63	1.50	5.37	2.17	0.12								
217	3	TRP004-8	a	116	117	126	120	6	209	0.76	0.68	47.14			0.0511	1.2080	0.6217	0.3630	0.0359	0.6470	0.7666	3.31	1.21	0.36	0.65	1.50	3.90	1.17	0.05	TRP004-8							
109	1	TRP008-1n		137	137	137	137	5	302	4.08	0.44	9.65	0.015	0.37	0.5124	0.2690	1.2118	1.0810	0.6441	1.0330	0.7999	2.43	0.27	1.08	1.03	1.50	3.24	1.57	0.05	TRP008-1N	1.57	0.05					
108	1	TRP008-9		148	148	148	148	5	353	4.37	0.34	7.26	0.187	3.56	0.6091	0.1700	1.7200	0.8170	0.6678	0.3970	0.8187	2.04	0.17	0.82	0.40	1.50	2.69	1.30	0.04	TRP008-9							
57	1	TRP009-2		82	82	82	82	5	152	0.13	0.67	84.50			0.0456	1.5250	0.2910	1.2850	0.1318	2.2230	0.9989	15.20	1.52	1.28	2.22	1.50	15.56	0.64	0.10	TRP009-2	0.64	0.1					
100	1	TRP016-1		170	170	170	170	5	420	8.49	0.38	4.29	0.013	0.15	0.5057	0.5340	1.7912	1.1600	0.7444	0.3470	0.8405	1.48	0.53	1.16	0.35	1.50	2.49	2.71	0.07	TRP016-1	2.65	0.31					
101	1	TRP016-10		90	90	90	90	5	291	1.52	0.38	16.61			0.1406	0.9010	0.8189	0.5300	0.3392	1.6700	0.7203	6.43	0.90	0.53	1.67	1.50	6.89	2.54	0.17	TRP016-10							
99	1	TRP016-2		157	157	157	157	5	377	9.79	0.44	4.28			0.5249	0.3540	1.8804	0.7940	0.7170	0.4150	0.8273	1.78	0.35	0.79	0.42	1.50	2.52	3.05	0.08	TRP016-2							
103	1	TRP016-8		120	120	120	120	5	267	2.51	0.41	14.02	0.038	1.52	0.1871	0.8790	0.7860	0.2300	0.4662	0.8650	0.7740	3.31	0.88	0.22	0.87	1.50	3.84	2.30	0.09	TRP016-8							
102	1	TRP016-9		100	100	100	100	5	279	0.89	0.34	27.64	0.095	10.40	0.0947	0.9470	0.4216	0.8970	0.3074	0.4590	0.7414	5.04	0.95	0.90	0.46	1.50	5.43	1.78	0.10	TRP016-9							
105	1	TRP018-1		135	135	135	135	5	332	4.03	0.43	9.72			0.2510	0.4110	0.8920	0.8910	0.5700	0.3970	0.8015	2.52	0.41	0.89	0.40	1.50	3.12	2.68	0.08	TRP018-1	2.38	0.33					
104	1	TRP018-10		140	140	140	140	5	284	3.03	0.40	11.63	0.039	1.28	0.2307	0.4900	1.0890	1.2540	0.5177	0.3510	0.8027	2.32	0.49	1.25	0.35	1.50	3.09	2.02	0.06	TRP018-10							
107	1	TRP018-4		122	122	122	122	5	232	2.14	0.51	19.17	0.057	2.59	0.1437	0.9000	0.7039	0.8680	0.4182	0.2870	0.7730	3.18	0.90	0.87	0.29	1.50	3.74	2.43	0.09	TRP018-4							
108	1	TRP018-5		101	101	101	101	5	259	1.41	0.58	29.26	0.222	14.60	0.0751	0.4480	0.5468	0.9140	0.2652	0.6190	0.7422	4.92	0.45	0.91	0.62	1.50	5.28	2.74	0.14	TRP018-5							
207	3	TRP019-2		97	96	91	95	3	304	2.05	0.70	25.35	0.005	0.25	0.0889	0.7010	0.5321	0.6630	0.0424	0.8260	0.7331	5.67	0.70	0.66	0.63	1.50	6.00	2.67	0.16	TRP019-2	2.19	0.25					
221	3	TRP019-3	a	108	111	114	111	3	250	3.87	0.60	13.43			0.5249	0.3540	1.8804	0.7940	0.7170	0.4150	0.8273	1.78	0.35	0.79	0.42	1.50	4.23	1.80	0.08	TRP019-3							
221	3	TRP019-3	b	112	110	117	113	4	278												0.7637	3.80	0.39	0.94	0.46	1.50	4.23	1.80	0.08								
212	3	TRP019-4	b	98	99	104	100	3	252	2.07	0.65	23.99	0.042	2.03	0.1052	0.8820	0.5851	0.6300	0.0504	0.2350	0.7378	5.04	0.88	0.63	0.23	1.50	5.37	2.30	0.12	TRP019-4							
202	3	TRP019-5	a	101	105	111	106	5	239	4.03	0.72	15.18	0.036	0.88	0.3035	0.8160	1.2514	0.5860	0.1255	0.5940	0.7481	4.40	0.82	0.59	0.59	1.50	4.80	2.07	0.10	TRP019-5							
202	3	TRP019-5	b	104	109	122	112	9	241												0.7589	3.88	0.82	0.59	0.59	1.50	4.32	2.04	0.09								
202	3	TRP019-5	c	100	108	116	108	8	248												0.7531	4.22	0.82	0.59	0.59	1.50	4.63	2.05	0.09								
224	3	TRP019-6	c	88	92	91	90	2	218	5.56	0.58	9.44	0.020	0.35	0.3367	0.4160	1.5314	0.6080	0.1262	0.3260	0.7095	6.43	0.42	0.61	0.33	1.50	6.65	2.02	0.13	TRP019-6							
224	3	TRP019-6	d	74	78	87	80	7	224												0.6828	8.43	0.42	0.61	0.33	1.50	8.61	2.10	0.18								
224	3	TRP019-6	e	110	107	111	109	2	214												0.7484	4.13	0.42	0.61	0.33	1.50	4.47	1.92	0.09								
224	3	TRP019-6	f	96	99	94	97	3	233												0.7284	5.40	0.42	0.61	0.33	1.50	5.67	1.97	0.11								
224	3	TRP019-6	g	106	105	94	102	7	214												0.7354	4.81	0.42	0.61	0.33	1.50	5.10	1.95	0.10								
226	3	TRP019-7	a	84	84	96	88	7	191	2.16	0.58	21.18			0.1263	0.6660	0.4501	0.4940	0.0600	0.8870	0.6987	6.77	0.67	0.49	0.89	1.50	7.04	2.14	0.15	TRP019-7							
228	3	TRP019-7	b	85	84	92	90	5	201												0.7061	6.43	0.67	0.49	0.89	1.50	6.71	2.12	0.14								
228	3	TRP019-7	c	86	91	93	90	4	199												0.7056	6.43	0.67	0.49	0.89	1.50	6.71	2.12	0.14								
197	3	TRP019-9	a	108	119	109	112	6	207	2.82	0.76	21.22			0.1334	0.4360	0.8540	0.5690	0.0608	0.4410	0.7528	3.88	0.44	0.57	0.44	1.50	4.24	2.22	0.09	TRP019-9							
197	3	TRP019-9	b	96	98	100	98	2	234												0.7314	5.28	0.44	0.57	0.44	1.50	5.55	2.28	0.13								
211	3	TRP020-10		71	78	88	79	9	177	0.60	0.67	52.92			0.0288	0.8490	0.2476	0.7720	0.0173	0.9450	0.6696	6.68	0.84	0.77	0.95	1.50	6.94	2.78	0.25	TRP020-10	2.35	0.6					
198	3	TRP020-6	a	92	94	94	93	1	222	1.73	0.77	30.86			0.0781	1.0310	0.8451	0.6460	0.0681	0.6350	0.7192	5.96	1.03	0.65	0.66	1.50	6.30	1.90	0.12	TRP020-6							
198	3	TRP020-6	b	78	90	83	84	6	222												0.6962	7.54	1.03	0.65	0.66	1.50	7.81	1.96	0.15								

Notes:

- (1) Sample age was calculated as average of valid aliquots, with 1 standard deviation as uncertainty
- (2) Data in bold was discarded (e.g. Farley and Clark, 2006)
- (3) Information for standards in Table B

Table B. Standards and Normal solution information U, Th, Sm ICPMS data

Batch	type	238U/235U	%RSD	232Th/230Th	%RSD	147Sm/149Sm	%RSD
1	SpikeBlkE1 F	0.0013	7.590	0.1294	0.412	0.0061	3.866
1	SpikeBlkE2 F	0.0012	8.348	0.1285	1.428	0.0065	10.791
1	NewNormalE	1.1939	0.617	3.0386	0.846	0.2850	0.929
1	NewNormalE	1.1752	0.669	2.8895	0.724	0.2792	1.587

A.3.2. Matlab® code used for (U-Th-Sm)/He data reduction

```
% (U-Th-Sm)/He data reduction:
%
% Spike:
% Amount: 0.1 ml
% IC: mixed 230/232Th, highly enriched 235/238U, and pure 149Sm
% (Exact IC and ID unimportant, since Normal solution serves to calibrate Spike each time)
%
% NewNormal (Standard Solution):
% Total Amount: 1 ml
% Thorium:
% IC: normal natural abundance (99.999% 232 Th)
% Th concentration = 1.9422 ppb
% Uranium
% IC: normal natural abundance (137.88)
% U concentration of U = 0.9950 ppb
% Samarium:
% IC: normal natural abundance
% Sm concentration = 0.9573 ppb
%
clear all;

AW238=238.02891;
AW232=232.0381;
AW147=146.914893;
lambda238=1.551e-10; %yr-1 from Farley 2002
lambda235=9.849e-10;
lambda232=4.948e-11; %yr-1
lambda147=6.539e-12; %yr-1 Sm-147

% all atomic weights from CRC handbook
NA=6.02e23;
volst=0.001; %(*liters*)
fracU238natural=1-1/137.88;
fracTh232natural=0.99999;
fracSm147natural=0.1502;
concUst =0.9950; %ppb
concThst=1.9422;
concSmst=0.9573;

load('uthsm.mat');
RUsst=0.0072;
RThst=0.00001;
RSmst=13.83/15.02;
RUst=0.0072;
RThst=0.00001;
RSmst=13.83/15.02;

%read info for spike and spiked standard measured...
%it uses only one point, but it can be adapted to incorporate both
%given measurements and to propagate this error into the U, Th, Sm
%determinations

RUsst=uthsm(size(uthsm,1)-1,1);
RUsst=uthsm(1,1);
RThst=uthsm(size(uthsm,1)-1,3);
RThst=uthsm(1,3);
RSmst=uthsm(size(uthsm,1)-1,5);
RSmst=uthsm(1,5);

RUsst=uthsm(3:size(uthsm,1)-2,1);
RThst=uthsm(3:size(uthsm,1)-2,3);
RSmst=uthsm(3:size(uthsm,1)-2,5);
```

```

concU238st = concUst*fracU238natural; %(fracU238natural=1-1/137.88) (*other values are
around*)
Mol238st = concU238st./AW238.*volst./1e6; %vol. must be liters...1e6 is from ppb to g/l)
At238st = Mol238st*NA;

At238spk = At238st.*(RUst-RUsst)./(RUsst-RUspk);
% (*RUst =235/238 ratio of standard solution from initial measurements*)
% (*RUsst=235/238 ratio of spiked standard solution measured, it is called normal*)
% (*RUspk=235/238 ratio of spike solution measured, it is called spike*)

At238sp = At238spk.*(RUspksp-RUspk)./(RUsp-RUspksp); %Atoms in the sample
% (*RUspksp = 235/238 ratio of spiked sample measured*)
% (*RUspk = 235/238 ratio of spike solution measured*)
% (*RUsp = 235/238 ratio of sample, assumed 0.0072*)

concTh232st = concThst.*fracTh232natural ;%(*0.99999 it can be set to 1 without loss of
acc*)
Mol232st = concTh232st./AW232.*volst./1e6;
At232st = Mol232st.*NA;

At232spk = At232st.*(RThsst-RThst)./(RThspk-RThsst); %(*RThst is approx. 0 or 0.00001*)
% (*RThst =230/232 ratio of standard solution measured*)
% (*RThsst=230/232 ratio of spiked standard solution measured*)
% (*RThspk=230/232 ratio of spike solution measured*)

At232sp = At232spk.*(RThspksp-RThspk)./(RThsp-RThspksp); % (*Atoms Th232 in the sample*)
% (*RThspksp = 230/232 ratio of spiked sample measured*)
% (*RThspk = 230/232 ratio of spike solution measured*)
% (*RThsp = 230/232 ratio of sample, assumed 0.00001*)

concSm147st = concSmst.*fracSm147natural; % (*0.1502 according to a JMS2002 paper*)
Mol147st = concSm147st./AW147.*volst./1e6;
At147st = Mol147st.*NA;

At147spk = At147st.*(RSmsst-RThst)./(RSmpk-RSmsst); %(*RSmst is approx. 13.83/15.02*)
% (*RSmsst =149/147 ratio of standard solution initially determined *)
% (*RSmsst=149/147 ratio of spiked standard solution measured*)
% (*RSmpk=149/147 ratio of spike solution measured*)

At147sp = At147spk.*(RSmpksp-RSmpk)./(RSmp-RSmpksp); %(*atoms Sm147 in sample*)
% (*RSmpksp = 149/147 ratio of spiked sample measured*)
% (*RSmpk = 149/147 ratio of spike solution measured*)
% (*RSmp = 149/147 ratio of sample, assumed natural 13.83/15.02*)

% now Ft corrections for all grains
Res1(1:size(uthsm,1)-4,1)=uthsm(3:size(uthsm,1)-2,7);
Res1(:,2)=At238sp;
Res1(:,3)=At232sp;
Res1(:,4)=At147sp;
%
Res1(:,5)=1./uthsm(3:size(uthsm,1)-2,2);% RMS in U atoms, taken same as RMS in ratio
Res1(:,6)=1./uthsm(3:size(uthsm,1)-2,4);
Res1(:,7)=1./uthsm(3:size(uthsm,1)-2,6);

load('dimap.mat'); %structure: average width=1 stdev width=2 length (apex-apex)=3

L=dimap(:,3); %length is always third column
R=dimap(:,1)/2; %radius is width/2 width is first column
%everything is in microns
beta=(2.31.*L+2.*R)./(R.*L); %Farley et al. 96, Geo Cosmo Acta,
%note:valid for truncated prism only
%it needs to be recalculated if used with other geometries...Montecarlo simulation needed
for k=1:size(dimap,1)
    Th(k,1)=Res1(find(Res1(:,1)==dimap(k,4)),3);
    U(k,1)=Res1(find(Res1(:,1)==dimap(k,4)),2);
end;

```

```

a238=1./(1.04+0.245./(Th./U));
a1(1)=-5.13;a1(2)=6.78; %Farley 2002
FTU238=1+a1(1).*beta+a1(2).*beta.^2;
a2(1)=-5.9;a2(2)=8.99;
FTTh232=1+a2(1).*beta+a2(2).*beta.^2;
MeanFT=a238.*FTU238+(1-a238).*FTTh232; %Farley 2002

load('he.mat');
%L,R,beta,V,MeanFT are sorted according to the order of dimap, col. 4, LabId
%calculate volumes
factpyr=0.72; %relation h/r on pyramid for apatites 0.72+-0.05
npyr=2;%assumes all is bypyramidal, but it can be easily adapted to read sample-specific
data
V=L.*3./2.*sqrt(3).*R.^2-npyr.*factpyr.*sqrt(3).*R.^3; %cubic micrometers

%He splitting and individual grain age calcs

for k=1:size(dimap,1)
    Het(k,1)=He(find(He(:,6)==dimap(k,4)),1).*1e-15*6.02e23; %total He atoms, column 1
    Age(k,1)=Res1(find(Res1(:,1)==dimap(k,4)),2);%total U atoms
    Age(k,2)=Res1(find(Res1(:,1)==dimap(k,4)),3);%total Th atoms
    Age(k,3)=Res1(find(Res1(:,1)==dimap(k,4)),4);%total Sm atoms
    Age(k,14)=Res1(find(Res1(:,1)==dimap(k,4)),5);%relative error U from ratio error (not
propagated!)
    Age(k,15)=Res1(find(Res1(:,1)==dimap(k,4)),6);%same for Th
    Age(k,16)=Res1(find(Res1(:,1)==dimap(k,4)),7);%same for Sm
end;
for k=1:size(dimap,1)
    %volumetric fraction
    Vtot(k,1)=sum(V(find(dimap(:,4)==dimap(k,4))));
end;
Het(:,2)=Het(:,1).*V./Vtot;
Age(:,4)=Age(:,1).*V./Vtot;
Age(:,5)=Age(:,2).*V./Vtot;
Age(:,6)=Age(:,3).*V./Vtot;
Age(:,7)=Het(:,2);
Age(:,8)=MeanFT; %MeanFT in case of regular samples, 1 in case of Durango standard
%proportional to volume He,U,Th,Sm, He proport. is also recorded as column2 of Het
%columns are 1:U total, 2:Th total, 3:Sm total, 4:U crystal, 5:Th crystal,
%6: Sm crystal, 7: He crystal, 8: Mean FT
%now gets the age... and then corrects for mean FT
for k=1:size(dimap,1);
Age(k,9)= fzero(@(x) Age(k,7)-8.*Age(k,4).*(exp(lambda238*x)-1)-
7./137.88.*Age(k,4).*(exp(lambda235*x)-1)-6.*Age(k,5).*(exp(lambda232*x)-1)-
Age(k,6).*(exp(lambda147*x)-1), 1e5);
end;
Age(:,10)=Age(:,9)./Age(:,8)./1e6;%Ma
Age(:,11)=dimap(:,4);%index LabId in dimap.
Age(:,12)=dimap(:,1);%dimensions of the grain-width microns
Age(:,13)=2.1e5.*Age(:,12).^(-2.31);%uncertainty in Ft ,relative (%), if Ft=1 then
uncertainty=0 (Durango)
% Age...14,15,16 uncertainties of U,Th,Sm relative%
Age(:,17)=1.5;%relative uncertainty of He measurement... (%) at Dalhousie
Age(:,18)=sqrt(Age(:,13).^2+Age(:,14).^2+Age(:,15).^2+Age(:,16).^2+Age(:,17).^2);%estimate
of error, grain, in (%)

```